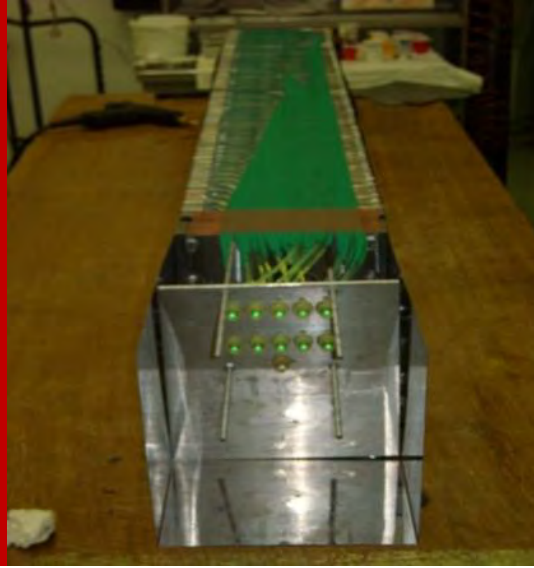
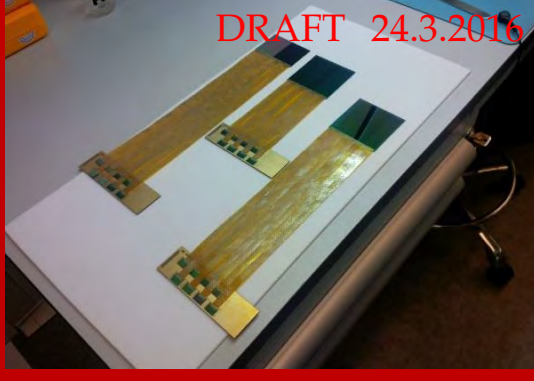
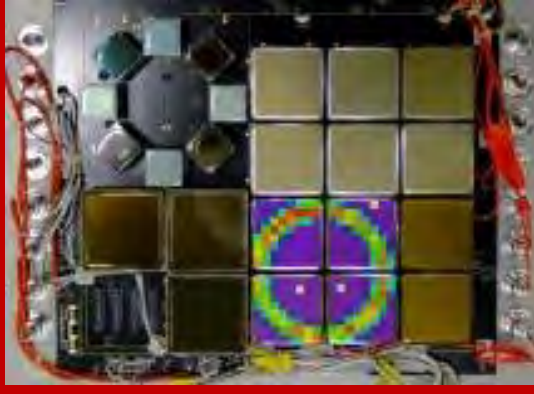
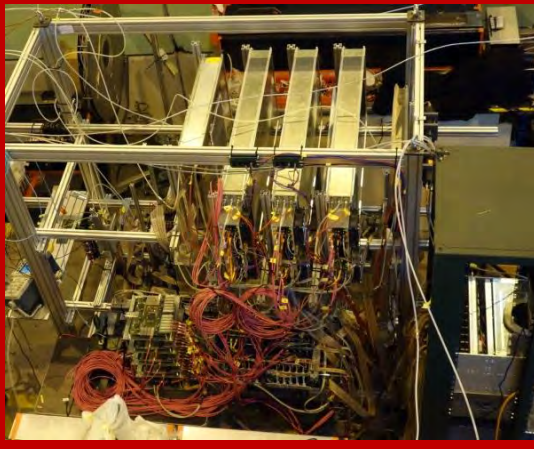
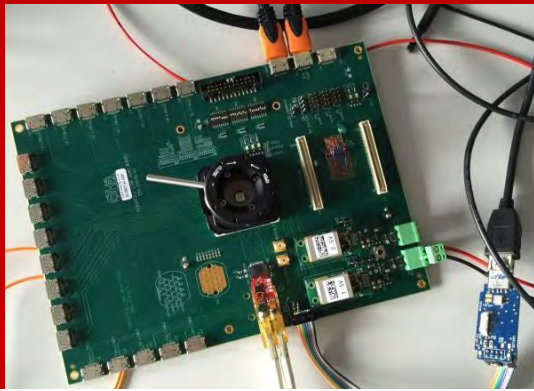


CBM PROGRESS REPORT 2015

Compressed Baryonic Matter Experiment at FAIR



DRAFT 24.3.2016 16:51

CBM Progress Report 2015

ISBN 978-3-9815227-3-0

Editors: Volker Frieze, Christian Sturm and Alberica Toia
v.frieze@gsi.de c.sturm@gsi.de a.toia@gsi.de

Reviewers: C. Blume, S. Chattopadhyay, V. Frieze, N. Herrmann, J. Heuser, C. Höhne, W. Müller, C. Müntz,
P. Senger, C. Sturm, A Toia

©2016 GSI Helmholtzzentrum für Schwerionenforschung GmbH, D-64291 Darmstadt, Germany
<http://www.gsi.de>

Printed in Darmstadt by GSI ????

This work was supported by
Romanian NASR/contract RO-FAIR F02 and NASR/NUCLEU Project PN09370103
National Natural Science Foundation of China under Grant No.11420101004, 11461141011 and 11275108
Ministry of Science and Technology under Grant No. 2015CB856905

BMBF grant 05P12VHFC7
EU/FP7-HadronPhysic3/WP19
European Union's Horizon 2020 research and innovation program under grant agreement No 654168

Several of the contributions to this volume also appear in the GSI Scientific Report 2015.

Preface

Dear colleagues,

— text to be added —

Darmstadt, March 2016

Volker Friese, Christian Sturm and Alberica Toia

Contents

Preface	i
Overview	1
P. Senger and the CBM Collaboration: <i>Status of the Compressed Baryonic Matter experiment at FAIR</i>	1
Magnet	3
Yu.V. Gusakov et al.: <i>Feed box for CBM superconducting dipole magnet</i>	4
Yu.V. Gusakov et al.: <i>CBM superconducting dipole magnet</i>	5
P. Kurilkin et al.: <i>The quench protection scheme based on the heating of the CBM magnet coil</i>	6
P. Kurilkin et al.: <i>3D calculations for the quench protection scheme based on the heating of the CBM magnet coil</i>	7
Micro-Vertex Detector	9
S. Amar-Youcef et al.: <i>CBM MVD simulation - performance and status</i>	10
D. Doering et al.: <i>High voltage CMOS Monolithic Active Pixel Sensors manufactured in a 0.18 μm CMOS process</i>	11
M. Koziel et al.: <i>Status of the CBM-MVD PRESTO Project</i>	12
T. Bus et al.: <i>Radiation damage due to neutron capture in boron doped silicon</i>	13
Silicon Tracking System	15
H. R. Schmidt and J. M. Heuser: <i>The CBM Silicon Tracking System: towards production readiness</i>	16
J. Heuser et al.: <i>Progress with micro-strip sensors for the CBM Silicon Tracking System</i>	18
E. Lavrik, I. Panasenکو and H.-R. Schmidt: <i>Optical quality assurance procedures for STS silicon sensors</i>	19
P. Larionov: <i>Automated quality assurance for the STS sensors of the CBM experiment</i>	20
I. Panasenکو et al.: <i>Equipment and procedures for electrical quality assurance of CBM-STs silicon microstrip sensors</i>	21
I. Momot et al.: <i>Charge collection of n-irradiated prototype CBM-STs microstrip sensors</i>	22
I. Momot et al.: <i>Charge collection studies for prototypes of CBM-STs sensors with the Alibava readout system</i>	23
V. Dobishuk et al.: <i>Characterization of CBM silicon microstrip sensors bonded by microcables to Beetle readout chips</i>	24
E. Friske and H. R. Schmidt: <i>A scalable neutron source for STS detector radiation hardness tests</i>	25
D. Dementyev and Yu. Murin: <i>Dependence of signal amplitude and noise of the n-XYTER v2.0 ASIC on capacitive input load</i>	27
J. Lehnert and P. Kozcon: <i>SEU Tests with the STS-XYTER Version 1 ASIC</i>	28
K. Kasinski et al.: <i>STS-XYTER2, a prototype detector readout chip for the STS and MUCH</i>	29
A. Rodriguez Rodriguez and J. Lehnert: <i>Test of prototype components for the CBM-STs readout chain</i>	30
S. Löchner, P. Koczoń and A. Rost: <i>Radiation hardness tests of electronic components for CBM-STs low voltage power supply</i>	31
V. M. Borshchov et al.: <i>Pre-series production of microcables for STS detector modules at LTU Ltd</i>	32
T. Blank et al.: <i>Investigation on low-mass copper flex cables for the STS detector</i>	33
C. Simons et al.: <i>Development of a workflow for the CBM-STs module-assembly</i>	34
C. Simons et al.: <i>Test sockets for quality measurements during the CBM-STs module assembly</i>	35
A. Sheremetev et al.: <i>Development of tooling for the STS module assembly at JINR's VB LHEP assembly laboratory</i>	36
S. Belogurov et al.: <i>Progress with the integration of the CBM Silicon Tracking System</i>	37

E. Lavrik: <i>Thermal simulations of CBM-STS read-out boards</i>	38
Ring Imaging Cherenkov Detector	39
J. Bendarouach and C. Höhne: <i>Design of a control and monitoring system for the mirror alignment of the CBM RICH detector</i>	40
J. Förtsch et al.: <i>Development of a MAPMT test stand and first results</i>	41
I. Kres, C. Pauly and K.-H. Kampert: <i>Deriving the effective focal plane for the CBM-RICH detector</i>	43
S. Lebedev, C. Höhne and E. Ovcharenko: <i>Implementation of the new RICH geometry in CBMROOT</i>	44
S. Lebedev and C. Höhne: <i>First simulation results with the new RICH geometry</i>	45
S. Lebedev and C. Höhne: <i>Electron identification performance with the new RICH detector</i>	46
E. Lebedeva and C. Höhne: <i>Size of the PMT plane vs. low-mass di-electron reconstruction</i>	47
T. Mahmoud and C. Höhne: <i>Optimization of the RICH geometry</i>	48
E. Ovcharenko et al.: <i>Update of the MC-geometry of the RICH detector</i>	50
E. Ovcharenko et al.: <i>Development of the magnetic shielding box for the CBM RICH camera</i>	51
E. Ovcharenko, S. Belogurov and C. Pauly: <i>Study of p-terphenyl WLS effect on timing in the CBM RICH prototype</i>	52
C. Pauly et al.: <i>CBM-RICH readout chain and data rates</i>	54
J. Eschke et al.: <i>Ordering of 1100 MAPMTs H12700 for the CBM-RICH photon detector</i>	56
T. Mahmoud et al.: <i>Radiation hardness tests of photon sensors for the CBM-RICH</i>	57
Ya. Berdnikov et al.: <i>CBM RICH mechanical design status</i>	60
J. Adamczewski-Musch et al.: <i>RICH summary</i>	62
Muon System	63
E. Nandy and S. Chattopadhyay: <i>Basic performance study of the new MUCH geometry for CBM</i>	64
S. Ahmad et al.: <i>Simulation of the beam pipe for MUCH</i>	65
E. Atkin et al.: <i>Prototype ASIC for Muon Chambers</i>	66
A. Kumar et al.: <i>Effect of parameter-settings of n-XYTER, self triggered electronics for CBM-MUCH</i>	67
S. Mandal et al.: <i>Control of XYTER emulator from DPB through GBTX emulator for the CBM-MUCH detector</i>	69
V. S. Negi et al.: <i>Design and development of a low-voltage distribution board for the CBM-MUCH</i>	70
Transition Radiation Detector	71
C. Blume: <i>Summary on the TRD project</i>	72
J. Book and C. Blume: <i>Physics performance of the CBM-TRD in Au+Au collisions at the SIS100</i>	75
C. Bergmann et al.: <i>Combined MWPC prototype test of Münster and Frankfurt using SPADICv1.0 data taking at CERN-SPS/T2-H4 in 2015</i>	76
A. Bercuci et al.: <i>Calibration and in-beam operation of the two-dimensional MWPC</i>	77
M. Kohn et al.: <i>Fe source measurements with CBM-TRD detector prototypes</i>	79
C. Bergmann et al.: <i>Construction of the first large prototypes for the CBM-TRD</i>	80
M. Tanha et al.: <i>CBM-TRD prototype tests in Frankfurt</i>	81
M. Kohn et al.: <i>Test of SPADICv1.0 readout on Bucharest CBM-TRD detector prototypes</i>	82
P. Kähler et al.: <i>Stress-test of a MWPC prototype from Münster reproducing meteorologic pressure changes</i>	83
G. Caragheorgheopol et al.: <i>First performance studies for FASP-02</i>	84
Time-of-Flight Detector	85
C. Simon et al.: <i>Narrowing down the MRPC design with heavy-ion beams at CERN/SPS</i>	86
P. Lyu et al.: <i>Performance of Strip-MRPC for CBM-TOF in beam test</i>	88
P. Lyu et al.: <i>A prototype of pad-readout MRPC towards CBM-TOF</i>	89
M. Petriş et al.: <i>Performance of MGMSRPC for the inner zone of the CBM-TOF wall in heavy ion beam tests</i>	91
V. Aprodu et al.: <i>MGMSRPC prototype with transmission line impedance tuned through the width of the readout strip</i>	93
V. Aprodu et al.: <i>Single - sided MGMSRPC prototype with 100 Ω transmission line impedance</i>	94
R. Sultanov et al.: <i>Progress in Ceramic RPCs for the Beam Fragmentation T0 Counter</i>	95
Calorimeters	97
S.G. Reznikov et al.: <i>Performance studies of the PSD readout board prototype.</i>	98

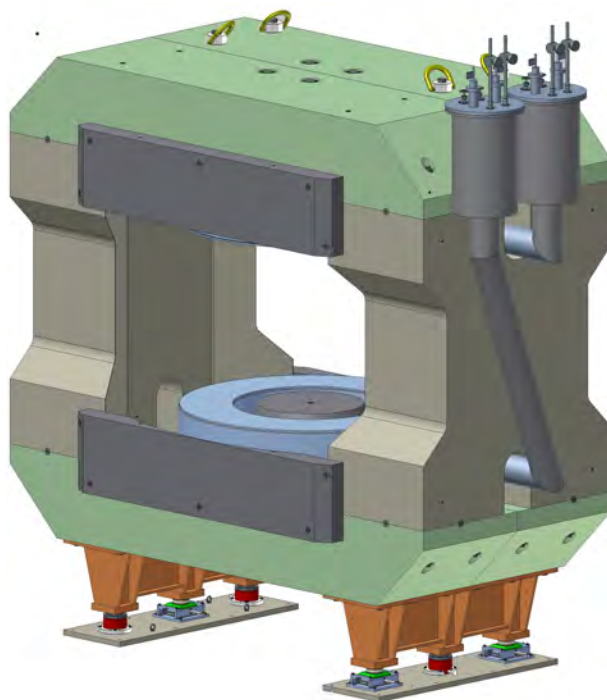
DAQ and Online Event Selection	99
W. Zabolotny et al.: <i>The AFCK Board as the Data Processing Board prototype for CBM experiment</i>	100
C. de J. García Chávez, C. E. Muñoz Castillo and U. Kebschull: <i>Status Update of the Feature Extraction Framework for Automatic FPGA Firmware Generation</i>	102
Swagata Mandal et al.: <i>Control of XYTER emulator from DPB through GBTX emulator for MUCH detector</i>	103
L. Meder and J. Becker: <i>Timing Synchronizer System Developments for pre-production Beam Test Setups</i>	104
A. Oancea and U. Kebschull: <i>Development of a channel layer for control and communication via GBT-SCA</i>	105
J.A. Lucio Martínez, J. Gebelein and U. Kebschull: <i>A low cost fault tolerant Commercial Off the Shelf MCU adapted with RTEMS/EPICS for controls and instrumentation</i>	106
D. Hutter, J. de Cuveland and V. Lindenstruth: <i>CBM FLES input interface developments</i>	107
H. Hartmann, J. de Cuveland and V. Lindenstruth: <i>The CBM first-level event selector, timeslice building and availability studies</i>	108
Computing	109
H. Malygina and V. Friese: <i>Determination of the cluster position in the CBM-STs</i>	110
H. Malygina, V. Friese and M. Zyzak: <i>Estimation of the hit position error in the CBM-STs</i>	111
G. Kozlov and I. Kisel: <i>Time-based cluster finder for the CBM-STs detector</i>	112
P.-A. Loizeau, N. Herrmann and the CBM ToF working group: <i>Improvements to the CBM TOF simulation in CBMROOT</i>	113
A. Zinchenko et al.: <i>Further development of the “vector finding” method for track reconstruction in the CBM-MUCH</i>	114
T. O. Ablyazimov and V. V. Ivanov: <i>Visualization of track reconstruction in the MUCH detector</i>	115
E. P. Akishina et al.: <i>Development of databases for the CBM experiment</i>	116
Physics Performance	117
P. P. Bhaduri and A. Toia: <i>J/ψ detection via di-muon channel in 15 A GeV Ni+Ni collisions with the CBM detector at FAIR</i>	118
Partha Pratim Bhaduri and Alberica Toia: <i>Simulation of di-muon continuum from correlated open charm decay at FAIR</i>	119
Hamda Cherif, Iouri Vassiliev and Alberica Toia: <i>Online reconstruction of Multi-strange hyperons at SIS 100</i>	121
I. Kisel et al.: <i>Σ⁺ and Σ⁻ reconstruction by the missing mass method</i>	123
S.M. Kiselev: <i>Reconstruction of ω(782), η'(958), Σ⁺ and Σ⁰ with ECAL in p+C at SIS-100</i>	124
V. Klochkov and I. Selyuzhenkov: <i>Centrality determination in heavy-ion collisions with the CBM experiment</i>	125
E. Krebs, T. Galatyuk and J. Stroth: <i>Background rejection in the dielectron analysis with the CBM Micro-Vertex Detector</i>	126
V.P. Ladygin et al.: <i>Deuteron coalescence for central Au + Au collisions at 4 A·GeV</i>	127
S. Reinecke et al.: <i>Results on the reconstruction of π⁰ with the conversion method</i>	128
I. Kisel, I. Vassiliev and M. Zyzak: <i>Reconstruction of D⁰ with KF Particle Finder</i>	129
I. Kisel, I. Vassiliev and M. Zyzak: <i>Hypernuclei reconstruction at the CBM experiment</i>	130
A. Weber, S. Lebedev and C. HÅrthne: <i>Feasibility studies for the measurement of J/ψ mesons in central Au+Au collisions at 25 AGeV beam energy</i>	131
I. Kisel et al.: <i>Reconstruction of dimuons with KF Particle Finder</i>	132
CBM Physics	133
S. Bashir, S. Ahmad and M. Farooq Mir: <i>Mass and Quark number dependence of elliptic flow with the AMPT model at FAIR Energies</i>	134
Publications	135
Activities	138
Collaboration	141

Status of the Compressed Baryonic Matter experiment at FAIR

P. Senger and the CBM Collaboration

— To be added —

Superconducting Dipole Magnet



Feed box for CBM superconducting dipole magnet *

Yu.V. Gusakov^{†1}, A.V. Bychkov¹, P.K. Kurilkin¹, V.P. Ladygin¹, A.I. Malakhov¹, and A.V. Shabunov¹

¹LHEP-JINR, Dubna, Russian Federation

The CBM superconducting dipole magnet has a total of about 3.5 tons cold mass, which needs at least 320.3 MJ cool-down energy from room temperature down to its operation temperature around 4 K [1]. The operating current of the magnet is about 690 A and provides a magnet bending power of ~ 1 T·m. A design of the cryogenic input lines, current leads and feed boxes has been performed to satisfy these working conditions.

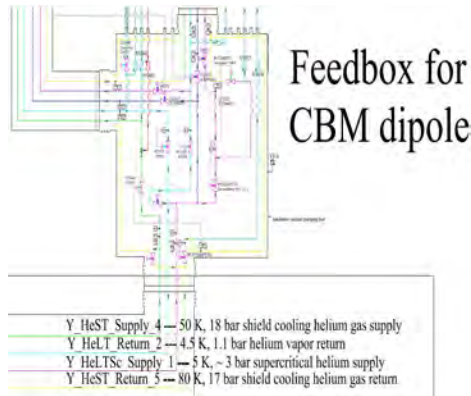


Figure 1: Flow scheme of feed box.



Figure 2: 3D model view of the feed box for upper coil.

Fig.1 shows the flow scheme of the cryogenic feed-box. During cool-down the cooling flow firstly cools the

two shields of the coils and afterwards the two cold masses in series. In such a way the temperature gradient over the shield structures and over the cold masses of the two coils could be conveniently adjusted, especially during the cooldown phase from 300 K to 100 K. During normal operation the two separate liquid helium baths for the upper and lower coils are to be re-filled with liquid helium independently by two JT valves. 3D model view of the feed box for upper coil is presented in Fig.2.

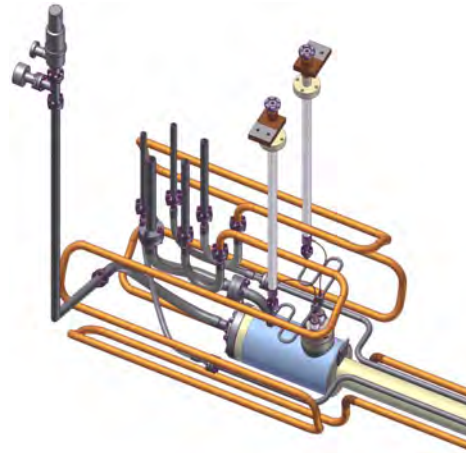


Figure 3: Helium pipes and current leads of the feed box for upper coil.

The helium pipes and current leads of the feed box for upper coil are shown in Fig.3. The vacuum vessel has flanges for connecting to the external cryogenic line, the turbo molecular pump, two 1000 A current leads, the multi-pin feed-through with plug connectors, the safety valve of the vessel and the warm multipurpose helium line (quench gas collection). Inner helium vessel containing 10 l of liquid helium has four flanges. The high voltage feed-through CF40HC8-CE-SST95 is connected to the top flange. It is necessary for passing superconducting wires with vaporized helium to current leads. The second flange is for the multi-pin feed-through with plug connectors. The third flange is connected to the helium return line. The last flange is connected through built-in safety valve to the warm multi-purpose helium line (for quench gas collection).

References

- [1] The CBM collaboration, Technical Design Report for the CBM Superconducting Dipole Magnet, Darmstadt 2014.

* Work supported by GSI(SIS)/GSI(ESR)/GSI(UNILAC)/GSI(PHELIX)/HI Mainz/HI Jena/HIC4FAIR/HGShire/EU, EURONS contract No. 506065/GSI cooperation with university Mainz/Helmholtz-Nachwuchsgruppe

[†] Iouri.Goussakov@cern.ch

CBM superconducting dipole magnet *

*Yu.V. Gusakov^{†1}, A.V. Bychkov¹, P.K. Kurilkin¹, V.P. Ladygin¹, A.I. Malakhov¹, G. Moritz²,
P. Senger², and A.V. Shabunov¹*

¹LHEP-JINR, Dubna, Russian Federation; ²GSI, Darmstadt, Germany

The CBM superconducting dipole magnet [1] has to provide the vertical magnetic field with a bending power of 1 T·m on the length 1m from the target. It is of H-type with a warm iron yoke/pole and cylindrical superconducting coils in two separate cryostats. The potted coil has 1749 turns. The wire, similar to the CMS wire, has Nb-Ti filaments embedded in a copper matrix and is soldered in a copper stabilizer with a total Cu/SC ratio of about 13 in the conductor. The operating current and the maximal magnetic field in the coils are 686 A and 3.25 T, respectively.

A full 3D model of CBM superconducting dipole magnet was completed by the feed boxes for the top and bottom superconducting coils presented in Fig.1. Each of the sections includes an inner helium vessel, thermal shield and vacuum vessel. The vacuum vessel has flanges for connecting to the external cryogenic line, the turbo molecular pump, two 1000 A current leads, the multipin feedthrough with plug connectors, the safety valve of the vessel and the warm multipurpose helium line (quench gas collection). Also, the vacuum vessel and the heat shield have a large diameter access hole to connect pipes of the external cryogenic line with helium pipes of coils. All these connections are made by means flexible metal hoses. Internal helium vessel containing 10 liters of liquid helium, and has four flanges.

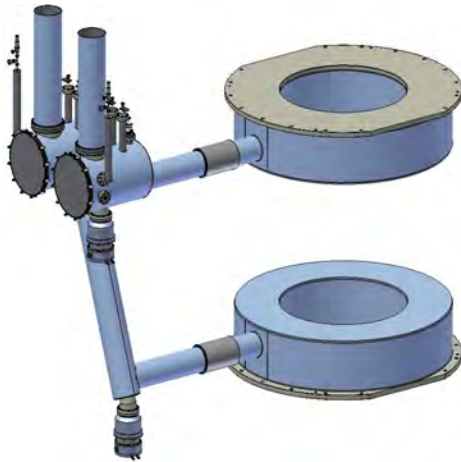


Figure 1: 3D model of cryostats with the feed boxes.

The 3D quench calculations have been performed for

* Work supported by GSI(SIS)/GSI(ESR)/GSI(UNILAC)/GSI(PHELIX)/HI Mainz/Hi Jena/HIC4FAIR/HGShire/EU, EURONS contract No.506065/GSI cooperation with university Mainz/Helmholtz-Nachwuchsgruppe

[†] Iouri.Goussakov@cern.ch

two quench protection schemes. One of them is based on the extraction of the energy stored in CBM magnet via external dump resistor of 1.9-2.1 Ohm. In this case around 80-86 % of the energy stored in the magnet (~5 MJ) will be dissipated outside of the cryostat [2]. Fig. 2 demonstrates the temperature distribution in the cross section of the coil winding when the 2.1 Ohm dump resistor is used. The maximum “hot-spot” temperature is about 70 K. The other quench protection scheme is based on the heating of the superconducting coil [3]. The quench protection system based on the energy extraction via dump resistor with resistance of 1.9-2.1 Ohm was chosen for CBM magnet due to the lower temperature gradient in the coil.

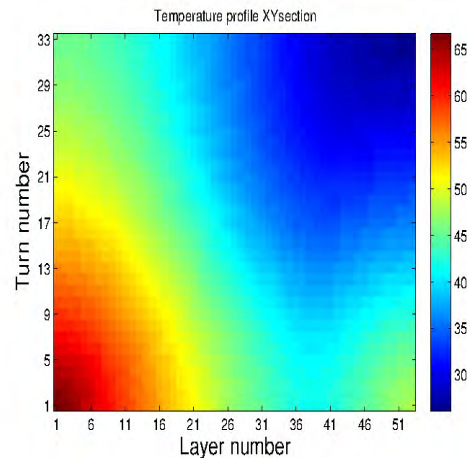


Figure 2: The temperature distribution in the cross section of the coil winding with the 2.1 Ohm dump resistor.

The electromagnetic calculation has been performed for the CBM dipole magnet with the distance between the poles of 1550 mm, what is 150 mm larger than required by TDR [1]. The bending power of enlarged magnet is about 0.88 T·m with the nominal operating current. The current must be increased by ~25% to reach the field integral of ~1 T·m [1]. However, in this case the reaction forces in the coil supports will increase by ~38%, what would require to change significantly the magnet design.

References

- [1] The CBM collaboration, Technical Design Report for the CBM Superconducting Dipole Magnet, Darmstadt 2014.
- [2] P.Kurilkin et al., CBM Progress Report 2013, Darmstadt 2014, p.8.
- [3] P.Kurilkin et al., CBM Progress Report 2015, Darmstadt 2016, to be published.

The quench protection scheme based on the heating of the CBM magnet coil*

P. Kurilkina[†], A. Bychkov, Yu. Gusakov, V. Ladygin, A. Malakhov, and A. Shabunov

LHEP-JINR, Dubna, Russian Federation

The CBM magnet is a H-type dipole, having two circular superconducting coils in two separate cryostats like the SAMURAI magnet at RIKEN [1]. The coil design for the CBM magnet is based on the design of the FAIR SuperFRS dipole. The detailed information about coil and conductor structure can be found in [2].

For design of any superconducting magnet, an analysis of its stability during the quench processes is necessary. The system based on the heating of the outer layer of the coil was considered as one of possible option of quench protection scheme for CBM dipole magnet, more suitable for the production of the superconducting coil by TOSHIBA company [1]. This note presents the results of the 1D quench simulation in case of the heating of the outermost layer of the CBM magnet coil.

The magnet power supply and quench protection system are presented in Fig.1. The superconducting coil is connected in parallel with the low-temperature (“cold”) diodes and a copper heater wire that are connected in series. In case of a quench, the coils are cut off from the power supply, and the current flows in the closed circuit consisting of the superconducting coil, the diodes and the heater wire. The outermost layers of both coils are forced to quench simultaneously due to the heat generated by the heater wire.

Fig.2 and Fig.3 present the voltage and the temperature distribution in the cross section of CBM magnet coil in case when the quench appears in the outer layer of the coil, respectively. For the heating of the outermost layer of the coil, the copper heaters with 35 turns of wire with the cross section $2.5 \times 3.0 \text{ mm}^2$ were used.

The current decay lasts 25 s (10% In). The maximum quench voltage is about 1200 V. It is less than the maximum level of quench voltage of 2 kV. The maximum heating of the winding occurs in the outer layers of the magnet coil and the maximum “hot-spot” temperature is about 135 K. The temperature difference between outer and inner layers of the coil winding is 90 K.

The numerical codes to perform the 1D quench simulation for the quench protection system based on the heating of the outer layer of the coil is developed. The results show the large temperature gradient in the CBM magnet coil cross section.

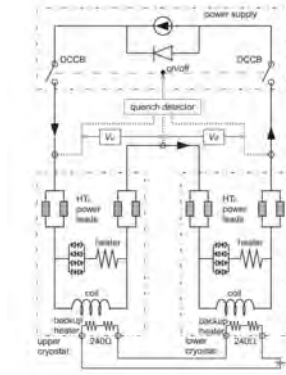


Figure 1: The power supply and quench protection scheme for CBM magnet, based on the coil heating. The arrows show the direction of current flow.

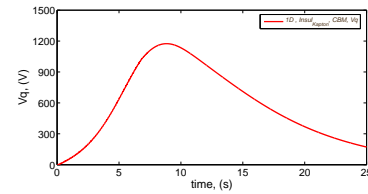


Figure 2: The results of the 1D quench simulation for the quench voltage as a function of a time.

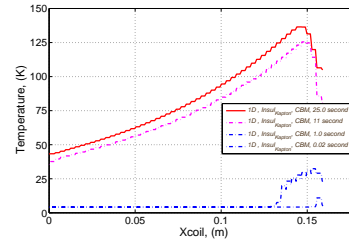


Figure 3: The results of the 1D quench simulation for the temperature distribution in the coil cross section. The blue, magenta and red curves correspond to the 0.02, 1.0, 11 and 25 seconds since the beginning of quench.

References

- [1] H. Sato et al., IEEE Transactions on Applied Superconductivity, **23** No.3 (2013) 4500308
- [2] The Technical Design Report for the CBM Superconducting Dipole Magnet.
http://www.fair-center.eu/fileadmin/fair/experiments/CBM/TDR/CBM_magnet.TDR_31_10_2013-nc.pdf

* Work supported by GSI(SIS)/GSI(ESR)/GSI(UNILAC)/GSI(PHELIX)/HI Mainz/Hi Jena/HIC4FAIR/HGShire/EU, EURONS contract No. 506065/GSI cooperation with university Mainz/Helmholtz-Nachwuchsgruppe

[†] pkurilkina@jinr.ru

3D calculations for the quench protection scheme based on the heating of the CBM magnet coil *

P. Kurilkin^{†1}, P. Szwangruber², E. Floch², F. Toral³, V. Ladygin¹, and A. Malakhov¹

¹LHEP-JINR, Dubna, Russian Federation; ²GSI, Darmstadt, Germany; ³CIEMAT, Madrid, Spain

The CBM magnet[1] is an important part of CBM experimental setup. It will store about 5.15 MJ at its nominal current of 686 A. The coil design for the CBM magnet is based on the design of the FAIR Super-FRS dipole. Two different quench protection schemes were proposed for CBM dipole magnet. One of them is based on the energy evacuation via external dump resistor[2]. The other is based on the heating of the outer layer of coil and its details can be found in [3].

The numerical codes based on CIEMAT program[4] were developed to perform the 3D quench simulation for the quench protection system based on the heating of the outer layer of the coil. This note presents the results of the quench simulation in case of the heating of the outermost layer of the CBM magnet coil. The calculation takes into account the field map distribution in the coil cross section of CBM magnet and dependence of the inductance as function of current[2].

Fig.1 presents the temperature distribution in the cross section of CBM magnet coil in case when the quench appears in the inner layer of the winding. For the heating of the outer layer of the coil, the copper heaters with 33 turns of wire with the cross section of $2.02 \times 3.25 \text{ mm}^2$ were used. The worst case is the appearance of a quench in the outer layer of winding of the CBM magnet coil. Fig.2 and Fig.3 present the simulation results in case of the quench appearance in the outer layer of winding. 33 turns of copper wire with cross-section of $2.02 \times 3.25 \text{ mm}^2$ and $3.02 \times 3.25 \text{ mm}^2$ were used to simulate the coil heating, respectively. In this case the maximum heating of winding of the CBM magnet coil occurs in the few outer layers. The use of two different heaters lead to a similar results.

The 3D quench calculations were done for the quench protection system based on the heating of the outer layer of the CBM magnet coil. The obtained results show the large temperature gradient in the coil cross section in case of the heating of the coil. The maximum "hot-spot" temperature is about 140 K. The quench protection system based on the energy extraction via dump resistor with resistance of 1.9-2.1 Ohm was chosen for CBM magnet due to the lower temperature gradient in the coil.

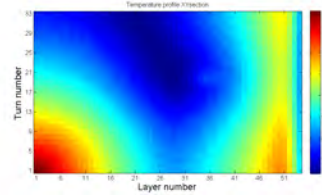


Figure 1: 3D quench simulation - Temperature distributions in the cross section of CBM magnet coil. The quench appeared in the inner layer of coil. Heater cross-section is $2.02 \times 3.25 \text{ mm}^2$

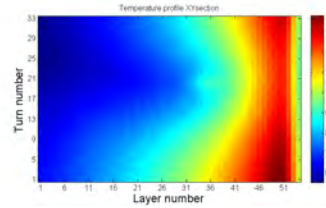


Figure 2: 3D quench simulation - Temperature distributions in the cross section of CBM magnet. The quench appeared in the outer layer of coil. Heater cross-section is $2.02 \times 3.25 \text{ mm}^2$

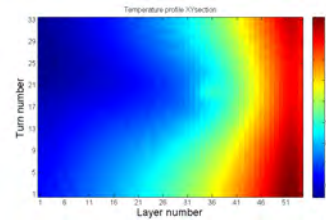


Figure 3: 3D quench simulation - Temperature distributions in the cross section of CBM magnet. The quench appeared in the outer layer of coil. Heater cross-section is $3.02 \times 3.25 \text{ mm}^2$

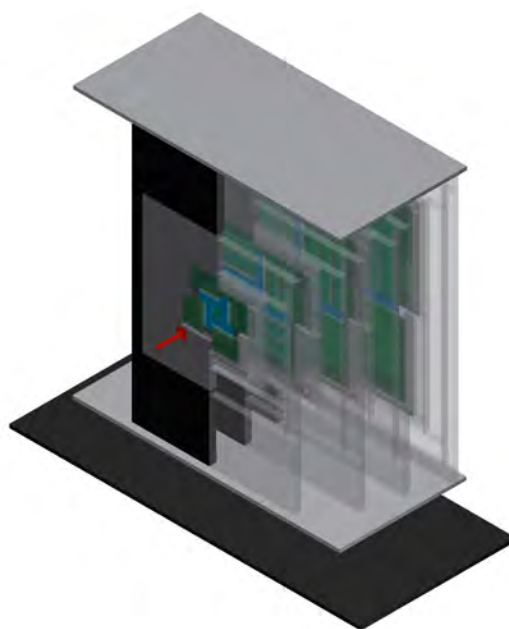
References

- [1] The Technical Design Report for the CBM Superconducting Dipole Magnet.
http://www.fair-center.eu/fileadmin/fair/experiments/CBM/TDR/CBM_magnet.TDR_31.10.2013-nc.pdf
- [2] P.Kurilkin *et al.*, *CBM Progress Report 2013*, Darmstadt 2014, p. 8.
- [3] P. Kurilkin *et al.*, *CBM Progress Report 2015*, Darmstadt 2016, to be published.
- [4] F. Toral, *Ph. D. Thesis*, Madrid, 2001

* Work supported by GSI(SIS)/GSI(ESR)/GSI(UNILAC)/GSI(PHELIX)/HI Mainz/Hi Jena/HIC4FAIR/HGShire/EU, EURONS contract No. 506065/GSI cooperation with university Mainz/Helmholtz-Nachwuchsgruppe

[†] pkurilkin@jinr.ru

Micro-Vertex Detector



CBM MVD simulation - performance and status*

S. Amar-Youcef¹, M. Deveau¹, E. Krebs¹, B. Linnik¹, B. Milanovic¹, Ph. Sitzmann¹, T. Tischler¹, and J. Stroth^{1,2}

¹Goethe-Universität, Frankfurt, Germany; ²GSI, Darmstadt, Germany

With the new realistic description of the CBM Micro-Vertex Detector (MVD) improved performance and physics case studies have been conducted.

The MVD is the dedicated detector to track particles with high precision in close vicinity to the target in CBM. It improves the tracking capabilities of the CBM Silicon Tracking System (STS) in the low momentum range (below 0.5 GeV/c) and allows applying keen topological criteria, needed as distinctive factor to reduce the combinatorial background. Topological cuts represent an integral part of different analyses. E.g. in the open charm analysis they allow to identify and favor potential decay particles indicating a definite displaced decay vertex. In the dielectron spectrometry (single) electron and positron tracks particularly from (incompletely detected) γ -conversion and π_0 -Dalitz decays need to be discriminated. Here, the topological features of particles not originating from the primary vertex or exhibiting small opening angles to its closest partner can be exploited. However, in this analysis the discriminating power has to be traded off against the additional background effected by the additional detector material close to the target, as further elaborated in refs [1,2].

Tracking capability

Monte Carlo (MC) simulations were carried out in order to access the tracking capability including the MVD. To this end a simple simulation task was defined using the box generator. Events with each 100 pions (uniformly distributed in emission angle, and momentum between 0.05 and 1.5 GeV/c) are transported at full magnetic field through the detector setup.

The setup including 4 MVD (geometry version v15a) and 8 STS (v15c) stations was compared to a setup with 8 STS (v15c) stations only. Just primary tracks are considered. The impact parameter resolution, the momentum resolution, the tracking efficiency (see fig.1) and hit mapping efficiency (see fig.2 for particles with momentum smaller than 0.5 GeV/c) serve as measures for the tracking performance. As a result, adding the MVD improves these performance parameters, as this detector provides additional spatial resolution as well as geometrical acceptance especially for low-momentum particles. Thus, as it can be seen in fig.2, the MVD supplements the tracking performance also in the STS. Here, the Monte Carlo tracks are compared to the reconstructed tracks hit by hit. The upper block shows the case when no MC hit is registered, and the lower block shows the case when a MC hit is registered in the

respective station.

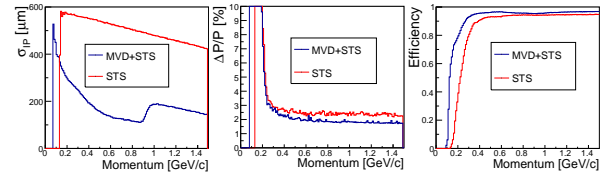


Figure 1: Impact parameter and momentum resolution, and tracking efficiency as a function of the momentum for a setup with STS and MVD (blue), and STS only (red). Only primary tracks originating from the primary vertex are considered.

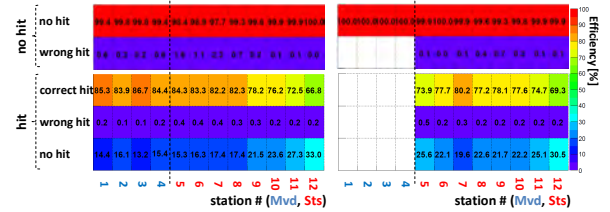


Figure 2: Hit mapping efficiency with STS and MVD (lhs) and STS only (rhs): Monte Carlo (MC) tracks are compared to the reconstructed tracks hit by hit and each station separately. Two cases are distinguished: No MC hit was detected (upper block), and a MC hit was detected (lower block) in the respective station. The different rows indicate the results from tracking.

Summary

The tracking performance was investigated using the new realistic description of the MVD. It was found that the MVD improves the CBM tracking capability due to the added value w.r.t. spatial resolution and geometrical acceptance. This result is completed by the findings reported in [2] on improving the signal-to-noise ratio in the dielectron invariant mass spectrum by adding the MVD in the analysis.

References

- [1] Philipp Sitzmann, this report.
- [2] Erik Krebs, this report.

* Work supported by BMBF (05P12RFFC7), HIC for FAIR and GSI

High voltage CMOS Monolithic Active Pixel Sensors manufactured in a $0.18\ \mu\text{m}$ CMOS process*

D. Doering¹, M. Deveau¹, B. Linnik¹, and J. Stroth^{1,2} for the CBM-MVD collaboration

¹Institut für Kernphysik, Goethe-Universität Frankfurt, Germany; ²GSI Darmstadt, Germany

Modern $0.18\ \mu\text{m}$ CMOS processes provide numerous features, which may allow for decisive progresses in the read-out speed and the radiation tolerance of the CMOS Monolithic Active Pixel Sensors (MAPS) to be used in the Micro-Vertex-Detector of CBM. Together with the PICSEL group of IPHC Strasbourg, we aim to exploit those features by migrating the successful architecture of our sensors toward this novel technology. This work reports on our findings on the first prototypes manufactured with this new technology.

A weak point of CMOS sensors is the slow diffusion of signal charge in the undepleted active medium. As the charge collection by fast drift is preferred to the slow diffusion, one aims for a large depleted volume. However, in CMOS sensors this was initially hampered by the low resistivity of the epitaxial layers available ($\sim 10\ \Omega\text{cm}$) and low depletion voltage CMOS processes feature. In 2010, high-resistivity epitaxial layer with $\sim 1\ \text{k}\Omega\text{cm}$ resistivity became available, which allowed to enlarge the depleted volume [1]. Further progress is expected by the use of the TOWER-0.18 process available since 2012 [2]. This process features an even higher resistivity of $> 1\ \text{k}\Omega\text{cm}$. Furthermore, an AC-coupling of the preamplifier to isolate the collection diode from the read-out chain was studied. This allows to apply a higher voltage to the diodes to increase the depleted volume. At the same time, this voltage is separated from the voltage sensitive input transistors of the in-pixel amplifier. For the same reason, the reset transistor has to be replaced by a self-bias diode.

The study was carried out in 2015 based on the PEGASUS sensors, which was provided by IPHC Strasbourg [3]. This sensor is manufactured in the TOWER-0.18 CMOS process on a $18\ \mu\text{m}$ thick high-resistivity epitaxial layer aiming for depleting a significant fraction of the epitaxial layer. PEGASUS hosts four matrices with 56×32 pixels with a pixel pitch of $25\ \mu\text{m}$. The preamplifier was modified with respect to a self-bias structure with an AC-coupling. The depletion voltage can be increased up to 12 V.

Figure 1 shows the response of a PEGASUS sensor to photons of an Fe-55-source. The spectrum exhibits a - in comparison to previous sensors [1] - large so-called *calibration peak* around 100% charge collection efficiency (CCE). The former *collection peak* is nearly smeared out, suggesting that nearly the whole charge is collected by one seed pixel. This can be related to the larger depleted volume due to applying a high depletion voltage. In addition, an-

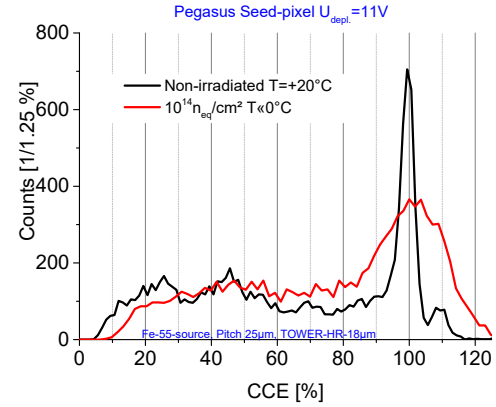


Figure 1: Signal response to photons of PEGASUS with 11 V depletion voltage. The charge collection efficiency (CEE) is normalized to the Mn K_{α} line.

other beneficial effect of a doping gradient might have to be considered, which shifts the electrons in vertical direction. This was studied in detail with other sensors produced in the same TOWER-0.18 CMOS process.

The spectrum of a PEGASUS sensor irradiated with a neutron dose of $10^{14}\text{ n}_{\text{eq}}/\text{cm}^2$ is added (figure 1). The calibration peak is broadened due to radiation induced noise, which may be suppressed to some extent by operating the sensors at $T \ll 0^\circ\text{C}$. Beyond this, the shape of the spectrum is mostly not modified. This suggests that the charge collection of the sensor was not substantially reduced by the high radiation damage.

In conclusion, combining a high-resistivity epitaxial layer and a high depletion voltage in PEGASUS allows to design mostly depleted CMOS-sensors, which turns into a significant progress in terms of radiation tolerance.

References

- [1] D. Doering et al., *Pitch dependence of the tolerance of MAPS to non-ionizing radiation*, NIM-A 730 111-114 (2013)
- [2] D. Doering et al., *Noise performance and ionizing radiation tolerance of MAPS using the $0.18\ \mu\text{m}$ CMOS process*, JINST 9 05 C0551 (2014)
- [3] M. Kachel et al., *Fully depleted MAPS : Pegasus and Mimosa 33 slides*, CPIX 2014, Bonn
- [4] D. Doering et al., *CMOS-sensors for energy-resolved X-ray imaging*, JINST accepted for publ. (2015)

* This work has been supported by BMBF (05P12RFFC7), HIC for FAIR and GSI.

Status of the CBM-MVD PRESTO Project *

M. Koziel¹, T. Tischler¹, P. Klaus¹, C. Müntz¹, and J. Stroth^{1,2} for the CBM-MVD collaboration¹

¹Institut für Kernphysik, Goethe-Universität, Frankfurt, Germany; ²GSI Darmstadt, Germany

This report summarizes the status of full-size prototyping the 2nd and 3rd station quadrants of the CBM Micro-Vertex Detector (MVD). The PRESTO project discussed in reference [1] aims at double-sided integration of 15 ultra-thin CMOS pixel sensors onto a 380 μm thin TPG carrier, representing a station quadrant. To limit possible risks related to integration, testing and vacuum compatibility, only the back side of the module has been integrated yet (6 MIMOSA-26 sensors plus 4 FPCs [2]), see figure 1a.

Yield: During a probe test campaign [3] working sensors were identified and then glued on the TPG carrier. Bonding of the sensors to the FPCs was done using a manual bonder. After wire bonding, 5 sensors are operating but with higher threshold values for each bank compared to the probe test setup. This can be associated with a voltage drop on the power supply lines of the sensor, caused by the length of the FPC of about 250 mm. With time, an additional sensor started to exhibit malfunctioning that can point to a problem with the reference voltage generation for each pixel due to the corresponding not ESD-protected sensor pad.

FPC quality:

Parameter	Test result
Eye diagram @ 40 MHz	passed
Cross-talk between sensors	not observed
Power ON/OFF influence	not observed
Voltage drop over the power lines	about 180 mV
Trace resistivity	$1.68 \cdot 10^{-6} \Omega\cdot\text{cm}$

Heat sink quality: In-vacuum the heat evacuation was addressed with a 500 μm thin TPG plate using a flexible Kapton heater glued on one side of the carrier. The heater was providing 350 mW/cm^2 of dissipated heat. The TPG carrier was clamped into a heat sink that was directly cooled by a cooling liquid with a temperature of -40°C . The temperature of the plate was measured by the means of 12 PT-100 temperature sensors uniformly distributed on the other side of the plate. The temperature gradient did not exceed the accepted limit of 8 K/cm and was in fact by a factor of about two lower.

Vacuum compatibility: The PRESTO sensors were also exposed to an ^{55}Fe source. In figure 1a the corresponding hit pattern is overlayed. Between the source and one of the sensors, metal wires forming the letters "MVD" were positioned, that can also be seen in the same picture. Several pressure cycles (standard pressure / 10^{-5} mbar) were

* This work has been supported by BMBF (05P12RFFC7), EU-FP7 HadronPhysics3, HGS-HIRe, GSI and HIC for FAIR.

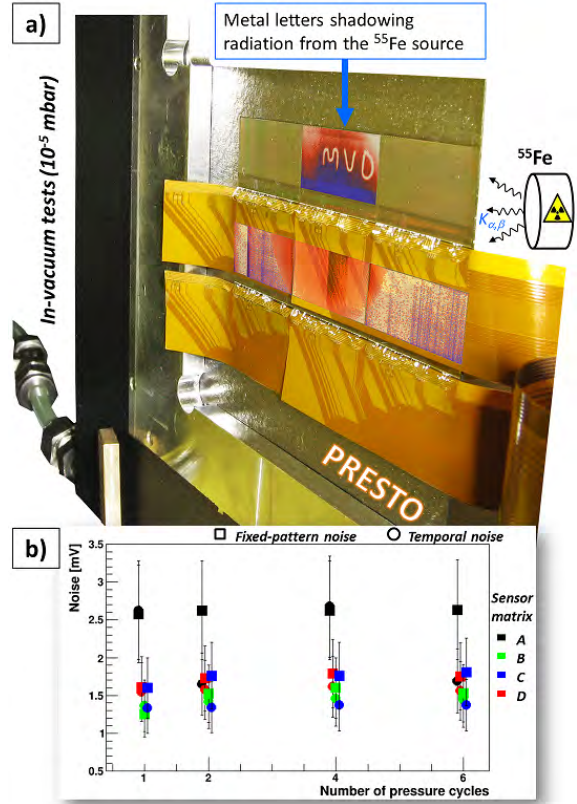


Figure 1: PRESTO: (a) The back side of the module clamped into an Al-based heat-sink and installed inside a vacuum chamber. The hit pattern from a radioactive ^{55}Fe source on four sensors is overlayed. (b) Measured sensor noise as a function of the pressure cycle number.

performed together with measurements of the sensor current consumption and noise (temporal and fixed-pattern), employing a TRBv3-based customized read-out. After several pressure cycles, the main sensor parameters remained unchanged, see figure 1b.

References

- [1] M. Koziel et al., "PRESTO: PREcursor of the Second sTatiOn of the CBM-MVD." GSI annual report 2014.
- [2] P. Klaus et al., "Ultra-low material budget Cu flex cable for the CBM-MVD." GSI annual report 2014.
- [3] M. Koziel et al., "The CBM-MVD: Progress in Mechanical Integration." GSI annual report 2014.

Radiation damage due to neutron capture in boron doped silicon*

T. Bus¹, M. Deveaux¹, D. Doering¹, and J. Stroth^{1,2} for the CBM-MVD collaboration

¹Institut für Kernphysik, Goethe-Universität Frankfurt, Germany; ²GSI Darmstadt, Germany

CMOS Monolithic Active Pixel Sensors (MAPS) are highly granular and ultra-thin silicon pixel sensors, which will be used for the Micro Vertex Detector (MVD) of CBM. Their sensitive volume, the moderately P-doped epitaxial layer, is surrounded by two layers made from P++ doped silicon (P-Well and substrate). The improvement of their non-ionizing radiation hardness is the topic of a joined R&D project of IKF Frankfurt and IPHC Strasbourg.

Non-ionizing radiation damage scales with the Non Ionizing Energy Loss (NIEL) of particles in silicon [1]. This NIEL is traditionally expressed in n_{eq}/cm^2 , which is the dose generated by a 1 MeV neutron. Tables allow for estimating the 1 MeV neutron equivalent dose for various types and energies of impinging particles. However, the tables hold for pure silicon and thus neglect the damage caused by $^{10}B + n \rightarrow Li + \alpha + 3 \text{ MeV}$ reactions in boron doped silicon. Due to its high cross-section, this process was feared to create an unpredicted vulnerability of P-doped MAPS to thermal neutrons.

An upper limit for the radiation damage created by this process was estimated by computing the additional radiation energy generated by this process as function of neutron energy and doping concentration [2]. The preliminary results suggest that this energy remains negligible for doping concentrations fairly below $10^{17}/cm^3$, which holds for the active medium of modern MAPS. However, the surrounding structures (substrate, P-Well) show a substantially higher doping. The daughter ions of the boron decaying there may penetrate the active medium by few μm before exhausting their decay energy.

The theory studies were complemented by an irradiation test with the sensor prototype MIMOSA-19 [3], which was exposed to $\sim 1 \text{ MeV}$ fission neutrons and 1.8 MeV cold neutrons from the MEDAPP[4] and the PGAA[5] beam line of the FRM-II reactor in Garching/Germany respectively. Hereafter, the sensors were bonded and tested and the leakage current of the collection diodes was measured.

The results are shown in figure 1, which indicates the measured leakage currents as function of the NIEL. For cold neutrons, dosimetry was once made according to the standard NIEL model for pure Si (red line). As expected, this scaling does not match the reference measurements made with the fast reactor neutrons (green line). In a next step we assumed in accordance with [1] that the leakage current scales linearly with the NIEL and derived a scaling factor for cold neutrons from the slope defined by the

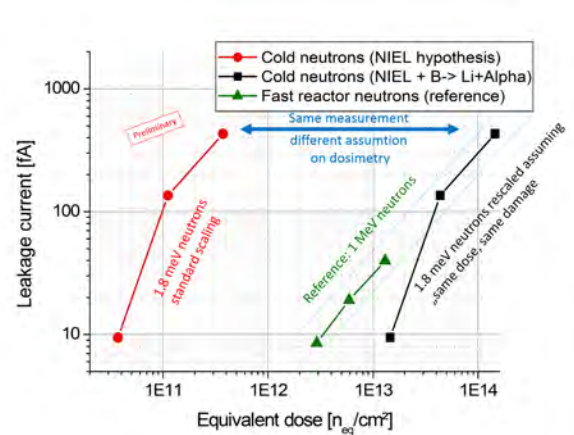


Figure 1: Leakage current of irradiated MAPS, for details see text.

reactor neutrons (black line). By doing so, we find a hardness factor of $\sim 1.5 n_{eq}/n_{cold}$, which exceeds the standard scaling by a factor of 500 and is compatible with a few $10^{19}/cm^3$ doping as found in the substrate of CMOS wafers. One may thus consider neutrons were captured in the substrate and that the fission products damaged hereafter the active volume of the MAPS.

Sizeable uncertainties remain in the experiment because the sensors were exposed to an unknown amount of γ -rays during the irradiation with cold neutrons, which may or may not have contributed significantly to the leakage currents. However, theoretical estimates and experiment match within their uncertainty and suggest that $^{10}B + n \rightarrow Li + \alpha + 3 \text{ MeV}$ processes have to be accounted for in the design of MAPS based detector systems.

References

- [1] Michael Moll, *Radiation Damage in Silicon Particle Detectors*, PHD-Thesis (1999).
- [2] T. Bus, Bachelor Thesis, Goethe-Universität Frankfurt, 2015.
- [3] D. Doering et al., *Annealing studies on X-ray and neutron irradiated CMOS Monolithic Active Pixel Sensors*, NIM-A 658-1-133-136 (2011).
- [4] Heinz Maier-Leibnitz Zentrum. (2015), MEDAPP, <http://dx.doi.org/10.17815/jlsrf-1-43>.
- [5] Heinz Maier-Leibnitz Zentrum. (2015), PGAA, <http://dx.doi.org/10.17815/jlsrf-1-46>.

* This work has been supported by BMBF (05P12RFFC7), HIC for FAIR and GSI.

Silicon Tracking System



The CBM Silicon Tracking System: towards production readiness

H. R. Schmidt¹ and J. M. Heuser²

¹STS Project Leader, Universität Tübingen, Germany; ²STS Technical Coordinator, GSI, Darmstadt, Germany

The Silicon Tracking System (STS) is the central detector of the CBM experiment. Located in the gap of the 1 Tm dipole magnet, its task is to provide track reconstruction and momentum determination of the charged particles originating from beam-target interactions. In this summary we give a brief overview of the STS components and the progress made with their development, and outline the timeline and milestones towards production readiness and construction of the detector.

Description of the STS detector system

The STS detector system will employ about 1200 double-sided silicon microstrip sensors arranged on eight tracking layers. The typical track multiplicity reaches up to 700 per central Au+Au collision in the aperture of $2.5^\circ < \theta < 25^\circ$, which corresponds to a rapidity range from mid rapidity to close to beam rapidity. A design momentum resolution of $dp/p \approx 1.5\%$ is achieved by a read-out strip pitch of $58 \mu\text{m}$, yielding a single-hit resolution of about $25 \mu\text{m}$. The momentum resolution is only limited by multiple scattering. Thus, one of the prime goals is the minimization of the material budget in the acceptance region. The STS is laid out such that front-end read-out electronics, cooling and mechanical infrastructure are located outside of the detector acceptance. Thus, specially designed low-mass micro cables are used to transfer signals from the sensors to the front end electronics. Charged particle rates of about 10 MHz per cm^2 are expected in the innermost regions of the STS. They fall off quickly in the outer regions of the STS. Different sensors sizes (6 cm width accommodating 1024 strips, and 2, 4, 6 and 12 cm height, corresponding to the strip lengths) were chosen to keep maximum strip occupancies at the level of a few percent. The running scenario of the experiment results in the fluence of up to $1 \times 10^{14} \text{ cm}^{-2}$ 1-MeV neutron equivalent in the innermost regions of the STS. The sensors need to be operated at up to 500 V bias and at a temperature of around -5°C to limit radiation damage induced leakage currents.

Progress with microstrip sensors and system interation

Significant progress has been made to (nearly) finalize the prototype sensor designs for all sizes, in cooperation with the two vendors CiS, Erfurt, Germany, and Hamamatsu Phototonics, Japan. Productions of small batches were ordered by GSI and JINR in close coordination at both companies. The layout of the four different sensors sizes was unified: contact pads for bias delivery and signal read-out were placed in accordance with the emerging

module assembly procedure, allowing best placement and attachment of the micro cables connecting the sensor to the read-out electronics and bias supplies. Thickest possible metal layers, ca. 800 nm, are realized on the sensors to minimize the resistive load on the read-out ASIC, resulting in minimized noise. The mechanical integration of the silicon sensors into a realistic detector setup is progressing with the strong support of a team of GSI engineers and draftsmen. Viable solutions for the 18 mechanical half units for mounting the ladders including cooling, cable routing and thermal insulation are being worked out.

Progress on R&D

While general R&D has ended with production-ready technical designs a few specific questions are still being addressed by several working groups. Charge collection studies to characterize irradiated and non-irradiated sensor are pursued employing a third party readout system based on the LHCb Beetle chip. It allows for flexible configurations of the read-out strips: (1) one strip connected to one read-out channel; (2) every second strip is readout; (3) two strips connected to one read-out channel. This enables, e.g., to study the important signal-to-noise ratio for the different strip readout configurations efficiently. A thorough understanding of the effect of intense irradiation on the sensors is addressed in a test stand employing a beta-source. The charge collection efficiency of sensors, which had been irradiated with reactor neutrons or in a proton beam, is measured. The prototype sensors from two vendors, in two technological configurations, show a reduction of charge collection by 15% to 25% after irradiation at twice the maximum neutron fluence expected in the CBM experiment. While, at reactors, the integrated neutron dose (flux) is accumulated within a few minutes, it appears also desirable get a more realistic representation of the irradiation process, i.e., with an exposure of days or weeks. For this goal a scalable DD neutron source at the Tübingen Van-de Graaff accelerator with good availability and accessibility is being built. It will allow to study the interplay of radiation induced damage and annealing phase in situ over extended periods.

Progress on the readout electronics

The STS readout ASICs are located just outside of the active area of the sensors and are exposed to high charged particles rates and a total integrated dose over the full lifetime of up to 100 kRad. In order to ensure proper functionality in this environment and to reduce single event upsets (SEU) which manifest themselves as bit flips, the ASIC de-

sign implements a DICE (Dual Interlocked Storage) cell architecture for the configuration settings of each channel as well as for critical global settings. A beam test at COSY was performed to quantitatively assess the cross section for SEUs of the STS-XYTER version 1 ASIC. As a result a SEU cross section below $1.1 \times 10^{15} \text{ cm}^2/\text{bit}$ for the DICE cells was found, which is consistent with literature values. Similarly, for components like DC/DC converters or LDO voltage stabilizers, the output voltage level as well as the expected transient voltage spikes rate due to single event upsets had to be monitored during irradiation. Here it was found that out of the tested DC/DC converters only FEASTMP survived more than 10^{13} protons which corresponds to a dose of $4 \times 10^{12} \text{ cm}^2$. No fast transients were observed on the LDO voltage stabilizer investigated. The STS-XYTER ASIC version 2 is a 128 channel full-size prototype IC dedicated to the STS and MUCH detectors' readout. After tests of the previous prototype (version 1), the chip design was largely revised. After a design review in October 2015, where simulations showed a significant reduction in noise down to an acceptable level, it is expected to be taped-out in the first quarter of 2016 via IMEC engineering run services. The STS readout chain including STS-XYTER v1, read-out board (ROB) with GBTx and Versatile Link components was tested with respect to their performance, system integration and functionalities. In particular it was shown that, with proper shielding of low voltage cables and a proper grounding the system, a noise performance can be achieved which is within expectations from simulations. In addition, thermal simulations of the ROB heat exchanger were carried out showing that the present design of the Aluminum carrier shelf should be sufficient to dissipate the produced heat of the boards.

Progress on components, module assembly and quality assurance procedures

Ultra-thin micro-cables are a key component for the CBM-STS. They inter-connect the silicon sensors and the readout electronics and should thus have minimal material budget. Pre-series batches of microcables with Aluminum signal lines have been developed and manufactured by LTU Ltd (Ukraine). They are being used for the development of the STS detector module assembly procedures both at GSI and JINR. While the TAB-bonding process of the Aluminum wires to pads is reliable and can be performed at room temperature, the alignment of the cables prior to the bonding process is, however, an elaborate process. Thus, an alternative cable design based on copper instead of aluminium, and a bump bonding interconnection, is proposed and prototype development pursued at KIT Karlsruhe. The assembly procedure of modules involves basically the connection of sensors and readout ASICs via the micro cables. The detailed procedures are very involved and required detailed planning of the workflow and the corresponding tooling. These procedures are presently being worked out both at the GSI detector laboratory and at the

JINR STS site. First (dummy) modules have been assembled.

Pre-requisite of functional modules is rigorous quality assurance (QA) of the components. A setup for optical inspection of sensors (and cables) has been developed at Tübingen university and will be employed to check the incoming batches of sensors from the manufacturer for defects (scratches, residues) prior to the assembly. Similarly, electrical QA will be performed for about 10% of the sensors using automated probe stations both at Tübingen and GSI. During module assembly quality measurements need to be performed to assure electrical contact of the TAB-bonds that join the micro cables with the STS-XYTER chips as well as the silicon micro strip sensors. Non-destructive, easy and fast procedures for a large amount of micro cables can be realized with *PogoPin* test sockets that are well adapted to the needs. These test socket are presently being developed together with industry.

Towards production readiness: Timeline and milestones

The STS team has worked out a detailed project plan to organize the various tasks for the development and construction of the detector system. Task inter-dependencies and resource loading were taken into account. The pre-construction phase with its R&D activities, preparation of technologies, sites and teams is to end in Summer 2017. The change-over to the construction phase is marked by several production readiness reviews during which the fitness for the start of series production of the detector components will be assessed. The first of such reviews will address the maturity of the silicon sensors (12/2016). Further reviews concern the assembly of detector modules, ladders, and the system integration (4/2017). The read-out electronics is scheduled last (8/2017). The construction of the STS detector system will then be carried out until Fall 2020. This is followed by a commissioning phase in the assembly laboratory without beam (until 6/2021) before the STS can be transferred to the CBM cave and is made operational there. This part of the schedule is still tentative as it depends on the detailed planning of civil construction. In parallel to the construction effort, full-system tests of STS detector parts and the read-out system will take place in common effort of the CBM collaboration and partners.

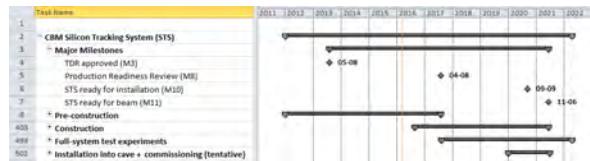


Figure 1: Outline of the STS project plan: Envelopes of pre-construction, construction and commissioning phases. Major milestones are indicated.

Progress with micro-strip sensors for the CBM Silicon Tracking System

J. Heuser¹, Y. Murin², C.J. Schmidt¹, D. Soyk¹, and C. Sturm¹

¹GSI, Darmstadt, Germany; ²JINR, Dubna, Russia

The eight tracking layers of CBM's Silicon Tracking System will be comprised of double-sided silicon micro-strip sensors in four geometrical dimensions. All sensors have the same width and numbers of strips but differ in the lengths of the strip-shaped electrodes. Those are matched to the particle densities in the respective aperture of the detector. Short strips are located close to the beam line where the particle densities are highest [1]. The main sensor parameters are:

- n-type silicon
- thickness: $285/320 \pm 15 \mu\text{m}$ (vendor dependent)
- double-sided segmentation
- 1024 strips per side of $58 \mu\text{m}$ pitch
- strip lengths: 2/4/6/12 cm
- strip angle w.r.t. vertical edge: 7.5 degree (*p*-side), 0 degree (*n*-side)
- AC coupled read-out
- read-out from top edge
- 2nd metal read-out routing lines interconnecting the AC layers of the corner strips
- outer dimensions: 6.2 cm width; 2.2, 4.2, 6.2 and 12.4 cm height

Near-final prototypes in all sizes have been designed in cooperation with two vendors: CiS, Erfurt, Germany [2], and Hamamatsu Phototonics, Japan [3]. Productions of small batches were ordered from GSI and JINR in close coordination at both companies. Figure 1 presents details of a recent sensor produced. The sensors with 12 cm long strips are new. They replace the initially foreseen daisy-chained pairs of 6 cm high sensors with monolithic sensors. This will facilitate the module assembly by making the double-sided attachment of daisy-chain cables unnecessary. Pre-requirement is the availability of 6" wafer processing capability at the fabrication lines. While this is the standard technology at Hamamatsu, the wafer processing at CiS is still based on 4", with 6" processing being in a development phase.

Progress has been made with unifying the layouts of the sensors in all four dimensions. Contact pads for bias delivery and signal read-out were placed in accordance with the emerging module assembly procedure, allowing best placement and attachment of the micro cables connecting the sensor to the read-out electronics and bias supplies. Thickest possible metal layers, ca. 800 nm, are realized on the sensors to minimize the resistive load on the read-out ASIC, resulting in minimized noise. The largest sensor can

be contacted also in the middle of the strips, reducing the resistive term further. Contact pads and other marks like labels, strip numbers and fields for serial number encoding were placed such that various quality assurance procedures are facilitated. Final inspection is part of the product deliverable. Detailed test parameters, specifications and test protocols have been worked out with the vendors. They cover both global sensor performance as current-voltage behavior, and strip-by-strip tests.

The prototypes are in the course of being qualified in the STS laboratories at GSI and Univ. Tübingen, using dedicated equipment for optical and electrical inspection. Also verified is their charge collection performance prior and after exposure to a neutron equivalent irradiation as later in the experiment, under the anticipated thermal operating conditions of $\leq -5^\circ \text{C}$. The aim is to establish sensor production readiness towards the end of 2016.

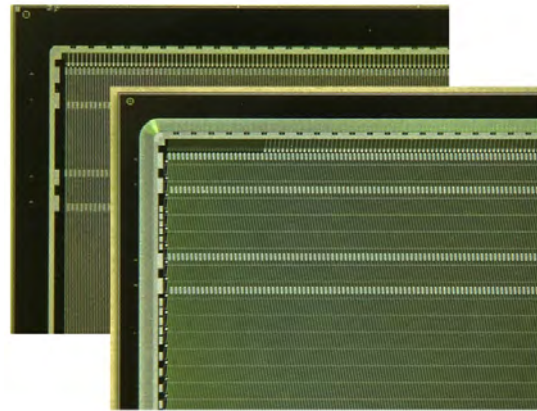


Figure 1: Microscope views of corners of two sides of a recent 6.2 by 2.2 cm prototype micro-strip sensor from CiS. Visible are the metal layers of the strips (lower photo: 0 degree orientation on the *n*-side, upper photo: 7.5 degree orientation on the *p*-side). The guard ring and bias ring structures surround the sensitive area. Rows of contact pads allow attaching the read-out cable. Horizontal routing lines on a second metal layer interconnect the read-out lines of the strips in opposite sensor corners for common read-out.

References

- [1] CBM STS Technical Design Report, GSI Report 2013-4 (2013), chapter 2.3
- [2] <http://www.cismst.org>
- [3] <http://www.hamamatsu.com>

Optical quality assurance procedures for STS silicon sensors

E. Lavrik, I. Panasenکو, and H.-R. Schmidt

Universität Tübingen, Tübingen, Germany

The CBM Silicon Tracking System (STS) is a compact detector built out of about 1220 double-sided silicon microstrip sensors. The sensors will be delivered from different manufacturers (current prototypes are from CiS, Erfurt, Germany and Hamamatsu Photonics, Japan) in 4 different form factors [1]. In order to assure the quality of these sensors an optical quality assurance test station was developed at the University of Tübingen, which allows to measure various QA parameters for the sensors such as surface conditions (scratches, dust grains, photo-resist residues, etc.) and geometry (wafer thickness and warp, edge parallelity and profile etc.)[2]. Having the sensors quality assured at a very early stage allows to reject the faulty sensors as well as provide the input data for further control stages such as electrical control.

The test station consists of an XY-inspection table with a vacuum chuck mounted, a microscope camera and an optical system with motorized zoom and focus mounted on the Z stage. The XY-stage allows to inspect sensors up to a size of $6.2 \times 12.4 \text{ cm}^2$. A highly customizable software solution, which allows the adaptation for other hardware as well as other inspection objects like sensor micro-cables, has been developed as a part of the project.

Sensor warp inspection

The system now allows to measure the sensor warp in non-destructive contactless way (Fig. 1). The acquisition of height profile is done by analyzing the magnitude of an FFT-transformed image of the target sensor region at different focus levels with roughly $1 \mu\text{m}$ accuracy. This approach employs the autofocus functionality of the system.

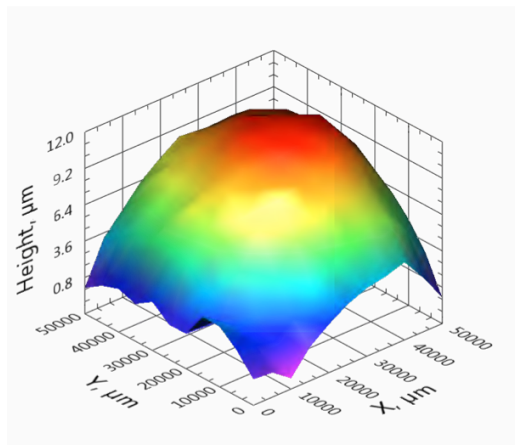


Figure 1: Warp (height profile) of a prototype sensor.

Edge profile inspection

Another important quality criterium is the recently implemented inspection of the sensor edge profile and their parallelism. This is particularly important for the module and ladder assembly of the detector. Figure 2 shows the principle of the edge profile control. The absolute deviation from the fitted sensor edge line is measured.

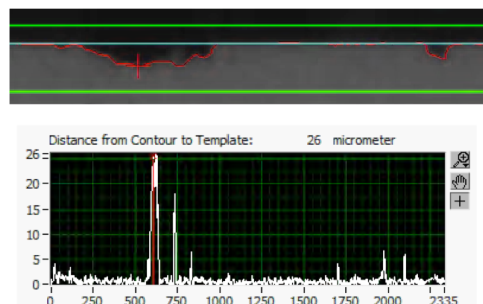


Figure 2: Close-up view of a prototype sensor's edge profile in near-defect area (top panel) and edge profile along 2335 μm region of interest (bottom panel).

Micro-cable inspection

The system was as well used to inspect also the sensor's micro cables. It is able to detect a variety of cable defects: broken and defect lines, foreign objects on a cable's surface, metal defects etc. Figure 3 shows the broken line detection principle based on the image intensity profile.

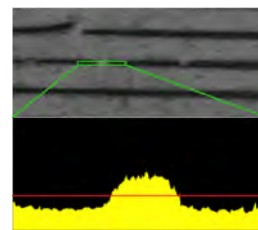


Figure 3: Broken line on a prototype micro-cable.

References

- [1] CBM STS Technical Design Report, GSI Report 2013-4 (2013), chapter 2
- [2] E. Lavrik *et al.*, CBM Progress Report 2014, p. 30

Automated quality assurance for the STS sensors of the CBM experiment*

P. Larionov

Goethe-Universität, Frankfurt, Germany

The Silicon Tracking System (STS) serves as the main tracking detector of the Compressed Baryonic Matter (CBM) experiment providing tracking information of charged particles propagation and determination of their momenta. The STS will be assembled with approximately 1220 double-sided silicon microstrip sensors in four different sizes.

Complicated fabrication technology of double-sided sensors and large-scale sensor production demands a reliable and efficient quality assurance of the STS sensors to ensure decent operation of the whole system [1]. Three quality test centers are being equipped in GSI and ECU Tübingen, Germany and in JINR, Russia to perform full-scale quality assurance of the STS sensors including optical inspection, bulk electrical tests and strip quality tests. The strip quality tests are particularly important to identify strip defects that can develop during fabrication, transportation or handling of sensors. The most commonly occurring strip defects include:

- pinholes, i.e. ohmic connections between an implant and a readout strip;
- strips with high leakage currents;
- strip “shorts” - ohmic connections between two or more readout strips;

The first two defects can pose a danger for the readout electronics. Therefore they must be identified and charged off for the readout coupling. The last one does not constitute a serious threat for the readout chain but degrades the spatial resolution of the system and thus has to be determined as well.

A test stand has been assembled in the cleanroom environment at GSI to enable efficient strip defects identification. The setup, featuring a probe station, several measurement instruments and a custom made software for test automation, provides a full scan of the quality of each strip. By making use of a switching matrix three tests in a row are performed, taking 4 seconds for each strip to test and provide the strip quality information. The software prints the results of the scan online to the user interface and also saves them in an ASCII file. Figure 1 illustrates the results of the full strip quality scan for the junction side of one of the STS prototype sensors demonstrating the strip leakage current distribution, the pinhole and the readout strip short circuit scans. During the scan one pinhole defect was identified showing the current through the coupling capacitor over 200 nA at 20 V applied. The setup will be used to

perform full or partial scans during mass production of the STS sensors in addition to final inspection by the manufacturers.

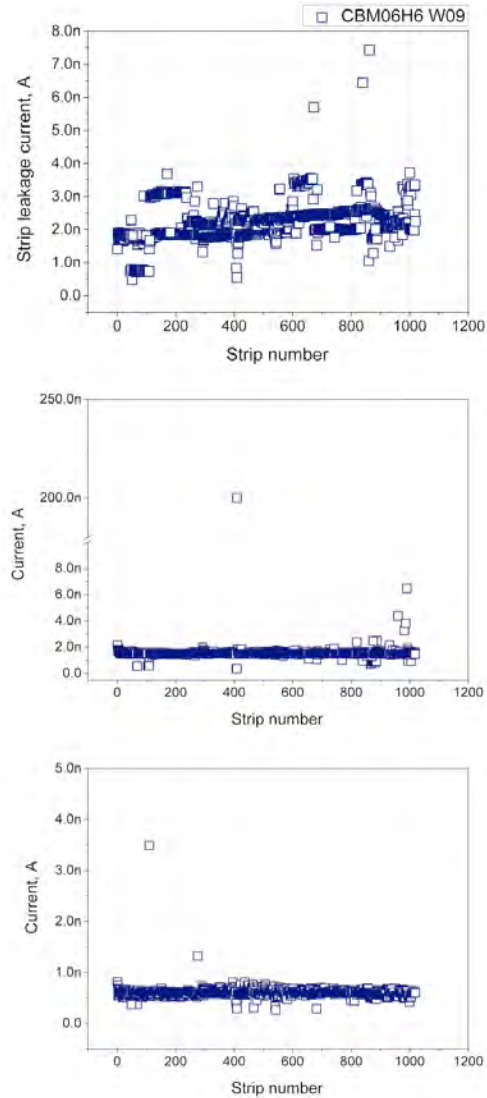


Figure 1: Output of the automated strip quality scan. Top: strip leakage current distribution; center: pinhole test scan; bottom: readout strip short scan.

References

- [1] P. Larionov and P. Ghosh, GSI Scientific Report 2012, p. 47

* This work is supported by HGS-HiRe, H-QM and HIC for FAIR.

Equipment and procedures for electrical quality assurance of CBM-STS silicon microstrip sensors

I. Panasenکو^{1,2}, E. Lavrik¹, A. Lymanets³, and H. R. Schmidt¹

¹Universität Tübingen, Tübingen, Germany; ²Institute for Nuclear Research, Kiev, Ukraine; ³GSI, Darmstadt, Germany

The silicon microstrip detectors for CBM's Silicon Tracking System (STS) are double-sided, and produced with integrated AC coupled read-out and poly silicon bias resistors. The strip pitch is $58\ \mu\text{m}$, the strip width $\sim 18\ \mu\text{m}$. The sensors have 1024 strips per side and will be produced in 4 sizes: $62 \times 22\ \text{mm}^2$, $62 \times 42\ \text{mm}^2$, $62 \times 62\ \text{mm}^2$ and $62 \times 124\ \text{mm}^2$. All sensors have to be characterized before being assembled into detector modules to ensure their compliance with specifications. The electrical QA program for sensors consists of:

- **Basic tests:** IV, CV curves for every received sensor.
- **Subset tests:** pinholes, metal shorts, strip leakage current — on $\sim 10\%$ of sensors which pass the basic tests.
- **Specific tests:** coupling and interstrip capacitances, polysilicon resistors — on a small fraction of sensors to measure in much more details electrical parameters.

To perform all those tests the following equipment has been installed in a clean room at the University of Tübingen around a custom-built probe station [1]: SourceMeter Keithley 2410, Picoammeter Keithley 6487, LCR-Meter QuadTech 7600, Switching matrix Keithley 708B. Current-voltage (IV) and capacitance-voltage (CV) measurements describe the sensor as a single entity and allow to extract V_{FD} , C_{bulk} , $I_{leakage}$ at Full depletion voltage. Figure 1 shows the CV characteristic plotted in a double logarithmic scale for the sensor labeled as CBM06C6-w18.

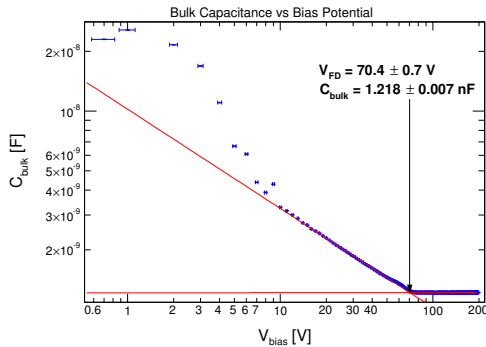


Figure 1: Capacitance-voltage measurements.

For strip-by-strip characterization (namely subset and specific tests) an automated probe station has been developed at Tübingen University. The drive motors which carry

a custom designed vacuum chuck receiving the silicon sensor under test have a positioning precision of $\sim 0.4\ \mu\text{m}$. A wide moving range (100 mm, can be expanded) of both optical and chuck positioning motors allows to contact needles to pads at opposite corners of the silicon sensor. This feature makes it possible to perform some specific tests like probing of the 2nd metal lines on the sensors' p-sides. Coordinate calibration for successful automated positioning during stepping through the strips, auto-alignment of the sensor and height adjustment at each step have been implemented in custom developed software (*Labview* based) for the probe station.

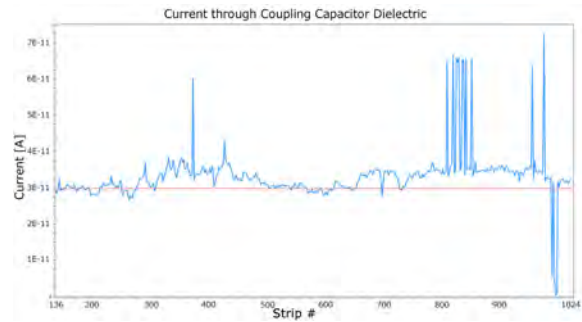


Figure 2: Pinhole test for p-side strips of the sensor.

The stepping procedure of our software for subset tests probes every strip of the sensor in order to check the capacitor dielectric for pinholes, to look for strip metal and implant shorts and opens and to determine the coupling capacitance of the readout strip. Figure 2 shows the results of one of the subset test — pinhole check performed on the CBM06C6-w18 sensor. The current through the capacitor for most of the strips is much less than $1\ \text{nA}$, i.e. no pinholes are present. A group of the strips reveals twice the current than normal, which is due to metal shorts between pairs of strips. Further specific tests (e.g. interstrip capacitance, polysilicon resistance, coupling capacitor breakdown) have also been implemented.

A time estimate for the complete testing protocol (consisting of 4 QA tests) is 4-5 hours per sensor. The specification requires $< 1\%$ defective strips on every sensor to be accepted for module assembly.

References

- [1] I. Panasenکو *et al.*, CBM Progress Report 2014, p. 31

Charge collection of n-irradiated prototype CBM-STs microstrip sensors

I. Momot^{2,3}, H. Malygina^{2,3}, M. Singla¹, P. Larionov², M. Teklishyn^{1,3}, J. Heuser¹, and C. Sturm¹

¹GSI, Darmstadt, Germany; ²Goethe University, Frankfurt, Germany; ³KINR, Kyiv, Ukraine

The STS will employ double-sided silicon microstrip sensors to detect the space-points of ionizing particles originating in beam-target interactions. The strips on the p side of the sensors are tilted with respect to the n side by 7.5° . To read out the sensor only from one edge, as required by the detector ladder structure, the end strips from one edge are connected to the end strips on the other edge. This interconnection can be provided via double metallization (DM) or using external interstrip cables (SMwC). The central strips are the full-length strips without any interconnection.

Current prototype sensors were tested for their charge collection performance both before and after a non-ionizing radiation dose corresponding to twice the end-of-life criterion defined for the STS detector: 1 MeV neutron equivalent fluence of $2 \times 10^{14} \text{ n}_{eq} \text{ cm}^{-2}$. The irradiations were performed at Karlsruhe Institute of Technology (KIT), Germany [1]. All measurements were made in a light-tight set-up with temperature control, operating the sensors at -5° C . The signals from a β -source (^{90}Sr) to mimic minimum ionizing particles (MIP) were read out with an n-XYTER based acquisition system. Four sensors were selected for the measurement of variation of leakage current with bias voltage (IV), bulk capacitance versus bias voltage (CV), and for charge collection tests with a ^{90}Sr source. The list of the sensors under test is given in Table 1 along with their sizes, thickness, types of the connections and full depletion voltage before irradiation (extracted from the capacitance-voltage measurements).

Table 1: Specifications for the sensors under tests. The naming convention in the left column encodes the prototype generation (5 or 6), the manufacturer (H = Hamamatsu, C = CiS), the sensor height/strip length in cm (4 or 6), and the wafer number.

name	size	thickness	inter-	$V_{fd} \pm 5$
CBM0-	cm \times cm	μm	connection	V
5H4-W18	6×4	327	SMwC	68
5H4-W10	6×4	331	DM	75
6C6-W14	6×6	293	SMwC	94
5C6-W6	6×6	291	DM	98

A coincidence scheme with a pin diode as trigger was used. A 2 mm Aluminum absorber behind the sensor cut away the low-energy β -spectrum. The obtained signal from MIPs was fitted with a Landau-Gauss convolution and the most probable value is interpreted as the collected charge. The results for charge collection efficiency, based on an

ADC-to-charge calibration and the expected charge in the detector according to the wafer thickness, are shown in Fig. 1.

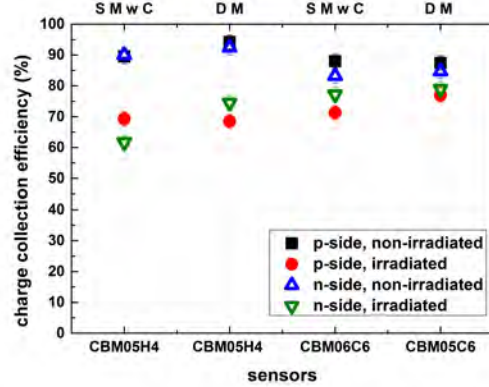


Figure 1: Charge collection results with ^{90}Sr .

The sensors were also tested with 2 GeV proton beams at COSY (Jülich) in December 2014. The result of charge collection efficiency which is defined from the simulation taking into account interstrip and coupling capacitance are shown in Fig. 2 for Hamamatsu sensors only.

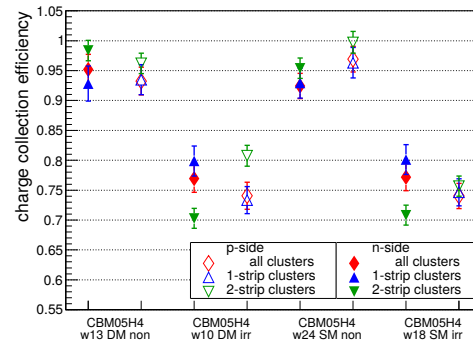


Figure 2: Charge collection results with proton beam.

The prototype sensors from two vendors, in two technological configurations, show a reduction of charge collection by 15% to 25% after irradiation to twice the maximum neutron fluence expected in the CBM experiment. New series of sensors from CiS and Hamamatsu are under preparation to forthcoming irradiation studies.

References

- [1] http://www.ekp.kit.edu/english/irradiation_center.php

Charge collection studies for prototypes of CBM-STS sensors with the Alibava readout system

I. Momot^{1,3}, M. Teklishyn^{2,3}, V. Pugatch³, and J. Heuser⁴

¹Goethe University, Frankfurt, Germany; ²FAIR, Darmstadt, Germany; ³KINR, Kyiv, Ukraine;

⁴GSI, Darmstadt, Germany

The CBM-STS front end electronics is currently under development. Before the dedicated STS-XYTER ASIC becomes available for tests of the sensor prototypes, front-end electronics based on the n-XYTER chip [1] is applied. However, in order to cross check the results one can include measurements performed with yet another read out system. The Alibava system [2] is a portable readout system for scientific purposes. It uses the *Beetle* readout chip which was developed for the tracker system of the LHCb experiment [3]. It is suitable for characterizing the properties of irradiated and non-irradiated microstrip sensors.

The Alibava readout system mainly consists of the two separate parts: the mother board and the daughter board. The primary analogue readout system is placed on the daughter board. It comprises two *Beetle* chips that operate in analogue readout mode. The Beetle chip is used for the readout and amplification of the collected charge from the individual sensor strips. It has 128 channels with an amplifier and a shaper. The readout, amplification and shaping of the collected signal pulses is then sampled into an analogue pipeline with a bunch-crossing frequency of 40 MHz. The analogue data is measured in analogue-digital-counts (ADC). The data that is brought off the chip is transferred via a flat cable to the mother board, where it is processed and digitized. The mother board communicates with the data acquisition software on a computer.

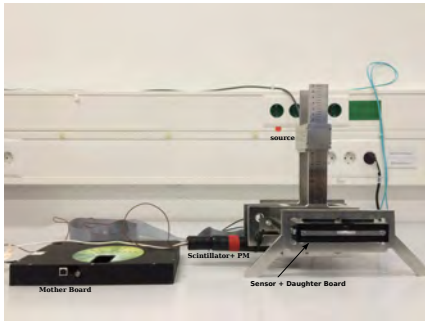


Figure 1: Set-up with the Alibava system.

A view of the set-up in the STS laboratory is shown in Fig. 1. Scintillator connected to photomultiplier tube is used as a trigger system. The scintillator, sensor and collimated source are aligned in such way that mostly perpendicular particles can penetrate. The source and the scintillator are mechanically interconnected and can move simultaneously in the X and Y direction. The height of the source above the sensor can be independently adjusted. Electrons

with energies in the range between 1 MeV and 2.28 MeV (^{90}Y β -decay energy) can be considered as minimum ionized particles. In order to avoid triggering on the soft component <1 MeV we applied a threshold for the signals from the photo multiplier. We assume the total electron energy to be absorbed in the plastic scintillator. The resulting spectrum was fitted with a Landau-Gaussian convolution and the most probable value (MPV) interpreted as collected charge. An example of the obtained spectra is shown in Fig. 2.

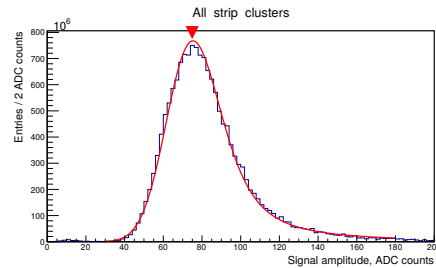


Figure 2: Signal of MIPs from the ^{90}Sr source fitted by Landau-Gaussian convolution; MPV = 71 ADC counts.

Two types of 6×6 cm² sensors were already studied with this system: single metal sensors without interconnection between short and long inclined strips (SM) and single metal with microcable interconnection (SMwC). They shown almost the same charge collection result for long strips; the signal-to-noise ratio is ≥ 20 for each case. The Alibava setup has an internal calibration procedure. By injecting test charge pulses to the preamplifier input and observing the response in the ADC units, one can later convert the output signal from the β -source in units of electron charge. Different sensor read-out schemes were examined: (1) one strip connected to one read-out channel; (2) every second strip is readout; (3) two strips connected to one read-out channel. For the moment we performed the measurements with only perpendicular tracks. The data is in the process of being analyzed in terms of signal for different cluster sizes yielded, and signal-to-noise ratios.

References

- [1] A. S. Brogna *et al.*, Nucl. Instrum. Meth. **A 568** (2006) 301
- [2] <http://www.alibavasystems.com>
- [3] S. Löchner and M. Schmelling, *The Beetle reference manual for Beetle version 1.3/1.4/1.5*, LHCb note 2005-105, August 22, 2006

Characterization of CBM silicon microstrip sensors bonded by microcables to Beetle readout chips

V. Dobishuk^{1,2}, J. Heuser³, V. Kyva¹, Ie. Momot^{1,3}, V. Pugatch¹, C. Sturm³, and M. Teklishyn^{1,4}

¹Institute for Nuclear Research NAS Ukraine, Kyiv, Ukraine; ²Taras Shevchenko National University of Kyiv, Kyiv, Ukraine; ³GSI, Darmstadt, Germany; ⁴FAIR, Darmstadt, Germany

The CBM Silicon Tracking System will be assembled with double-sided silicon microstrip sensors connected to the readout electronics placed outside of the physics acceptance by microcables of different length. For connecting 58 μm pitch strips of the sensor two microcables with a pitch of 116 μm are to be used: the upper one for odd numbered strips, the bottom one for even numbered strips.

Characterization studies of prototypes of such assemblies are under way at KINR. First results are reported here for a silicon microstrip sensor (6 by 6 cm, CiS) bonded to the two readout *Beetle* [1] chips mounted on the daughter board of an Alibava [2] system. The Alibava mother board digitizes analogue data from 256 charge-sensitive preamplifiers with 25 ns peaking time and provides control of the system. The sampled pulse is stored in an analogue pipeline with a fixed latency which is determined by the scintillator trigger adjusted for triggering from the MIP hits. A photo of the part of the daughter board with *Beetle* chips bonded by microcables to the microstrip sensor is shown in the left part of the Fig.1. Drawings of the connecting microcables are shown on the right part of Fig. 1.

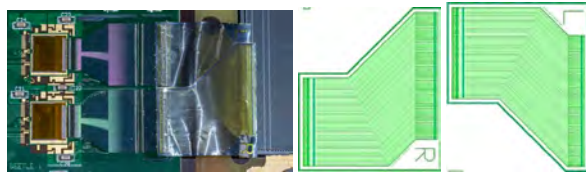


Figure 1: Left: Photo of the CBM microstrip sensor bonded by two microcables to Beetle chips of the Alibava Daughter Board. Right: Drawings of the microcables.

The sensor was operated at 80 V. Figure 2 (left, blue histogram) shows the noise distribution over the 256 channels of the readout microchips. The first *Beetle* chip accounts for the channels between 0 and 127, while channels from 128 to 255 correspond to the second chip. As one can see the noise grows up in both chips up to the channel no. 42. This is due to the fact that those channels are connected to the strips at the wafer edge where the length of the strips steadily increments accordingly to their layout at 7.5° stereo angle. The geometry of the microcable is such that the length of the connecting lines grows up here as well. The noise distribution as a function of the strip number on the wafer is shown by the red histogram. One may see that it goes abruptly down where the strip length as well as the length of the microcable lines becomes constant (from the strip-channel no. 85). The verification of the

strip map (red histogram) has been performed by scanning focused laser beam (640 nm wavelength) with a diameter of 10 μm over the wafer. The response of operational strips was in accordance with the laser spot position.

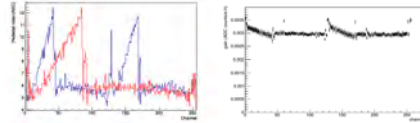


Figure 2: Left: Average noise of two Beetle chips as a function of their input channel number connected by microcables to the sensor (blue histogram); Noise assigned to the sensor strip number (red histogram). Right: Calibration histogram as a function of the readout chips' input channel.

In its left panel, Fig. 3 illustrates the two-dimensional amplitude distribution of the sensor response for two-strip clusters measured with the laser beam moving across the wafer. The right part shows similar data measured for cosmic rays, triggered by a scintillator detector on events with trajectories perpendicular to the sensor surface. Charge sharing in the interstrip gap is observable for the laser beam case. We shall accumulate more events for the cosmic rays with a statistics sufficient for making conclusion on the signal-to-noise performance in the interstrip gap.

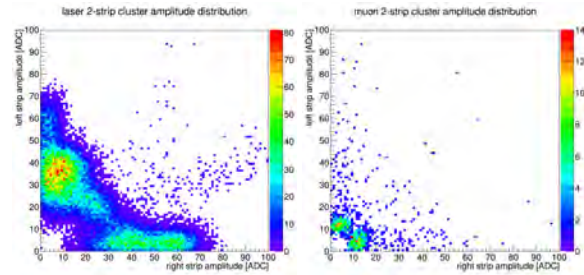


Figure 3: Left: Two dimensional amplitude distribution of the sensor response for two-strip clusters measured with the laser beam moving between adjacent strips. Right: Two-strip cluster data measured for cosmic rays.

References

- [1] <http://www.kip.uni-heidelberg.de/lhcb/Publications/BeetleRefMan.v1.3.pdf>
- [2] <http://www.alibavasystems.com>

A scalable neutron source for STS detector radiation hardness tests

E. Friske and H. R. Schmidt

Universität Tübingen, Tübingen, Germany

During operation of CBM's Silicon Tracking System, the microstrip sensors are expected to be irradiated with neutrons in excess of of $10^{12} \text{ n}_{\text{eq}}/\text{cm}^2/\text{month}$ [1], with an accumulated dose of $10^{14} \text{ n}_{\text{eq}}/\text{cm}^2$ [2]. To test detector performance in response to neutron induced lattice damage, a source with high flux is necessary. Typically, at reactors, irradiation campaigns are short (in the order of minutes) in which the desired neutron dose is achieved. To get a more realistic representation of the irradiation process, an exposure of days or weeks is desirable, including defined annealing phases. In addition, studying the detector changes while it is being irradiated helps with checking theoretical predictions. For both of these goals, a scalable neutron source with good accessibility is required.

Neutron source

The Van de Graaf accelerator located at the Rosenau facility of Univ. Tübingen can produce neutrons of variable flux through the $\text{D(d,n)}^3\text{He}$ reaction. Gas targets used before consisted of a gas cell filled with deuterium gas under a pressure of a few bar. A deuteron beam with an energy of $\approx 2 \text{ MeV}$ from the accelerator passes an entrance window of a few microns thickness to induce the aforementioned reaction. The accelerator can be operated for longer periods of time without interference from other projects. However, the heat load on the thin entrance window limits both the beam current and the pressure of the gas cell. This leads to a reduced neutron production rate as the number of incident ions is low and a considerable fraction of the deuterons hit the end cap before they can react with the deuterium gas. Due to the limitations of both the accelerator and the window the neutron production is currently limited to a rate of $\approx 10^{12} \text{ n}_{\text{eq}}/\text{cm}^2/\text{week}$. As this rate is about two orders of magnitude below the required total dose, it would take over a year of continuous operation to accumulate the necessary dose with the current setup. To solve these issues, a new gas cell has been manufactured in our workshop, based on the work reported in [3].

New gas cell

The new neutron source consists of a steel endcap for the accelerator beam pipe, so an insulating vacuum is generated by the beampipe's vacuum pumps. Additional insulation will be provided by styrofoam attached to the outside of the endcap where no other parts are affected. Mounted inside the endcap is the actual cell, cooled by liquid nitrogen. In contrast to [3], the gas cell is cooled by a copper finger reaching into a dewar filled with liquid nitrogen. The

entrance window is fixed to a thick copper disk which is also thermally connected to the gas cell. This setup has several advantages over the previous cell designs:

- The entire cell wall acts as a cooler for the enclosed deuterium gas, reducing its heat buildup.
- The gas is currently cooled down to $\approx 170\text{K}$, which increases the density by a factor of 2 compared to room temperature while maintaining the same pressure. With additional insulation the temperature of the gas should drop even further.
- The entrance window is cooled by both the copper plate and the deuterium gas, which should enable it to withstand higher pressure and beam currents without breaking.

Combining these effects, it should be possible to increase both beam current and beam energy (to the accelerator's limit of $\approx 2.5 \text{ MeV}$), which both significantly increases the neutron yield. In addition, the detector can be put behind the gas cell at a distance of a few cm, providing maximum solid angle coverage and using the neutron boost provided by the incident deuterons. These improvements should increase the neutron flux by at least one order of magnitude, the actual gain has to be measured with scintillation detectors which are currently being refurbished for service. A schematic view of the irradiation setup is shown in Fig. 1, a photo of the finished gas cell in Fig. 2.

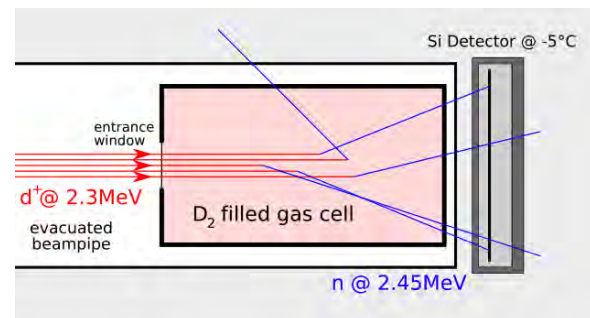


Figure 1: Schematic view of the irradiation setup at the end of the accelerator beampipe.

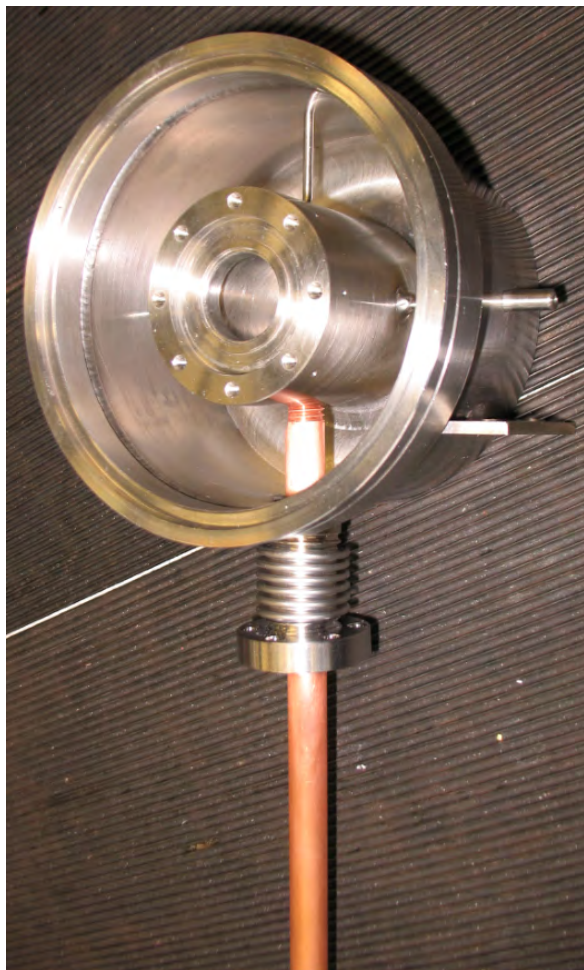


Figure 2: Image of the finished gas cell without the entrance window.

Ancillary works

Window materials and thickness

Previous designs used an entrance window made from Havar[®]. As this is an alloy including several high-Z materials¹, the beam energy loss in the window is severe at the energies provided by the accelerator. Instead, ready-made windows consisting of 1 μm thick silicon have been installed. Silicon nitride is an alternative material in case pure silicon proves to be insufficient. Silicon carbide and sapphire windows were considered but rejected because they were both unavailable in the desired thickness and impossible to work into the desired format with the available equipment.

Gas handling system

A pressure regulation system has been installed and connected to the present gas cell to test regulation capabilities

¹see e.g. www.hpmetals.com/download/Havar.pdf

and failover behavior. Simulations have been performed to determine the optimal pressure for the different beam energies possible with the accelerator.

Liquid nitrogen reservoir

The liquid nitrogen dewar has been installed and provides constant cooling for over one week. The exact cooling time depends on the additional energy deposited.

Detector test stand

Since the detectors to be measured need to be as close to the source as possible, a custom detector chamber is being manufactured. A cooling system will keep the ambient temperature of the detector at -5°C , the same as during operation of the STS.

Readout system

Live monitoring of the detector performance will be done using the Alibava[®] readout system. This system has been tested using the built-in simulation functions, once the detector strips are bonded to the readout chips it will read out 5 separate sections of the detector area simultaneously. A β emitting source in front of the detector provides the signals to be captured by the readout system.

References

- [1] CBM STS Technical Design Report, GSI Report 2013-4 (2013), chapter 3
- [2] I. Sorokin, *Characterization of silicon microstrip sensors, front-end electronics, and prototype tracking detectors for the CBM experiment at FAIR*, PhD thesis, Goethe-Universität Frankfurt, 2013
- [3] Nucl. Instrum. Meth. **A 138** (1976) 13

Dependence of signal amplitude and noise of the n-XYTER v2.0 ASIC on capacitive input load

D. Dementyev and Yu. Murin

JINR, Dubna, Russia

The n-XYTER ASIC is widely used by CBM groups for laboratory and in-beam tests of prototype detectors. It is a chip with self-triggering architecture which can operate with both polarities of input signals and has sufficient signal-to-noise ratio that allows to detect MIP signals in $300\ \mu\text{m}$ silicon. The first version of the chip was extensively tested. Significant dependence of the base line level on temperature was found ($4\%/^\circ\text{K}$). Together with high power dissipation it makes operation of this chip difficult. A water cooling system and regular measurements of the bias line levels are needed. To solve this problem a new version of the n-XYTER ASIC was developed. The redesign was primarily focused on the supply of several bias potentials from outside the chip and correction of various layout deficiencies. As a result, the temperature coefficient was reduced by a factor of 200 [1].

Front-end boards with the n-XYTER v2.0 were assembled at JINR with the help of specialists from LTU Ltd. The main difference from the FEB generation E is that on these PCBs chips were mounted on a aluminum heat-sink on the bottom and on the aluminum double-layer microcable on the top. The assembly of ASIC to microcable and PCB was made with TAB-bonding technology by specialists of LTU Ltd. [2].

Signal-to-noise ratio is one of the most important characteristics for the readout ASICs. There are three main sources of noise in readout chain: (1) shot noise of leakage current, (2) thermal noise of the resistive elements between detector and preamplifier, and (3) noise of the preamplifier. In case of the CBM STS long aluminum cables will be used to connect sensor strips to the ASIC. Thermal noise of the cables is negligible, the total resistance should be less than $20\ \Omega$. However, the noise of preamplifier should be taken into account and it strongly depends on the input capacitive load, i.e. the total capacitance of the detector and the cable. The maximum total capacitance is expected on the level of $50\ \text{pF}$. Since the charge sensitive preamplifier of the n-XYTER chip has a finite capacitance, the output amplitude also depends on the input capacitance.

A dedicated setup was assembled at JINR to measure the n-XYTER v2.0 output amplitude and noise as a function of the capacitance at the chip input. Six ceramic capacitors with different capacitances were installed at the input of a selected channel of the chip in course. The capacitance was measured when the setup was already assembled, in order to make sure that parasitic capacitances are taken into account. A AKTAKOM AM-3016 LCR precision meter was used to determine the input capacitive load. Measurements were done at a frequency of $200\ \text{kHz}$ in parallel mode with

an accuracy of $100\ \text{aC}$. A SRS DG645 Pulse Generator was used to provide the input signal. The pulses were attenuated down to the amplitude of $4.6\ \text{mV}$ and passed over a capacitor of $1.6\ \text{pF}$ to the n-XYTER input. A photo of the setup and the connection scheme are shown in Fig. 1.

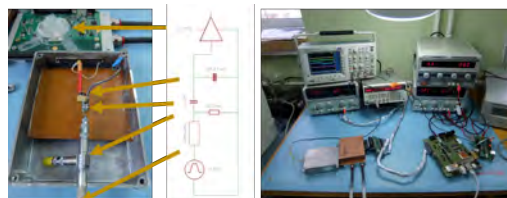


Figure 1: Set-up for measurements of the dependency of amplitude and noise of n-XYTER v2.0 on input capacitance.

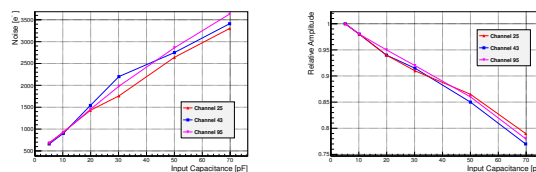


Figure 2: Dependency of the noise (on the left) and relative amplitude (on the right) on input capacitance.

The n-XYTER output signal was measured as a function of the capacitance at the input. The amplitude was normalized to the amplitude with the minimum capacitance at the input. With $50\ \text{pF}$ input load, 15 percent of amplitude loss can be expected; this should be taken into account during the calibration of the chip. The same measurements were done for the noise of the preamplifier. As expected, the noise grows proportionally to the input capacitance and is of the level of $2700\ e^-$ for $50\ \text{pF}$ input load.

The results are in good agreements with those made for the previous version of the n-XYTER [3]. That means that redesign of the ASIC did not influence the behavior of the preamplifiers.

References

- [1] D. Dementyev et al., CBM Progress Report 2012, Darmstadt 2013, p. 15
- [2] V. M. Borshchov et al., CBM Progress Report 2013, Darmstadt 2014, p. 34
- [3] I. Sorokin, *Characterization of silicon microstrip sensors, front-end electronics, and prototype tracking detectors for the CBM experiment at FAIR*, PhD thesis, Goethe-Universität Frankfurt, 2013, p. 77

SEU Tests with the STS-XYTER Version 1 ASIC

J. Lehnert and P. Kozcon

GSI, Darmstadt, Germany

The sensors of the CBM Silicon Tracking System (STS) are connected to 8 STS-XYTER frontend ASICs with 128 channels each developed at AGH Cracow [1]. The ASICs are located just outside of the active area of the STS and exposed to high charged particles rates and total integrated doses over the full lifetime up to 100 kRad. In order to ensure proper functionality in this environment and to reduce single event upsets (SEU) which manifest as bit flips, the ASIC design implements a DICE (Dual Interlocked Storage) cell architecture for the configuration settings of each channel as well as for critical global settings.

SEU Testing of DICE Cells at COSY

During the CBM electronics beam test at COSY Jülich¹ in October 2015, the first version of the STS-XYTER frontend ASIC, produced in a UMC 180 nm process, was characterized for the first time with respect to single-event effects in its DICE cell architecture. Goal was the quantitative assessment of SEU cross sections for the DICE cells, which may strongly depend on the actual cell architecture, and the comparison to the regular flip flops in the design [2]

Tests were performed in a dedicated high-intensity proton beam used in parallel for multiple irradiation studies within CBM, which allowed running at rates up to 3×10^9 protons per spill on the setup, which provided a good compromise between sufficient statistics for the SEU investigations and a stable (not fully DICE protected) readout interface. Device under test was a single STS-XYTER version 1 ASIC bonded to a prototype frontend board (FEB). The ASIC was centered in the proton beam. The FEB was connected to a standard readout and control chain with a SYSCORE3 readout board and a data acquisition PC with a HTG-K7 board and a FLEsnet based readout. For the purpose of the test only the control functionality of the system was used, i.e. reading and writing to ASIC registers. The test used 32240 bits each of DICE cells and flip flops respectively, arranged in a two-dimensional structure of 8bit DICE discriminator threshold values and 8bit flip-flop counters for 130 channels with 31 discriminators each. The test procedure consisted in a continuous readback of a predefined pattern from the DICE cells and of fixed random values from the read-only counters and a check for bit flips in the expected register values. Repeated readback allows to distinguish SEUs from readout errors. An ionisation chamber from GSI detectorlab (B. Voss) with QFW based readout was placed behind the ASIC to provide an accelerator-independent and continuous measure-

ment of beam intensities².

SEU Test Results

The test was done for a total of 48 hours of effective irradiation. In this period, 3467 bit flips for the flip flops were observed and 116 bit flips for the DICE cells. These numbers provide a direct quantification of the relative SEU rate of the DICE cells with respect to flip flops. The factor of 29.9 is in the expected range for DICE cells. With a preliminary estimate of the proton fluence larger than $2 \times 10^7/\text{cm}^2/\text{s}$, the SEU counts translate in an SEU cross section below $1.1 \times 10^{-15} \text{ cm}^2/\text{bit}$ for the DICE cells which is consistent with literature values.

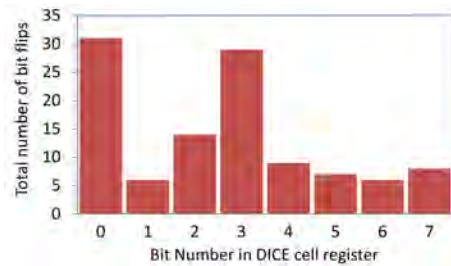


Figure 1: SEU counts for the individual bits of the DICE cell threshold registers

The DICE cells exhibit significant differences in bit flip count over the 8 bits of the individual DICE registers (see Fig. 1). This observation could be correlated with different distance from bulk/well contacts for the individual bits in the DICE cell layout. Consequently the upcoming revision 2 of the STS-XYTER ASIC [3] will implement a modified DICE cell layout. The expected improvement in DICE SEU rate by a factor of up to 3 will be verified in a forthcoming beam test.

References

- [1] K. Kasinski *et al.*, *STS-XYTER, a High Count-Rate Self-Triggering Silicon Strip Detector Readout IC for High Resolution Time and Energy Measurement*, IEEE NSS/MIC, 2014
- [2] S. Löchner *et al.*, *Radiation Studies on the UMC 180 nm CMOS Process at GSI*, RADECS 2009 Proceedings, p. 614
- [3] K. Kasinski *et al.*, *STS-XYTER2, a prototype detector readout chip for the STS and MUCH*, this report

¹Various support by IKP, FZ Jülich is acknowledged.

²Various support by S. Löchner, GSI, is acknowledged.

STS-XYTER2, a prototype detector readout chip for the STS and MUCH

K. Kasinski¹, R. Kleczek¹, R. Szczygiel¹, P. Otfinowski¹, and C. J. Schmidt²

¹AGH University of Science and Technology, Cracow, Poland; ²GSI, Darmstadt, Germany

STS-XYTER2 is a 128 channel full-size prototype IC dedicated for the STS and MUCH detectors' readout. After tests of the previous prototype, the chip design was revised.

The analog front-end was modified to reach the noise requirements, improve testability, ensure fail-safe operation and support gas detectors of MUCH. The charge amplifier (CSA) was re-designed. As a result of amplifier-cable-detector co-design and optimization [1] [2], a NMOS input transistor and direct cascode amplifier was used for the input stage. This architecture results also in a significant improvement of the CSA amplifier PSRR from the positive power supply rails. The amplifier's buffer structures are configurable for best usage of available output voltage swing while working with holes or electrons as input charge. The CSA gain is configurable to support STS (7.5 mV/fC $\pm 20\%$) and MUCH (1.32 mV/fC $\pm 3\%$) detectors. The channels have 58 μm pitch, but the detector-side pads are staggered. The channels associated with 1st row and 2nd row of pads have individual control of CSA input branch current. Therefore it is now possible to switch off every second channel (feature used in MUCH mode). Detailed post-layout studies towards front-end susceptibility to cross-talk and instability caused by external parasitic components (especially series resistance of power rails, wire-bond resistance and inductance, PCB components etc.) were performed. The resistance of power rails of the FE amplifiers were reduced by factor of 2 (shapers) and 4 (CSA) compared to the previous prototype. By n-well shielding of all pads and splitting the protection diodes rings and connecting them to different potentials (1.2 V low-noise VDDM, and 1.8 V VDD_ADC) the crosstalk between back- and front-side of the AFE and the leakage current of the protection diodes (significant at larger temperatures) are reduced. The reference potentials distribution was improved by adding more on-chip capacitors and by using separate output drivers if more than one processing stage is to be driven from a single reference (to cut the possible feedback path). Shaper amplifiers and CSA enable individual switching-off the buffer branches in each channel to cut the signal path (and prevent interferences) of faulty channels. Slow shaper enables selection of shaping time (90 ns – 280 ns in 4 steps) to trade between speed and noise. Fast discriminator was supplied with output gating and a counter to enable fast signal path characterization. The analog-to-digital converter was modified to increase temperature stability and to speed up the calibration procedure (by adding global threshold and direct driving of the ADC input).

The layout and circuit modifications include many im-

provements towards microassembly of cables, wafer-level and post-assembly test procedures and FEB boards design. In particular: the front part of the ASIC was extended by 200 μm , adding 150 $\mu\text{m} \times 150 \mu\text{m}$ pads for pogo-probing, using fiducial markers on the visible 6th metal layer; the power supply pads support multiple wire-bonds or ribbon-bonding (to reduce resistance and inductance). A 64-bit eFuse cell was implemented to assign individual ID at wafer-level testing stage. The number of power domains was reduced to make FEB design easier. The bulk connection quality was improved to reduce cross-talks through the bulk.

The digital back-end has been completely re-designed. A new read-out protocol and interface was designed and implemented. It is scalable (bandwidth: 9.4 – 47 MHit/s/chip) and is optimized for operation with the GBTx data concentrator [3] in the presence of AC-coupled, multidrop electrical SLVS links. The most interesting features of the protocol are: fully deterministic delay from DPB to ASIC, link synchronization procedure which does not require any phase regulation at the ASIC, lossless data compression optimized for the payload and expected front-end load. The protocol was verified in hardware (Kintex FPGA boards). A 15-bit address space in the front-end registers was used to accommodate additional counters (working with fast discriminator) and registers for controlling in-channel features. Based on the beam-tests [4], the DICE-based register cells layout was improved towards even better SEU immunity. SEU protection of the digital back-end is enhanced by using logic triplication in the control path and data parity in FIFO-based circuits of the data path. Radiation tolerance of the AFE part is increased by using NMOS transistors in the enclosed-layout geometry.

The STS-XYTER2 ASIC is currently being under development. It is expected to be taped-out in Q1 of 2016 via IMEC engineering run services.

References

- [1] K. Kasinski, R. Kleczek and C. J. Schmidt, Proc. SPIE **9662** (2015) 96622T
- [2] K. Kasinski, R. Kleczek and R. Szczygiel, JINST **11** (2016) C02024
- [3] K. Kasinski, W. Zabolotny and R. Szczygiel, Proc. SPIE **9290** (2014) 929028
- [4] J. Lehnert *et al.*, *SEU Tests with the STS-XYTER Version 1 ASIC*, this report

Test of prototype components for the CBM-STS readout chain

A. Rodriguez Rodriguez¹ and J. Lehnert²

¹Goethe University, Frankfurt, Germany; ²GSI, Darmstadt, Germany

The front-end board (FEB) with STS-XYTER ASICs and the read-out board (ROB) with GBTX and *Versatile Link* components are main elements of the STS read-out chain [1]. A FEB with a single prototype of STS-XYTER v1 and a Versatile Link Demonstrator Board (VLDB), implementing 4 custom radiation hard devices to be used on the ROB, are currently available in the STS laboratory. Several test have been carried out to check their performance, system integration and functionalities. A brief description about devices tests, experimental setup and results are presented here.

Test of STS-XYTER v1

One of the goals of the STS-XYTER [2] design is to achieve a low level noise performance (below 1000 e⁻ rms in noise charge in the final system). Realistic post-layout simulations for the prototype version of the chip estimate an Equivalent Noise Charge (ENC) around 1600 e⁻. Noise measurements were carried out using different sensor modules. The FEB with 1 ASIC and 14 connected channels is linked to a Syscore3 v1 board; the system is configured over the CBMnet protocol.

The chip response in connected and non-connected channels was studied. During the measurements two-stages LC and RC filters are used to reduce the noise ripple in the sensor bias and common mode noise. A significant reduction in the system noise can be achieved by shielding low-voltage cables and properly grounding the system. Sensor and FEB were placed inside a shielded box made of steel of 2 mm thickness. The box and FEB board share a common ground point which is connected to the ground potential of the low-voltage supplies.

Figure 1 shows the equivalent noise charge (ENC) in the 128 channels of the chip; these correspond to average values over the 31 comparators of every channel. Values for each comparator are estimated from the respective S-curves. Results are shown for 2 daisy-chained sensors of 6.2 cm × 6.2 cm readout by a 30 cm polyimide microcable. The measurements have shown noise levels around 1800 e⁻ for connected channels. This value is higher than the requirements but still consisted with simulations. The redesigned revision 2 of the STS-XYTER will have significantly reduced noise.

VLDB tests

The VLDB is an evaluation board for the radiation hard GBT and Versatile Link ecosystem [3]. It implements 4 custom designed modules: a GBTX ASIC, a VTRx, GBT-

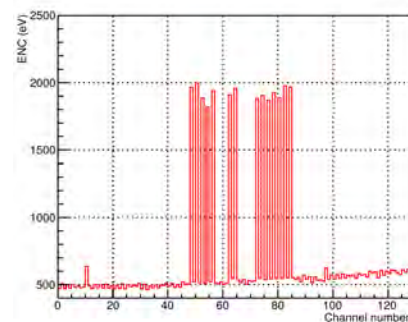


Figure 1: ENC in every channel estimated as an average value for all channel's discriminators.

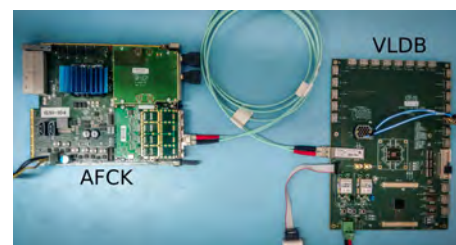


Figure 2: Experimental setup for VLDB system test.

SCA and FEAST_MP DC-DC converters. The VLDB can be configured and controlled by I²C. A Java Programmer Tool allows to configure the GBTx. The experimental setup for system tests is shown in Fig. 2. It consists of the VLDB with the AFCK board as optical backend. The setup allows to check the optical data path and to develop and test firmware and software tools. Furthermore, the addition of an STS-XYTER emulator to the AFCK gives the possibility to test the full data round trip with the VLDB electrical front-end interface and the STS-XYTER communication protocol. The setup allows to have a test bench ready upon availability of the STS-XYTER v2.

References

- [1] J. Lehnert *et al.*, GSI-SR2014-NQM-CBM-26, GSI Report 2015-1, DOI:10.15120/GR-2015-1-MU-NQM-CBM-26
- [2] K. Kasinski *et al.*, *STS-XYTER, a High Count-Rate Self-Triggering Silicon Strip Detector Readout IC for High Resolution Time and Energy Measurement*, IEEE NSS/MIC, 2014
- [3] P. Moreira *et al.*, *The GBT Project*, Proceedings of Topical workshop on electronics for particle physics (TWEPP-09), doi:10.5170/CERN-2009-006, p. 342

Radiation hardness tests of electronic components for CBM-STS low voltage power supply

S. Löchner¹, P. Koczoń¹, and A. Rost¹

¹GSI, Darmstadt, Germany

Electronic components installed in the field of reaction products in future experiments at FAIR have to be radiation hard. At present, selected parts like DC/DC converters and LDO voltage stabilisers undergo exhaustive tests with use of intense minimum ionising particles' beams, mostly about 3 GeV protons at the COSY facility, Jülich¹.

Test setup

For components like DC/DC converters or LDO voltage stabilisers the output voltage level as well as the expected transient voltage spikes rate due to single event upsets have to be monitored during irradiation. Voltage level monitoring (input and output) requires relatively low readout frequency below 1 Hz and can be implemented on the inexpensive ARDUINO system [1]. Fast transients have been monitored on a 4-trace digital oscilloscope Rhode-Schwarz RTO1044 [2]. Measurement results have been recorded in nonvolatile memory and analysed.

Selected ASICs

For the radiation hardness tests several DC/DC converters have been chosen. Selection criteria like circuit efficiency, chip size, coreless inductivity, appropriate output voltage and sufficient output power as well as voltage setting flexibility have been applied.

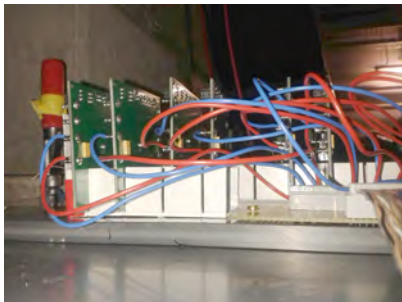


Figure 1: Base plate with PCB card holder and wiring.

Only one model of the LDO stabilizer produced in rad hard technology has been examined until now. Altogether 10 test boards with LTC3605, 3 boards with LTC3610 (Linear Technology), 4 boards containing LM2596S (Texas Instruments) as well as 4 FEASTMP boards [3] have been tested in two beam times. All tested ASICs were powered on during the irradiation runs. The test boards were placed

in a holder fixing their positions with respect to the proton beam during the measurement as shown in Fig. 1.

Test results

The PCBs with tested chips were placed in a row along the beam axis such that the irradiating beam punched through all of them. A small ionisation chamber placed on the beam axis behind tested chips was used to monitor the beam intensity (Fig. 2, left).

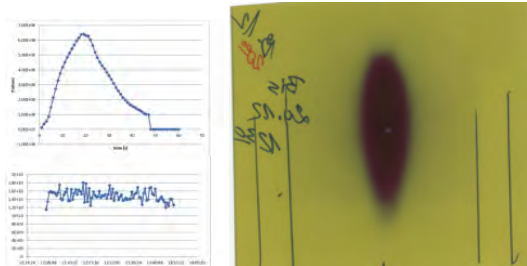


Figure 2: Beam intensity in one spill (upper left panel) and average proton current (lower left panel). Beam spot on Gafchromic self-developing dosimetric film (right panel).

The beam profile has been investigated with Gafchromic dosimetric film [4]. In the course of the irradiation the film develops a spot corresponding to the shape of the proton beam with the optical density corresponding to the integrated beam intensity (Fig. 2, right). The total dose is known from the measurement with the ionisation chamber and the position of the irradiated chips marked on the film. A fractional dose can be estimated for each point on the film by scanning the optical density. This allows to estimate precisely the beam intensity integral and - consequently - the dose at the ASICs' positions. Out of the tested DC/DC converters only FEASTMP survived more than 10^{13} protons which corresponds to a dose of $4 \times 10^{12} \text{ cm}^{-2}$. No fast transients were observed on LDO voltage stabilisers.

References

- [1] S. Löchner and P. Koczoń, GSI Annual Report 2014
- [2] <http://www.rohde-schwarz.de/de/Produkte/messtechnik-testsysteme/aerospace-and-defense/messtechnik/oszilloskope-fuer-ad/RTO.html>
- [3] http://project-dcdc.web.cern.ch/project-dcdc/public/Documents/FEASTMod_Datasheet.pdf
- [4] <http://www.ashland.com/products/gafchromic-radiotherapy-films>

¹ Various support by IKP, FZ Jülich is acknowledged.

Pre-series production of microcables for STS detector modules at LTU Ltd

V. M. Borshchov¹, Yu. A. Murin², C. J. Schmidt³, M. A. Protsenko¹, I. T. Tymchuk¹, J. M. Heuser³,
R. A. Kushniruk¹, M. S. Tykhomirova¹, K. M. Liholitova¹, and L. V. Klimova¹

¹LED Technologies of Ukraine (LTU) Ltd, Kharkov, Ukraine; ²JINR, Dubna, Russia; ³GSI, Darmstadt, Germany

Pre-series batches of microcables for CBM-STS detector modules have been developed, manufactured and delivered. They are being used for the development and verification of work flows and tooling for STS detector module assembly at GSI and JINR. The work was carried out within the STCU project P635 by the partners GSI and LTU, and additionally in cooperation with JINR.

Microcables for STS detector modules

Ultra-light micro-cables are the key component for the CBM-STS. They are employed to realize the analogue signal interconnection between silicon sensors and readout electronics, providing minimized material budget. For the detector modules two kinds of interconnection components will be employed [1, 2]:

- ultra-light interconnection microcables based on aluminium-polyimide adhesiveless dielectrics: connecting microcables, interstrip cables (optional), daisy-chain cables (optional), and shielding layers.
- meshed spacers based on Kapton or polyimide (narrow and wide meshed spacers).

The amount of microcables and meshed spacers required for the STS totals to more than 75 thousands.

Pre-series microcables

For working-off the assembly approaches test sets of microcables (100 pcs.) and 24 pre-series batches of microcables (about 900 pcs.) have been manufactured and delivered to JINR and GSI. Microcables and spacers have been manufactured at the microcables production site [3] and laminated with spacers at the assembly site of LTU Ltd. The length of the microcables is chosen as it was done for the first ladder mechanical mock-up, namely 111 mm, 212 mm and 252 mm. According to the base approach [1, 2] each pre-series set of microcables includes about 40 components – mainly those depicted in Fig. 1:

- analog connecting cable with glued narrow meshed spacer – 32 pcs (8 types);
- shielding layer with wide meshed spacer – 2 pcs. (2 types);
- wide meshed spacer – 2 pcs. (2 types);
- interstrip cable – 1 pc. or 2 pcs. (optional);
- daisy chain cable – 2 pcs. (2 types) (optional).



Figure 1: Analogue cable with narrow meshed spacer (top); shielding layer with wide meshed spacer (middle); wide meshed spacer (bottom).

The manufactured microcables are being used for developing and verifying work flow and tooling for the STS detector module assembly at GSI and JINR [4, 5].

Conclusions

The manufactured pre-series microcables allow verifying the assembly approaches for the STS detector modules. The obtained results will be applied for the forthcoming CBM STS detector modules series production.

References

- [1] C. J. Schmidt *et al.*, CBM Progress Report 2012, p. 18
- [2] V. M. Borshchov *et al.*, CBM Progress Report 2014, p. 47
- [3] V. M. Borshchov *et al.*, CBM Progress Report 2014, p. 45
- [4] C. Simons *et al.*, *Development of a workflow for the STS module assembly*, this report
- [5] A. Sheremetev *et al.*, *Development of tooling for the STS module assembly at JINR's VB LHEP assembly laboratory*, this report

Investigation on low-mass copper flex cables for the STS detector

T. Blank¹, C. J. Schmidt², C. Simons², and D. Soyk²

¹KIT, Karlsruhe, Germany; ²GSI, Darmstadt, Germany

The silicon sensors of the Silicon Tracking System (STS) will be connected to the read-out chips (RoC) with up to 0.5 m long and 100 μm thin flex cables. The aluminium conductors of these cables are 30 μm wide and 14 μm high. The conductor pitch is 100 μm . The production of these cables is demanding. The cables will be tab-bonded to the sensors and the RoCs in two overlapping layers, which is a time-consuming process. Thus, an alternative based on a double-layered copper flex cable with vias is under investigation, having the potential to ease and accelerate the manufacturing processes. This paper presents the current development status of the cable and the planned production steps.

Silicon Tracking System Design – Micro Cable Interconnects

The silicon sensor measures $62 \times 62 \text{ mm}^2$ and is a double-sided strip sensor with 1024 signal channels and a bias ring on both sides of the sensor, top and bottom. The signal and sensor bias lines are connected to eight RoCs with eight flex cables, which are staggered in two rows. As the distance between the RoCs and the sensors varies due to layout restrictions of the read-out PCB carrying the RoCs, two different staggered cable length are required. Furthermore, due to the placement of the bias connector pads on the edges of the sensor two different bias cables are needed. Therefore, eight different cable types are used to connect the signal of both signal contact rows of the sensor to the RoCs. Figure 1 shows a cross section through the sensor and the tab bonded micro cables. The aluminium signal lines are bonded to the pads of the sensor through openings in the cable. The tab-bonding process is reliable and can be performed at room temperature. Alignment of the cables prior to the bonding process is an elaborate process, however. Thus, an alternative cable design based on copper instead of aluminium is proposed.

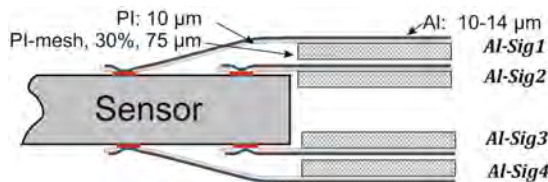


Figure 1: Connection scheme of the tab-bonded micro-cables with aluminium signal traces to the top and bottom side of the sensor.

Copper Micro Cable Design

Copper offers higher conductivity in comparison to aluminium, it is widely used for the production of PCBs and can be readily structured by subtractive (etching) or additive (galvanic) methods. Disadvantages of smaller radiation length can be compensated through narrower signal lanes maintaining line resistivity. The copper process allows to route the signals over various planes, as they can be connected electrically by means of micro-vias. Thus, the two different layers “Al-Sig1” and “Al-Sig2” can be combined in a single layer, reducing the amount of total cables required for the silicon tracking system by a factor of two. Figure 2 depicts a cross section of the cable mounted on the RoC. The bottom and top copper lines are 6-10 μm thick and will be coated with an EPIG-layer (Electroless Palladium Immersion Gold). The top and bottom PI-layers are 12.5 μm thick. They are laminated to a meshed PI-layer with a filling factor of 30% by a 12.5 μm thick epoxy-glue layer. The low fill factor reduces the capacity of the cable and the signal noise.

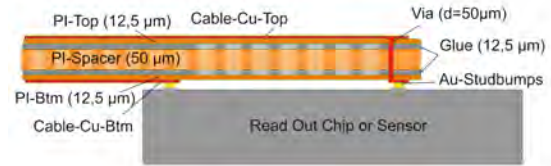


Figure 2: Cross section through the copper cable mounted on the RoC or sensor.

The cable will be connected by means of gold stud bumps to the pads of the sensor. The stud bumping process is very reliable and fast. More than 15 bumps can be placed per second; hence, the bumps required for one sensor side can be produced in less than two minutes. As a main source of noise linearly depends on the capacitance of the cable, various designs have been simulated with the tool “TNT” to evaluate its capacitance. The capacitance of the cable shown in Fig. 2 aggregates to 0.82 pF/cm. If the thickness of the meshed layer is increased to 150 μm as indicated in Fig. 1, the capacity reduces to 0.67 pF/m. In the simulation, the ground-plane is assumed to be located 165 μm below the bottom PI-layer.

Status and outlook

A batch of four different test cables with a length of 200 mm and 186.5 mm with and without bias lines was ordered. The cables will allow the validation of the succeeding manufacturing processes as the attachment of the cable to the RoCs and the sensor.

Development of a workflow for the CBM-STS module-assembly

C. Simons¹, D. Soyk¹, R. Visinka¹, and I. Tymchuk²

¹GSI, Darmstadt, Germany; ²LTU, Kharkiv, Ukraine

The Silicon Tracking system will consist of eight tracking stations that are built from different types of basic functional modules. Those are made from a double-sided silicon microstrip sensor that is connected via microcables to two front-end electronics boards. For one module 32 polyimide microcables, each with 64 aluminum traces, have to be connected on one end to 16 STS-XYTER ASICs, and on the other end to the p and n sides of the sensor, in two staggered layers with TAB-bonding. Additionally, the chips have to be wire-bonded to the front-end electronics boards and shielding layers have to be fixed. The aim was to find the best order for the process steps and to optimize aligning, bonding and glueing processes to obtain reliable and reproducible results. Fixtures had to be developed to facilitate the work and to make results as independent as possible from the personnel involved. UV-curing glues for the protection of the ASICs were tested to reduce the curing time of the glue to a minimum and to accelerate the workflow.

Assembly workflow

Having tried different orders of process steps we agreed on one workflow that turned out to be the most workable one. At the beginning the necessary material has to be arranged and a process slip is prepared for the module to keep records.

Step 1: The 32 microcables for p and n sides have to be TAB-bonded to the 16 STS-XYTER-ASICs in two layers. After bonding a quality measurement is performed with a pogo pin testsocket to find out if each bond has electrical contact. Reworking in case of failure is possible. Finally a protective glue is applied on the TAB-bonds (Fig. 1).

Step 2: These semi-modules now have to be TAB-bonded to the p side of the silicon sensor in two layers. After bonding quality measurements are performed with a pogo pin testsocket that puts the STS-XYTER in minimal operation and tests the electrical contact of the TAB-bonds. The application of glue protects the TAB-bonds at the end (Fig. 2).

Step 3: Now four STS-XYTER ASICs are die and wire bonded to the first row of the front-end board. If measurement results are ok, this first row is protected with globtop glue. Afterwards the procedure is repeated for the second ASIC row on the board (Fig. 3).

Step 4: At the end shielding layers and spacers are glued onto the microcables. Then the module has to be turned over to the n side of the sensor and the four steps have to be repeated for the this side (Fig. 4).

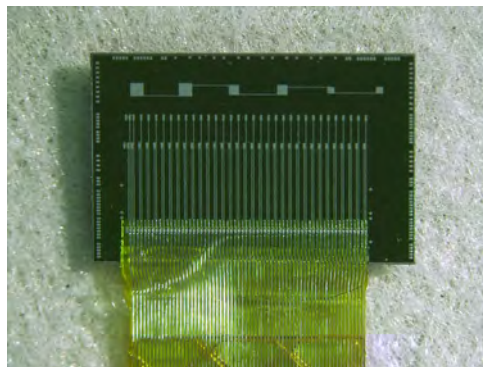


Figure 1: Microcables TAB-bonded to the ASIC.

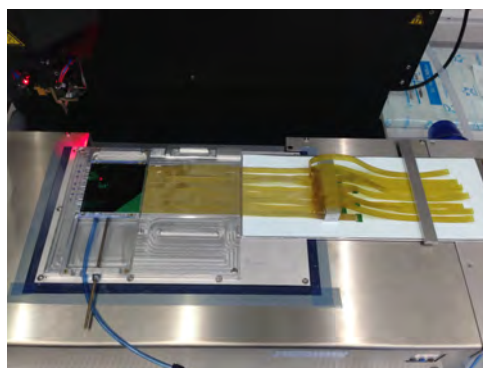


Figure 2: Microcables TAB-bonded to the sensor.

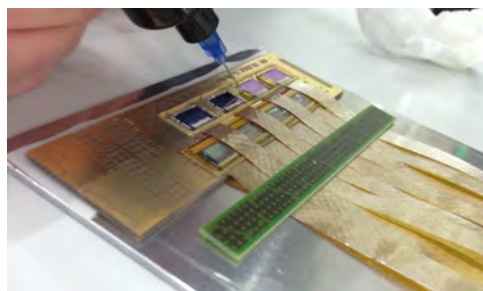


Figure 3: Globtop on the STS-8 board.



Figure 4: Dummy module with a 62x62 sensor.

Test sockets for quality measurements during the CBM-STS module assembly

C. Simons¹, V. Kleipa¹, C. J. Schmidt¹, D. Soyk¹, K. Kasinski², and I. Tymchuk³

¹GSI, Darmstadt, Germany; ²AGH University of science and technology, Krakow, Poland; ³LTU, Kharkiv, Ukraine

During the CBM-STS module assembly quality measurements need to be performed to assure electrical contact of the TAB-bonds that connect the microcables with the STS-XYTER chips as well as the silicon microstrip sensor. Non-destructive, easy and fast procedures for a large amount of microcables can be realized with Pogo Pin test sockets that are well adapted to the needs. In case of failure rebonding is possible while the devices are on the machine. Bonds are then finally protected with a globtop glue.

Test socket for the STS-microcables

After having TAB-bonded the Aluminum traces of the microcables to the pads of the STS-XYTER chip, the contacts can be checked through a test socket that provides easy connection to a dedicated testfan on the microcables (see Fig. 1). This testfan increases the pitch of the 42 μm wide traces from 116 μm to 200 μm . The testpads are staggered in two rows and have an approximately size of 200 by 600 μm . Because of the very thin microcables (thickness 24 μm) the company could only deliver the top socket with the Pogo Pins. The bottom socket will be designed in-house, a draft already exists (see Fig. 2). The microcable will be fixed by vacuum on a plate and aligned with pins.

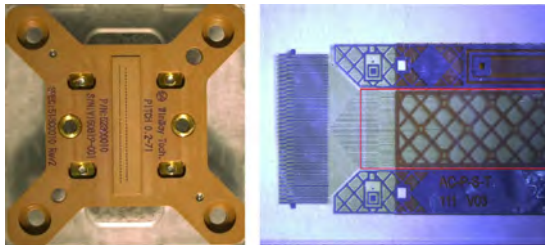


Figure 1: Top Pogo Pin socket (WinWay Technology) and testfan of the microcable.

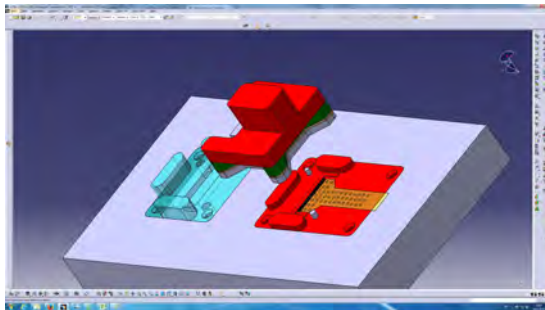


Figure 2: Draft design of the bottom socket.

For the bond connectivity test the Aluminum traces of the microcables are connected through a 64-pin adapter. The test consists of applying a small current to a single wire while the ASIC substrate is grounded. Testing neighboring wires will indicate shorts. The amount of current is measured and will indicate the quality of wire and ASIC-connection. The test needs to be done separately on each wire.

Test socket for the STS-XYTER chip

The electrical contact of the TAB-bonds that connect the semi-modules (STS-XYTER chips with two layers of microcables) with the silicon microstrip sensors can be put into practice by taking the chip into operation. A satisfactory bond will show through an increase in noise level attributed to the additional capacitance on the pre-amplifier input. The chip designers have elaborated a minimal set of 50 larger test pads for essential connectivity, that are placed near to the ordinary bonding pads. It allows full operation of the chip and to perform a rapid noise level estimate. Procedures for this estimate are wired into the ASIC. The testpad for a Pogo Pin has to be at least 150 μm x 150 μm in size, the pitch should be at least 200 μm (see Fig. 3, red marked pads). The design for the socket was made by *aps Solutions GmbH*, Munich, in cooperation with *WinWay Technology*, Taiwan. The socket will be manufactured after forwarding the final coordinates of the testpads to *aps Solutions*.

The chip by itself is placed upside down into the socket that will have an opening for the microcable. Further tasks for this test procedure are the development of a modified STS-XYTER board and suitable software.

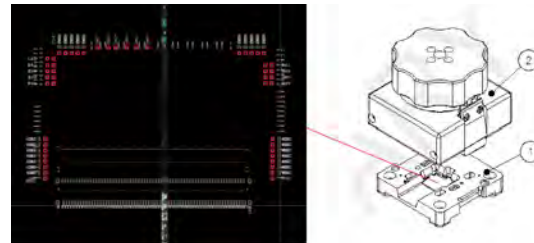


Figure 3: STS-XYTER with test pads and test socket by WinWay Technology.

Development of tooling for the STS module assembly at JINR's VB LHEP assembly laboratory

A. Sheremetev¹, Yu. Murin¹, V. M. Borshchov², M. A. Protsenko², and V. V. Elsha¹

¹JINR, Dubna, Russia; ²LED Technologies of Ukraine (LTU) Ltd, Kharkov, Ukraine

According to the FAIR-JINR-CBM Collaboration Contract, JINR's VB LHEP STS work group develops methods to manufacture around 600 STS modules for the first four stations of the CBM Silicon Tracking System.

In 2015 the laboratory for the module assembly was installed at VB LHEP JINR [1] with equipment adjusted and optimized for TAB bonding technology of the module components [2]. The assembly process comprises the following steps:

- Bonding of ASIC to the microcable;
- Bonding of the microcable to the double-sided silicon sensor (DSSD);
- Mounting of the ASIC on the Front-End Board (FEB);
- Gluing of meshed spacers and the shielding layers onto the microcables;
- Assembly of the interstrip cable to the n-side of the DSSD (optional).

At present time all two ultrasonic machines of the Lab are tuned for the module assembly with all appropriate parameters adjusted. The ultrasonic bonder EM-4370 (Planar, Belorussia) is upgraded for the TAB technology while the manual machine Ibond 5000 is used only for wire bonding.

The first set of custom designed tooling was developed for the EM-4370 ASIC-to-microcable bonding. It allows high-accuracy positioning of two layers of the microcable with regard to the ASIC input signal bonding pads (Fig. 1).

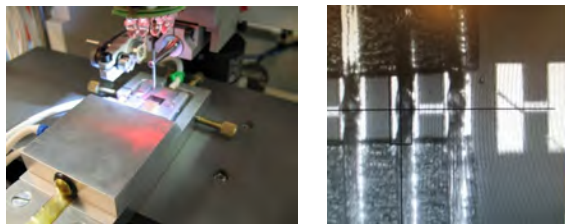


Figure 1: Custom-designed tooling for assembly of ASIC and microcable (left); realized TAB bonds (right).

Next step with the assembly of modules is the welding of the chip cables to the p-side of the DSSD. This is done with the ultrasonic automatic tab-bonding machine EM-4370 and special fixtures developed for this purpose. After welding all bonds are encapsulated with special protective adhesive (Fig. 2). Welding is carried out in the semi

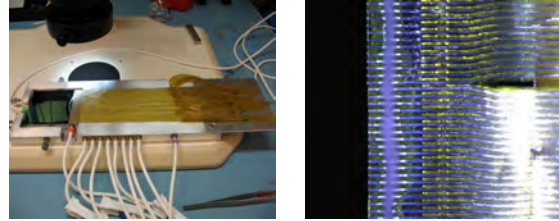


Figure 2: Special tooling for the assembly of DSSD and the cable (left); encapsulated signal pads (right).

automatic mode with six semi-modules assembled at the moment.

The assembly of the ASICs onto the front-end boards is the third step. Next, the ASICs are mounted onto the FEB. They are fixed to the heat sink with adhesives, and then wire bonding of the ASIC-to-FEB links are carried out with the help of the Ibond 5000 instrument. Welding is carried out with aluminum wire of 25 μm diameter and utilizes custom-designed tooling. After welding the meshed spacers and shielding layers are glued onto all microcables (Fig. 3).

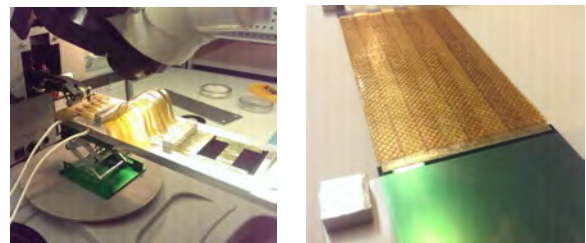


Figure 3: Custom-designed tooling for mounting ASICs onto FEBs (left); view of adjusted meshed spacers on the read-out cables (right).

After this step the assembly of the p-side of the module is completed. Similar operations are repeated for the n-side of the DSSD which eventually leads to the final product - the CBM-STS module ready for the QA testing and certification.

References

- [1] Yu. A. Murin *et al.*, CBM Progress Report 2014, Darmstadt 2014, p. 50
- [2] V. M. Borshchov *et al.*, CBM Progress Report 2013, Darmstadt 2014, p. 41

Progress with the integration of the CBM Silicon Tracking System

S. Belogurov¹, D. Emschermann², M. Faul², U. Frankenfeld², J. Heuser², S. Koch², P. Koczon², J. Kunkel², J. Lehnert², T. Morhardt², W. Niebur², C. J. Schmidt², H. R. Schmidt³, S. Schwab², O. Vassyliev², and J. Weinert²

¹ITEP, Moscow, Russia; ²GSI, Darmstadt, Germany; ³Universität Tübingen, Germany

The STS system integration effort targets a detector that can be installed in the gap of the superconducting dipole magnet and taken out for system maintenance [1]. The current engineering activities address the detailed structure of the detector system, the space requirements of the mechanical STS building blocks along with technical solutions to their installation, geometrical precision, the cooling of electronics and sensors, and routing of the supplies and services within and through the thermal enclosure.

System design and mechanical units

The eight tracking stations of the STS are composed of 18 mechanical *half units*. The base of a half unit is a C-shaped frame onto which the detector ladders, assemblies of sensor modules mounted on carbon fiber carriers, are placed. The opening of the C-frames cover the detector's physics aperture, while at its perimeter the read-out electronics and power distribution boards are located and can be cooled. After optimization of the sensor placement in the units, the ladder structure and cable lengths have been defined, a pre-requisite for designing C-frames and cooling plates. Figure 1 depicts the current CAD design of a corner of detector half unit 7 in the most downstream station, the largest one with about 1 m height. Progress has been made with the arrangement of ladders, their detailed mounting on the C-frame, the cooling plates, the locations of electronics and powering boards and routing of signal and power cables. The dimensions of the STS main frame, receiving the half units and the thermal insulating walls, meet the spatial boundary conditions. The design aims at a mechanical precision of half unit/ ladder placement of better than 100 μm .

Cooling plates

The cooling system has to remove more than 40 kW of power dissipated by the front-end electronics located inside the thermal enclosure. The stacks of front-end electronics boards are to be mounted onto cooling plates. Those are aluminum plates with millimeter-diameter cooling channels through which bi-phase CO_2 will be circulated. The engineering team is currently prototyping such cooling plates in cooperation with industry using specific pressure-standing welding techniques.

Carbon fiber ladders

Prototypes of carbon fiber ladders have been manufactured at GSI in a winding technique. They were meant to

prove the feasibility of a request for series production in aerospace industry. They are also used to explore a specifically low-mass construction of central ladders surrounding the beam pipe. A technical solution is depicted in Fig. 2, employing thin rods rather than a hollow cone as reported in [2] that turned out to involve too much material in the respective CBM arrangement.

Further tasks

The studies on the STS integration comprise further topics that are in different stages of completion: the rails for units and system, the base support plate, the realization of real-size models of C-frames with attached components, beam pipe and window towards target chamber/Micro Vertex Detector.

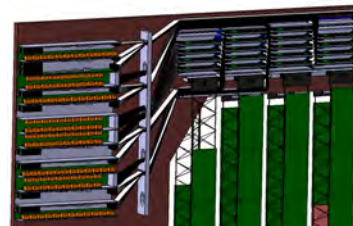


Figure 1: CAD design of a corner of a C-frame with detector ladders (center), front-end electronics (top), and powering and read-out boards (left), indicating also cable routing.

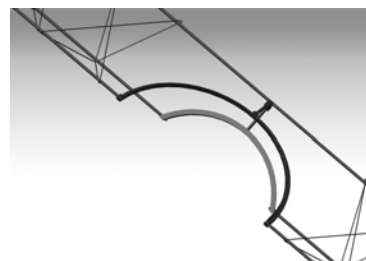


Figure 2: Design of a carbon fiber ladder with a particularly low-mass central region to surround the beam pipe.

References

- [1] CBM STS Technical Design Report, GSI Report 2013-4 (2013), chapter 5.1
- [2] S. Igolkin *et al.*, CBM Progress Report 2014, p. 48

Thermal simulations of CBM-STS read-out boards

E. Lavrik

University of Tübingen, Tübingen, Germany

The CBM Silicon Tracking System (STS) is a compact detector that consist of double-sided silicon microstrip sensors. It is mounted within a thermal insulation box with an overall volume of about 2 m^3 defined by the aperture of the dipole magnet [1]. In order to reduce the material budget of the detector all heat producing readout electronics were moved outside of the acceptance zone, which in turn greatly reduced the space available for cooling the front end electronics. In order to avoid thermal runaway during the operation of the detector, silicon sensors have to be kept at temperatures below -5°C . This is quite challenging as up to around 40 kW of power is dissipated from the STS Front-End-Electronics (FEE) in a rather small volume with very limited space for heat exchanger plates. Bi-phase CO_2 cooling is to be used in the STS detector due to its superior volumetric heat transfer coefficient, which is about an order of magnitude better than for conventional freons. The aim of this research project is to optimize the read-out board elements in terms of heat transfer efficiency under the given space constraints.

Thermal simulations

The Read-out Boards (ROB) (Fig. 1), connecting to the Front-end electronics boards located on the detector ladders, are located on the peripheral parts inside the STS thermal insulation box and the heat dissipation could impact the thermal distribution inside the detector box. Each board produces dissipates 7,25 W which equals to 72,5 W per ROB assembly. In order to optimize the cooling of these boards and space required to accommodate them, a series of Finite Element Method (FEM) thermal studies have been carried out in the Solidworks simulation package with the same approach as described in [2].



Figure 1: Layout of the read-out board with heat producing components shown in bright-red color.

Simulation results

Figure 2 shows the temperature distribution of the ROB holding assembly with the point of maximum temperature marked. The thermal studies show (Tab.1) that already a 1 mm thick shelf provides enough cooling power to effectively dissipate the heat produced by the electronics and

keep the assembly at a temperature below -5°C . The desired temperature regime is as well achieved at higher initial coolant temperature of -30°C which in turn allows to move further away from the triple point of liquid CO_2 (-56.6°C , 5.11 bar) and mitigate the risk of solidifying the coolant, effectively making the cooling safer.

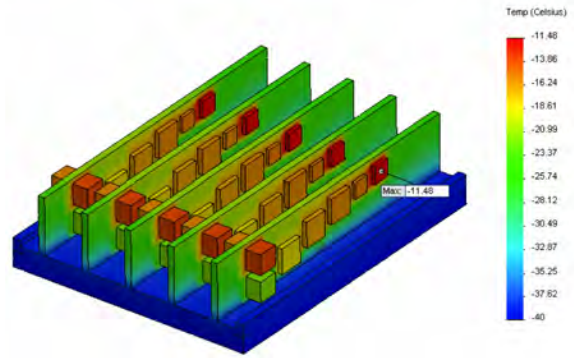


Figure 2: Temperature distribution on ROB holding assembly with 1 mm thick shelves computed for -40°C initial coolant temperature.

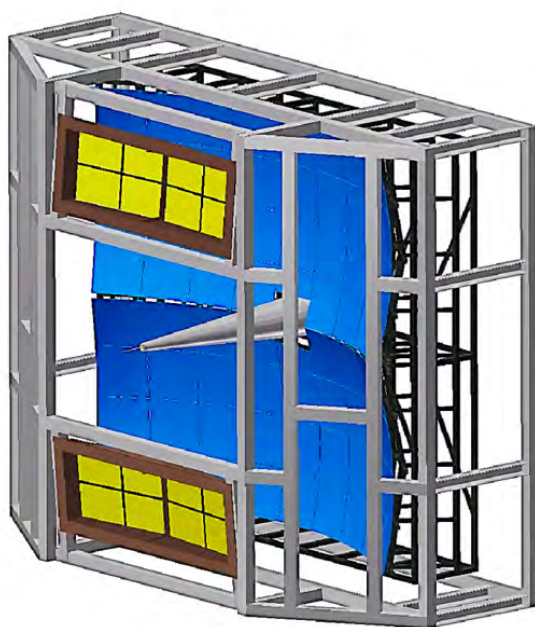
Table 1: Simulated maximal temperature on the ROB box in dependence of the shelf thickness and initial coolant temperature.

Shelf thickness	Maximum temperature vs. CO_2 temperature, $^\circ\text{C}$				
	-40	-30	-20	-10	0
1 mm	-11.48	-6.49	-1.49	3.49	8.723
2 mm	-16.16	-10.01	-3.85	2.31	8.63
3 mm	-18.2	-11.51	-4.81	1.87	8.62

References

- [1] CBM STS Technical Design Report, GSI Report 2013-4 (2013), chapter 2
- [2] E. Lavrik *et al.*, CBM Progress Report 2014, p. 52

Ring-Imaging Cherenkov Detector



Design of a control and monitoring system for the mirror alignment of the CBM RICH detector*

J. Bendarouach^{†1} and C. Höhne¹

¹Justus Liebig University, Gießen

An important aspect to guarantee a stable operation of a RICH detector is the alignment of the mirrors. A first method to qualitatively assess whether misalignment is present, CLAM (Continuous Line Alignment Monitoring [1]), has been implemented in the RICH prototype and successfully tested during a beamtime at CERN. A correlation has been highlighted between reflected stripes appearing broken and corresponding reconstructed rings [2].

In order to quantify the highlighted misalignment, a second method, inspired by the HERA-B experiment [3], was developed and uses recorded data. The principle of the method is as follow. When a particle enters the RICH vessel, it emits Cherenkov light, which is reflected by one or several mirror tiles to the PMT plane, see red crosses on Fig. 1. These photon hits are then reconstructed together

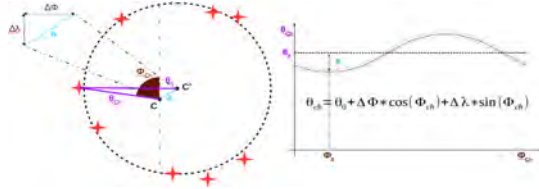


Figure 1: A sinusoidal behaviour between Cherenkov distances and angles has been demonstrated [3], allowing a misalignment quantification of mirror tiles.

as a ring, whose center C' differs in case of misalignment from the point C , representing the extrapolated particle hit to the PMT plane, if the incident particle had been reflected by the same aligned mirror tiles. Measuring Cherenkov distances (θ_{Ch}) and angles (Φ_{Ch}) for each photon hit, a sinusoidal dependence has been demonstrated between these two parameters (see formula Fig. 1). For a sufficient number of accumulated events hitting a particular mirror tile, those measurements can reveal and quantify potential misalignments of the considered tile (via $\Delta\Phi$ and $\Delta\lambda$, see Fig. 1) [4].

This technique has been adapted and tested for the CBM RICH detector with simulations in the CbmRoot framework. It produces good results for misalignments ranging from 0.2 mrad up to 12 mrad, as seen in Fig. 2. If possible mirror misalignment is revealed, it can be subsequently included and rectified by correction routines. A first correction cycle has been successfully implemented. A mirror tile has been artificially misaligned by 5 mrad around its

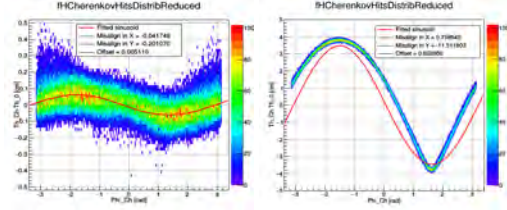


Figure 2: Plot of $(\theta_{Ch} - \theta_0)$ as function of Φ_{Ch} . For a 0.2 (left) and 12 (right) mrad rotation around the horizontal axis, a fit of the sinusoid (red curves) returns 0.2 and 11.5 mrad misalignment respectively.

horizontal axis and this misalignment has been evaluated using the described method. The extracted misalignment is 5.26 mrad around the horizontal axis and 0.37 mrad around the vertical one. A new simulation using the corrected mirror geometry has then been run and at the reconstruction level the mean position between the points C and C' has been compared before and after corrections were applied (see Fig. 3).

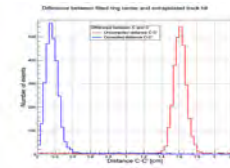


Figure 3: Distance between the fitted ring center C' and the extrapolated track hit to the PMT plane C . For the uncorrected case (red), the mean distance was 1.6 cm, whereas once the correction has been calculated and applied (blue), it was reduced to 0.15 cm.

It is foreseen to use these correction routines to compare ring reconstruction and ring-track matching efficiencies. In a next step, the CLAM technique will also be used to quantify misalignment via photogrammetry.

References

- [1] L. Steiger et al., Nucl. Instr. Meth. Phys. Res. A 639 (2011) 219
- [2] J. Bendarouach et al., CBM Progress Report 2014, p.56
- [3] A. Gorisek et al., Nucl. Instr. Meth. Phys. Res. A 433 (1999) 408
- [4] M. Staric et al., Nucl. Instr. Meth. Phys. Res. A 586 (2008) 174

* Work supported by HGS-HIRE, the GSI F&E cooperation with Gießen and BMBF grants 05P15RGFCA and 05P12RGFCG.

[†] jordan.bendarouach@exp2.physik.uni-giessen.de

Development of a MAPMT test stand and first results*

J. Förtsch^{†1}, C. Pauly¹, D. Pfeifer¹, and K.-H. Kampert¹

¹University of Wuppertal, Germany

In Summer 2015, a total of 1100 multianode PMTs of type HAMAMATSU H12700 (HAMAMATSU internal name H13708) were ordered by GSI for use in the CBM and HADES RICH photon detectors. Delivery of these PMTs started in November 2015, with up to 50 PMTs per month, the last PMT will be received around mid 2017. Detailed acceptance criteria were defined with HAMAMATSU to ensure optimal quality of these PMTs [1]. A dedicated single photon scanning test stand was developed in Wuppertal, in order to fully characterize each PMT, to survey the PMT quality, and also to provide quick feedback to HAMAMATSU for further optimization of the PMT production line. The goal is to obtain a full spatially resolved single photon scan of every delivered PMT. Automated analysis of these data can provide all important characteristic PMT features except absolute quantum efficiency, which will be measured separately for a subselection of all PMTs (see [2] for more details).

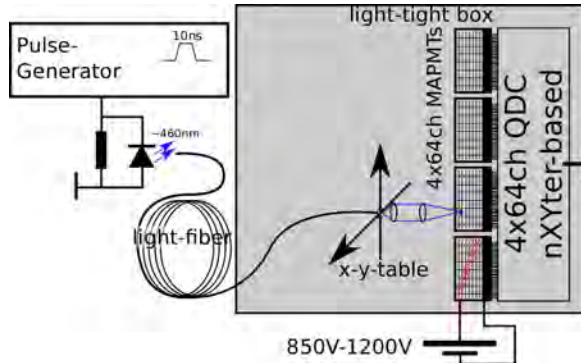


Figure 1: Scheme of the test setup showing the housing, light source, X-Y-table and the nXYter ADC

A sketch of the test stand scheme is shown in Figure 1. The main component is an EPICS controlled XY stepper-motor drive (see Figure 2) for scanning the PMT surface (precision better 0.1 mm) with a light fiber attached to a focusing optic, focusing the single photons to a spot size of about 1 mm. The light is produced using a pulsed LED source (with wavelength 460 nm) at very low intensity, such, that only in $\approx 10\%$ fraction of pulses a single photon is detected by the PMTs. Up to 4 MAPMTs can be scanned simultaneously, one of them kept unchanged and used as reference PMT. Using this reference PMT, data from individual scans can be normalized and compared relative to

each other by compensating for long term variations of the LED light source.

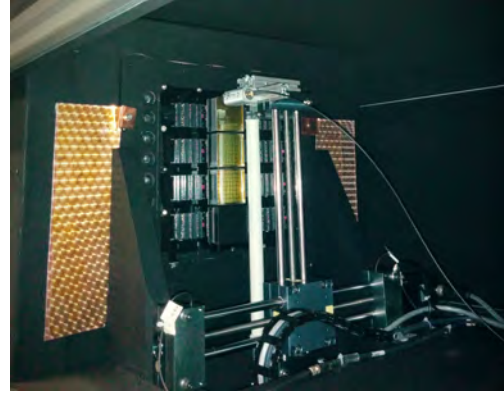


Figure 2: Picture of the test stand showing the inside of the coated aluminum box. Here the fiber attached to the XY-table hovers over one of the four PMTs

The PMTs are read out using two 128ch nXYter FEBs (see [3]), providing a free streaming digitization of PMT pulses (above an adjustable threshold) with ADC- and TDC information. A DABC based DAQ system (see [4]) is used to store both nXYter- and EPICS slow control data in the same data file, such that the precise table position can later be synchronized offline with the PMT data stream. The fraction of detected photons over total number of pulses for a given scan point is used as a measure of the relative PMT efficiency at this point. Averaging this efficiency over the full active PMT area yields a single "efficiency index" number, a good quantity to compare the single photon detection efficiency of all tubes relative to each other.

The ADC readout allows to measure the single photon amplitude spectrum, the mean value of this spectrum is used to derive the PMT gain for a given channel. Additional automatic HV scans for a subset of pixels (using the EPICS controlled HV system) are also included in the standard measurement procedure, and allow to derive the gain variation ($\Delta_{Gain} / \Delta_{HV}$) and optimal HV setting for each tube. These data will be used to sort all PMTs in gain classes, since groups of six PMTs will share a common HV supply line in the CBM/HADES RICH detector setup.

The described test stand setup is installed inside a light-tight aluminum box. The inside coated with a special black spectrometer paint (811/21 NEXTEL VELVET). Careful construction of this box assured the total suppression of any stray light from outside, allowing to derive even the thermal

* Work supported by GSI and BMBF contract No. 05P15PXCA

[†] j.foertsch@uni-wuppertal.de

photon dark rate of each PMT, thanks to the self-triggered readout scheme.

The scan procedure, as well as the subsequent data analysis, is fully automated, including QR-code scans of the PMT serial numbers to minimize chance for mixing PMTs. A single scan of 3+1 PMTs (with reference PMT) takes around nine hours, including sufficient time for the PMT dark-rate to level off and the gain to stabilize. Using this setup enables us to fully characterize up to 30 PMTs per week. Routine scanning operation has been started in February, meanwhile around 70 PMTs could be characterized. Further plans include to automatically derive characteristic performance numbers for storage in a common CBM / FAIR component database, and the automatic distribution of key performance plots and trend analysis for each measured PMT via a web page. This will allow for a continuous control of the production process, and will provide direct feedback to the manufacturer.

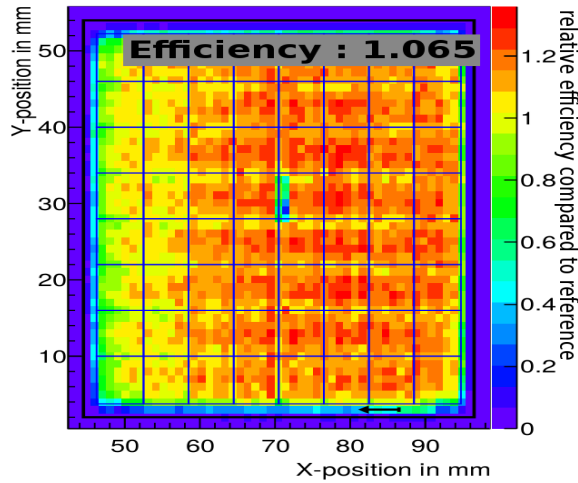


Figure 3: Single photon efficiency scan of a H12700 counting all events compared to the trigger rate for each measurement bin. The scaling of the plot is done in terms of the reference PMT

A first spatially resolved scan of a MAPMT from one of the first delivery batches is shown in Figure 3, together with the efficiency index relative to our reference PMT HA0230. The step size resolution in this scan is around 1 mm in X- and Y-direction, matching well the spot size of ca 1 mm. This PMT shows a distinct feature, namely a strong horizontal efficiency gradient, which has been observed on nearly all of the early delivered PMTs. The overall averaged efficiency nevertheless is quite good, about 6.5% better than the reference PMT, which itself already shows better than average efficiency. This observation was communicated to HAMAMATSU, who thereupon tried to further optimize the production process to increase the homogeneity. Scans from PMTs out of recent delivery batches indeed show an improved homogeneity, though together with a slight decrease of overall efficiency. Further investigations

are ongoing.

Another efficiency artifact can be seen in the middle of the PMT, which is a unique feature of this special PMT, and has been not observed on any of the other PMTs so far.

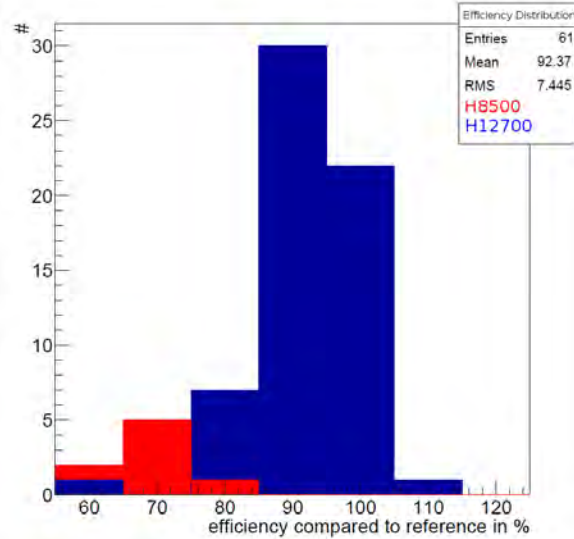


Figure 4: Efficiency of 61 H12700 (blue) and 8 H8500 (red) in terms of the same reference PMT

Figure 4 shows a comparison of all measured PMTs so far with respect to the total efficiency index. An efficiency value of 100% corresponds to an efficiency index of 1.00, and thus is equal to our reference PMT. The plot also includes data of a few older H8500 type MAPMTs measured in parallel, with its data shown in red. One can clearly see the increased efficiency of the new H12700 PMTs, which, at the given wavelength of 460 nm, are about 20% more efficient than the old H8500.

Similar distributions, also as function of PMT serial number or production time, are done for gain, dark rate and other predicative quantities, giving the possibility to quickly distinguish between good and bad PMTs.

Although the amount of measured PMTs is still quite small one can already see the importance of the qualification tests. The test stand gives valuable and quick information allowing to immediately sort out PMTs not fulfilling the selection criteria. The test stand gave already valuable information resulting in important feedback for the manufacturer.

References

- [1] J.Eschke et al., "MAPMTs ordered - list of specifications, first delivery", this report
- [2] C.Pauly et al., "Single photon XY scans of various MAPMTs", CBM Progress Report 2013 p.56
- [3] "<https://cbm-wiki.gsi.de/pub/Public/PublicNxyter/nXYTER.pdf>"
- [4] "<http://dabc.gsi.de/doc/manuals/dabcuser.v1.0.01.pdf>"

Deriving the effective focal plane for the CBM-RICH detector *

I. Kres¹, C. Pauly¹, and K.-H. Kampert¹

¹Bergische Universität Wuppertal, Germany

The RICH detector is designed to provide identification of electrons and suppression of pions in the momentum range below 10 GeV/c. This will be achieved using a gaseous RICH detector with focusing mirror elements and a photon detector consisting of a plane of MAPMTs. In our current "standard" design, the photon detector has a "wing-shaped" construction consisting of 4 individual plane elements, two of them above and two below the beam pipe respectively. This design approximates the ideal focal sphere, and is the result of a detailed optimization procedure [1].

The detailed mechanical design, however, shows that this geometry introduces significant dead space regions between the two tilted halves of each wing. This is due to the required additional volume behind the PMTs needed for electronic readout components. It turns out that a continuously curved detection plane might be mechanically easier to implement, and would help to overcome the dead space limitation. In this report we present a study to derive the ideal 3-dimensional shape of the focal plane based on full Monte Carlo simulations, using the ring sharpness as optimization criterion.

To obtain the optimal focal position, the tilted wing-shaped PMT planes were rotated back, such that a single, flat detection plane is used in the simulation. Using individual Monte Carlo simulations, this flat plane was moved upstream and downstream along the beam direction such, that the optimal focal position will be crossed for each point (x, y) . For each step, the dR-value (based on ellipse fitting of the Cherenkov rings) was mapped as a function of (x, y) . dR, the mean distance of each individual hit to the fitted ellipse, is used here as criterion for ring sharpness. Finding the minimum dR value along z for a given point in (x, y) yields a 3d shape of the optimal focal plane.

The study was carried out for two different mirror rotation angles of -1° with respect to the beam axis (rich.v14a.1e geometry version) and for 10° (rich.v16a.1e). Single electrons and positrons were generated uniformly on all planes, with transverse momenta ranging from 0.75 to 3 GeV/c. Due to bending of low momentum electrons in the magnetic field the different energies might lead to different focal spheres. Figure 1 shows the derived shape of the ideal focal plane.

Figure 2 shows a fit of these data with a cylindrical shape aiming to derive the optimal radius and tilt angle of this shape. This simplified form was chosen because it will be easier to implement in the Monte Carlo simulation, and also for the later mechanical design. As a result, we find a cylin-

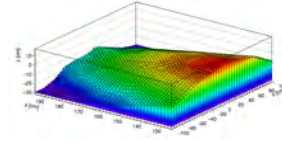


Figure 1: Ideal focal plane, based on the calculation of dR for geometry rich.v16a.1e.

der basis radius of 2m, and a cylinder tilt angle of 11.5° with respect to beam axis.

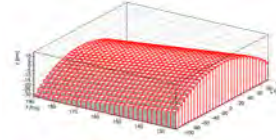


Figure 2: Fit, based on data from figure 1.

Based on these parameters, we performed a comparison between the extracted optimal focal shape and the currently implemented "standard" wing-shaped geometry. Figure 3 shows, that the currently used geometry roughly matches the "optimal" focal plane. However, there is a striking difference in the tilt angle. The tilt angle of the standard geometry is not only based on ideal focussing, but the result of a more involved optimization procedure taking into account also the size of focal plane, the ring ellipticity A/B, and the photon incident angle α . A similar optimization procedure now also has to be done to determine the optimal tilt angle in the cylindrical focal plane geometry.

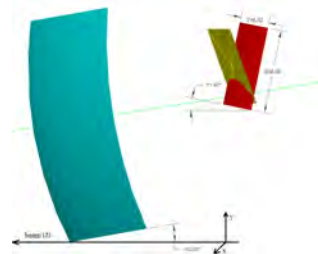


Figure 3: Comparison of the extracted geometry (red) with a wing-shaped (yellow).

References

- [1] T. Mahmoud et al. CBM Progress Report (2015)

* Work supported by BMBF 05P15PXFCA, and GSI

Implementation of the new RICH geometry in CBMROOT *

S. Lebedev^{1,2}, C. Höhne¹, and E. Ovcharenko^{2,3}

¹Justus Liebig University Giessen, Giessen, Germany; ²LIT JINR, Dubna, Russia; ³ITEP, Moscow, Russia

The RICH geometry has been considerably changed and updated [1, 2]. Many new features were introduced with this version which required significant changes in the code. In this report an overview of the implementation of the new RICH geometry in CBMROOT is discussed.

Geometry. The new geometry is very detailed. Each photon detector pixel is implemented as separate node. The geometry hierarchy is kept rather flexible in order to be able to create different variants of the PMT plane and to allow simple creation of new RICH versions using CATIA.

Simulation. The first changes were done in the simulation code, namely, *CbmRich* class. The changes relate to the new hierarchy and naming scheme of the geometry.

Pixel address scheme. In the simulation pixel addresses are assigned on the fly from geometry. Since each pixel is implemented as separate node, the routine loops over all pixel nodes, increments address counters and assigns to each pixel an unique address. For the beamtest and real data, the address scheme can be stored in a separate file as well. The main implementation is done in *CbmRichDigiMapManager* class. There are two main methods: 1) *GetAddressByPath* which returns the pixel address by pixel node path and is used in the digitizer; 2) *GetDataByAddress* which returns pixel data by pixel address and is used in the hit producer.

Detector response simulation. The *CbmRichDigitizer* class simulates the detector response, i.e., quantum efficiency, cross talk and noise digis. the digitizer creates *CbmRichDigis* which contain pixel addresses and pointers to *CbmMatch*. *CbmMatch* stores all references to Monte-Carlo points which contribute to a certain digi. Also, it is assumed that only one digi can be produced for one pixel. Figure 1 shows the block diagram of the *CbmRichDigitizer* class.

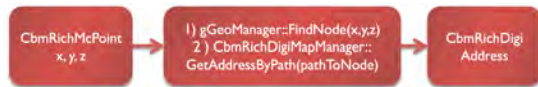


Figure 1: Detector response simulation block diagram.

Hit producer. The hit producer creates *CbmRichHits* from *CbmRichDigis*. Hits are rotated in order to get a perpendicular view on the PMT plane. Figure 2 shows the block diagram of the *CbmRichHitProducer* class.

Projection producer. The projection producer projects STS tracks onto the PMT plane. Two variants are imple-



Figure 2: Hit producer block diagram.

mented, an analytical and universal. The analytical algorithm can work only with the current "two wings" geometry. The universal algorithm can work with complicated PMT plane shapes. It uses *TGeoManager* to find intersections with nodes.

Ring reconstruction. The ring reconstruction and electron identification algorithm has been optimized with respect to the new geometry.

Matching to MC data. Significant changes had to be done for matching reconstructed to Monte-Carlo data. Previously, there was a one-to-one correspondence between *CbmRichHit* and *CbmRichPoint*. For several photons crossing one pixel only the first fired *CbmRichPoint* was matched to the hit. The new scheme is shown in Figure 3, now all *MotherIds* contributing to a hit are stored.

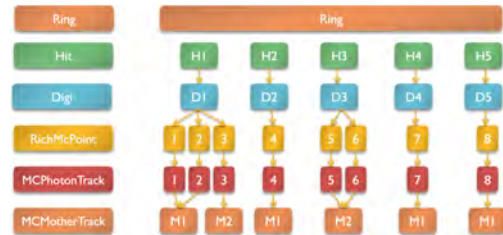


Figure 3: Matching to Monte-Carlo data in the RICH.

Backward compatibility. The new software update does not support the old RICH geometries. They were removed from the repository. This has been done, because the support of the old geometries would have resulted in a significant complexity of the code. Also, the old geometries are not realistic and should not be used further.

In summary, the RICH software was considerably updated due to the new RICH geometries. All changes were thoroughly tested showing no major problems. The software and geometries were committed to the repository and can be used by other groups.

References

- [1] T. Mahmoud, this report.
- [2] E. Ovcharenko, this report.

* Work supported by BMBF grants 05P15RGFCA and 05P12RGFCG.

First simulation results with the new RICH geometry *

S. Lebedev^{1,2} and C. Höhne¹

¹Justus Liebig University Giessen, Giessen, Germany; ²LIT JINR, Dubna, Russia

A new version of the RICH geometry has been implemented in CBMROOT [1]. In this report, first simulation results are discussed.

RICH geometries. Four versions of the RICH geometry are tested, two for each beam energy. First version contains all mirror tiles, the corresponding geometries are *rich_v16a_1e* for SIS100 and *rich_v16a_3e_full_mirror* for SIS300. In the second version 4 most inner mirror tiles close to the beampipe are removed in order to reduce the ring density in the central part of the PMT plane, the corresponding geometries are *rich_v16a_1e_nobpmt* for SIS100 and *rich_v16a_3e* for SIS300. Note that SIS100 and SIS300 versions of the RICH geometry are the same except beampipe implementation.

Geometry test with e^\pm pairs. In simulations one e^- and one e^+ from the primary vertex were generated with the box generator with the following parameters $p_t = [0, 3]$ GeV/c, $\phi = [0, 360]^\circ$, $\theta = [2.5, 25.]^\circ$. Figure 1 shows the geometrical acceptance for SIS100 and SIS300 versions of the RICH detector. The integrated geometrical acceptance with respect to the above mentioned simulation is 88.5% for *rich_v16a_1e* and 80.4% for *rich_v16a_3e*. The main difference between the two geometries is losses at high particle momenta due to the fact that the inner part of the mirror was reduced for the SIS300 geometry.

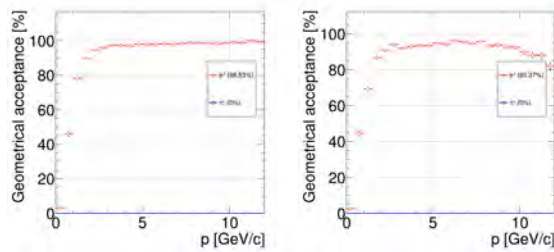


Figure 1: Geometrical acceptance for *rich_v16a_1e* (left) and *rich_v16a_3e* (right) geometries.

The mean number of hits per electron ring is 28. This number does not include crosstalk hits.

Test with UrQMD events. The RICH geometries were also studied with simulations for central Au+Au collisions at 8AGeV (SIS100) and 25AGeV (SIS300) beam energies. The STS geometry version *sts_v15c* was used. Figure 2 shows all particles detected in the RICH detector for 8AGeV and 25AGeV beam energies. Results comparing

all 4 geometry versions are summarized in Table 1.

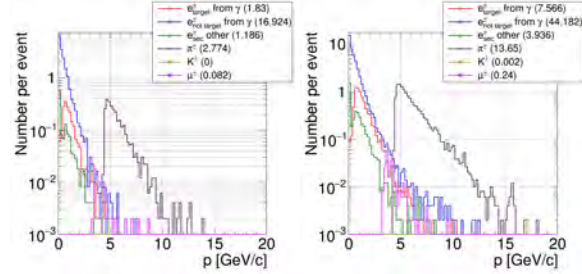


Figure 2: Detected particles in the RICH detector (with at least one hit) in dependence on momentum. Left: 8AGeV, *rich_v16a_1e*. Right: 25AGeV, *rich_v16a_3e*

Table 1: Comparison of the 4 introduced RICH geometries.

SIS100		SIS300	
v16a_1e	v16a_1e_nobpmt	v16a_3e	v16a_3e_full_mirror
Number of hits/event			
463	396	1312	2035
Number of rings/event (≥ 1hit)			
22.8	19.2	69.5	122.0
Number of rings/event (≥ 7hits)			
18.6	15.8	56.0	96.0
Number of e^\pm_{target} from γ/event			
1.8	1.7	7.5	8.5
Number of $e^\pm_{nontarget}$ from γ/event			
16.9	14.9	44.1	59.0
Number of π^\pm/event			
2.77	1.5	13.6	49.4

For 25AGeV beam energy the majority of fast pions and many secondary electrons not stemming from the target (lower two rows of Table 1) are at low polar angles close to the beampipe. In- or excluding the innermost four mirror tiles thus has a large effect on the hit and ring density. For stable operation of the SIS300 geometry in the current settings we thus propose to skip the innermost mirrors for the moment on account of some acceptance losses as shown in Figure 1. The SIS300 geometry is open for further optimizations, e.g. also by using different radiator gases.

References

- [1] Implementation of the new RICH geometry in the CBM-ROOT, this report.

* Work supported by BMBF grants 05P15RGFCA and 05P12RGFCG.

Electron identification performance with the new RICH detector *

S. Lebedev^{1,2} and C. Höhne¹

¹Justus Liebig University Giessen, Giessen, Germany; ²LIT JINR, Dubna, Russia

A new version of the RICH geometry was implemented in CBMROOT [1]. In this report, first results on the electron identification performance are discussed.

The tracking performance was studied with simulations for central Au+Au collisions at 8AGeV and 25AGeV beam energy embedding 10 additional e^\pm in each event. The following geometries were used: *sts_v15c*, *rich_v16a_1(3)e*, *trd_v15a_1(3)e* (smearing), *tof_v16a_1(3)e*. Note that the SIS300 version of the RICH geometry (*rich_v16a_3e*) has a reduced geometrical acceptance in order to decrease the ring density at low polar angles to an acceptable level [2].

Figure 1 shows the ring reconstruction efficiency for primary electrons. The mean efficiency for 8AGeV beam energy is 96.5% for electrons with at least 7 hits (red) and 97.9% for electrons with at least 15 hits (blue). The corresponding numbers for 25AGeV beam energy are 92.5% and 94.6%, respectively.

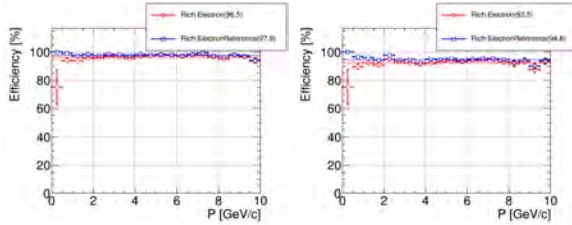


Figure 1: Ring reconstruction efficiency for primary electrons. Left: 8AGeV. Right: 25AGeV beam energy.

Figure 2 shows the global track reconstruction efficiency for primary electrons. Mean efficiencies are 70% for 8AGeV beam energy and 56% for 25AGeV beam energy.

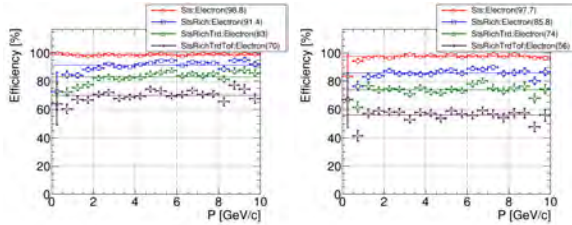


Figure 2: Global track efficiency for primary electrons. Left: 8AGeV. Right: 25AGeV beam energy.

Figures 3 and 4 show the electron identification efficiency and the pion suppression factor for 8AGeV and

25AGeV beam energies, respectively. The RICH detector alone gives pion suppression factor of 760 at 83.6% of the electron identification efficiency for 8AGeV beam energy and factor of 300 at 78.9% for 25AGeV beam energy.

The RICH and TRD combined pion suppression factor is 9100 at 65.7% electron identification efficiency for 8AGeV beam energy. For 25AGeV beam energy the final pion suppression factor is 30000 at 53.0% electron identification efficiency.

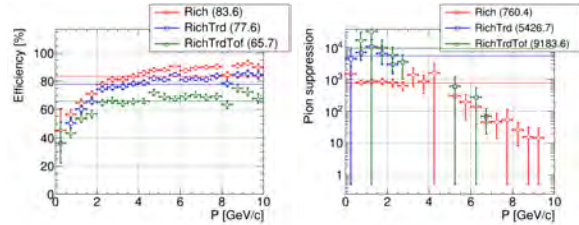


Figure 3: Electron identification efficiency and pion suppression factor for 8AGeV beam energy.

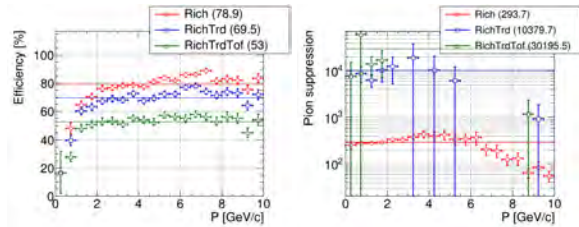


Figure 4: Electron identification efficiency and pion suppression factor for 25AGeV beam energy.

In summary, the performance of the updated RICH detector with respect to its geometry and ring reconstruction is 5–10% better comparing to the previous version of the RICH detector.

References

- [1] Implementation of the new RICH geometry in the CBM-ROOT, this report.
- [2] First simulation results with the new RICH geometry, this report.

* Work supported by BMBF grants 05P15RGFCA and 05P12RGFCG.

Size of the PMT plane vs. low-mass di-electron reconstruction*

E. Lebedeva¹ and C. Höhne¹

¹Justus-Liebig University Giessen, Germany

A gaseous CBM-RICH detector with focusing mirror elements and a photon detector is designed to provide identification of electrons and suppression of pions in the momentum range below 10 GeV/c. This report is an update of the studies in which the dimensions of the photon detector planes were decreased in order to investigate the influence on the reconstruction of low-mass di-electrons [1]. This time the enlargement of the PMT planes was studied as well.

Several cases of PMT plane reduction and enlargement were studied. The photodetector planes were changed a) from the sides; and b) from top and bottom (see Figure 1). 10% or 20% of the overall PMT plane size were cut or enlarged.

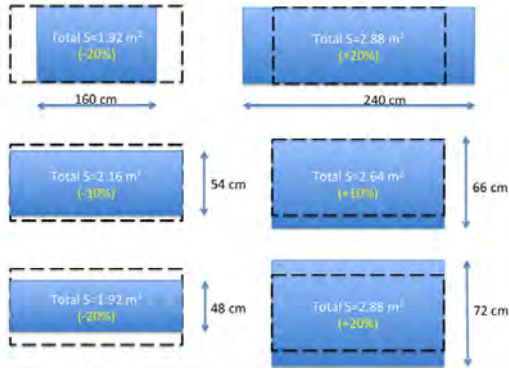


Figure 1: Different cases of changing the PMT planes.

Reducing each PMT plane from the sides decreases the number of fully reconstructed electrons from γ -conversion and π^0 -Dalitz decay by 10%. The number of reconstructed electrons from γ -conversion and π^0 will decreased more significantly when reducing the photon detector planes from top and bottom. Enlarging the PMT planes at bottom and top will increase the number of electrons from π^0 -Dalitz decay by 20-30%. Reconstruction of the low-mass di-electron pairs was performed with the standard procedure (for more information see [2]). Electron identification was performed with the RICH, TRD and ToF detectors. The combinatorial background was reduced using the γ -conversion cut, two topology cuts and a transverse momentum cut.

The final signal to background ratios and reconstruction efficiencies of mesons for central Au+Au collisions at 25 AGeV beam energy are presented in Table 1. The signal to background ratio stays more or less at the same level when reducing/enlarging the photon detector planes. However, reconstruction efficiencies change drastically if reducing the PMT plane, as well as final reconstruction efficiency will increase if enlarging the photon detector planes.

Table 1: S/B ratios and reconstruction efficiencies after applying all cuts for central Au+Au collisions at 25 AGeV beam energy.

	Full size	L&R sides [%]	T&B sides[%]	
		20	10	20
Reduced PMT planes				
ρ [eff.]	2.61	2.45	2.13	1.62
ω [eff.]	2.73	2.54	2.26	1.72
ω [S/B]	0.19	0.2	0.202	0.181
ϕ [eff.]	3.69	3.54	3.25	2.45
ϕ [S/B]	0.095	0.103	0.111	0.115
Enlarged PMT planes				
ρ [eff.]	2.61	2.49	2.90	3.04
ω [eff.]	2.73	2.66	3.08	3.20
ω [S/B]	0.190	0.231	0.191	0.200
ϕ [eff.]	3.69	3.57	4.10	4.29
ϕ [S/B]	0.095	0.083	0.091	0.105

In summary, the conceptional studies show, the enlarging or reducing the PMT plane does not change the signal to background ratios for low-mass di-electron pairs significantly as both, signal and background are reduced/enhanced. However, signal efficiencies are easily changed by $\pm 20\%$ or more.

References

- [1] E. Lebedeva and C. Höhne, CBM Progress Report 2014, p. 58
- [2] E. Lebedeva and C. Höhne, CBM Progress Report 2012, p. 106

*This work was supported by HIC for FAIR, by the GSI F&E-Cooperation with Giessen, and by BMBF grants 05P15RGFCA and 05P12RGFCG.

Optimization of the RICH geometry*

T. Mahmoud¹ and C. Höhne¹

¹II. Physikalisches Institut, JLU-Gießen, Germany

Introduction

The modifications of the CBM dipole magnet had two main consequences for the geometry of the RICH detector. First, the RICH had to be shifted downstream by 20 cm thus requiring a slight increase of the mirror and PMT-planes to cope with the acceptance. The second, more significant change is related to the stray field in the vicinity of the PMT-plane, which downgrades the quantum efficiency of the PMTs. To escape the stray field we consider two steps: rotating the system of mirror-PMT-planes by $\beta = 10^\circ$ outwards in the $y - z$ -plane and shielding the PMT-plane with a box of steel.

The RICH geometry versions used so far (*v08a*, *v14a*) have had to be modified accordingly, which called for re-optimization of the orientation of the PMT-plane in space. In particular the rotation angles around the x - and y -axis, θ_x and θ_y , and the y and z position coordinates had to be fine-tuned to keep the ring ellipticity and ring resolution minimal. A measure for the ellipticity is the ratio of minor to major axis of an ellipse fit to the ring, B/A . The ring resolution can be characterized by the parameter dR being the RMS of the distribution of the distance between the fit and the individual hits forming the ring.

The optimization procedure[1] consists of four steps, in which wide ranges of θ_x , θ_y , dy , and dz are scanned systematically to determine a set of these variables with the optimal ring parameters. dy and dz are displacements around the current position coordinates y_0 and z_0 respectively. In the study single electrons and positrons were generated isotropically in space with a flat distribution in transverse momentum from 0 to 4 GeV/c. Due to symmetry reasons only one of the four PMT-plane wings is considered. To ensure a full coverage of the CBM acceptance at all rotations and displacement scans, an enlarged area of the PMT-plane is used in the first three steps.

As control parameters we consider the incident angle α of photons on the PMT-plane with respect to its normal and the detection efficiency E being the ratio of particles seen by the RICH detector to all generated particles. In this report, final results of the study will be presented.

Optimization of θ_x and θ_y

Figure 1 shows dR and B/A as functions of θ_x and θ_y . The lowest dR value of 0.36 cm is achieved at $\theta_x = 22^\circ$ and $\theta_y = 9^\circ$ (best- dR case). B/A at these rotation an-

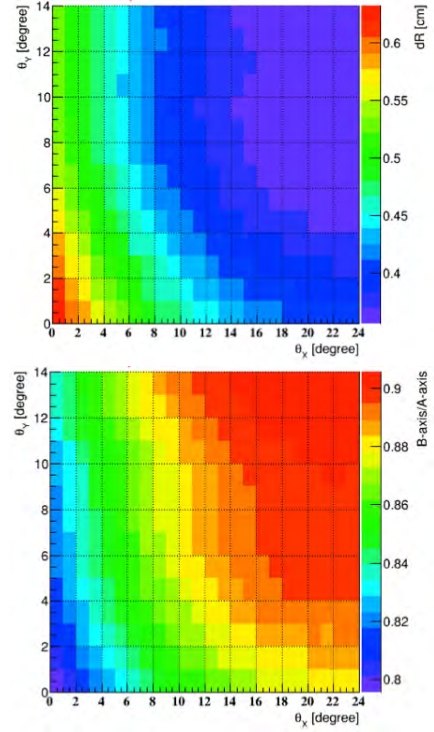


Figure 1: dR (up) and B/A (low) as functions of rotation angles of the PMT-plane around x and y .

gles is 0.9. The maximal B/A value of 0.905 is achieved at $\theta_x = 20^\circ$ and $\theta_y = 13^\circ$ (best- B/A case). dR at these rotation angles is 0.359 cm. Obviously, in both cases the dR values and those of B/A are very similar. These broad minimum and maximum of dR and B/A are clearly seen in figure 1. Looking closely one concludes that any combination within the range $17^\circ < \theta_x < 25^\circ$ and $7^\circ < \theta_y < 15^\circ$ ensures optimal ring quality.

Taking the control parameters, α and E , into account the values of $\theta_x = 20^\circ$ and $\theta_y = 10^\circ$ are chosen. The integrated α value at this combination is about 19° . Figure 2 shows the differential distribution of α on one of the four wings of the RICH PMT-plane. On the upper ($y > 150$ cm) α is around 20° . Even at the edges it does not exceed 35° , which can still be tolerated. The QE for photons impinging on the PMT with angles up to 40° does not suffer any reflection on the PMT glass window.

*Work supported by HIC for FAIR and by BMBF grants 05P12RGFCG and 05P15R6FCA.

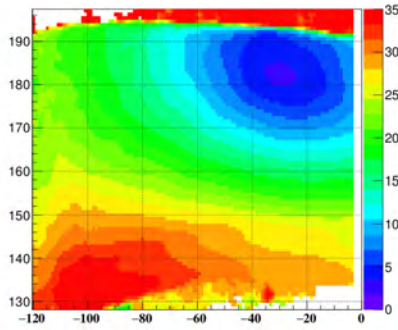


Figure 2: α distribution on the PMT-plane for $\theta_x = 20^\circ$ and $\theta_y = 10^\circ$.

Optimization of the PMT-plane position

In the second step of the optimization procedure the PMT-plane position was adjusted. To find the optimal position to the local z and y coordinates in the new geometry, we scanned wide ranges in 2-cm steps; $y_0 - 12$ cm to $y_0 + 44$ cm and $z_0 - 40$ cm to $z_0 + 50$ cm with $y_0 = 162$ cm and $z_0 = 212.6$ cm. z and y are correlated since any change in z requires a change in y to keep the acceptance. Again we maximize B/A and minimize dR and take the y and z values at these extremes keeping an eye on α . Detailed simulations show that the optimal values of $B/A = 0.9$ and $dR = 0.35$ cm are given with $\Delta y = 18$ cm and $\Delta z = 8$ cm.

In the third step, a second iteration of a θ_x - θ_y scan was performed with the new optimized position of the PMT-plane. No changes on the results were observed.

Adjusting the PMT-plane dimensions

As mentioned earlier, the simulations were carried out with an enlarged size of the PMT-plane. In the last step the width (w) and height (h) of the PMT-plane were adjusted to cover the acceptance and to be integer multiples of modules containing 2×3 PMTs each. This module structure was motivated by the new scheme of the readout electronics [2]. The module structure yields a (106×63.6) cm² wide plane corresponding to 4×10 modules. However, in context of designing the shielding box [3] it was required to have some space between the PMT-plane and the box walls. Technically this was achieved in the geometry by adding two rows of PMTs on top of the plane and one column on the side¹. The overall dimensions after all these considerations are (111.3×74.2) cm² corresponding to 7×7 modules in each of the four PMT-planes. Table summarizes the optimized geometry parameters of the RICH detector. Figure 3 shows the dR and B/A distributions on the PMT-plane after the optimization procedure.

¹While the lower border stays the same. Technically, this requires a change in the center y -position from 162 cm to 158 cm

β	y	z	θ_x	θ_y	w	h
10	158	220.6	20	10	111.3	74.2

Table 1: Optimized parameters of the PMT-plane. β , θ_x , and θ_y in degrees. y , z , w , and h in cm.

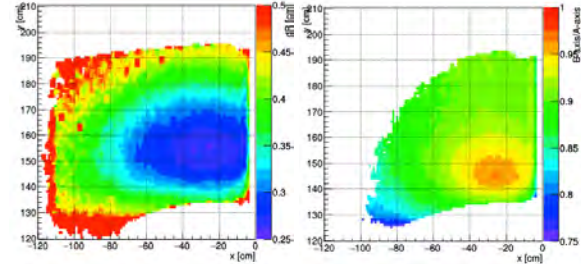


Figure 3: dR (left) and B/A (right) distribution on the PMT-plane for the optimized geometry.

Next steps

The left panel of figure 4 shows a sketch of two of the PMT-plane wings (green lines) as they are implemented in the current geometry. In [2] it is shown that the height of the power board of the readout electronics is 10 cm. Taking this into account the two wings have to be separated by 18.2 cm. It is obvious that this acceptance loss has to be avoided by rearranging the modules. The right panel of figure 4 illustrates some ideas for the rearrangement, which are subject of ongoing work.

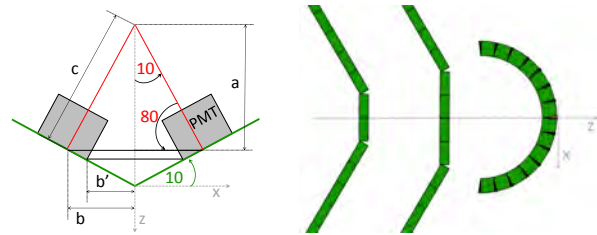


Figure 4: Left: loss of acceptance due to the height of the electronics. The two PMT-planes must be separated by a distance of $2b' = 18.2$ cm. Right: possible solutions with less acceptance losses.

References

- [1] T. Mahmoud, C. Höhne, CBM Progress Report 2014, (2015) 60
- [2] C. Pauly et al., "CBM-RICH readout chain and data rates", this report
- [3] E. Ovcharenko, P. Akishin, "Development of the magnetic shielding box for the CBM RICH camera", this report

Update of the MC-geometry of the RICH detector*

E. Ovcharenko^{†1,2}, S. Lebedev^{‡2,3}, T. Mahmoud^{§3}, C. Pauly⁴, Yu. Ryabov^{5,6}, C. Höhne³, and V. Schetinin^{2,7}

¹ITEP Moscow, Russia; ²LIT JINR Dubna, Russia; ³Justus Liebig University Giessen, Germany; ⁴University Wuppertal, Germany; ⁵PNPI, Gatchina, Russia; ⁶SPbSPU, St.Petersburg, Russia; ⁷BMSTU, Moscow, Russia

The Monte-Carlo model of the RICH detector has been updated according to the optimized RICH geometry [1]. In the new model details down to single pixels are implemented, and the volume hierarchy has significantly changed following the evolution of the engineering design.

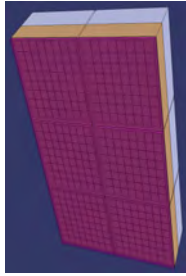


Figure 1: One block of 6 PMTs without FEBs in MC geometry.

Most changes are related to the photosensitive camera. The basic unit for camera building is called block and consists of 2 by 3 PMTs with partial common FEE for HV distribution and data collection. This is a common development with HADES RICH upgrade [2]. Figure 1 shows the ROOT-compatible geometry of one block without FEBs inside CATIA. As the MAPMTs to be used for the CBM RICH have already been ordered [3], information from PMT specification is used to model details like single pixels and glass window.

There are two different configurations of the photosensitive camera under consideration - "two wings" and "cylindrical".

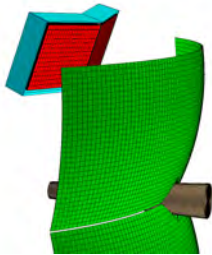


Figure 2: Detailed "two wings" camera geometry in CbmRoot.

The full camera consists of two halves - top and bottom. In the "two wings" configuration one half consists of two planes; we call them quarters. In the basic configuration one quarter is 7 by 7 blocks - 1112mm by 741mm. On half would thus give room for $21 \times 14 = 294$ PMTs, however the upper two rows and one row on each of the outer sides would not be equipped with PMTs but offer space for cabling, cooling and more. We thus have only $19 \times 13 = 247$ PMTs per quarter which makes 988 in total. Figure 2 shows the "full camera" configuration in CbmRoot. The position and rotation of the sensitive planes are optimized for high ring quality [1].

In order to minimize the gap between the quarters and approximate the ideal focal surface with smaller error the

usage of a cylindrical camera is investigated [4]. One cylinder of the camera is formed by 14 vertical columns of blocks. The angle between the columns is approx. 5° while the angle between the "wings" is 20° (see figure 3). The cylindrical configuration thus requires no extra space between the modules, however needs more complicated implementation in the RICH software (ongoing work).

Shape of the mirrors has been updated. The new shape covers full geometrical acceptance and has no gaps between the top and the bottom halves.

Both versions of geometry, with "two wings" and cylindrical camera, are available in two configurations - with perfect spherical mirror and with separate mirror tiles with the possibility to introduce individual misalignments. This specific geometry is

used to study techniques for the correction of possible mirror misalignment [5]. All geometries include aluminum support structures in order to have realistic material budget of the detector. New geometry requires significant changes in software. This changes are discussed in [6].

The MC-geometry of the CBM RICH detector was created and maintained using the "CATIA-GDML geometry builder" inside CATIA [7].

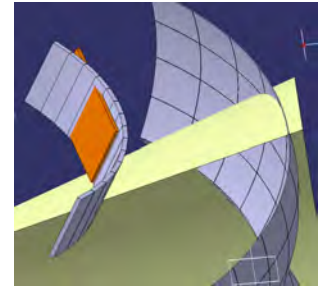


Figure 3: Cylindrical camera overlaid with one quarter of "two wings" camera. Yellow cone shows an opening angle of 25° from the target point.

References

- [1] T. Mahmoud et al, Optimization of the RICH geometry
- [2] C. Pauly et al, CBM-RICH readout chain and data rates
- [3] J. Förtsch et al, MAPMT test stand and first results on MAPMT series tests
- [4] I. Kres et al, Deriving the effective focal plane for the CBM-RICH detector
- [5] J. Bendarouach et al, Design of a control and monitoring system for the mirror alignment of the CBM RICH detector
- [6] S. Lebedev et al, Implementation of the new RICH geometry in CBMROOT
- [7] Development and application of CATIA-GDML geometry builder S Belogurov et al 2014 J. Phys.: Conf. Ser. 513 022003

*Work supported by HIC for FAIR, FRRC, and BMBF grants 05P15RGFCA and 05P12RGFCG

[†] eovchar@jinr.ru

[‡] s.lebedev@gsi.de

Development of the magnetic shielding box for the CBM RICH camera*

E. Ovcharenko^{†1,2}, P. Akishin^{‡2}, C. Pauly³, T. Mahmoud⁴, Yu. Ryabov^{5,6}, C. Höhne⁴, and V. Schetinin^{2,7}

¹ITEP Moscow, Russia; ²LIT JINR Dubna, Russia; ³University Wuppertal, Germany; ⁴Justus Liebig University Giessen, Germany; ⁵PNPI, Gatchina, Russia; ⁶SPbSPU, St.Petersburg, Russia; ⁷BMSTU, Moscow, Russia

The design of the CBM dipole magnet revealed a stray field in the region of the RICH photon detector of about 50-100 mT, too high for the operation of MAPMTs. A design for a magnetic shielding box has been developed to reduce the stray field in the region of photon sensors to less than 1 mT.

The size of the shielding box has currently been fixed following these considerations: The active PMT area of one quarter is 19x13 MAPMTs [1]. Sticking to the 3x2 PMT module design [2] that makes 7x7 modules leaving the upper two rows and the outer row on the sides not equipped with PMTs. This space is necessary for cabling, cooling, etc. In addition some 5cm free space is added at the outer edges plus 3cm free space on the lower border.

Once the shielding box is designed, the RICH vessel has to be adopted to carry its weight. Also, the free space towards the magnet has to be considered. Furthermore, the design of the box has to keep the acceptance angle unaffected. In a first step, the box will simply be designed from steel which provides high magnetic permeability.

Later, it can be investigated whether layers of mu-metal might help to reduce the weight while offering the same shielding capability. The box presented in the figure 1 would weigh around 850kg; further optimization is still ongoing.

Finite element model simulations of magnetic field for several geometrical models have been performed showing that there is high influence of shield shape and configuration on the magnetic field distribution inside the shielding box. The thickness of the box is 1cm except bottom and back planes which have a thickness of 3cm. The crucial component of the shielding box showed to be the bottom side of the box. It has thus been extended longer and thicker into the RICH volume. This hanging part is 3.5cm thick.

The shielding box needs to have holes for high-voltage, low-voltage, signal cables and air flow for cooling the electronics. The cables will be taken out of the box to the sides. For cooling with air, the box needs to have holes at least on the top side. Holes in the bottom side are hardly possible

because the magnetic field is the strongest here. For the lower box the cooling concept has thus to be studied thoroughly.

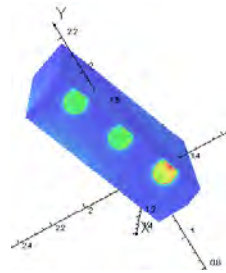


Figure 2: Distribution of the absolute value of magnetic field inside the shielding box in the area of holes.

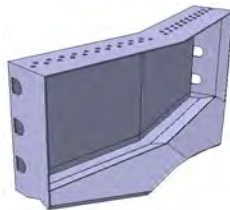


Figure 1: Latest design of the shielding box.

Different geometric models of the shielding box have been created in the geometry sub-system of the OPERA package and then exported into a STEP file which has been used to perform space analysis in CATIA and later to create a ROOT-compatible geometry using the "CATIA-GDML geometry builder" [3].

Detailed physics simulation of the RICH including the shielding box is planned to be performed in CbmRoot in the nearest future.

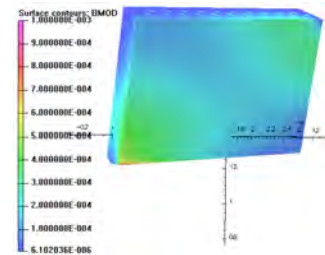


Figure 3: Distribution of the magnetic field inside the shielding box.

References

- [1] T. Mahmoud et al, Optimization of the RICH geometry
- [2] C. Pauly et al, CBM-RICH readout chain and data rates
- [3] Development and application of CATIA-GDML geometry builder S Belogurov et al 2014 J. Phys.: Conf. Ser. 513 022003

* Work supported by HIC for FAIR

[†] eovchar@jinr.ru

[‡] akishin@jinr.ru

Study of p-terphenyl WLS effect on timing in the CBM RICH prototype*

E. Ovcharenko^{† 1,2}, S. Belogurov¹, and C. Pauly³

¹ITEP Moscow, Russia; ²LIT JINR Dubna, Russia; ³University Wuppertal, Germany

Introduction

The CBM RICH detector will use Hamamatsu H12700 multi-anode photomultiplier tubes (MAPMTs, PMTs) working in the single-photon regime to detect Cherenkov photons [1]. There are two different configurations of H12700 PMTs available - with Borosilicate glass window or with UV glass window, the latter having much higher response in the UV range.

Cherenkov light is emitted according to a $1/\lambda^2$ intensity distribution, with most photons in the UV range (limited by the transparency of the medium). PMTs with BiAlkali cathode have maximum sensitivity at around 450nm, and only limited sensitivity in the UV range down to 200nm (limited by glass window transparency). WLS layers can help to overcome this sensitivity mismatch [2, 3].

The readout scheme for the CBM RICH detector will detect only timestamps and no amplitude information. The final front-end board (FEB), the DIRICH board, will have most part of its functionality implemented inside an FPGA [4, 5]. A current prototype of the readout electronics is implemented in two FPGA-based boards PADIWA and TRBv3. These boards have been used during Nov 2014 CERN beamtests [6, 7]. The same readout system has also been tested in the laboratory.

Any scintillator has some timing characteristics. Contemporary electronics allow a direct measurement of the time profile. For the first time, the time effect of p-terphenyl WLS layers on the distribution of the leading edges of the hits belonging to the same ring is studied. The WLS luminescence time profile was derived from the measurements with sub-nanosecond precision.

Readout system time resolution

We have performed measurements of time resolution of TDCs [8], implemented in TRBv3 board, and full electronics chain PADIWA + TDC. For these measurements, a 10ns-wide pulse from a high-precision pulse generator was split into two and sent to different pairs of input channels using identical cables. An example of the distribution of the difference between the two registered timestamps $\Delta t_i = t_i - t_j$ which were sent directly to TDC simultaneously is shown in the fig. 1.

RMS of the distribution is under 20ps for all channels and most probably the quality of the measurements is limited by the precision of the pulser. The same technique has

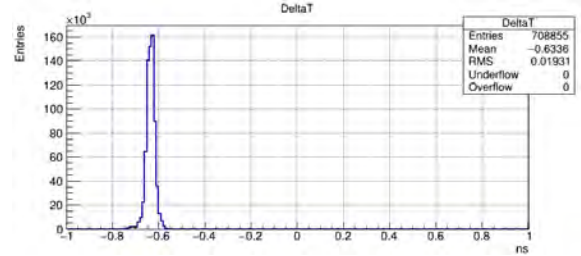


Figure 1: Δt distribution in direct TDC measurements.

been employed to perform the measurements of the time resolution of the electronics chain consisting of PADIWA and TDC. In this case the RMS is less than 70ps. For the full readout chain including PMT, the time resolution turned out to be 640ps with main contribution coming from PMT transition time jitter.

Procedure description

During RICH prototype beam tests there were 3 groups of PMTs in the camera: (1) covered with WLS layers for the first runs, then cleaned and used without WLS films for the second set of runs, (2) covered with WLS layers for the whole beamtime and (3) not covered for the whole beamtime. By comparison of the data received using the PMTs from the first group (1) we can analyse the effect of WLS layers.

Each set of data contains signals from at least two sources - beam and picosecond laser. Laser flashes illuminate the full PMT surface with an intensity which is intentionally set very low such that PMTs worked in single-electron regime. The laser wavelength is outside of the WLS absorption range, therefore the data from the laser is used only to calibrate inter-channel delays of the readout chain.

Beam events may contain Cherenkov rings on the camera plane. The analysis technique for the time precision is based on the fact that signals in different channels within one event coming from one laser flash or one charged particle emitting Cherenkov light are simultaneous. For beam data, analysis cuts on ring centers have been applied in order to filter real rings and thus increase the quality of the analysis. Analysis of those PMTs which were always covered (2) or always not covered (3) across all sets of data give additional check of analysis procedure, external conditions and software implementation.

* Work supported by HIC for FAIR and FRRC

[†] eovchar@jinr.ru

WLS time profile

In each event, the first hit in time is used to define the reference time t_{ref} . For all other hits in the event, the time difference, $\Delta t_i = t_i - t_{ref}, i \neq ref$ is computed. The Δt distributions for two sets of data are shown in fig. 2 and 3.

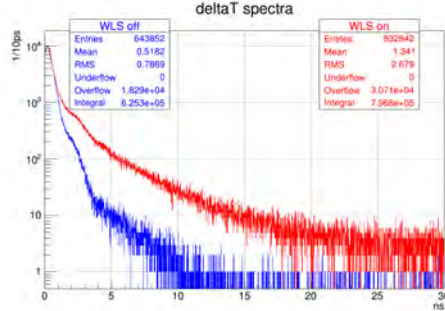


Figure 2: Δt distributions. Blue (lower) - without WLS layer, red (higher) - with WLS coverage.

The two data sets with and without WLS coverage were obtained during two minutes of data taking. The peak values are very close (see fig. 3) which means that the number of detected photons not affected by the WLS layer is the same; there is no normalization in analysis. If the photon is absorbed by the WLS it takes some time before it is emitted and then registered, so WLS-affected hits are located in the "long times" wing of the distribution.

In order to check if there is any other influence than the removal of WLS coating on the Δt distributions which are compared in fig. 2, we analyzed the results for set (2) and set (3) separately for the time slots used for the measurements of set (1) with and without WLS film. If the PMTs are unchanged as it is the case for set (2) and set (3), we find identical Δt distributions in both time slots. Thus any other influence than the change in coating can be excluded.

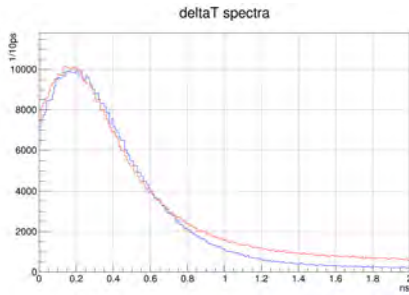


Figure 3: Δt distributions zoomed to the area of peaks. Blue (lower) - without WLS, red (higher) - with WLS.

Both distributions are shifted to the right by approx. 200 ps which probably comes from the transition time jitter of the MAPMT. There is also one more feature - the distributions have distinguished shoulders in the area of 2-3 ns. Detailed analysis showed that the channels which give in-

put into this area are generally more noisy, so most of them have been ignored for the WLS analysis.

Subtracting the blue distribution (no WLS layer) from the red (WLS layer) in fig. 2, we subtract the timing information for all hits not being affected by the WLS layer. The resulting WLS time profile is shown in fig. 4. It consists of two major exponential components with decay times τ_1 and τ_2 , so the difference is fitted by

$$f(t) = A \cdot e^{-t/\tau_1} + B \cdot e^{-t/\tau_2},$$

$$t \in [1.5\text{ns}; 20\text{ns}]$$

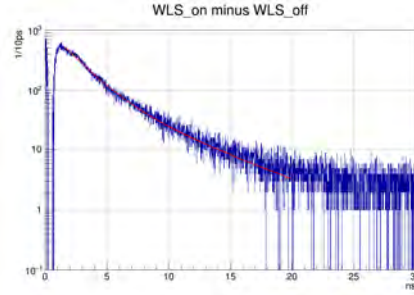


Figure 4: WLS time profile. Red line is fitting result.

Thus the measured p-terphenyl WLS time profile consists of two components, a fast (2ns) and somewhat slower (6ns). Precisely, the fit values are:

$$\text{Fast: } \tau_1 = 1.92\text{ns}$$

$$\text{Slow: } \tau_2 = 5.69\text{ns}$$

Even for the maximum interaction rates in CBM of 10MHz, time constants below the 10ns range will not harm the event-by-event timing resolution.

References

- [1] J. Förtsch, C. Pauly, S. Querschfeld, and K.-H. Kampert, The new H12700 PMT for CBM RICH, CBM progress report 2014, p. 63.
- [2] J. Kopfer et al., Cherenkov photon detection with WLS coated MAPMTs, CBM progress report 2013, p. 52.
- [3] J. Adamczewski-Musch et al., Influence of wavelength-shifting films on multianode PMTs with UV-extended windows, NIM A 783, 43 (2015).
- [4] C. Pauly, CBM RICH development - and possible synergy with HADES, HADES collaboration meeting slides, 27.10.2014.
- [5] M. Traxler, TRB developments, DIRC 2015 slides, 13.11.2015.
- [6] J. Förtsch, C. Pauly, D. Pfeifer, S. Reinecke, and K.-H. Kampert, The CBM RICH camera and readout chain for the 2014 CERN PS beamtest, CBM progress report 2014, p. 61.
- [7] S. Lebedev, E. Ovcharenko, and C. Höhne, Data analysis for the RICH prototype beamtest data 2014, CBM progress report 2014, p. 64.
- [8] C. Ugur, E. Bayer, N. Kurz and M. Traxler, Implementation of a High Resolution TDC in a FPGA, PoS BORMIO2012 (2012) 015.

CBM-RICH readout chain and data rates*

C. Pauly¹, K.-H. Kampert¹, S. Lebedev², J. Michel³, P. Skott⁴, and M. Traxler⁴

¹Wuppertal university; ²Giessen university; ³Frankfurt university; ⁴GSi Darmstadt

Concept

The front-end part of the CBM-RICH readout chain is sketched in Figure 1. It consists of units of 6 MAPMTs each, which are plugged on a common PMT carrier PCB. Each such module will be mounted to an aluminum frame structure, where the PCB provides mechanical fixation for the PMTs. The backplane is designed to be gas- and light-tight, it also serves as enclosure of the radiator gas volume.

The PMT carrier PCB also serves as backplane for the readout frontend electronics, which is plugged into connectors on the backside. The backplane provides all necessary data-, power- and clock interconnects between the readout modules to minimize the amount of cable connections to the modules.

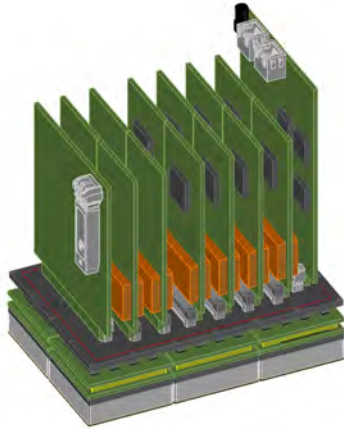


Figure 1: CBM-RICH readout module for 6 MAPMTs with front-end modules (from left to right): Data Combiner Module (DCB), 12x DiRICH frontend module, Power Distributor (PD)

Front end modules

Three different front end electronic modules are used in the CBM-RICH readout chain:

DiRICH Module:

The DiRICH ("Dirich RICH readout module", a common development for CBM-RICH and PANDA-DIRC detectors, is the core digitization module comprising of analog preamp-, discriminator-, and TDC stages for 32 individual

input channels. Each PMT (64ch) is read out via 2 such DiRICH Modules. The DiRICH analog inputs are galvanically decoupled from the PMT using SMD wideband transformers for each channel in order to minimize common mode noise and ground loops. Before discrimination, the single-ended analog PMT signal (1-2 ns FWHM, 5-10 mV on 50 Ohm, 300 fC charge pulse for a single-photon signal) is amplified (x25) and shaped using a high-bandwidth (≈ 4 GHz) transistor amplifier stage. Signal discrimination is achieved using the input comparators of the LVDS line receivers of the Lattice ECP5 FPGA. Individual threshold reference voltages for each channel are generated using PWM with subsequent filtering by the FPGA itself. The same FPGA hosts 32+1 FPGA-TDC stages (tapped delay-line approach, 200 MHz / 240 MHz coarse counter, adapted from HADES TRB3 Trigger and readout board [1]), digitizing the leading- and trailing edge of the discriminated analog signal to measure both signal arrival time and Time-over-Threshold for amplitude measurement. The aim for leading edge time precision is in the order of the Transit Time spread (TTS) of the PMT itself (better than 300 ps RMS). Data from all 32 channels are sent out using a single 2 Gbps serial link (TRBnet protocol) routed via the backplane to the Data Combiner Module. A regular readout trigger with gap-less readout window is used to implement a quasi self-triggered readout scheme.

Data Combiner Module (DCM):

The main purpose of the DCM is to combine data from all 12 DiRICH cards mounted on a 6-PMT readout module to a single output link. It is based on a Lattice ECP3 FPGA, and is connected via individual 2 Gbps serial links to each of the DiRICH modules via the backplane. Data is sent out using a 13th 2 Gbps link, connected to an optical SFP transceiver on the board. The link speed of the output link might later be increased to 2.4 Gbps (without hardware modification, simply by increasing the basic clock from 200 MHz to 240 MHz). This will be sufficient for application of the readout chain in the HADES RICH detector. For the "hot" regions of the CBM-RICH camera, a second version of the DCM will be later developed, providing faster output link capability.

The DCM receives external clock- and trigger/synchronisation signals (via RJ45 connectors) which are distributed via LVDS fanout chips to each DiRICH module via individual clock / trigger lines located on the backplane. The DCM also implements slow-control functionality (controlled via the TRBnet protocol), and can poweroff / reboot individual DiRICH modules via Power-enable lines to each DiRICH module.

* Work supported by BMBF 05P15PXFA

Power Module (PM):

The PM hands over all 1.1 V / 1.2 V / 2.5 V / 3.3 V DC power supply lines from external cable connection to the backplane for distribution to the individual DiRICH- and DCM modules. The PM provides active voltage measurement of the external provided supply lines, allowing for a coarse regulation of the supply voltages on a further distant PowerSupplyBoard. It also provides current monitoring for each supply line. Alternatively, the use of DCDC converters on the PM is under investigation. In addition, the PM serves as HV interface, distributing the HV supply (-1100 V max, via LEMO-0S connector) via a common HV supply line on the backplane to each of the 6 PMTs.

Expected single photon hit rates

Data rate estimates are based on the expected single photon hit rate per readout pixel in 10 MHz minimum bias Au+Au collisions at 10 AGeV, shown in Figure 2. The expected hit rates are unevenly distributed over the active area, with largest hit rates encountered in the detector regions located closer to the beam pipe, also depending on beam energy. A maximum of 120 kHz/pixel is expected in the inner region of the photon detector, and ≤ 10 kHz in outer regions. The total number of hits at 10 AGeV can rise up to 1000 single photon hits per event, with a mean value of 190 hits/event (see Figure 3). Thus, the total expected hit rate from the CBM-RICH at 10 MHz interaction rate is expected in the order of 1.9 Ghits/s. These numbers do not contain additional cross talk hits ($\approx 10\%$), contributions from darknoise (≤ 1 kHz/pixel, ≤ 60 MHz total, $\leq 3\%$ of total photon hit rate), or background from direct charged particle hits. A reasonable safety margin (≥ 2) should be considered.

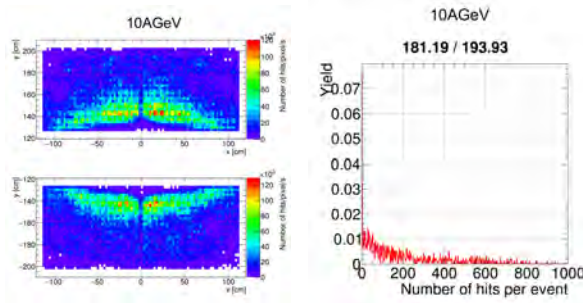


Figure 2: Expected single photon hit rate per readout pixel (left) and number of detected hits per event (right) for CBM-RICH operation at SIS100, 10 AGeV Au+Au collisions, 10 MHz interaction rate.

Expected data rates and link speed

Based on the expected hit rates, the data rates can be estimated. This estimate is based on the present TRBnet decoding format, with 4 bytes per single time stamp. A

“hit” consists of leading- and trailing edge timestamp: 8 bytes. In addition, some data overhead must be added, eg for EPOCH messages (4 bytes) in the TRBnet data stream. A maximum of 12 bytes per detected photon hit is considered for further data rate estimates (being aware that this is slightly overestimated). Intelligent data compression (transmitting ToT directly instead of a full trailing edge timestamp with channel information) might later be applied to further reduce the payload per hit.

A single DiRICH module with 32 channels in the “hot” region, 120 kHz/pixel, can produce 120 kHz x 32 ch x 12 byte = 50 MB/s of data. It is connected via a 2 Gbps serial link to the concentrator board, capable of a maximum of 150 MB/s effective data rate. 12 DiRICH modules together in the “hot” region of the detector, connected to a single DCB, will produce up to 12x 50 MB/s = 600 MB/s. The presently foreseen, single 2 Gbps TRBnet output link (1.4 Gbps effectively) on the DCB (as it is being built now for the HADES RICH) will not be capable of handling these data rates. Using the same hardware, the link speed could be extended to 2.4 Gbps (1.7 Gbps effectively) by increasing the clock frequency to 240 MHz, allowing for a maximum output rate of 210 MB/s. This would correspond to a maximum pixel hit rate of 40 kHz, 1/3 of the expected rate.

This will be sufficient to equip the outer regions of the CBM-RICH, reusing the DCBs produced now for HADES. For the inner detector regions, a new DCB will be developed, with one (or even two) 4.8 Gbps output links.

The total number of optical fiber output links from the detector frontend electronics is in the order of 170 links, one link per 6 PMTs. Depending on the DCB board, these can be 2 Gbps or 4.8 Gbps links, with large differences in link utilizations depending on PMT position. These links will be connected to the CBM Data Processing Boards (DPB), where the data are aggregated to a fewer number of 10 Gbps links to the FLIB/FLES. Proper distribution of input links to the DPBs will allow for a fairly homogeneous link utilization of the 10 Gbps output links to the FLIB/FLES.

The number of required 10 Gbps output links to the FLIB/FLES can thus be estimated based on total data rate of the CBM RICH detector, but must include sufficient safety margin to accommodate for luminosity variations and peak loads. We expect up to 1.9 GHits/s total detector rate with 12 byte/hit data volume, yielding an average data rate of 25 GB/s (excluding any safety margin !)

About 50 piece 10 Gbps links to the FLIB/FLES will be needed to handle the maximum data rates encountered at SIS100 in the maximum rate scenario. Number of output links and DPBs can be fairly flexible adapted to adjust for increasing data rate requirements, since these components are well accessible, outside the detector.

References

- [1] M. Traxler et al., 2011 JINST 6 C 12004

Ordering of 1100 MAPMTs H12700 for the CBM-RICH photon detector*

J. Eschke¹, J. Förtsch², K.-H. Kampert², and C. Pauly²

¹GSI / FAIR, Darmstadt; ²University of Wuppertal, Germany

An important milestone towards building the CBM-RICH detector was the conclusion of the contract with Hamamatsu by GSI on the delivery of 1100pc of H12700 MAPMTs (internal name H13708) in summer 2015. The signing of contract was preceded by several years of detailed photon sensor evaluation in beamtests and in lab measurements. Several different sensor candidates were considered, among them the Hamamatsu MAPMTs H8500 (2x2 inch, 64ch) and R11265 (1x1 inch 16ch). The finally selected H12700 is a fairly new development, combining the good single photon properties of the R11265 with the form factor of the H8500 (see [1] for further details).

In order to ensure optimum PMT performance and validity of the prototype R&D results, a detailed list of specifications was worked out in cooperation with Hamamatsu with the goal to define precise acceptance criteria for the PMTs. In some parts, (e.g. dark current, gain) these specifications were slightly more strict compared to the data sheet standards, causing a slight price increase of about 5%. Most of the specifications are based on Hamamatsu standard measurements, some will have to be checked by our own detailed acceptance measurements (see [2]).

The list of detailed specifications include the following:

- $\geq 25\%$ peak q.e. for the Bi-Alkali cathode type
- Cathode uniformity variation $< 25\%$
(defined as maximum difference between 100% and relative minimum)
- Average gain $\geq 0.8 \times 10^6$ at nominal supply voltage (1000 V)
- Maximum anode uniformity ratio better 1:3
- Clear single photon peak with a peak-to-valley ratio of ≥ 1.2 in at least 61 out of 64 channels
- Cathode dark current < 5 nA at nominal supply voltage
- Average dark rate ≤ 100 Hz/pixel, no individual pixel above 1kHz/pixel
- Afterpulse probability $\leq 5\%$ in time window 70ns - 1.7 μ s after prompt signal

In addition, several general durability criteria were fixed in the written specifications:

- Continuous operation of the PMTs at up to 700 kHz/pixel single photon rate
- Life time ≥ 10 C/cm² collected anode charge
- $\leq 20\%$ transmission loss of the PMT window at 200 Gy ionizing irradiation
- Size tolerance ≤ 0.3 mm



Figure 1: First 30 MAPMTs delivered in November 2015

Delivery of the first 30 MAPMTs took place in November 2015 (see Figure 1). Meanwhile, we receive 50 MAPMTs per month, 180 MAPMTs have been delivered by March 2016.

Prior the start-up of CBM in 2022 (first commissioning), about 410 of these MAPMTs will be used already before in the upgraded HADES RICH detector, these PMTs later have to be shared between the HADES and CBM experiments. The remaining PMTs will be stored under nitrogen atmosphere until their usage in the CBM-RICH detector, to prevent premature aging due to corrosion or He diffusion.

References

- [1] C.Pauly et al., “The new H12700 PMT for CBM RICH”, CBM Progress Report 2014, page 63.
- [2] J.Förtsch et al., “MAPMT test stand and first results on MAPMT series tests”, this report.

* Work supported by GSI and BMBF contract No. 05P15PXFCA

Radiation hardness tests of photon sensors for the CBM-RICH*

T. Mahmoud¹, C. Pauly², M. Dürr¹, J. Eschke³, J. Heep¹, C. Höhne¹, and K.-H. Kampert²

¹University of Wuppertal; ²University of Giessen; ³GSI/FAIR Darmstadt

The CBM-RICH photon sensors will be exposed to substantial amounts of ionizing radiation from photons and charged particles, as well as non-ionizing radiation from neutrons originating from the target or the material around. Sufficient radiation hardness of the sensors is important for the successful operation over the full CBM lifetime, given the significant investment costs for the sensors. A coating of the PMT windows using wavelength-shifting films (WLS) made of p-Terphenyl is foreseen to enhance the UV sensitivity and photon statistics. An advantage with respect to an enhanced quantum efficiency of PMTs for $\lambda \leq 300$ nm even in the case of PMTs with UV-extended windows has been recently shown [1], but again sufficient radiation hardness of the WLS layer must be assured for long term application in the photon detector.

Detailed FLUKA simulations of the CBM detector setup within its cave [2] provide an estimate of the integral radiation dose for the individual RICH detector components, assuming a realistic CBM operation scenario for the next 20 years. For the CBM-RICH photon sensors, an integral dose of up to 100 Gy ionizing radiation, and 1×10^{12} neq/cm² neutron dose (1 MeV equivalent) must be expected. According to these simulations, the spectral distribution of the neutrons peaks below 1 MeV.

To approve sufficient radiation hardness of all components, we carried out irradiation tests on five PMTs, two samples of PMT glass windows (Borosilicate / UV glass, 2 mm thick), several quartz substrates dip-coated with p-Terphenyl wavelength-shifter (200 nm thickness), and two individual PMT voltage dividers (without the attached PMT). The samples were irradiated at two different facilities: At the JSI "Jozef Stefan Institute" in Ljubljana, we made use of the TRIGA nuclear reactor facility to irradiate probes directly inside the reactor core (Triangular In-Core channel, TIC) with high thermal neutron flux rates up to 10^{12} neq/cm²/s, allowing us to apply the expected CBM lifetime dose within minutes (or even seconds). In the "Strahlenzentrum Giessen", we used a ⁶⁰Co source to irradiate the samples with energetic gammas of 1.2 MeV / 1.3 MeV at up to 150 Gy/h, depending on the distance to the source. The glass window samples were irradiated at even higher rate, up to an integral dose of 30 kGy. It is important to note, that also at the reactor facility, a significant additional ionizing dose (in the order of 10 Gy per 1×10^{12} neq/cm², depending on the operation cycle) is unavoidable due to the radioactive fission products in the fuel elements.

Radionuclide	Activity [Bq]	Half-life	Used in
Br-82	1.70×10^3 ($\pm 3.4 \times 10^2$)	1.5 days	Voltage Divider PCB
Au-198	6.63×10^2 ($\pm 1.4 \times 10^2$)	2.7 days	Gold-plated contacts
Na-24	2.46×10^2 ($\pm 5.1 \times 10^1$)	15 hr	Glas window
Co-58	3.03×10^1 ($\pm 7.3 \times 10^0$)	71.3 days	Covar metal case
Co-60	7.13×10^1 ($\pm 1.5 \times 10^1$)	5.3 years	Covar metal case

Figure 1: Radioactive isotopes identified using gamma-spectroscopy of a H8500 MAPMT after being irradiated with 1.18×10^{11} neq/cm² neutron dose.

Characterization of possible radiation damage to the PMTs is based on single photon XY scans (see [3] for details), which were carried out before irradiation, after irradiation with neutrons, after subsequent ⁶⁰Co irradiation, and once again after 12 weeks of "cool-down" time. These scans can provide information on the PMT efficiency, gain, dark rate, and the single photon pulse height spectrum. The quantum efficiency of the PMTs and the spectral transmission of the glass window samples was measured before irradiation and after each step of radiation exposure. For the WLS samples, the fluorescence light yield before and after irradiation was compared. Moreover, gamma-spectroscopy of a single H8500 PMT after irradiation with 1.2×10^{11} neq/cm² neutron dose was performed using a germanium detector to determine possible activation effects. The voltage dividers were irradiated during operation by applying nominal high voltage. Using long, shielded cables connected to an adapter PCB, the HV potential of the last 5 dynodes (last three of them being transistor stabilized) was monitored using an electronic data logger.

Several possible damage scenarios can be imagined, and could be verified / excluded by these measurements:

- The PMTs have a metal housing made of COVAR, an alloy containing 17% of ⁵⁹Co, nickel, and iron. ⁶⁰Co could be produced by neutron capture, which is a beta emitter (0.31 MeV, $\tau=5.7$ y), and might lead to a permanent increase of the PMT darkrate.
- Radiation damage of the photocathode or dynodes could lead to efficiency losses, gain decrease, or increased dark rate.
- Radiation damage to the glass window will cause colouring and loss of transmission.
- Fluorescence output or transmission of the or-

* Work supported by BMBF 05P15PXFCA

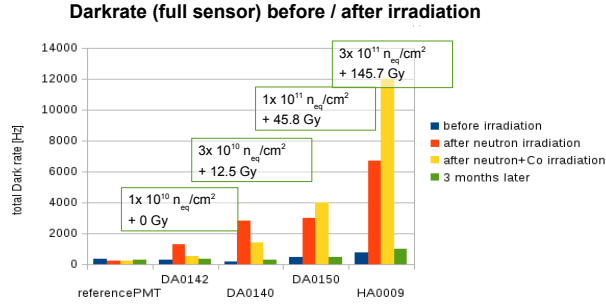


Figure 2: Darknoise of several H8500 and H12700 MAPMTs before any radiation, after neutron irradiation, and after subsequent ^{60}Co irradiation.

ganic wavelength-shifter could suffer from radiation-induced damage.

- The PMT-integrated active voltage divider uses transistor stabilization for the last 3 dynodes. Radiation damage to these transistors could lead to a drift or breakdown of the dynode voltages.

The first result, obtained from gamma-spectroscopy of a H8500 MAPMT after thermal neutron irradiation with $1.3 \times 10^{11} \text{ neq/cm}^2$, is shown in Figure 1. Main activation effects stem from short-lived isotopes like ^{82}Br in the PCB material (half-life $\tau=1.5$ days), or ^{198}Au from gold-plated contacts ($\tau=2.7$ days). These isotopes pose no problem for the MAPMTs in the CBM-RICH due to their short half-life time, which prevents any significant dose build-up. ^{60}Co activation is indeed observed, but at a very low level of only 70 Bq, which should not cause any critical dark-rate increase. However, a slight increase of PMT dark rate over the years may be expected.

The PMT dark rate before, inbetween, and after irradiation of PMTs with different non-ionizing neutron- and ionizing gamma dose rates was determined from the single-photon scan data with results summarized in Figure 2. Indeed, a clear increase of PMT darknoise is observed first after neutron-, and then again after subsequent gamma irradiation, reaching values up to 12 kHz/PMT (sum over all 64 channels) for $3 \times 10^{11} \text{ neq/cm}^2$ non-ionizing dose plus 150 Gy ionizing gamma dose. This applied dose is close to (neutron dose) or even above (gamma dose) the 20 year CBM expectation. An additional measurement 4 weeks after the last irradiation shows a quick decrease of darkrate to values close to before the irradiation. This indicates, that basically short-lived radionuclides are responsible for the activation, and that ^{60}Co activation only plays a minor role here.

Figure 3 shows single photon scan results for a H12700 MAPMT being irradiated with the highest integrated dose of $3 \times 10^{11} \text{ neq/cm}^2$ neutrons, and 145.7 Gy gamma. The upper plots compare the measured single photon efficiency as function of position on the PMT. The "corrected Effi-

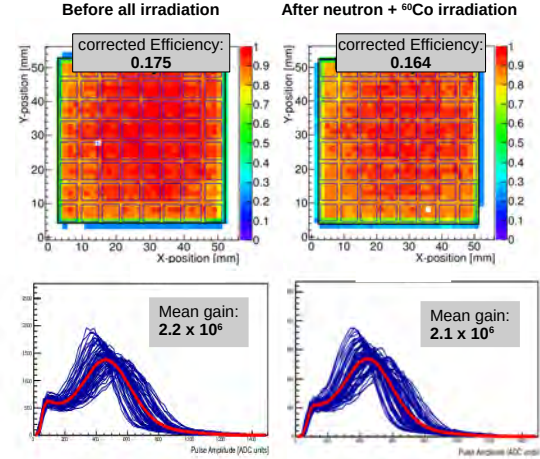


Figure 3: Single photon efficiency and ADC spectra of a H12700 MAPMT before and after irradiation with $3 \times 10^{11} \text{ neq/cm}^2$ and 145 Gy ionizing photon dose.

ciency index" is a relative measure (in artificial units) of the single photon detection efficiency, averaged over the full active surface. By normalization of each measurement to a reference PMT, this number allows for a direct comparison of detection efficiency before- and after irradiation. A slight decrease in efficiency is observed (0.175 down to 0.164, minus $\approx 6\%$), which might be caused by a slight transmission loss of the glass window. Extrapolated to the expected CBM lifetime dose, only a minor decrease ($\leq 20\%$) in sensor efficiency is expected. The lower part of Figure 3 shows single photon ADC spectra for each of the 64 channels (blue) and the average ADC response (red) before and after irradiation. A fit of the peak position is used to derive the average PMT gain. Both the spectral shape as well as the PMT gain are unaffected by the irradiation.

Figure 4 presents results on radiation damage of the UV glass window by gamma irradiation. Here, a significant colourization, and thus transmission loss, is observed for irradiation doses above a few 100 Gy. About 40% transmission loss (below 400 nm) is observed at the maximum applied ionizing dose of 32 kGy. For the expected CBM lifetime dose of $\approx 100 \text{ Gy}$, the transmission loss at short wave lengths should not amount to more than a few percent. It is to be noted, that the transmission loss can be partly recovered by exposing the PMT window to UV-light after each operation period, causing a healing effect.

No significant effect was observed for neutron irradiation up to $3 \times 10^{12} \text{ neq/cm}^2$, in agreement with measurements provided by Hamamatsu [4]. According to these measurements, significant transmission loss effects of UV glass windows are to be expected only above $1 \times 10^{14} \text{ neq/cm}^2$. However, results from [4] were based on irradiation with 14 MeV neutrons on different glass material.

Possible radiation damage to the dip-coated p-Terphenyl

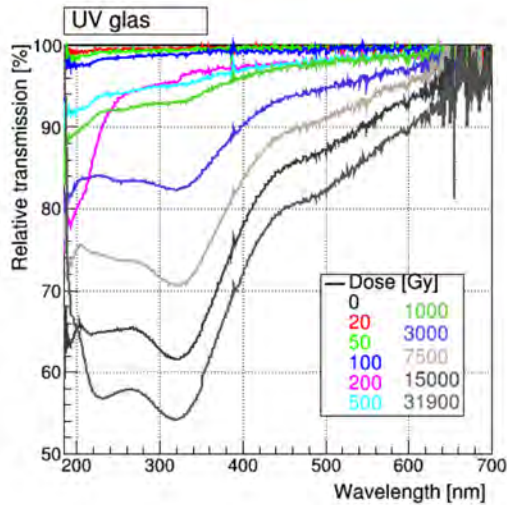


Figure 4: Relative transmission of the UV glass PMT window sample after gamma irradiation up to 30 kGy.

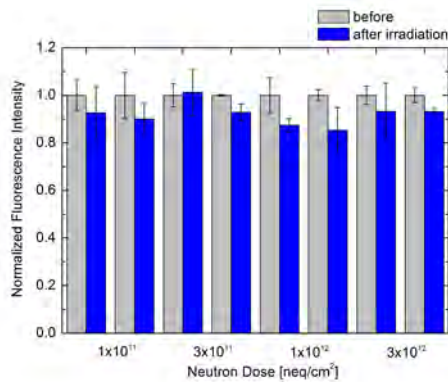


Figure 5: Integrated fluorescence intensity before and after irradiation of dip-coated WLS films with thermal neutrons. Two samples were measured per dose.

WLS samples was determined by fluorescence spectroscopy before and after irradiation. Several samples were irradiated with thermal neutrons at different doses (1×10^{11} , 3×10^{11} , 1×10^{12} and 3×10^{12} neq/cm²), and also γ irradiation (50 Gy and 100 Gy). For each probe, the fluorescence yield before and after irradiation was compared. As a result, the spectral response did not change significantly with neutron or γ irradiation. In Figure 5, results for the integrated fluorescence intensity before and after irradiation with thermal neutrons are shown. Although the overall fluorescence is slightly reduced, no systematic dependence on neutron dose is observed. The same observation was made when irradiating the films using the ^{60}Co source with 50 Gy and 100 Gy. The observed overall reduction in fluorescence intensity is within the reproducibil-

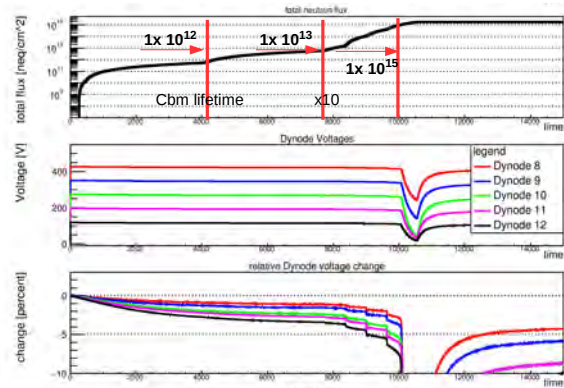


Figure 6: Total accumulated neutron dose (top) and drift of the last 5 dynode voltages (center and bottom) as function of time during irradiation.

ity of the measurement and is also observed for films which have not been irradiated. A good radiation hardness of the WLS films can thus be concluded.

Finally, results for the active voltage divider test under neutron irradiation are summarized in Figure 6. Non-ionizing neutron irradiation was applied by stepwise increasing the reactor power up to 100 kW, corresponding to a thermal neutron flux of 1×10^{12} neq/cm²/s. Up to 1×10^{13} neq/cm² integrated dose, no significant effect could be observed apart from a small drift of dynode voltages (less than 3%), which could well be attributed to a temperature change inside the reactor core. Above 1×10^{13} neq/cm², a steadily increasing voltage drift was observed, with total breakdown of the last three transistor-stabilized dynode voltages at around 10^{15} neq/cm². When the irradiation was ended, a partial recovery of the dynode voltages could be observed. For gamma irradiation up to 1000 Gy at the ^{60}Co source, no severe effect in terms of voltage breakdown or drift could be observed.

In summary, these measurements clearly show, that the H12700 photon sensor (including WLS coating) can be safely operated over the full CBM expected life time (1×10^{12} neq/cm² integrated neutron flux plus ≈ 100 -200 Gy ionizing dose). A moderate increase of dark-rate and minor loss of efficiency ($\leq 10\%$) towards the end of lifetime might occur, but this should have no major effect to the overall detector performance.

References

- [1] M. Dürr, J. Kopfer et al., "Influence of wavelength-shifting films on multianode PMTs with UV-extended windows", NIMA 783 (2015) 43–50
- [2] A. Senger, "FLUKA for RICH", CBM week spring 2014.
- [3] C. Pauly et al., "Single Photon XY scans [...]", CBM Progress report 2013.
- [4] Hamamatsu, "Photomultiplier Tubes - Basics and application", Hamamatsu handbook.

CBM RICH mechanical design status

Ya. Berdnikov⁴, A. Berdnikov⁴, C. Höhne², D. Markushin¹, C. Pauly³, Yu. Ryabov^{1,4}, V. Samsonov¹, O. Tarasenkova¹, and D. Tyts¹

¹PNPI, Gatchina, Russia; ²Justus Liebig University, Giessen, Germany; ³Bergische Universität Wuppertal, Germany; ⁴SPbPU, St.Petersburg, Russia

In 2015, the main focus in the mechanical design of the RICH detector was related to the development of lightweight mirrors support structures. In accordance with the basic layout of CBM spectrometer the RICH detector will be installed right behind the magnet [1], thus the mirror supporting frame will be located in the acceptance of downstream detectors like TRD and TOF. The basic variant of the mirror support structure that provides the necessary stability of the mirror system was developed earlier [2]. However this variant proved to be rather massive and we developed a lighter version of the mirror supporting structure to reduce the impact on of the detectors located behind the RICH.

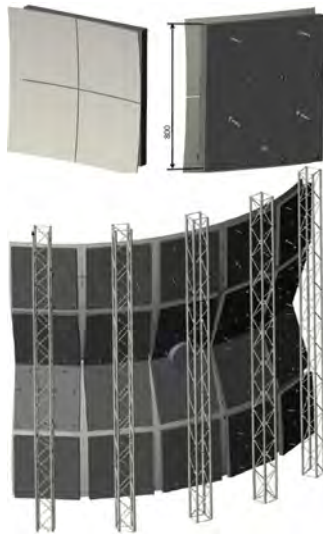


Figure 1: Foam version of mirror supporting frame design.

As a result, two new proposals of the mirror supporting structure design have been developed. According to the first estimates both new design versions can provide the required structure rigidity with significantly reduced amount of material in the acceptance of the detector.

The first variant is based on the use of foam as a radiation transparent material. In the current view, we can have a block of coated foam for 4 mirror tiles (see Fig. 1, top). Four of these blocks (with four mirror tiles each) are mounted on a vertical pillar (Fig. 1, bottom). As a result, we will have five vertical pillars attached to the outer rigid frame. Estimations show that with such a construction we can improve radiation transparency of the detector by more

than a factor of 1.5.

The second version also uses pillars (see Fig. 2). Here, one pillar carries 2 rows of mirror tiles. Aluminum can be used as a material for pillars. In this case, the overall material budget and thus weight of the construction will be reduced by a factor of 1.5 compared to the basic design. We also considered an option where carbon is used as a material for pillars and mirror tiles frame. In this case radiation transparency of the structure can be further reduced.

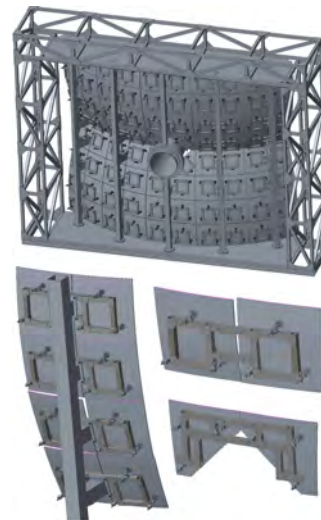


Figure 2: Design version with pillars carrying two rows of mirror tiles.

Thus, two additional designs for mirror support structure were developed. Both models satisfy the requirements and improve radiation transparency of the detector by at least a factor of 1.5. Further development of the models will require construction of the prototype [3], as was previously done for the basic version.

This work was partly supported by the Ministry of Education and Science of the Russian Federation Program “5-100-2020”.

References

- [1] V. Dobyryn *et al.*, CBM Progress report 2012, Darmstadt 2013, p. 40
- [2] V. Dobyryn *et al.*, CBM Progress report 2013, Darmstadt 2014, p. 57

- [3] V.Dobryn *et al.*, CBM Progress report 2014, Darmstadt 2015,
p. 57

RICH summary

*J. Adamczewski-Musch^a, K.-H. Becker^b, S. Belogurov^c, J. Bendarouach^d, N. Boldyreva^e, A. Chernogorov^c, C. Deveau^d, V. Dobryn^e, M. Dürr^d, J. Eschke^a, J. Förtsch^b, J. Heep^d, C. Höhne^{*d}, K.-H. Kampert^b, L. Kochenda^{e,f}, P. Kravtsov^{e,f}, I. Kres^b, S. Lebedev^d, E. Lebedeva^d, E. Leonova^e, S. Linev^a, T. Mahmoud^d, J. Michel^g, N. Miftakhov^e, W. Niebur^a, E. Ovcharenko^c, C. Pauly^b, D. Pfeifer^b, S. Querschfeld^b, J. Rautenberg^b, S. Reinecke^b, Y. Riabov^e, E. Roshchin^e, V. Samsonov^{e,f,h}, O. Tarasenkova^e, M. Traxler^a, C. Ugur^a, E. Vznuzdaev^e, and M. Vznuzdaev^e*

^aGSI Helmholtzzentrum für Schwerionenforschung GmbH, D-64291 Darmstadt, Germany; ^bDepartment of Physics, University Wuppertal, D-42097 Wuppertal, Germany; ^cSSC RF ITEP, 117218 Moscow, Russia; ^dInstitute of Physics II and Institute of Applied Physics, Justus Liebig University Giessen, D-35392 Giessen, Germany; ^eNational Research Centre "Kurchatov Institute" B.P.Konstantinov Petersburg Nuclear Physics Institute, 188300 Gatchina, Russia; ^fNational Research Nuclear University MEPhI (Moscow Engineering Physics Institute), 115409, Moscow, Russia; ^gInstitut für Kernphysik, Goethe University Frankfurt, D-60438 Frankfurt am Main, Germany; ^hSt. Petersburg State Polytechnic University (SPbSPU)

The CBM RICH project has made substantial progress in various fields in 2015 as will be presented in the following articles. Despite the fact that the FAIR start has been shifted to 2022, the project has gained momentum because a close collaboration with the HADES collaboration for an upgrade of the HADES RICH detector has been initiated. This update shall be ready for the new A+A and π +A beam-times of HADES in 2018 at SIS18. For this update, part of the CBM MAPMTs will already be used together with the frontend electronics. The benefit is, that in addition to significantly contributing to the physics output of HADES, the performance of the MAPMTs including WLS layers, the electronics, ring finding and calibration routines can be tested prior to the start of CBM. This should give the CBM RICH a very smooth start in CBM delivering physics from the first day on.

In detail, major progress was made in the following aspects: In spring 2015 radiation hardness tests of the H8500 MAPMTs and WLS layers (p-terphenyl) were made with thermal reactor neutrons at the TRIGA reactor in Ljubljana and with gamma rays from a ⁶⁰Co source in Gießen. No major degradation of the MAPMT was observed for doses expected for 10 years running CBM at full SIS300 performance. Therefore, 1100 Hamamatsu H12700 MAPMTs were ordered and the first batch was received in October. A new test stand has been established which is used for routinely testing the incoming MAPMTs. Detailed analysis of the PADIWA+TRB3 readout chain used for the RICH test-beam November 2014 at CERN has been performed, giving major input for the further development of the RICH front end electronics concept. As a very interesting side aspect, the decay constant of the WLS layers (p-terphenyl) could be determined to be 2 ns with a second, smaller 6 ns contribution. The design of the RICH FEE based on the future DiRICH modules with 32 channels has made major steps forward and first modules will be available early sum-

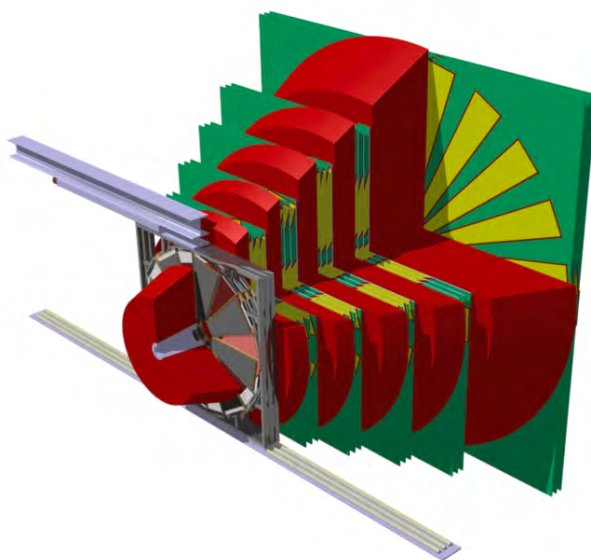
mer 2016 for labtests and later also testbeams. The concept foresees 2×3 MAPMT arrangements as basic modules sharing also one power distribution and data concentration board.

Major progress has also been achieved with a number of subjects related to the RICH geometry and technical/mechanical design. Finally, a new RICH geometry has been developed that is adjusted to the new CBM dipole magnet and its stray field. The whole RICH detector was shifted and the mirrors tilted in order to move the PMT planes out of the stray field. The photodetector planes are arranged as tilted wings, four in total. A first realistic design of a shielding box proves that the stray field can be reduced to values below 1 mT in the photocathode plane. A drawback of the wing geometry is a rather large central gap due to geometrical constraints and space required for arranging PMTs and FEE cards, therefore conceptual studies for further improvement of the PMT plane geometry have been done and will be finalized in 2016. The essential idea is to change the wing geometry to a cylindrical one. The new four wing geometry has been implemented in CbmRoot and major updates of the RICH software have been done in order to cope with this. The new geometry also allows for misalignment of single mirror tiles. Routines for determination of misalignment as well as later software correction have been developed and a first version has been implemented in CbmRoot. The mounting system of the RICH mirror wall has been critically assessed. New concepts for the structure holding the single mirror tiles with substantially reduced material budget have been developed. In a next step, prototype systems will be build and tested.

In summary, the RICH project is running well and if no major drawbacks e.g. in funding arise the RICH detector will be ready for first beams at SIS100.

* claudia.hoehne@physik.uni-giessen.de

Muon Detection System



Basic performance study of the new MUCH geometry for CBM

E. Nandy and S. Chattopadhyay

Variable Energy Cyclotron Centre, Kolkata, India

A most realistic geometry, designed according to the mechanical requirements of the SIS100-B set-up of the CBM experiment has been implemented. In this new geometry, the shapes of the absorbers are re-defined; conically shaped absorbers used earlier are replaced by parallelepipeds, except for the first absorber. The first absorber has a bi-conical shape instead of the cylindrical shape used earlier and is divided into two parts – one inside the magnet and the other one outside. The dimensions of the first absorber are also changed – its first part is now 24 cm long, the second part 36 cm in place of 40 cm and 20 cm used earlier. The entire MUCH set-up is shifted by 5 cm downstream. The Z position of the first absorber is shifted to $z = 125$ cm, which was at 120 cm in the previous geometry. The magnet geometry is modified as well to avoid overlap with the MUCH. The shielding bar of the magnet is removed.

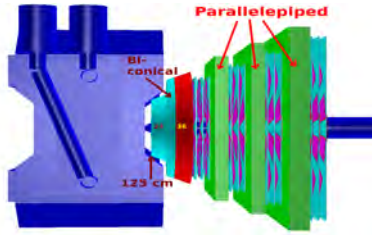


Figure 1: MUCH set-up with the new configuration.

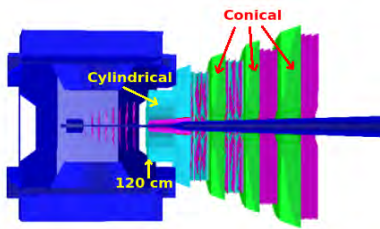


Figure 2: MUCH set up with the old configuration.

Simulations were performed with this new MUCH geometry as shown in Fig. 1, to be compared to the previous geometry displayed in Fig. 2. To study the performance of this new geometry, the *CbmRoot* framework was used with the GEANT3 transport code to transport the particles through the CBM set-up using UrQMD and PLUTO as background and signal generators, respectively.

Fig. 3 shows the comparison of the point density distributions in the first station for both the new and old configuration. The point density is somewhat higher in case of the

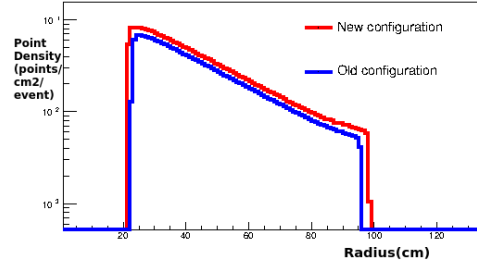


Figure 3: Comparison of point density in the first station for old and new configuration.

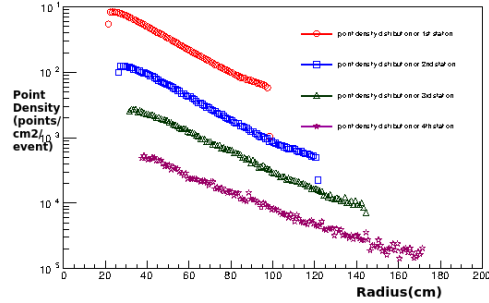


Figure 4: Point density distribution in all stations.

new geometry. Fig. 4 shows the point density distributions of MUCH points for the new configuration for all the stations. Fig. 5 shows the variation of the radial distribution of the occupancy for all stations.

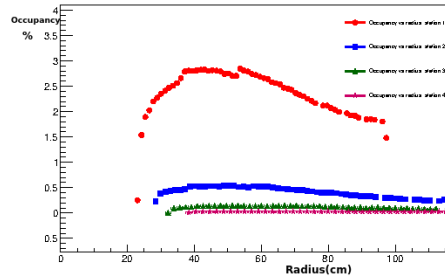


Figure 5: Occupancy distribution in all stations.

From these plots we can conclude that the most realistic MUCH geometry does not change previously obtained results significantly except that the point density increases somehow.

Simulation of the beam pipe for MUCH

S. Ahmad¹, M. Farooq¹, E. Nandy², S. Chattopadhyay², and S. Bashir¹

¹University of Kashmir, Srinagar India; ²Variable Energy Cyclotron Center, Kolkata India

The CBM experiment is expected to have 1% beam-target interactions, which demands a highly efficient beam pipe to carry 99% of the beam to the beam dump. In the present work, the beam pipe of the MUCH system is analysed. Figure 1a shows the sketch of the present configuration of the beam-pipe and shielding used in MUCH simulations which leaves empty spaces between the shielding and beam-pipe more prominent below first absorber, and empty spaces between the MUCH absorbers and the shielding. These gaps have been filled in new proposed configuration as shown in a sketch shown in figure 1b.

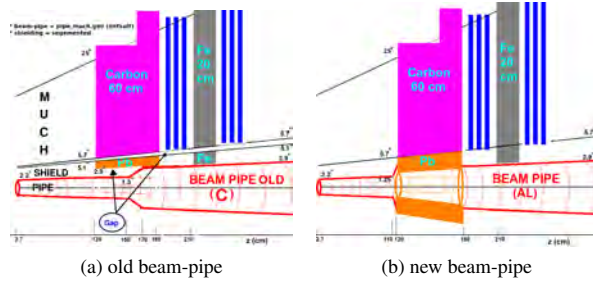


Figure 1: Sketch of the muon detector setup showing the first two stations and absorbers with the old (left) and new (right) MUCH beam pipe

The lead shielding in the region of the first absorber is made as a part of the beam pipe. As expected, 10% reduction in occupancy is seen when compared to present configuration. Moreover, no effect on the S/B ratio is observed for different beam pipe materials which justifies the use of the less expensive aluminium.

The CBM-ION generator was used to optimise the lead shielding opening, which is part of the beam pipe in our proposed configuration. The generator provides beams of gold ions the profile of which is determined by four Gaussians, two representing the spatial distribution (x, y) and two the angular distribution ($p_x/p, p_y/p$). For 4A GeV and 8A GeV, the beam-spot radii are expected to be 1 mm and 0.5 mm, respectively. In the simulation, the beam starts just after the target and is transported using GEANT3 in the CBM magnetic field through the beam pipe until the ECAL.

CBM-MUCH with ECAL was used for the purpose. The deposited energy of the beam is intergrated in the ECAL and compared with the input (using the ratio E_{ecal}/E_{in}) to look for the losses expected from interactions with the lead

hole. We also analyse the hits on both sides of the lead hole, i.e. in the STS (upstream) and the first station of the MUCH (downstream), to look for beam-lead interactions.

From Fig. 2a it is seen that until the 20 mm radius of the leadhole there are more beam-lead interactions at the beginning reflected in having more STS hits than MUCH hits. If we increase the hole radius, a reduction of STS hits and increase in the MUCH hits is seen up to $r \sim 30$ mm, suggesting beam-lead interactions inside and downstream of the hole.

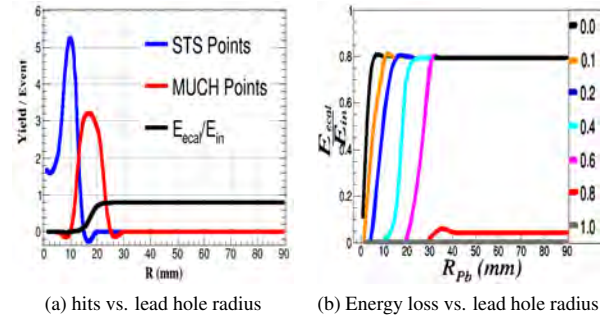


Figure 2: (a) Hits(points) of STS & MUCH, and E_{ecal}/E_{in} as function of the lead-hole radius at 4 GeV. (b) E_{ecal}/E_{in} energy ratio as function of the lead-hole radius at different magnetic field strengths (scale 1 corresponds to 2 T)

A similar conclusion can be drawn from the ratio E_{ecal}/E_{in} shown in Fig. 2a. It is clear from the above discussions that beam particles find a safe passage above 30mm radius of the lead opening. We usually take 3° as outer acceptance angle of the beam pipe, which is a safe limit in any case.

The effect of the magnetic field effect on the beam was also studied, varying its strength scale 1 (~ 2) T to 0 in steps. The corresponding E_{ecal}/E_{in} ratio was analysed as function of the lead-hole radius. Fig. 2b shows that up to the scale 0.6 there is a corresponding value of the lead-hole radius above which almost no loss in the incident beam energy is seen, but above 0.6 the beam gets lost as reflected by vanishing energy ratio. If the same is repeated for 8 GeV, no such disappearance of the beam is seen at any field scale.

In conclusion, the magnetic field strength for 4A GeV beam energy need to be lowered below 1.2 T. We take the safe value of 0.8 T for the magnetic field for 4A GeV incident beam energy.

Prototype ASIC for Muon Chambers*

E. Atkin¹, I. Bulbakov¹, V. Ivanov³, P. Ivanov¹, E. Malankin¹, D. Normanov¹, I. Sagdiev¹, V. Samsonov^{1,3}, V. Shumikhin¹, O. Shumkin¹, S. Vinogradov¹, and A. Voronin^{1,2}

¹National Research Nuclear University "MEPhI", Moscow, Russia; ²Moscow State University, Moscow, Russia;

³Petersburg Nuclear Physics Institute, NRC Kurchatov Institute (PNPI), Gatchina, Russia

On the basis of the previous prototype ASIC designs and lab test results [1, 2, 3] the new prototype chip for the CBM MUCH has been developed. The current design is a prototype of the full readout channel for GEM that can provide both the signal amplitude and the timestamp.

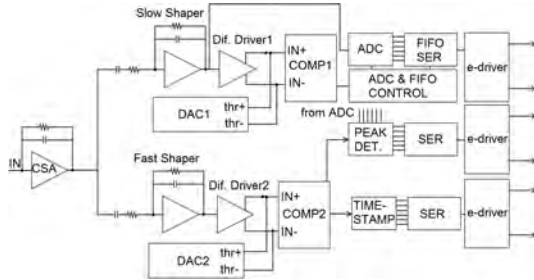


Figure 1: Schematic of readout channel

The chip contains two data processing channels. The structure of the channel is shown in Fig. 1. Each analog channel contains a preamplifier, followed by two shapers (fast and slow). The shapers outputs are connected to the drivers, which make a single-ended input signal to differential signal output. Furthermore, the signals are supplied to the differential comparator inputs. For regulating the threshold of the comparator a current DAC is used. The fast shaper output is connected to a timestamp block. The data from ADC, peak detector and timestamp are serialized and sent via SLVS transmitter (a simulated output eye diagram at 320 Mbps is shown in Fig. 2) out of the chip. The signal from the slow shaper is processed by a SAR ADC (INL – 0.3 LSB, DNL – 0.4 LSB, a simulated single-tone spectrum is shown in Fig. 3). The ADC is followed by a digital peak detector.

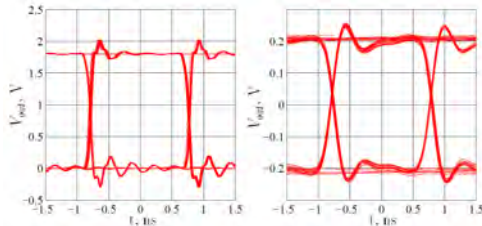


Figure 2: SLVS Rx and Tx simulation results

* Work supported by SAEC "Rosatom" and Helmholtz Association and the Ministry of Education and Science of the Russian Federation (Grant No. 14.A12.31.0002)

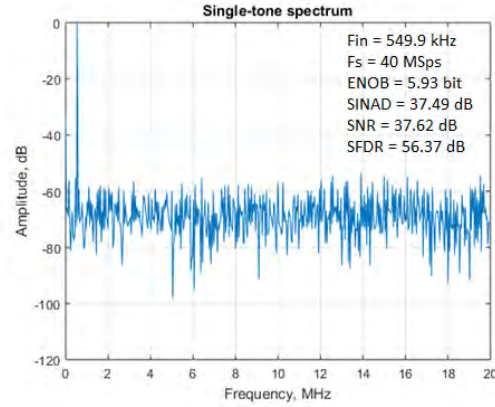


Figure 3: Spectrum of single-tone digitized signal

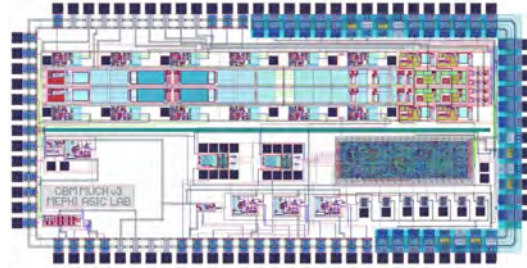


Figure 4: Prototype ASIC for CBM-MUCH layout

The chip also contains additional test blocks and pads for probe station tests.

The ASIC layout is shown in Fig. 4, its area is 3240 x 1525 μm^2 . The chip was fabricated via Europractice in 2015 in the UMC MMRF 180 nm process.

We plan to carry out the electrical measurements and tests with GEM detector prototypes. The next multi-channel version of the ASIC, which contains digital interface, slow control and improvement of the calibration system, is under development.

References

- [1] E. Malankin *et al.*, Instrum. Exp. Tech. **57** (2014) 286–290
- [2] E. Atkin *et al.*, JINST **10** (2015) C04006
- [3] V. Samsonov *et al.*, JINST **11** (2016) C01084

Effect of parameter-settings of n-XYTER, self triggered electronics for CBM-MUCH

A. Kumar, A. K. Dubey, J. Saini, and S. Chattopadhyay

VECC, Kolkata, India

Introduction

Triple-GEM detectors will be used for muon tracking in the CBM experiment at FAIR. Positioned in the first two stations of MUCH, these detectors will have to cope up with a high particle density. For the operation of CBM-MUCH at high interaction rates, a self triggered fast read-out electronics is required. For the beamtest of GEM detector prototypes, n-XYTER ASIC was used for reading out the signal. It has several registers via which one can set the optimum values for operating the ASIC. Parameters such as V_{biasS} , V_{th} , V_{bfb} are some of the main ones which directly affect the signal amplitude or the noise characteristics of the detector. V_{th} is the global threshold voltage for the comparators i.e. it defines the pulse strength that is necessary to trigger the comparator. V_{biasS} is the bias voltage for the first stage of slow shaper of n-XYTER and sets the baseline. V_{bfb} sets the discharge time for preamplifier by controlling the resistance of the transistor used in preamplifier of n-XYTER and its setting governs the behaviour of the response at high rates. In this report, we discuss the variation of signal and baseline with varying FEB parameters.



Figure 1: Experimental Setup in at VECC

Experimental Setup

The tests have been carried out using a triple GEM detector of 10 cm x 10 cm and Fe^{55} source. The picture of the setup is shown in Figure 1. The readout plane consists of 512 pads, each of 3 mm x 3 mm in size, and read out using two n-XYTER FEBs. Fe^{55} source was placed at a fixed position of the detector such that the same pad was hit most of the times. Only one setting parameter was changed at any given time and data were acquired using DABC software [1] developed at GSI.

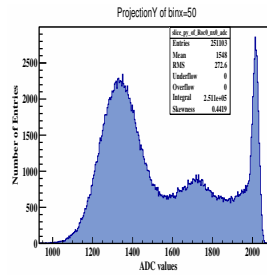


Figure 2: Raw spectrum of Fe^{55} .

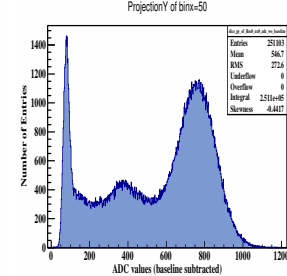


Figure 3: Baseline corrected spectrum of Fe^{55} .

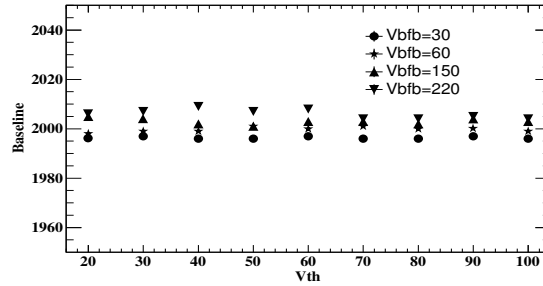


Figure 4: Variation of baseline with V_{th} at different V_{bfb} .

Results and Discussion

The baseline of the n-XYTER is set internally at average value of 2000 ADC channel for negative signals. Figures 2 and 3 show the raw and baseline corrected pulse height spectra of Fe^{55} , respectively. The accuracy in baseline determination is an important issue and can directly affect the

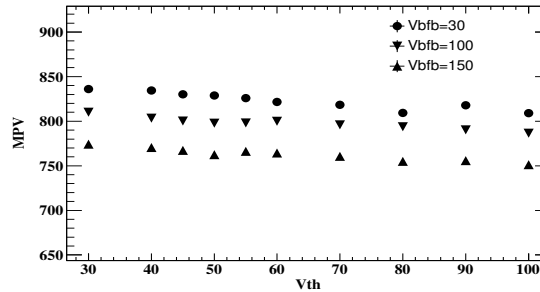
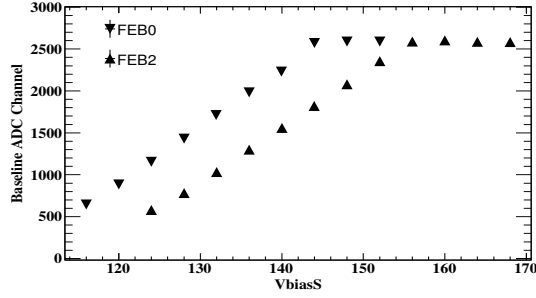


Figure 5: Variation of MPV of the pulse height spectra with V_{th} .

Figure 6: Variation of baseline with V_{biasS} .

amplitude estimation of the signal. Figure 4 shows the variation of baseline with V_{th} at different V_{bfb} settings. Negligible effect of V_{th} is seen on the baseline values. There is a systematic change, but at an insignificant level ($<0.5\%$), in the baseline with increase in V_{bfb} parameter. The noise in the detector can be controlled by increasing the value of V_{th} , which if set too high can affect the pulse height. At any given V_{bfb} , how the change in V_{th} affects the signal amplitude is shown in Figure 5. These pulse heights are normalized at T/P = 0.2980 K/hPa. It is seen that the peak pulse height gets affected only slightly (less than 3%) if the V_{th} value changes from 30 to 100. At the same time, on varying the V_{bfb} value from 30 to 150 at a fixed V_{th} (say 50) a decrease in pulse height of about 9% is observed. This can also be gathered from Figure 8. This decrease in ADC channel by increasing V_{bfb} can be understood by the faster dissipation of charges on the readout pads. Figure 6 shows the variation of baseline with V_{biasS} for two different FEBs. The baseline increases linearly with V_{biasS} and gets saturated above certain V_{biasS} setting, because of the reference level of n-XYTER. Saturation value of baseline is fixed but the settings of V_{biasS} parameter will vary from one FEB to another FEB. The “autovbias” command in DABC sets the average baseline around 2000 ADC channel. The temperature variations in FEB also affects the baseline of the n-XYTER. We have allowed only a small variation of temperature by $\sim 1^\circ\text{C}$.

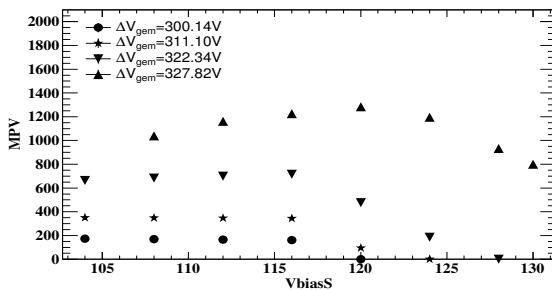
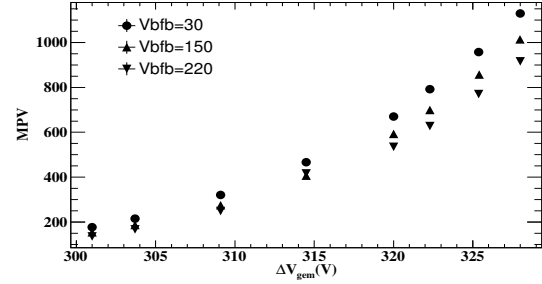
Figure 7: Variation of peak pulse height with V_{biasS} at different ΔV_{gem} .

Figure 7 shows the variation of peak pulse height (the

Figure 8: Variation of peak pulse height with ΔV_{gem} .

Most Probable Value, MPV) with V_{biasS} at different ΔV_{gem} . It remains flat with V_{biasS} for lower ΔV_{gem} upto a particular value, beyond which it decreases to zero. But for high amplitude signals (higher ΔV_{gem}), the MPV values are lower at lower V_{biasS} as compared to intermediate ones in the figure, and then starts to decrease after a particular value, as before. V_{biasS} sets the DC reference level for each channel. If the level goes below the output low of slow shapers, then the signal is clipped from the lower side and we get no output at low input signal. If the DC level is set to very high, then high input signal is saturated. This observation is in line with the expected behaviour of electronics. This study indicates the range of V_{biasS} values within which one can expect a stable signal.

For a stable operation of the detector at high rates in test beams, V_{bfb} parameter had to be set at a high value of about 150. to avoid pre-amp saturation. However, high values of V_{bfb} may result into some amplitude loss, owing to faster dissipation of charge from the pads as discussed before. This effect of the varying V_{bfb} values on signal amplitude has been systematically studied in Fig. 8. Shown in this figure is the variation of peak pulse height with ΔV_{gem} at three different V_{bfb} settings (30, 150, 220). These pulse heights are normalized at T/P=0.2980 K/hPa. As observed from the figure, the gain reduction is at the level of about 10% in the MPV at $\Delta V_{gem} = 328\text{V}$, when going from $V_{bfb} = 30$ to 150.

Summary

The baseline of the n-XYTER does not depend on the V_{th} , but it depends on the V_{biasS} settings. The peak pulse height is affected by only about 3% on varying the V_{th} in the range of our study. A high value of V_{bfb} affects the peak pulse height slightly. A decrease of 10% in signal amplitude as seen from the MPV values from the Fe^{55} tests is observed when changing V_{bfb} settings from 30 to 150.

References

- [1] J. Adamczewski-Musch, H. Essel and S. Linev, IEEE Trans. Nucl. Science **58** (2011) 1728

Control of XYTER emulator from DPB through GBTX emulator for the CBM-MUCH detector*

S. Mandal^{†1}, W. M. Zabootny², S. Saw³, J. Saini¹, A. Chakrabarti³, and S. Chattopadhyay¹

¹VECC, Kolkata, India; ²Warsaw University of Technology, Warsaw, Poland; ³University of Calcutta, Kolkata, India

For efficient data aggregation from the Muon Chamber front-end electronics (MUCH-FEE), a GBTx [1] emulator is planned to be used in between FEE and the Data Processing Board (DPB) [2] in the MUCH Data Acquisition (DAQ) system (in the final experiment, the GBTx emulator will be replaced by the GBTx ASIC). In the front end, GBTx receives data from the FEE through an electrical link (E-link), and in the backend it sends data to the DPB through 4.8 Gbps optical links. This article focuses on the controlling of the E-Link protocol from the DPB through optical links.

Each E-link [3] basically consists of three signal lines. They are differential clock lines (used to provide a clock to the FEE device), differential downlink data output (used to send data from the GBTx to the FEE) and differential uplink data input (used by the GBTx to receive data from the FEE). A simple synchronous communication protocol is developed using some special characters like K28.5, K28.1, Start of Synchronization (SOS) and End of Synchronization (EOS) for establishing communication between the GBTx and the FEE through the differential E-Link. A schematic flow chart in Fig. 1 describes the basic E-Link protocol. In the downlink direction, data are transferred using the GBT frame with a data rate of 160 Mbps. In the uplink direction, transmission is done via a wide frame mode with a data rate of 320 Mbps.

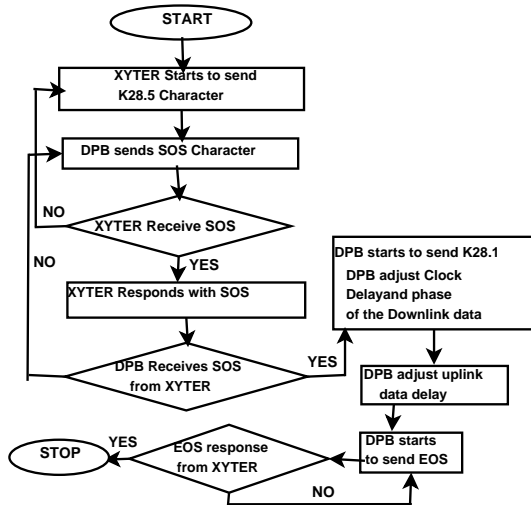


Figure 1: Flowchart for the E-Link protocol

The E-Link protocol will be completely controlled from the DPB. Therefore for controlling the E-link protocol, different registers in the DPB and the GBTx have to be accessed continuously. Internal registers within the GBTx and the DPB are monitored online using the IPbus protocol over a 1Gbps Ethernet link.

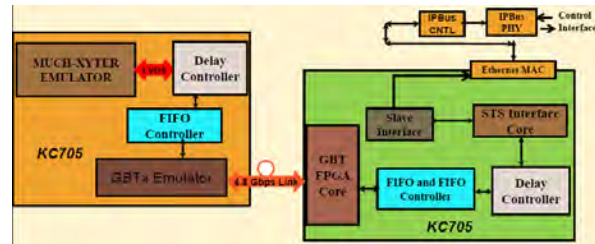


Figure 2: Integration of GBTx with XYTER and DPB

The controlling of the XYTER emulator using IPbus through the GBTx is shown in Fig. 2. Here, two KC705 evaluation boards were used, and in one board the XYTER emulator, a delay controller, a FIFO and the GBTx emulator were implemented. On the other KC705 board the GBT FPGA core, a FIFO, a delay controller and IPbus over 1 Gbps Ethernet were implemented. We have used a Python script to continuously monitor internal registers on the two boards.

The XYTER emulator sends data at a data rate of 320 Mbps, and GBT is running at 40 MHz. For clock domain crossing a synchronous FIFO is used, the write frequency of which is 320 MHz; the read frequency is 40 MHz. As the 320 MHz clock in the XYTER and the GBTx are different in phase, a delay controller is used to match the phase of these two clock domains. At the output of the FIFO, the data width is 40 bit (5 x 8 bit), which is sent through the GBT frame. In the downlink direction the GBT sends data at 40 MHz and the XYTER receives data at 160 Mbps. The write frequency of the FIFO is 40 MHz, and the read frequency is of MHz in the downlink.

References

- [1] P. Moreira, J Christiansen and K Wyllie, *The GBTx Link Interface Asic*, v1.7 (2011)
- [2] W. M. Zabootny and G. Kasproicz, Proc. SPIE 9290 (2014) 929023
- [3] K. Kasinski, W. Zabootny and R. Szczygiel, *STXSYTER – DPB Protocol v.1.5* (2014)

* Supported by BI-IFCC,DST and DAE, Govt. of India

[†] swagata.mandal@vecc.gov.in

Design and development of a low-voltage distribution board for the CBM-MUCH*

V. S. Negi[†], V. Jain, J. Saini, and S. R. Narayan

Variable Energy Cyclotron Centre, Kolkata, India

A GEM-based tracking system is planned to be used for muon tracking in the proposed CBM experiment at FAIR. This experiment requires high position resolution and high rate capabilities of a tracking detector, which led to more complex and densely packed electronics. To cope up with the high interaction rate, self-triggered electronics is chosen for data acquisition, and there is a very stringent requirement on noise levels. In such a system power consumption and space are always big issues to address. The hit density at the first station is very high with minimum pad size of 3 mm × 3 mm. In addition, a careful design of the low voltage distribution is needed for optimized performance and less cable count.

The LVDB is an active system which divides a single channel high power low voltage (LV) into a several low power LV channels as per the requirement. One LVDB is going to supply mainly nine FEE boards, each of which requiring the three voltages 1.6 V, 1.8 V and 2.2 V with a current of 1 A, 7.5 A and 0.25 A, respectively. The LVDB has over-current protection and monitoring facility of voltage and current. The prototype design has been tested for two channels as shown in Fig. 1. The LV power supply has very stringent requirement of sector isolation (to avoid sector-to-sector noise coupling), so in this prototype two DC to DC converters are used.

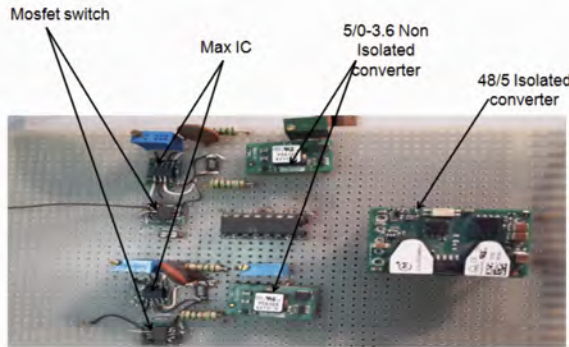


Figure 1: Two channel LVDB prototype

The 48 V supply is stepped down to 5V using a DC to DC SMPS base isolated converter with forward topology. The outputs of the isolated converter are further stepped down by buck converters (non-isolated) to meet the required voltages (1.6 V, 1.8 V and 2.2 V). In the final design of the LVDB, all output channels are supposed to

* Supported by BI-IFCC, DST and DAE, Govt. of India

[†] vnegi@vecc.gov.in

have over-current protection. This protection isolates faulty channels immediately, keeping the rest of the channels in a working state. This minimizes the data loss due to unexpected glitches in the system.

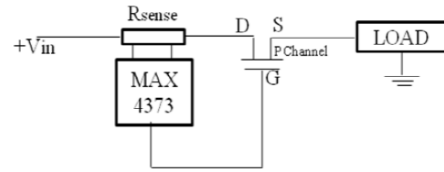


Figure 2: Over-current protection circuit

Figure 2 shows the basic building block of the over-current protection circuit using MAX4373, sense resistors, control logic and switching elements. MAX4373 is a low-cost, micro-power IC containing current sense amplifier, band gap reference and a comparator with latch. The current sense resistor is connected in series to the load, so the resistance chosen should be as low as possible to minimize the voltage drops and must be very stable.

The efficiencies of both the converters on and above 50% load are found to be above 93% as shown in Fig. 3.

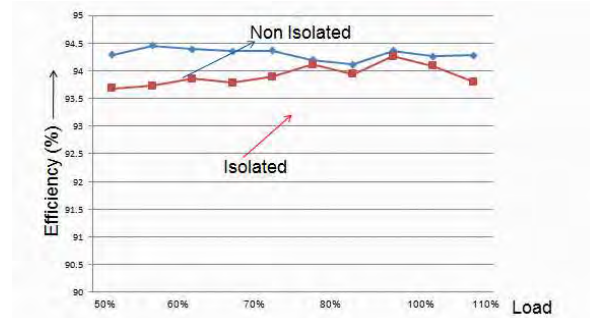
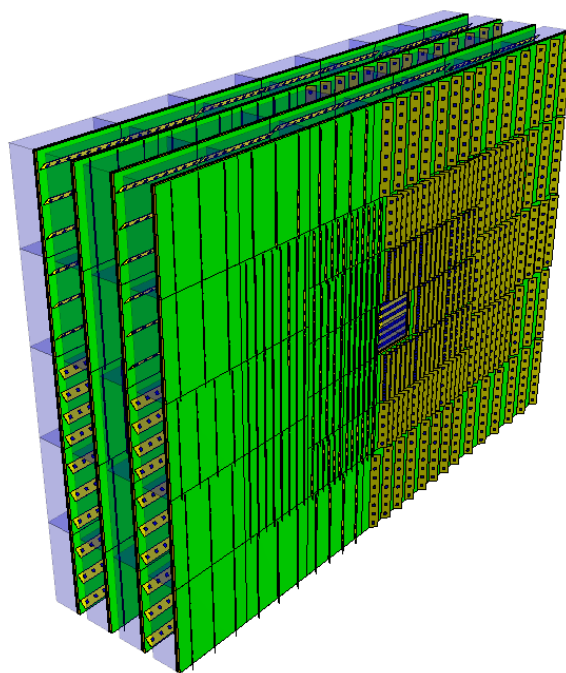


Figure 3: Efficiency of converters

References

- [1] P. Moreira, J Christiansen and K Wyllie, *The GBTx Link Interface Asic*, v1.7 (2011)
- [2] W. M. Zabołotny and G. Kasproicz, *Proc. SPIE 9290* (2014) 929023
- [3] K. Kasinski, W. Zabołotny and R. Szczygiel, *STXSYTER – DPB Protocol v.1.5* (2014)

Transition Radiation Detector



Summary on the TRD project

C. Blume¹

¹Institut für Kernphysik, Frankfurt am Main, Germany

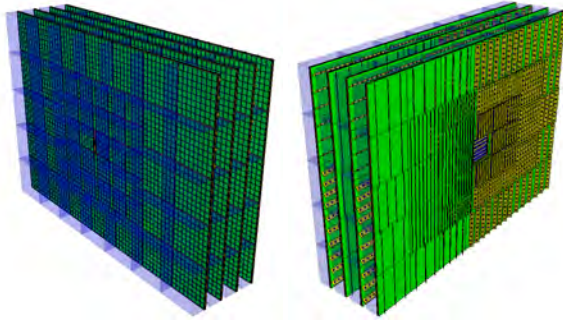


Figure 1: CBM-TRD geometry for SIS100, consisting of one station with four layers of detectors. Shown here is the implementation of the TRD geometry in the simulation framework. Visible are the ROCs with the radiator boxes in the front view (left), while the rear view (right) shows the backpanels of the ROCs together with the front-end electronics.

Introduction

The main task of the Transition Radiation Detector (TRD) is to identify electrons above momenta of 1 GeV/c and thus to extend the electron identification capabilities of the Ring Image Cherenkov (RICH) detector above momenta of $p \sim 5$ GeV/c. In this region the TRD should provide a pion suppression factor in the range 10 – 50, in order to allow for a high quality measurement of dielectrons in the mass range from below the ρ and ω masses to beyond the J/ψ mass. Due its capability to identify charged particles via their specific energy loss, the TRD in addition will provide valuable information for the measurement of fragments.

These requirements can be fulfilled with a Xe/CO₂ based Multi-Wire Proportional Counter (MWPC) detector in combination with an adequate radiator. The default MWPC design is composed of a symmetric amplification area of $3.5 + 3.5$ mm thickness, followed by a 5 mm drift region to enhance the TR-photon absorption probability in the active gas volume. This geometry provides also efficient and fast signal creation, as well as readout, with timescales below 200 μ s per charged particle track. The performance of the detector is maximized by reducing the material budget between radiator and gas volume to a minimum.

The baseline design for the TRD currently foresees one station composed of four detector layers (see Fig. 1). It will

be positioned between the RICH and the Time-Of-Flight (TOF) detector and thus will help to reduce the background in the TOF resulting from track mismatches by providing additional position information between RICH and TOF. The TRD will also be used as tracking station behind the last absorber of the MUCH detector in the muon configuration of CBM.

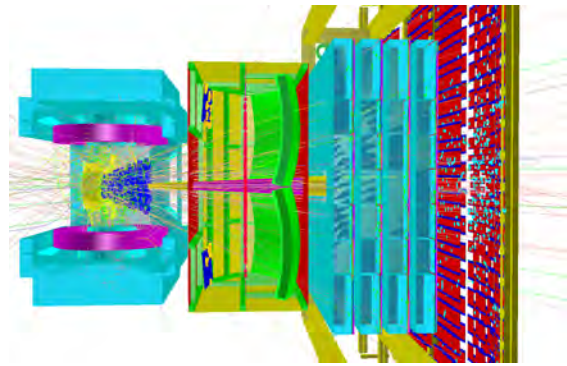


Figure 2: Visualization of one simulated central Au+Au collision at 10 AGeV.

Physics performance

In the last year a lot of effort has been invested to define the physics case of the TRD at the SIS100 and to closely investigate the performance of CBM for physics observables that can be addressed with the help of the TRD. Figure 2 shows as an example a display of one simulated Au+Au event at 10 AGeV, including the four layer TRD in the setup. As a device dedicated to electron identification at higher particle momenta, the TRD will play a decisive role in the measurement of dielectrons in the intermediate mass region ($m_{ee}(\phi) < m_{ee}^{\text{IMR}} < m_{ee}(J/\psi)$). This region is of particular interest, since it provides access to thermal radiation from the hot and dense medium produced in heavy-ion collisions and thus allows to measure its temperatures in very early stages of the medium evolution [1]. Using the dilepton MC event generator provided by [2] the CBM performance to measure thermal radiation is currently being studied. The results summarized in [3] illustrate the importance of the TRD for this kind of measurements.

Also discussed in [3] are the possibilities offered by the TRD to identify fragments via their specific energy loss dE/dx in the TRD gas. This is in particular important for the separation of, e.g. deuterons and ⁴He, which cannot be achieved using a time-of-flight measurement alone.

A clean deuteron identification is a prerequisite for the detection of the double- Λ hypernuclei ${}^6_{\Lambda\Lambda}\text{He}$. The TRD will provide sufficient dE/dx resolution for this purpose and thus allow to address this kind of physics.

Test beam activities

The TRD participated in the test beam at the CERN-SPS in Nov./Dec. 2015 with in total five different readout chamber prototypes [4, 5]:

- A chamber built in Münster that closely corresponds to the current TRD baseline design with $3.5 + 3.5$ mm amplification and 5 mm drift region, and outer dimensions of $57 \times 57 \text{ cm}^2$ [6].
- A thinner, symmetric prototype from Frankfurt (dimensions $67 \times 67 \text{ cm}^2$) with $4 + 4$ mm amplification region but without drift. It is equipped with an anode wire plane of alternating HV [7].
- Three prototypes from Bucharest of different dimensions (two smaller ones with $23 \times 8 \text{ cm}^2$ and one large one with $60 \times 60 \text{ cm}^2$). All have $3.5 + 3.5$ mm amplification and 5 mm drift region and pad planes featuring triangular pads. This pad configuration allows for a two-dimensional position reconstruction [5].

The Münster and Frankfurt prototypes were read out with the SPADICv1.0/SysCore/FLIB readout chain, while the Bucharest chambers mainly used a readout employing the FASP-01 chip. One of the Bucharest chambers was in addition also successfully connected and read out by a SPADIC ASIC [8]. The SPADIC readout chain generally performed stably during the test beam, which to a large extent was the consequence of extensive preparations and tests in the laboratory beforehand [6]. The laboratory tests using ${}^{55}\text{Fe}$ sources as well as cosmics will be continued at all involved laboratories (Bucharest, Frankfurt and Münster).

Apart from commissioning the readout chain, the main objective of this SPS test beam was the investigation of the behaviour and stability of the readout chamber prototypes in a high rate environment. Special care was taken to record the HV currents [4] under these conditions. The Frankfurt prototype was in addition equipped with a highly segmented HV supply to ensure stable voltages also under extreme conditions [7]. The results from the ongoing analyses of the test beam data will provide important informations for the operation of MWPCs in the high rate environment.

Prototype developments

The next step in the development of readout chamber prototypes is the construction of large type modules. The current design of the TRD foresees smaller modules ($57 \times 57 \text{ cm}^2$) for the inner regions of the detector, while for the outer regions large modules ($95 \times 95 \text{ cm}^2$) are planned (see Fig. 3). The design of the large chambers is

currently being finalized and the production processes are being worked out [9]. It is planned to use these new prototypes in tests with electron beams at DESY in fall 2016. They should also be used in the CBM demonstrator setup currently being planned for the SIS18. In this setup four layers of detectors are foreseen, corresponding to the final setup in CBM, however, providing only a much smaller acceptance.

Of special importance in the design of the MWPCs is the stability of the entrance window foil under changes in the ambient atmospheric conditions. A special stress-test was therefore performed on one of the prototypes from Münster, showing that the foils provide sufficient tightness against oxygen influx even on longer time scales [10].

8	8	7		7		7		8	8
8	6	3	3	3	3	3	6	8	
		2	1	1	1	2			
7	6	2	1		1	2	6	7	
		2	1	1	1	2			
8	6	3	3	3	3	3	6	8	
		3	3	3	3	3			
8	8	7		7		7		8	8

Figure 3: The arrangement of the different module types in one TRD layer. A layer can be separated into three vertical sections, two outer ones (shown in light gray), consisting of large modules, and a center one (shown in dark gray), containing small modules in the middle and large modules at the top and bottom.

Front-end electronics

A new version of the SPADIC ASIC, v1.1, is currently being prepared. It incorporates the experiences made in the previous year in laboratory and beam test and also fixes several bugs, which were still present in v1.0 [11].

The Fast Analog Signal Processor (FASP) chip has been further developed by the Bucharest group [12]. Among other changes, it now features an elaborated control interface and a pad pairing option. Preliminary tests showed very promising results.

Technical design report

The technical design report of the TRD is currently being finalized. Its submission is planned still this year. The report describes the setup of the TRD planned for operation at the SIS100 (i.e. four detector layers), the details of the readout chamber design, the expected detector performance and also the physics observables that can be addressed with the help of the TRD. These studies are currently being finalized and details on services and support

structures for the TRD are being defined right now.

Outlook

Along with the technical design report also the design of the TRD will be finalized in the course of 2016. Several further test beams are planned in order to validate this design. One is foreseen in fall 2016 with an electron beam at DESY in Hamburg and will allow to determine the optimal detector parameters (e.g. radiator design and gas volume thickness) for a maximal pion suppression factor. Further tests in a high rate environment are also planned, either again at the CERN-SPS or at the GIF++ facility at CERN. For the upcoming tests a new version of the SPADIC ASIC (v1.1) will be used, which should be packaged and ready in the next months.

References

- [1] R. Rapp and H. van Hees, *Thermal Dileptons as Fireball Thermometer and Chronometer*, Phys. Lett. **B753**, 586 (2016).
- [2] T. Galatyuk et al., *Thermal Dileptons from Coarse-Grained Transport as Fireball Probes at SIS Energies*, arXiv:1512.08688.
- [3] J. Book et al., *Physics performance of the CBM-TRD in Au+Au collisions at the SIS100*, this report.
- [4] C. Bergmann et al., *Combined MWPC prototype test of Münster and Frankfurt using SPADICv1.0 data taking at CERN-SPS/T2-H4 in 2015*, this report.
- [5] A. Bercuci et al., *Calibration and in-beam operation of the two-dimensional MWPC prototype for CBM-TRD*, this report.
- [6] M. Kohn et al., *^{55}Fe source measurements with CBM-TRD detector prototypes*, this report.
- [7] M. Tanha et al., *CBM-TRD prototype tests in Frankfurt*, this report.
- [8] M. Kohn et al., *Test of SPADICv1.0 readout on Bucharest CBM-TRD detector prototypes*, this report.
- [9] C. Bergmann et al., *Construction of the first 1 m^2 prototypes for the CBM-TRD*, this report.
- [10] P. Kähler et al., *Stress-test of a MWPC prototype from Münster reproducing meteorologic pressure changes*, this report.
- [11] M. Krieger et al., *Progress in TRD readout using SPADIC 1.0*, CBM Progress Report 2014, Darmstadt 2015, p.80.
- [12] G. Caragheorgheopol et al., *First performance studies for FASP-02*, this report.

Physics performance of the CBM-TRD in Au+Au collisions at the SIS100*

J. Book¹ and C. Blume¹

¹Institut für Kernphysik, Frankfurt am Main, Germany

The capability to measure dielectrons with high precision and low background in the low, intermediate ($m_\phi < m_{inv} < m_{J/\psi}$) and higher mass range is of essential relevance for the CBM physics program at SIS100. The CBM-TRD provides the necessary hadron suppression capabilities in cooperation with the RICH detector to precisely identify electrons at all momenta. For momenta above $p = 5$ GeV/c pions produce Cherenkov photons in the RICH detector gas and thus limit its electron identification capabilities in the high momentum region. Therefore, the TRD will be mandatory as an additional device to allow the access to thermal radiation from the hot and dense medium created in heavy-ion collisions.

Four layers of TRD detectors provide a pion suppression up to a factor ~ 8 at an electron efficiency of 90 %. In Fig. 1 the different particle identification strategies are shown together with the combined scenario as simulated for minimum bias Au+Au collisions at 8 AGeV beam energy.

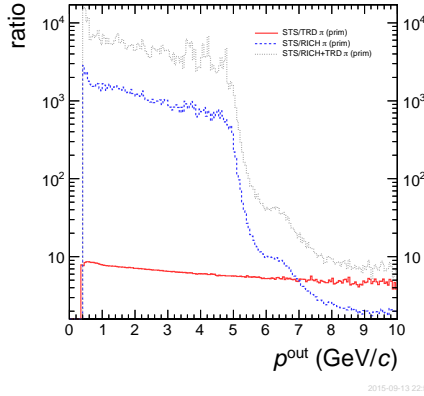


Figure 1: The pion suppression factor as a function of momentum for different detector combinations: TRD (red), RICH (blue) and RICH+TRD (black).

The additional pion suppression provided by the TRD in higher momentum region is clearly visible and it will be decisive for the study of intermediate mass dileptons. Electron pairs of unlike and like-sign are shown in Fig. 2, assuming a scenario where RICH and TRD informations are combined. The like-sign distribution is used to subtract the combinatorial background, such that the thermal component in the region above 1 GeV/c² can be extracted.

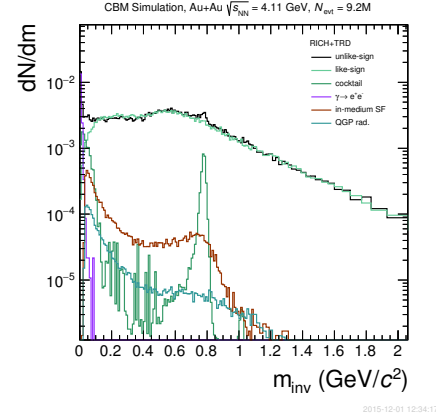


Figure 2: The invariant mass spectrum of dielectron pairs (black) together with signal and background components.

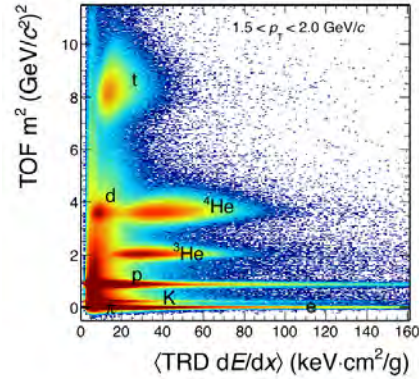


Figure 3: Comparison of the TRD signal to the mass squared measured by TOF in central Au+Au collisions. Shown is the momentum interval $1.5 < p < 2.0$ GeV/c.

Since the TRD also measures the specific energy loss of charged particles in the detector gas, it will support the identification of nuclear fragments. In particular, the TRD can differentiate between singly and doubly charged fragments such as d and ⁴He-particles, which cannot be separated via a time-of-flight measurement (TOF) alone and are important for the detection of hyper- and anti-nuclei. Fig. 3 shows the TRD signal compared to the mass squared as measured by the TOF detector. A separation power larger than 2.5σ is found for all momenta.

* Work supported by BMBF and HIC4FAIR.

Combined MWPC prototype test of Münster and Frankfurt using SPADICv1.0 data taking at CERN-SPS/T2-H4 in 2015*

C. Bergmann¹, P. Kähler¹, R. Berendes¹, N. Heine¹, M. Kohn¹, J.P. Wessels¹, W. Amend², C. Blume², S. Gläsel², F. Roether², and D. Emschermann³

¹Institut für Kernphysik, Münster, Germany; ²IKF Frankfurt, Germany; ³GSI, Darmstadt, Germany

During the CERN SPS/T2-H4 Pb+Pb 30 AGeV high rate test beam [1] a setup combining the prototypes of the institutes in Frankfurt and Münster has been operated. A floor-plan of the full setup is presented in Fig. 1.

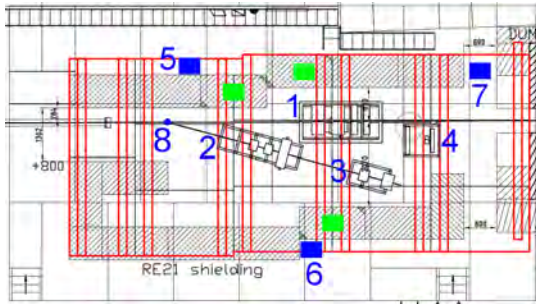


Figure 1: The CBM cave at SPS/T2-H4 beam line in 2015 is presented. The Frankfurt/Münster setup is located at position 4 and the supply/read-out rack at position 7.

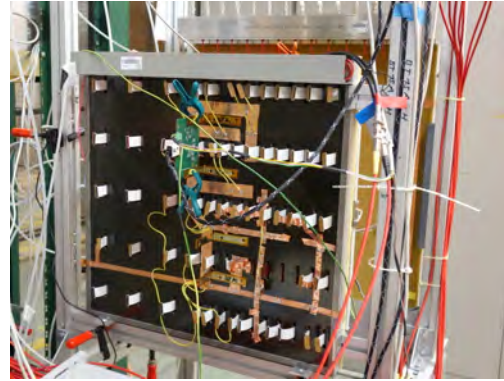


Figure 2: Combined TRD setup consisting of Frankfurt (front) and Münster (back) prototypes at the CERN-SPS Pb+Pb 30 AGeV high rate test beam.

The combined setup of two MWPC prototypes read-out via SPADICv1.0 is presented in Fig. 2 from the back side. The high voltage currents and potentials on the anode and drift wires have been monitored every 0.4 s using an SNMP program written by P. Kähler.

The detectors are mounted in a combined frame with a distance of 30 cm to each other and with parallel wire direction. The combined setup is designed to study saturation effects of the alternating wire 4 + 4 mm (Frankfurt [2]) and drift MWPC 3.5 + 3.5 + 5 mm (Münster [3]) as function of particle rate. The detector configuration allows also for offline event building based on SPADIC time-stamps and in a later analysis step, for tracking.

First preliminary estimations on the data processing rate and the anode as well as the drift wire currents of the Münster detector are presented in Fig. 3.

References

- [1] D. Emschermann et al., *Common CBM beam test at CERN SPS 2015*, this report.
- [2] M. Tanha et al., *CBM-TRD prototype tests in Frankfurt*, this report.
- [3] C. Bergmann et al., *Test of Münster CBM-TRD real-size detector and radiator prototypes at the CERN PS/T9 beam line*, CBM progress report 2014 p.78.

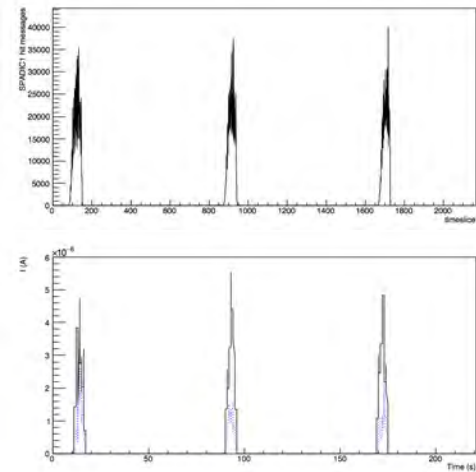


Figure 3: First analysis results of the SPADIC-recorded data based on the Münster prototype. Upper panel: three beam spills of the SPS cycle are shown. Lower panel: The integrated anode wire (continuous black) and integrated drift wire currents (dashed blue) are shown for the same time window as in the upper figure.

* Work supported by BMBF, HadronPhysics3 project financed by EU-FP7 and IP@WWU (<https://www.uni-muenster.de/IPID4all>)

Calibration and in-beam operation of the two-dimensional MWPC prototype for CBM-TRD*

A. Bercuci¹, D. Bartoş¹, G. Caragheorgheopol¹, V. Cătănescu¹, F. Constantin¹, M. Petriş¹, and M. Petrovici¹

¹IFIN-HH, Bucharest, Romania

The prototype developed in Bucharest for operating the central part of the TRD layers of the CBM experiment is characterized by fast charge collection (mean $t_{drift} \approx 120$ ns), read-out granularity of ≈ 1 cm² and a read-out topology defined by triangularly shaped pads with 2D position sensitivity capabilities [1]. For an optimum operation of the detector in high counting rates and high local particle multiplicities a dedicated ASIC FEE has been developed, FASP-01 [2]. Recently a new FASP-02 version has been designed [3], manufactured and tested [4] in both triggered and free running mode [5].

Detector Characterization

High performance in position resolution can be obtained using precise calibrations of both, FEE channels on the detector and non-uniformities in the detector response, due to its special read-out. Precise references, available on the operational detector at low cost, fast response and high portability are mandatory.

Percentage differences between the FASP chip channels are inherent due to technological limitations. In addition, detector-FEE matching is a key factor which has to be considered. Signal injection on the anode electrode provides a fast and cheap method to characterize all channels in working conditions. The calibration procedure consists in scanning the FEE response with a set of pulser generated signals and aligning all channels to a common reference.

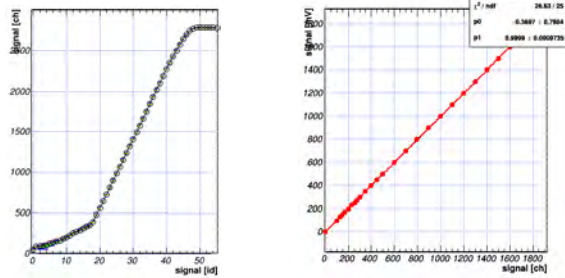


Figure 1: Left : FEE response for 56 non-uniformly distributed generated pulses for the first FASP-02 channel. Right : Similar representation after linearization for one FASP-01 channel for 0 – 1800 mV range.

In Fig. 1 (left) the response of the first FASP-02 channel is shown for 56 different signal values injected on the anode electrode of the TRD. The signals are generated non-uniformly in the range 0–5 V, with a finer granularity in the low range. Both FASP operation modes, Semi-Gaussian (SG) and Flat-Top (FT) for under and respectively above the channel threshold produce Gaussian shaped responses (mean values marked on the figure with open symbols). Moreover, the saturation of the FEE is tested for high injected signals, above 3 V (see plateau). In Fig. 1 (right) the linearized spectrum for one FASP-01 channel is presented. The mean response of FEE in ADC channels is correlated with the injected pulser signal in mV. It is shown that by combining the two operation modes, SG and FT of FASP, a continuous working range from baseline (0 injected signal) to almost 2 V can be reached with gain 1, as shown by a linear fit to this correlation also presented in the figure.

The triangular pad architecture has the potential to provide 2D position information as described in [1] for the same read-out channels/area ratio. The method relies on identifying the anode wires by correlating the detector responses along the pads (qq) and the position reconstructed across pads (x). In Fig. 2 (left) such correlation is measured for a detector operated with FASP-01 boards and illuminated uniformly with an ⁵⁵Fe source.

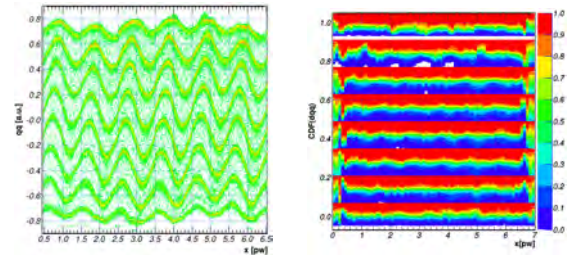


Figure 2: The correlation of the qq observable with the reconstructed position across pads x giving access to anode wire identification (left) and the CDF calibration technique for rendering uniformly distributed position information along pads (right).

The details of the position information along the pads rendered by our pad-plane design has the feature of the working principle of the multiwire proportional chambers, i.e. is highly peaked around the *loci* where the avalanche develop, i.e. the anode wires. The method of Cumulative Distribution Function (CDF), based on the displacement of individual measurements from the anode identification

* Work supported by Romanian ANCSI/CAPACITATI Modul III Contract F02 and NUCLEU Project Contract PN 09370103.

locus, can convert such measured non-uniform distribution to uniform. In Fig. 2 (right) the CDF calibration is constructed using the uniform detector illumination with ^{55}Fe for all identified wire (rows in the figure) as function of reconstructed position across pads x . Point-to-point variations in the detector response due to the heterogeneous detector design can be thus accounted for.

The assessment of the position sensitivity (systematic effects and uncertainties) is of paramount importance for a tracking device. In order to measure the performances of our prototype with a systematic free and infinite precision device we select a passive method of illuminating the detector through perforated opaque foils (copper in our case).

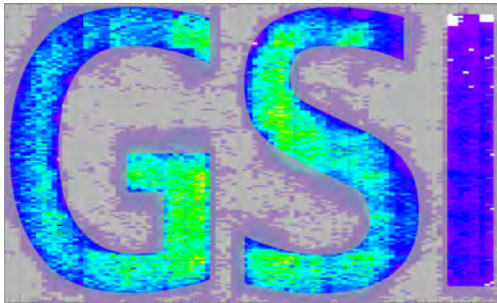


Figure 3: Assessing the precision of 2D position measurements by registering the image given by a ^{55}Fe X-ray source through a collimator (the letters "G", "S" and "I") cut out from a $\approx 45 \times 27 \text{ mm}^2$ copper foil (shaded area) fixed on the entrance window of the detector.

A qualitative example of the method outlined here is depicted in Fig. 3. A copper foil (the shaded area in the figure) of $\sim 45 \times 27 \text{ mm}^2$ and $\sim 3 \text{ mm}$ thickness of which the letters "G", "S" and "I" were cut out was used as a collimator. The detector is illuminated with the ^{55}Fe source from a large distance such to generate a relative uniform distribution over the foil. For quantitative estimates of the position performance regular perforations can be used with absolutely known (x, y) correlations. By comparing the reconstructed yield distribution with the shape of the perforations and the smearing of the edges one can get quantitative estimations on the systematic and uncertainties of the reconstructed (x, y) position.

Test Beam Measurements

The TRD prototype was tested in a high counting rate and high multiplicity environment at the CERN-SPS in February 2015. The detector was illuminated with the fragments produced by bombarding a Pb target with 13.4 GeV Ar projectiles. The detector setup was composed of three prototypes, two of small size of approx. $23 \times 8 \text{ cm}^2$ and one real size of approx. $60 \times 60 \text{ cm}^2$. One row of triangular pads for each of the three detectors was read-out. Small detectors were operated on a surface of 12 rectangular pads (24 read-out channels) and the real size on 42 rectangular pads (84 read-out channels). All three detectors were

mounted parallel to each other and aligned relative to the operated rows. A combination of plastic scintillators and RPC detectors were used for triggers.

To estimate the position resolution for in beam conditions, single hit events on the operated area on all detectors were selected. The linear correlation of hit positions provide a measure of the position resolution between three identically read-outs. In order to estimate systematic effects the data sample was divided according to the position of the hit in the real sized prototype.

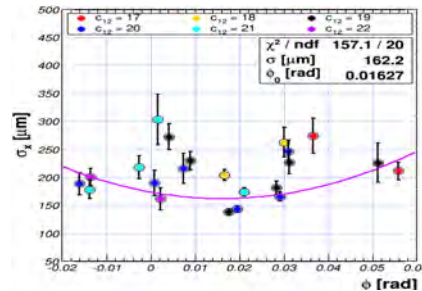


Figure 4: TRD resolution across pads as function of track inclination. Correlations generated by each real size TRD prototype pad column (c_i $i = 17, 24$) are emphasized by different colors and a parabolic fit to the data gives a resolution of $160 \mu\text{m}$ at normal incidence.

A summary of the position resolution measurements is presented in Fig. 4 for different track inclinations and different incident positions in the real size prototype. The σ_x correspond to the parameter/error of the Gauss fit to the experimental residual distributions. A parabolic fit is added to emphasize the track inclination dependence and the theoretical value at normal incidence of $\sim 160 \mu\text{m}$ across pads.

Conclusions

A detailed understanding of the TRD prototype was established for characterizing the position sensitivity of the detector. Close to real detector operation conditions show that the prototype, fulfilling design requirements, performs at least as good as requested as a tracking device. The novel pad-plane design adds up to these characteristics the possibility to perform 2D position sensitive measurements with a projected value of potentially halving the number of detection units in the final CBM set-up.

References

- [1] A. Bercuci et al., CBM Progress Report (2014) 81.
- [2] V. Cătănescu et al., CBM Progress Report (2009) 47.
- [3] V. Cătănescu et al., CBM Progress Report (2014) 82.
- [4] G. Caragheorgheopol et al., this report.
- [5] F. Constantin et al., CBM Progress Report (2014) 83.

Fe source measurements with CBM-TRD detector prototypes*

M. Kohn¹, C. Bergmann¹, M. Fehrenbacher¹, R. Berendes¹, N. Heine¹, P. Kähler¹, and J.P. Wessels¹

¹Institut für Kernphysik, Münster, Germany

Subsequent to the first ^{55}Fe source measurements with a CBM-TRD detector prototype and the SPADICv1.0 [1] / SysCore [2] / FLIB [3] data acquisition chain at GSI in 2014, we set up the necessary components in Münster to perform further measurements. The assembly and verification of the several components were also one of the main topics of a bachelor thesis (M. Fehrenbacher).

Overview on the setup in Münster

Only those components that can be deployed in beam time measurements were used. Even the grounding scheme was applied to be as close as possible to the grounding scheme used at the CERN-PS beam time in Nov./Dec. 2014. The gas system was kept to be as simple as possible. A flow of approx. 3 l/h was applied to the chamber. The chamber tightness was monitored by using an Orbisphere sensor for oxygen at the gas outlet of the detector. A premixed counting gas based on Ar/CO₂ (80/20) has been used for the following measurements. A combination of Wiener LV power supply modules and ISEG HV power supply modules has been used to operate the data acquisition-chain (LV) and MWPC module (HV). The data acquisition chain consists of one single SPADICv1.0 front end board connected to a SysCore board, which sends the data to the FLIB board in the computer.

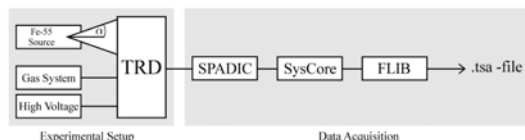


Figure 1: Overview of the experimental setup on the left side and the data acquisition on the right. The angle α illustrates that only a small spot of approx. 5 cm diameter on the chamber is illuminated by the ^{55}Fe source [5].

Lab measurements

Up to now, it was not possible to achieve a sufficient signal to noise ratio due to the low activity of the available ^{55}Fe source at Münster. Nevertheless, the gained knowledge on trigger settings and appropriate grounding scheme will be essential for future beam tests.

* Work supported by BMBF and HadronPhysics3, project financed by EU-FP7

Outlook

Exercising the full readout in the laboratory was very useful during the SPS beam time measurements in Nov. 2015 [4]. Several electronic components have been added to the DAQ chain (e.g. SysCore boards), so that we will be able to operate two independent DAQ chains in 2016. Furthermore, the feature freeze in SysCore firmware and in CBMnet part of the FLIB/FLES decreases immensely the complexity of hardware tests and measurements in the near future. The availability of the second DAQ chain now also enables the possibility to build a cosmic trigger setup using eventually an existing cosmic trigger using plastic scintillators in addition to ongoing ^{55}Fe source measurements.



Figure 2: View onto both sides of the CBM-TRD detector prototype. In the left picture the position of the collimated ^{55}Fe can be recognized. In the right picture the chamber is shown from the front-end electronic side. One pad group of two rows with each 16 channels is read out with a single SPADICv1.0 [5].

References

- [1] M. Krieger and P. Fischer, CBM Progress Report 2014, Darmstadt 2015, p.80.
- [2] J. Gebelein et al., *SysCore v3.1 – A universal Read Out Controller and Data Processing Board*, CBM Progress Report 2013, Darmstadt 2014, page 88.
- [3] D. Hutter and J. de Cuveland, *CBM FLES input interface developments*, CBM Progress Report 2014, Darmstadt 2015, p.101.
- [4] D. Emschermann et al., *Common CBM beam test at CERN SPS 2015*, this report.
- [5] M. Fehrenbacher, *Characteristics of a CBM Transition Radiation Detector*, Bachelor thesis, Münster 2015.

Construction of the first large prototypes for the CBM-TRD*

C. Bergmann¹, R. Berendes¹, N. Heine¹, P. Kähler¹, M. Kohn¹, J.P. Wessels¹, W. Amend², C. Blume², S. Gläsel², F. Roether², and D. Emschermann³

¹Institut für Kernphysik, Münster, Germany; ²IKF Frankfurt, Germany; ³GSI, Darmstadt, Germany

The institutes for nuclear physics at Frankfurt and Münster started the engineering and production process for the first four large TRD prototypes of type 8 with an outer dimension of $95 \times 95 \text{ cm}^2$. The delivered pad-plane segments are presented in Fig. 1.

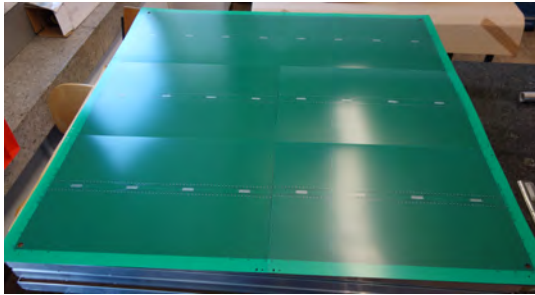


Figure 1: Pad-plane segments for type 8 detectors designed by D. Emschermann. This module type is foreseen to be used in the outer part of the TRD layers 1 – 4, where the charged particle rates will be lowest.

Since the outer dimensions of commercially available PCBs is of the order of $35 \times 50 \text{ cm}^2$ only, the pad-plane has to be subdivided into six pieces, two columns and three rows. The most demanding part of the chamber construction based on six pad-plane pieces is to ensure gas tightness at the segment borders and crossings. The back-panel production procedure is still under development. First demonstrator tests have been done in Frankfurt.

The TRD default design combines considerations developed during the last two small prototype generations [1]. Namely, all supports like gas, high voltage and signal read-out are applied from the back side of the module and the mechanical mounting of the detector is fully integrated within the chamber frame resulting in maximum acceptance. The PID-performance is maximized by minimizing the material budget between the active gas volume and the radiator by using a $25 \mu\text{m}$ aluminized Kapton foil. Gain variations due to pressure dependent foil deformation are minimized by an CF lattice structure. A cross section of one module is presented in Fig. 2.

The mechanical stability of the entrance window has been successfully tested in 2015 for small detector modules (results are presented in this report [3]). For the large modules these tests still have to be performed.

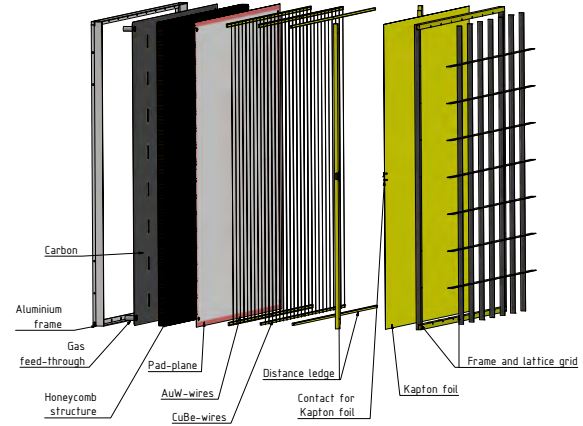


Figure 2: A chamber cross section is presented [2]. The back-panel of the module on the left is composed of a Kevlar honeycomb structure sandwiched between two layers of CF in an aluminum frame. The signals are read-out via a segmented PCB (pad-plane). The anode wires with a pitch of 2.5 mm are positioned in a distance of 3.5 mm relative to the pad-plane. The cathode wire plane follows the anode wire plane with a distance of 3.5 mm. The Kapton foil is separated from the cathode wire plane by 5 mm. The last component on the right side is the CF lattice structure.

The first building block, the back-panel, will be constructed in the institute IKP at Münster in spring 2016 together with colleagues from Frankfurt. The following production and gluing of the wire planes will be done at GSI or Frankfurt were the production of the entrance window is done at Münster. The finished Modules will be tested in beam at DESY in August and SPS November 2016.

References

- [1] C. Bergmann et al., *Test of Münster CBM-TRD real-size detector and radiator prototypes at the CERN PS/T9 beam line*, CBM progress report 2014, p.78.
- [2] The CBM Collaboration, *Technical Design Report for the CBM Transition Radiation Detector (TRD)*, to be published.
- [3] P. Kähler et al., *Stress-test of a MWPC prototype from Münster reproducing meteorologic pressure changes*, this report.

* Work supported by BMBF, HadronPhysics3 project financed by EU-FP7 and IP@WWU (<https://www.uni-muenster.de/IPID4all>)

CBM-TRD prototype tests in Frankfurt*

M. Tanha, C. Blume, J. Book, F. Roether, S. Gläsel, W. Amend, and E. Bechtel

Institut für Kernphysik, Goethe-Universität Frankfurt, Germany

Two new transition radiation detectors based on a thin Multi Wire Proportional Chamber (MWPC) without drift region have been developed at the Institut für Kernphysik in Frankfurt (IKF) for tests in a high rate beam. The prototypes have a dimension of $67 \times 67 \text{ cm}^2$ and a gas volume thickness of 4+4 mm and 5+5 mm (see Fig. 1). The former one was tested during a CERN-SPS beam test in November 2015. The prototype has wires with alternating high voltage (anode plane) as previous prototypes developed at IKF [1].

To sustain the high load at the CERN-SPS beam and to ensure the stability of the detector, 13 new high voltage cables are added to provide a more segmented high voltage supply to the detector. Applying an anode voltage of up to 1450 V, the prototype behaved normally and was operated stably during the high rate beam test (with varying beam intensities) at the CERN-SPS [2]. A first preliminary result is shown in Fig. 2.

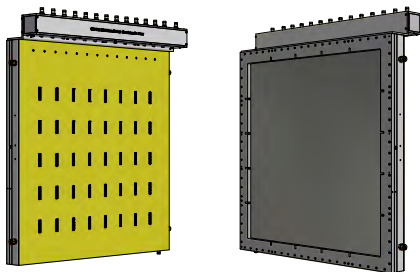


Figure 1: Schematic drawing of the prototype design showing the front (left) and rear view (right). The 13 HV connectors of the chamber are visible on the top.

The analysis of the data from the CERN-PS beam test in November 2014 progressed. A correction of the signal baseline and a noise detection and rejection has been implemented. After clusterization the pad response function has been determined from the corrected signals (see Fig. 3). During the 2014 PS beam test, a prototype with carbon frame ($58 \times 58 \text{ cm}^2$) and a gas volume thickness of 3.5+3.5 mm was used. This prototype was recently irradiated with a ^{55}Fe source in the laboratory and signals from raw data with different electronics configuration and different high voltages are being recorded. The energy resolution is currently being analyzed from a ^{55}Fe source spectrum.

A large-size ($95 \times 95 \text{ cm}^2$) prototype is currently under construction at the IKF and the IKP in Münster [3].

* Work supported by BMBF, HIC4FAIR and HGS-HIRE.

These large chambers are foreseen for the outer regions of the final detector setup, where the hit densities are lower. It is planned to test the performance of this prototype in upcoming beam times. To investigate the performance of the large size prototype, and test the new electronic read out, a participation in an electron beam test at DESY in Hamburg is planned.

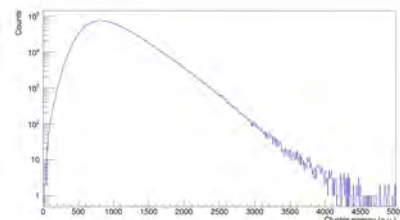


Figure 2: Uncalibrated energy spectrum for three and four-pad clusters as measured at the CERN-SPS in 2015.

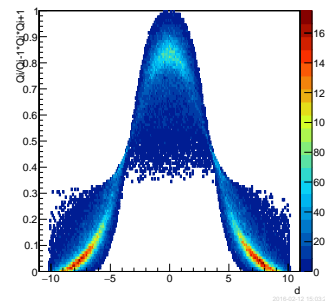


Figure 3: Pad response function as obtained from the data measured at the CERN-PS in 2014.

References

- [1] M. Tanha et al., *Construction and test of a new CBM-TRD prototype in Frankfurt*, CBM Progress Report 2014, Darmstadt 2015, p 79.
- [2] C. Bergmann et al., *Combined MWPC prototype test of Münster and Frankfurt using SPADICv1.0 data taking at CERN-SPS/T2-H4 in 2015*, this report.
- [3] C. Bergmann et al., *Construction of the first large prototypes for the CBM-TRD*, this report.

Test of SPADICv1.0 readout on Bucharest CBM-TRD detector prototypes*

M. Kohn¹, A. Bercuci², C. Bergmann¹, R. Berendes¹, N. Heine¹, P. Kähler¹, M. Petris², M. Petrovici², C. Schiaua², and J.P. Wessels¹

¹Institut für Kernphysik, Münster, Germany; ²IFIN-HH, Bucharest, Romania

After successful measurements with TRD chambers from Münster and Frankfurt using SPADICv1.0 [1] in the laboratories as well as in the beam tests of 2014, the next step was to test the SPADIC v1.0 chip on the Bucharest TRD prototypes which was not done before. Signal connectors for the SPADIC were already foreseen. Having a common data acquisition for all three types of chambers opens the possibility to make directly comparable measurements in further beam tests with all the detectors from the different laboratories.

Lab measurements

During a two week visit at IFIN-HH laboratory in Bucharest a running SPADIC v1.0 DAQ chain with SysCore v3.1 [2] and FLIB [3] was assembled. For the TRD chamber, a small size prototype from 2011 was used [4]. The main difference to the Frankfurt and Münster prototypes is the geometry of the readout pads, which is of triangular and not rectangular shape. For signal generation a ⁵⁵Fe source was installed near the pad plane (see Fig. 1).

Beam time measurements

The SPS beam time in 2015 was used to reassemble the setup used in Bucharest in order to obtain results in a high multiplicity environment like at SIS100 conditions. For the position of the chambers in the experimental cave a close distance to the lead target was chosen. The SPADIC was mounted on the first Bucharest TRD chamber, as presented in Fig. 2 (see also [4, 5]).

Results and Outlook

It was proven that the SPADIC readout is working with the Bucharest TRD prototype. Further analysis of the recorded data will follow. In the future, it will also be possible to use SPADIC readout for the real size prototype of Bucharest. I would like to thank the whole NIHAM Group; especially G. Caragheorghopol and A. Radu for the mechanical infrastructure.

References

- [1] M. Krieger and P. Fischer, CBM Progress Report 2014, Darmstadt 2015, p.80.

* Work supported by BMBF, HadronPhysics3 project financed by EU-FP7 and IP@WWU (<https://www.uni-muenster.de/IPID4all>)

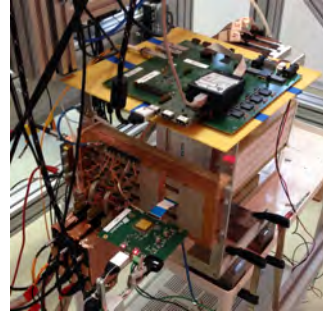


Figure 1: Overview of the setup, consisting of the SysCore placed on top and the single SPADIC front end board mounted to the central pad group of the chamber. On the left side of the SPADIC, the FASP readout electronic is mounted. Behind the TRD chamber is the ⁵⁵Fe source positioned - not visible from this perspective. The DAQ computer with FLIB interface is also not shown.



Figure 2: Side view on the setup used at CERN-SPS. The TRD prototype is rotated by 180° in comparison to Fig. 1 and also the SPADIC is mounted tilted by 90°, so that only the back side of the front-end board is visible.

- [2] J. Gebelein et al., *SysCore v3.1 – A universal Read Out Controller and Data Processing Board*, CBM Progress Report 2013, Darmstadt 2014, page 88.
- [3] D. Hutter and J. de Cuveland, *CBM FLES input interface developments*, CBM Progress Report 2014, Darmstadt 2015, p.101.
- [4] A. Bercuci et al., *Calibration and in-beam operation of the two-dimensional MWPC prototype for CBM-TRD*, this report.
- [5] D. Emschermann et al., *Common CBM beam test at CERN SPS 2015*, this report.

Stress-test of a MWPC prototype from Münster reproducing meteorologic pressure changes*

P. Kähler¹, F. Fidorra¹, R. Berendes¹, C. Bergmann¹, N. Heine¹, M. Kohn¹, and J.P. Wessels¹

¹Institut für Kernphysik, Münster, Germany

The entrance window confining the active MWPC gas volume of the CBM-TRD detectors are projected [1] to be built from aluminium-coated foils of Kapton®. Since the detector gas system is closed towards the surrounding atmosphere, changes of the absolute outer pressure will stress especially the foil window. The results shown in this report are obtained in the recent Bachelor project of F. Fidorra [2], employing a self-constructed ARDUINO®-controlled gas system on a real-size TRD prototype.

Flow resistance of a real-size prototype

The measured pressure drop across the chamber is shown in Fig. 1. A realistic flow of 3 l/h leads to a pressure drop of (0.16 ± 0.02) mbar, which allows to operate up to five chambers in one sequential gas line. We assume the main contributions to this flow resistance to be turbulence effects in a T-connector splitting before the chamber and the used elbow connectors at the two chamber inlets. Both components can be changed in future prototypes. Implications of the test are considered in the ongoing development.

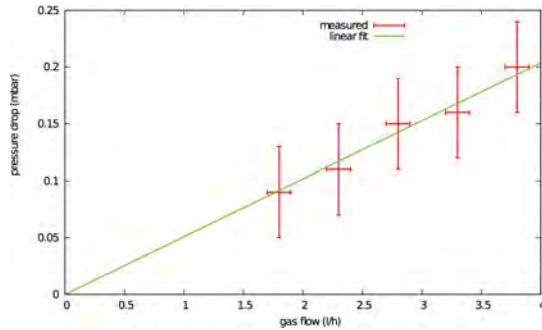


Figure 1: Pressure drop across one chamber prototype and its T-shape split supply line in dependence of the total gas flow. The linear fit is required to be offset-free and yields a slope of (0.054 ± 0.005) mbar h^{-1} .

Stress-testing a real-size prototype in atmospheric pressure changes

Oxygen and/or humidity will significantly quench the gas amplification in the detector volume. Thus, the reliability of the entrance window in terms of gas tightness is mandatory to reliably operate the CBM-TRD. We analysed meteorologic measurements of a local climatology

* Work supported by BMBF, HadronPhysics3 project financed by EU-FP7 and IP@WWU (<https://www.uni-muenster.de/IPID4all>)

group [3]. Pressure changes within a representative time of half a year are shown in Fig. 2. Upper limits of these changes have been applied to the chamber prototype, as e.g. shown in Fig. 3. A simulated time of one year did not effect any measurable change in the tightness of the entrance window against ambient oxygen.

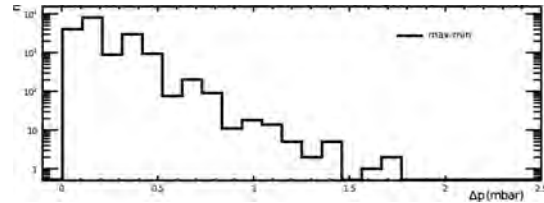


Figure 2: Atmospheric pressure changes within half a year. Counted as maximum differences within 10 min. time intervals.

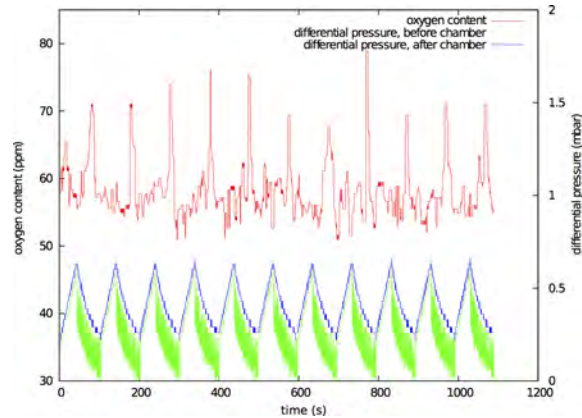


Figure 3: Example from the applied stress procedure. The lower curves show the pressure relative to environment before and after the chamber, while the upper red curve displays the monitored oxygen content of the detector gas.

References

- [1] The CBM Collaboration, *Technical Design Report for the CBM Transition Radiation Detector (TRD)*, to be published.
- [2] F. Fidorra, *Aufbau und Charakterisierung eines Gassystems für den CBM TRD*, Bachelor thesis, September 2015, Westfälische Wilhelms-Universität Münster.
- [3] O. Klemm et al., Mail exchange (May 2015), Climatology working group, Westfälische Wilhelms-Universität Münster.

First performance studies for FASP-02*

G. Caragheorghopol¹, D. Bartoș¹, A. Bercuci¹, V. Cătănescu¹, F. Constantin¹, M. Petriș¹, and M. Petrovici¹

¹IFIN-HH, Bucharest, Romania

The Fast Analog Signal Processor (FASP) [1] is an ASIC designed for the TRD prototype [2] developed for the CBM experiment. It is designed to access the special features of this detector in a free running mode with optimum ratio between data output and detector tracking/PID capabilities. The branding features of FASP are independent channel processing and Flat-Top (FT) output. The second version of the chip [3] comes with an elaborated control interface and pad pairing for robust output.

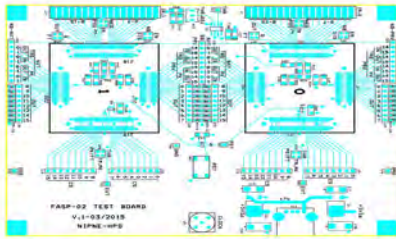


Figure 1: FASP-02 test board.

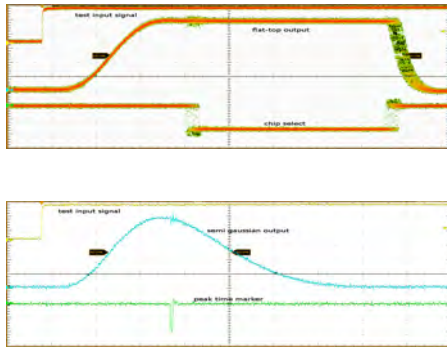


Figure 2: Characteristic FASP-02 signal output on step input. Flat-Top (FT) / Chip-Select (CS) (top) and semi-Gaussian / peak-time-marker (bottom).

Electronic and ^{55}Fe tests

The test-board (see Fig. 1) provides housing and chaining functionality for two FASP-02 chips with test points for output and Chip Select (CS) signals. Configurable features like *input signal polarity*, *output shaping*, *trigger* and

* Work supported by Romanian ANCSI/CAPACITATI Modul III Contract F02 and NUCLEU Project Contract PN 09370103.

neighbor wake-up and a 32 MHz clock mounted on the board, control the chips.

In Fig. 2 (top plot) the input, FT and CS signals are shown. The CS signal lasts for 14 CLK to match the free running ADC convertor. A $1/2$ CLK (15 ns) jitter of the CS is inherent. If FT is inhibited, the semi-Gaussian output (Fig. 2 (bottom plot)) is produced. Configurable time-markers are generated at the threshold or at the peak (as in the figure) for further processing.

A mother-board with one chip on it was further build to operate the FASP-02 on detector/DAQ. Gain calibration/uniformity was performed for the TRD operated with FASP-02 [4] with very good results.

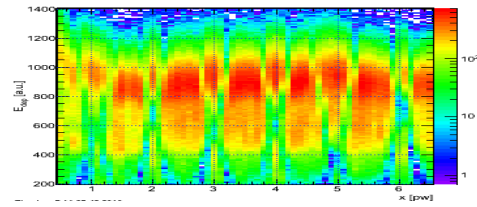


Figure 3: Energy-position reconstruction for a uniform ^{55}Fe illumination of the TRD operated with FASP-02.

An area of approx. $6 \times 8 \text{ cm}^2$ was uniformly illuminated with a ^{55}Fe source and the position across pads (x in pad width [pw]) and energy was reconstructed for each hit as presented in Fig. 3. A DAQ trigger was generated by FASP-02. The results show a good uniformity over the operated area with discontinuities close to pad centers due to missing under-threshold signals. The *neighbor wake-up* feature of FASP-02 is meant to cure this problem.

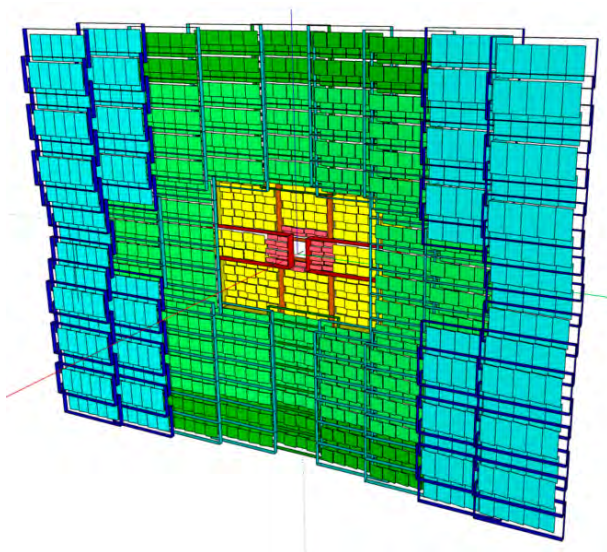
Conclusions

Preliminary tests of the FASP-02 produced very promising results. Besides curing the problems observed for FASP-01, the new chip comes with an externally controlled interface which is mandatory for fine tuning TRD prototype design for CBM running conditions.

References

- [1] V. Cătănescu et al., CBM Progress Report (2009) 47.
- [2] A. Bercuci et al., CBM Progress Report (2014) 81.
- [3] V. Cătănescu et al., CBM Progress Report (2014) 82.
- [4] A. Bercuci et al., this report.

Time-of-Flight Detector



Narrowing down the MRPC design with heavy-ion beams at CERN/SPS *

C. Simon¹, I. Deppner¹, N. Herrmann¹, A. Akram¹, E. Bao¹, J. Frühauf², M. Kiš², P.-A. Loizeau², P. Weidenkaff¹, and the CBM ToF working group¹

¹Ruprecht-Karls-Universität Heidelberg, Heidelberg, Germany; ²GSI, Darmstadt, Germany

By the end of 2016, the ToF working group plans to freeze the design of their MRPC prototypes for mass-producing detector components to be used in the actual CBM setup. Therefore, the in-beam performance of prototypes needs to be evaluated against—not limited to—the criteria formulated on detection efficiency ($> 95\%$), system time resolution (< 80 ps) and rate capability (from 1 to several tens of kHz/cm^2 , depending on the foreseen module position in the ToF wall). To get the full picture, conditions at test-beam facilities should reflect the SIS100 environment as closely as possible, i.e. should allow for a flood illumination of the detector surfaces with particle fluxes of $10 \text{ kHz}/\text{cm}^2$ and above. Such realistic conditions can only be achieved by heavy-ion beams impinging on a dedicated target creating secondary particles at small angles and high track densities.

As in October 2014 at GSI/SIS18 [1][2] particle fluxes of only several hundreds of Hz/cm^2 could be reached and GSI accelerators were not available in 2015, the ToF working group decided to continue their prototype testing efforts at CERN/SPS in February and in November 2015. Since 2011 CBM is a CERN recognized experiment under the name RE21. ToF and TRD working groups of CBM jointly operated their prototypes in a dedicated concrete cave (dimensions: $2.6 \text{ m} \times 2.4 \text{ m} \times 9.6 \text{ m}$) at the H4 beam line of the North Area. While in February 13.4 GeV Ar ions hit a Pb target, the November beam consisted of 30.4 GeV Pb ions which is close even to SIS300 conditions. Particle fluxes of a few kHz/cm^2 were observed on the detectors under test.

In the February in-beam test, the ToF working group essentially extended the measurement program of the prototypes already tested in the October 2014 beam time to higher particle fluxes. Prototype designs were not modified. Based on these results, for November, the group agreed on systematically assessing certain MRPC engineering design aspects by developing a set of new prototypes differing from each other only by single components. This way, an unbiased evaluation of the following questions was aimed at:

- single HV stack or double HV stack
- impedance matching to the front-end electronics
- design of the high-voltage electrode
- benefits of gas-tight designs (sealing)

* This project was partially funded by BMBF 05P12VHFC7 and by EU/FP7-HadronPhysic3/WP19 and has received funding from the European Union's Horizon 2020 research and innovation program under grant agreement No 654168.

As the data analysis is ongoing, final conclusions cannot be drawn yet.

Figure 1 depicts the setup during the November campaign comprising 20 MRPC detectors including 10 newly developed ones. Several boxes housing the counters are visible. The beam enters the setup from the right side. The target was placed about 4 m in front of the setup. The setup is arranged in two levels (cf. Fig. 2), one above the beam height of 1.2 m, one below. Foreseen for the higher-rate regions of the ToF wall, the prototypes on the lower level are positioned closer to the beam and exposed to a three times higher particle flux than the detectors on the upper level. The counters on both levels are arranged in several detection stations (8 on the upper level, 7 on the lower level) to allow for charged-particle tracking. The properties of the prototypes can be studied in much greater detail if single detector hits can be matched to global particle tracks. The lower-rate counters numbered #2, #3 and #4 in Fig. 2 are equipped with resistive plates made of float glass. The prototypes numbered #14 use ceramics as resistive material to withstand the rate conditions close to the beam pipe [3]. All other counters contain low-resistive glass from China as electrodes.

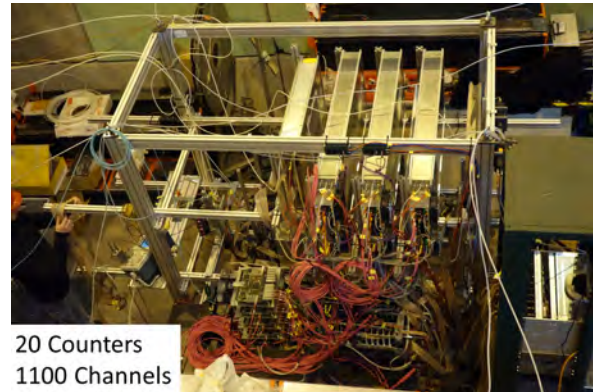


Figure 1: CERN November 2015 setup photography. The beam enters the setup from the right side.

An offline event display of the setup is shown in Fig. 3. The detection stations of the upper and lower levels are marked in pink. Red dots symbolize hits on a counter's active area. Hit-to-track matching with different detection stations leads to the extrapolated track lines. In this event, the tracking algorithm found several tracks which, however, cannot be shown all for readability reasons. Only

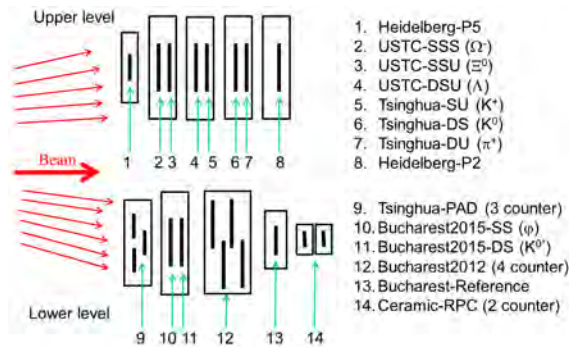


Figure 2: CERN November 2015 setup sketch. Lower-rate prototypes sit on the upper level, higher-rate prototypes on the lower.

tracks with hit multiplicities of 5 (lower pink line), 7 (green lines) and 8 (upper blue line) are visualized.

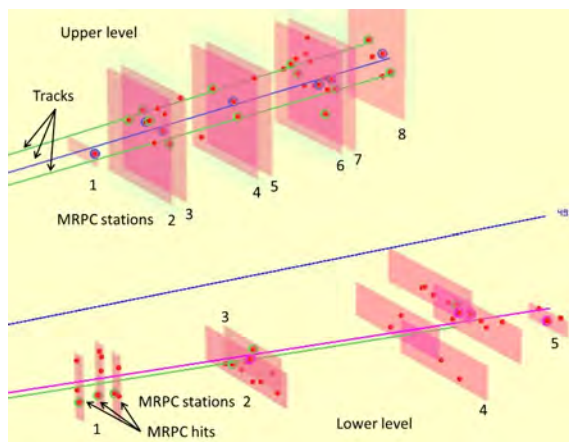


Figure 3: Exemplary event display of the CERN November 2015 setup showing fitted particle tracks with 8 (blue) and 7 (green) associated hits.

Complementing the MRPC prototype studies, two 16-strip pcCVD-DDs [4] (polycrystalline Chemical Vapor Deposition diamond detector) and a 4-segment mosaic scCVD-DD [5][6] (single crystalline) were placed in beam for trigger purposes and to improve the tracking of particles in the MRPC setup.

Signal arrival time digitization was based on a 32-channel FPGA-TDC [7] residing on front-end cards (CBM-TOF-FEE) hooked up in close vicinity to the MRPCs. The readout process took place via TRB3 [8] data hubs. Analog MRPC signals of most prototypes under test were preamplified and discriminated by the final iteration of the PADI ASIC [9]. In total, more than 1000 electronics channels (1 % of the final ToF channel count) were successfully operated during the beam time. The data taking period was about 4 days. In total, about 1 TByte of data were acquired.

First preliminary results are presented in Figure 4. It shows the time difference spectrum between the counters

Bucharest2015-SS and *Bucharest2015-DS* (numbered #10 and #11 in Fig. 2). The width (Sigma) of a Gaussian fit (red line) denotes the time resolution of this system which amounts to 84 ps. The single counter resolution including all electronic contributions can be obtained by dividing the system time resolution by the square root of 2 assuming both counters contribute equally. By comparing the time resolutions obtained with different such MRPC pairs the individual counter resolutions can be teased out. In order to get an estimate of the distribution tails the RMS value can be compared to the Gaussian sigma. In Figure 4, these two quantities are very similar.

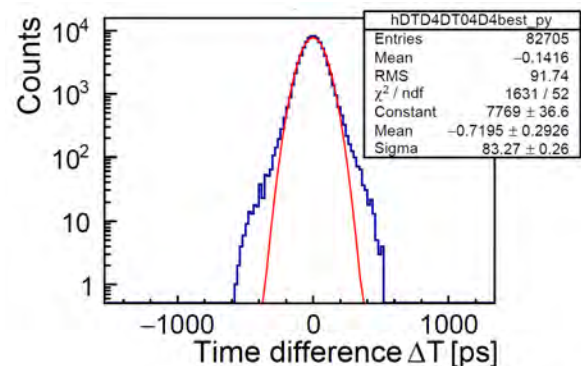


Figure 4: Time difference spectrum between the *Bucharest2015-SS* and the *Bucharest2015-DS* prototypes. The Gaussian sigma and the histogram's RMS are very similar.

References

- [1] I. Deppner et al., “MRPC performance evaluation in a heavy ion beam test at GSI”, CBM Progress Report 2014 (2015) 86
- [2] M. Petriș et al., “Performance of MGMSRPC for the inner zone of the CBM-TOF wall in heavy ion beam tests”, CBM Progress Report 2015 (2016)
- [3] R. Sultanov et al., “Progress in Ceramic RPCs for the Beam Fragmentation T0 Counter”, CBM Progress Report 2015 (2016)
- [4] F. Schirru et al., “Development of large area diamond detectors for time-of-flight measurements of heavy ions”, GSI Scientific Report 2014 (2015) 502
- [5] J. Pietraszko et al., “Low-purity IIa scCVD diamond material for high-current heavy-ion experiments in FAIR”, GSI Scientific Report 2014 (2015) 31
- [6] J. Pietraszko et al., “High-resolution tracking based on scCVD diamond detector for straw tube detector tests”, GSI Scientific Report 2014 (2015) 32
- [7] C. Ugr et al., “FPGA based multi-channel TDC development”, GSI Scientific Report 2014 (2015) 212
- [8] M. Traxler et al., “Applications of the TRB3 and Associated Front End Electronics in Recent Beam Times”, GSI Scientific Report 2014 (2015) 514
- [9] M. Ciobanu et al., “PADI-8 – a new ASIC prototype for the CBM ToF Wall”, CBM Progress Report 2013 (2014) 84

Performance of Strip-MRPC for CBM-TOF in beam test*

P. Lyu¹, Y. Wang¹, X. Huang¹, D. Han¹, B. Xie¹, Y. Li¹, N. Herrmann², I. Deppner², C. Simon², P. Loizeau², P. Weidenkaff², J. Frühauf³, and M. Kis³

¹Department of Engineering Physics, Tsinghua University, Beijing, China; ²Physikalisches Institut, Heidelberg University, Heidelberg, Germany; ³GSI, Darmstadt, Germany

For the Time-of-Flight system (TOF) of the CBM experiment MRPCs will be used aiming at an unprecedented precision of hadron identification by benefiting from its excellent time resolution and high detection efficiency as well as from low construction costs. Different types of MRPCs will come into application based on the expected particle flux rate distributions [1]. We have developed a double-ended readout Strip-MRPC towards the counter type *MRPC3a*.

Since CBM-TOF requires a rate capability up to 30 kHz/cm², a newly developed low resistive glass is applied for the prototype to keep the excellent time resolution. The Strip-MRPC has 24 strips per counter, each strip is 270mm long, 7mm wide and the gap between strips results to 3mm. The differential double stack structure of 2x4 gas gaps helps to reduce the required high voltage. Each gas gap has a width of 250μm, the ground is placed onto the MRPC readout electrodes and the feed through is carefully designed to match the 100Ω impedance of the PADI electronics, shown in fig. 1.

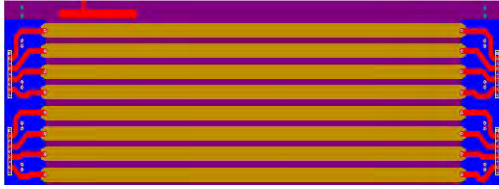


Figure 1: Strip-MRPC's readout PCB: strip and feed through are designed for a 50Ω impedance. The differential combination of two readout PCBs matches the 100Ω impedance of the PADI electronics.

This strip prototype has been tested in the 2014 October GSI beam test with a 1.1A GeV ¹⁵²Sm beam. The detailed layout is described in [3], the Strip-MRPC is located in the lower part of the setup together with HD-Ref counter, where a counting rate of a few 100 Hz/cm² was achieved.

The calibration of Strip-MRPC is done within the CBM-ROOT framework, developed by TOF Group. We choose the HD-Ref counter as reference counter to calibrate with, and diamond detector as start counter for events. Time-walk correction, gain correction, strip alignment correction and velocity correction are taken into consideration in the process of calibration in an iterative fashion. The

results with respect to Time-over-Threshold(TOT) and velocity dependence are shown in Fig. 2.

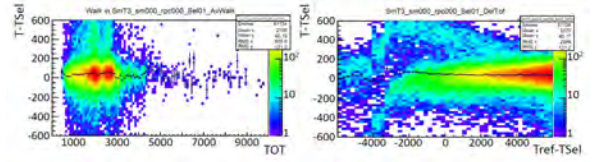


Figure 2: TOF calibration results with TOT (left) and particle velocity (right) in Strip-MRPC at a HV of 5500V.

The results are shown in Figs. 3 and 4. The efficiency stays at 97%, and the cluster size always maintains a low value of 1.6. Assuming an equal performance with the reference counter we get a time resolution of the Strip-MRPC around 50ps.

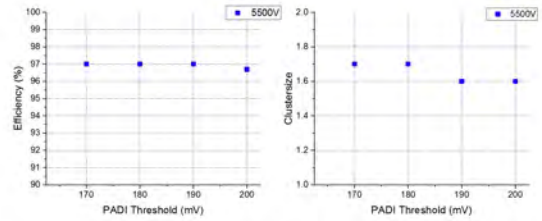


Figure 3: Efficiency (left) and cluster size (right) as a function of PADI threshold from 170mV to 200mV when working at 5500V HV.

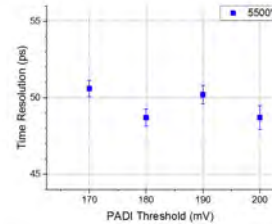


Figure 4: Time resolution of Strip-MRPC prototype as a function of PADI threshold from 170mV to 200mV when working at 5500V HV.

References

- [1] Technical Design Report for the CBM Time-of-Flight System (TOF) - GSI-2015-01999
- [2] Wang Jingbo, et al. Nucl. Instr. and Meth. A713 (2013) 40.
- [3] I. Deppner, et al. CBM Progress Report 2014, 86.

* This work is supported by the National Natural Science Foundation of China under Grant No.11420101004, 11461141011, 11275108. This study is also supported by the Ministry of Science and Technology under Grant No. 2015CB856905.

A prototype of pad-readout MRPC towards CBM-TOF*

P. Lyu¹, Y. Wang¹, X. Huang¹, D. Han¹, B. Xie¹, Y. Li¹, N. Herrmann², I. Deppner², C. Simon², P. Loizeau², P. Weidenkaff², J. Frühauf³, and M. Kis³

¹Department of Engineering Physics, Tsinghua University, Beijing, China; ²PI, Heidelberg University, Heidelberg, Germany; ³GSI, Darmstadt, Germany

Towards CBM-TOF's requirement of high rate capability, a pad-readout MRPC applying low resistive glass is developed. The Pad-MRPC has 6x2 pads of size 2cmx2cm each, with an interval between pads of 2 mm (occupancy smaller than 5%). It applies the double stack structure of 2x5 gas gaps. Compared to Strip-MRPC, the pad readout is designed for fewer electronics channels and smaller cluster size. Aiming at the inner region of the TOF wall, we've designed a supermodule which could be a small part of the future inner wall, containing 3 overlapped MRPC to eliminate the dead area between the counters.

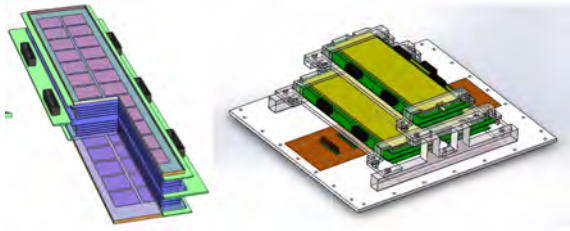


Figure 1: Structure of 6x2 Pad-MRPC (left) and super module with 3 counters (right).

A cosmic test system was set up to test the performance of the pad-MRPC supermodule. The time reference is given by a plastic scintillator readout by photomultiplieres (PMT). Fig. 2 shows the timing difference between the tested module MRPC1 and the PMT reference. Each bin represents 25 ps and the PMT reference timing resolution is 62 ps. Fig. 3 summarizes the performance of these 3 MRPC modules studied in the cosmic test.

In order to further examine the performance of this supermodule working under higher particle flux, it has been tested in the 2014 October GSI beam time using the secondary particles from a ¹⁵²Sm beam hitting a Pb target. The layout of the beamtest is described in [2]. The pad MRPC modules and a thin strip MRPC module BucRef are the target detectors in the upper part of the setup. Based on strategy implemented in the common TOF - CBMROOT framework, an independent code is developed for calibration of the Pad-MRPC by the Tsinghua group. In this code, the pad MRPC and BucRef are used to calibrate each other, and the diamond detector is used as a second reference. Several correction steps are coded. Velocity correction is

* This work is supported by the National Natural Science Foundation of China under Grant No.11420101004, 11461141011, 11275108. This study is also supported by the Ministry of Science and Technology under Grant No. 2015CB856905.

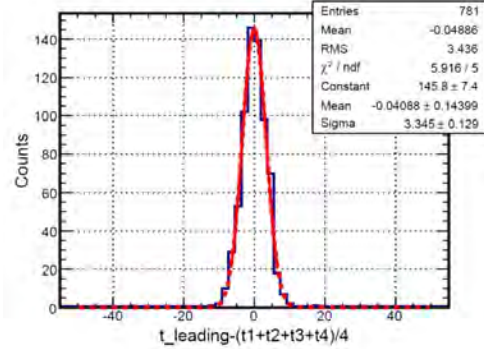


Figure 2: The timing difference between tested module MRPC 1 and PMT timing reference. The solid curves are Gaussian fit to the distribution to obtain the total MRPC+ref timing resolution.

Module	Efficiency	Timing resolution	Dark rate	Cluster size
MRPC1	98.4%	56.1 ps	0.57 Hz/cm ²	1.23
MRPC2	98.6%	58.7 ps	0.53 Hz/cm ²	1.30
MRPC3	98.2%	63.3 ps	0.61 Hz/cm ²	1.27

Figure 3: Performance of Pad-MRPC prototype for CBM-TOF in cosmic test.

the first to be carried out, and Fig. 4 provides an example of it: $\Delta T = \text{tdc}_{\text{BucRef}} - \text{tdc}_{\text{Pad}}$ is evaluated versus $\Delta T_{\text{dia}} = \text{tdc}_{\text{BucRef}} - \text{tdc}_{\text{Diamond}}$, and the Gaussian means of each ΔT_{dia} bin are fitted with a piecewise function. By subtracting this value, the velocity dependence is removed from the timing difference.

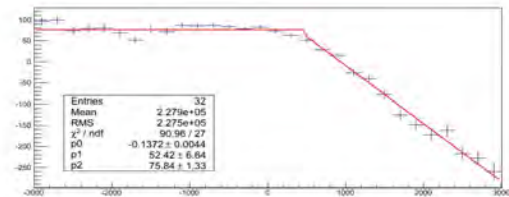


Figure 4: An example of velocity correction curve: the Gaussian mean $\Delta T = \text{tdc}_{\text{BucRef}} - \text{tdc}_{\text{Pad}}$ as a function of $\Delta T_{\text{dia}} = \text{tdc}_{\text{BucRef}} - \text{tdc}_{\text{Diamond}}$. This curve is a piecewise function fit to the data points.

Another correction step taken into consideration is the

slewing correction, also called walk correction. It removes the ΔT dependence caused by the signal amplitude. Fig. 5 shows an example of slewing correction: ΔT is shown as function the time over threshold (TOT) of the MRPC output signal, which is a good representative for the signal amplitude. In the plot, the Gaussian means of each TOT bin are fitted with a 3^{rd} -order polynomial. The slewing correction is done by subtracting this 3^{rd} -order polynomial, both for Pad-MRPC and BucRef. After all corrections, we can get a Gaussian fit to ΔT distribution in Fig. 6, showing a system time resolution of 95ps for Pad-MRPC and BucRef resulting in $95\text{ps}/\sqrt{2} = 67\text{ps}$ for single detector. The efficiency is calculated within the CBMROOT framework, and for this dataset is 98.2%.

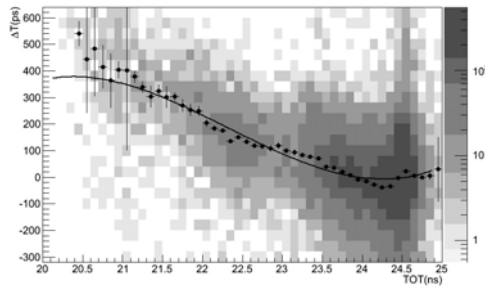


Figure 5: An example of slewing correction curve, the Gaussian mean ΔT as a function of TOT. The curve is a third order polynomial fit to the data points.

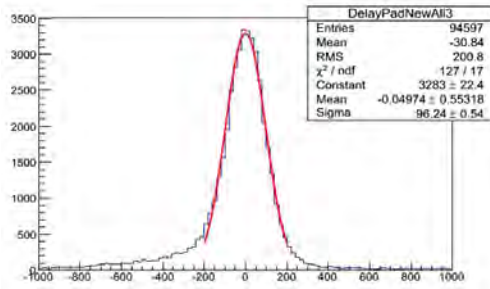


Figure 6: The ΔT distribution after all corrections. The curve is a Gaussian fit to the distribution to obtain the system timing resolution of Pad-MRPC and BucRef.

The data is also used to build clusters to measure the crosstalk in chambers. Connected fired pads are required in cluster construction, and the resulting average cluster size we get for Pad-MRPC is 1.78.

The same prototype has been tested at the Nuclotron in JINR at Dubna in 2013, however, the time resolution of Pad-MRPC is 45ps at that time [3]. In order to clarify this difference, we define a single-hit event for Pad-MRPC/BucRef as there is only one pad/strip fired in this event. As is shown in Fig. 8, the time resolution doesn't improve much when choosing single-hit event for Pad-

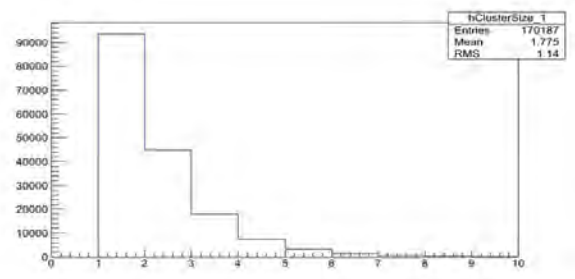


Figure 7: Cluster size distribution of pad MRPC.

MRPC. When cutting other events despite single-hit for BucRef, the time resolution improves to 89ps. Finally, only single-hit event is chosen for both two counters, and this system resolution improves a little to 87ps. With better reference, the Pad-MRPC module gets an enhancement on time resolution. In next step, we will introduce clusterisation to combine the fired strips in BucRef (average hit multiplicity is around 3) to a cluster, which will improve the system time resolution in analysis of all events.

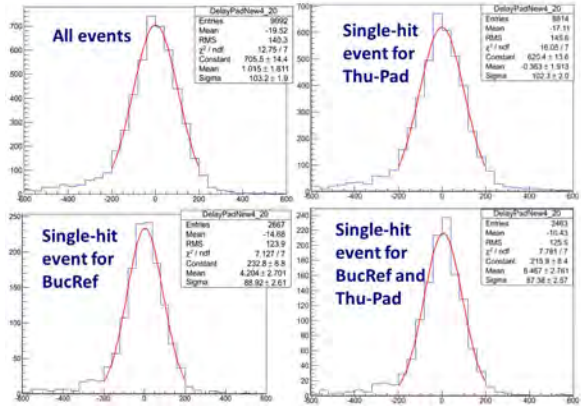


Figure 8: The ΔT distribution of single-hit event study. The time resolution changes not much when choosing single-hit event for Pad-MRPC, but improves much when choosing single-hit event for BucRef. The relatively worse time resolution for all events is due to a missing of clusterisation of fired strips in BucRef, and this will be resolved in next working steps.

All these results show that the real-size Pad-MRPC prototype is fully capable of the requirement of the CBM-TOF.

References

- [1] Wang Jingbo, et al. Nucl. Instr. and Meth. A713 (2013) 40.
- [2] I. Deppner, et al. CBM Progress Report 2014, 86.
- [3] W. Zhu, et al. Sci China Tech Sci, Vol.56 (2013) 11.
- [4] Y. Wang, et al. Nucl. Instr. and Meth. A661 (2012) 134.
- [5] I. Deppner, et al. Nucl. Instr. and Meth. A661 (2012) 121.

Performance of MGMSRPC for the inner zone of the CBM-TOF wall in heavy ion beam tests *

M. Petriş¹, D. Bartoş¹, G. Caragheorgheopol¹, I. Deppner³, V. Duţă¹, J. Frühauf², N. Herrmann³, M. Kiš², P.-A. Loizeau², M. Petrovici¹, L. Rădulescu¹, V. Simion¹, and C. Simon³

¹NIPNE, Bucharest, Romania; ²GSI, Darmstadt, Germany; ³PI, Heidelberg University, Germany

Two in-beam tests using heavy ion induced reactions were focused on the counter behavior in high counting rate and multiplicity environment. The first one, carried out at GSI in October 2014, with a Sm beam of 1.1 A GeV was followed by a CERN SPS beam time in February 2015 with an Ar beam of 13 A GeV. In both cases the experimental setup was divided in "low rate" and "high rate" arms, the last one being positioned at polar angles of a few degree relative to the beam axis. The detector under test [1, 2], called Buc2013, was positioned in the "high rate" setup. A narrow strip MGMSRPC, called BucRef, described in [3, 4] and positioned behind the detector under test was used as time reference. Both of them were sandwiched between two plastic scintillators for rate estimates. A diamond detector positioned in front of the target was used as beam reference. The signals delivered by Buc2013 prototype were processed by a new front-end electronics (FEE), called PADI8 [5], developed within the CBM-TOF collaboration. For BucRef an older version of PADI, called PADI3, was used in the GSI beam time and PADI8 FEE in CERN SPS beam time. The digital conversion of the LVDS signals was performed by FPGA based TDCs [6].

An overview of the October 2014 setup is presented in [7]. The "high rate" setup was positioned at ~ 7 degree relative to the beam line. However, the measured particle flux for this setup did not exceed 1 kHz/cm^2 . The steps followed in the data analysis, based on cbmroot software, are comprehensively described in [7].

The efficiency obtained with Buc2013 as a function of the PADI8 thresholds for two applied high voltages ($\pm 5.5\text{ kV}$ and $\pm 5.6\text{ kV}$), corresponding to 157 kV/cm and 160 kV/cm electric field, respectively, is shown in Fig. 1 (left side). The efficiency is estimated as the ratio of the number of matched hits between Buc2013, BucRef and diamond detector and the number of matched hits between BucRef and diamond detector. A value larger than 98% is still observed at the largest value of the threshold used in these measurements, of 240 mV. The statistical errors are within marker size. Figure 1 - right side presents the mean cluster size (consecutive fired strips in a hit) as a function of FEE threshold, for the two mentioned applied high voltages (HV). One can see the expected behavior of decreasing of the cluster size with the increase of the threshold. At the highest applied threshold (240 mV) the mean cluster size value is of 3 strips. As it was already shown in reference [3], this gives the possibility to reconstruct the posi-

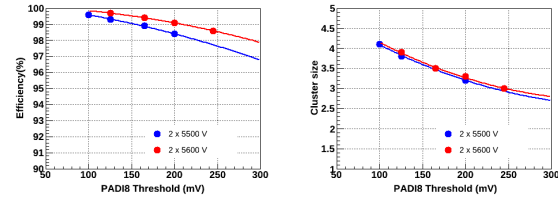


Figure 1: Efficiency(left side) and cluster size (right side) as a function of PADI8 threshold at two applied HV ($\pm 5.5\text{ kV}$ and $\pm 5.6\text{ kV}$).

tion across the strip with a position resolution better than the one based on the pitch size, in addition to the position information along the strip (obtained from the difference of the times measured at the both ends of the strip). In a

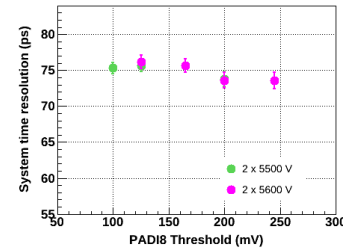


Figure 2: System time resolution as a function of PADI8 threshold at two applied HV ($\pm 5.5\text{ kV}$ and $\pm 5.6\text{ kV}$).

collision event, multiple hits can occur on the counter surface. In the performed analysis, the time of flight (TOF) spectrum was obtained as the time difference of the best correlated clusters/hits in time and space (χ^2) in Buc2013 and BucRef. In addition to the slewing effect correction, the TOF information was corrected for reaction product velocity spread and hit position. The system time resolution, presented in Fig. 2 for each value of the PADI8 thresholds, improves slightly with the increasing threshold, the best value results to $74\text{ ps} \pm 1\text{ ps}$ including the contribution by electronics.

Figure 3 presents the time resolution as a function of cluster size. The best time resolution is obtained for events with three or four strips in a cluster due to the larger amplitude of these signals. The system time resolution as a function of hit multiplicity is presented in Fig. 4. As it is expected, the best time resolution of 70 ps is obtained for single hit events, a slight increase with the hit multiplicity in Buc2013 prototype is being observed for multiple hits.

In February 2015 the same detectors were tested at

* Romanian NASR/contract RO-FAIR F02 and NASR/NUCLEU Project PN09370103

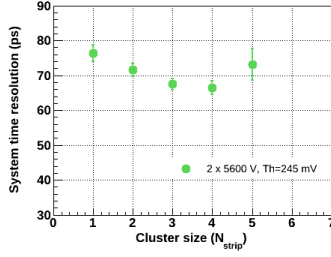


Figure 3: System time resolution as a function of cluster size of Buc2013 (± 5.6 kV HV, 245 mV threshold).

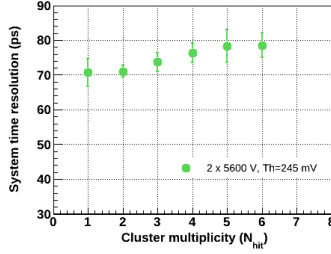


Figure 4: System time resolution as a function of hit multiplicity in Buc2013 (± 5.6 kV HV, 245 mV threshold).

CERN SPS with lighter beam ions (Ar) but of higher energy (13-A GeV). This time the "high rate" setup was positioned at ~ 4 degree relative to the beam line. The hit multiplicity was higher in the experiment performed at CERN SPS, as can be observed in the correlation plots between the time of flight distribution and hit multiplicity (left side - October 2014, right side February 2015), presented in Fig. 5 for Buc2013 counter, at 200 mV PADI8 threshold.

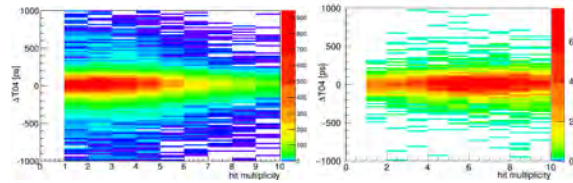


Figure 5: Correlation between the TOF distribution and hit multiplicity in Buc2013 at 200 mV PADI8 threshold for GSI (left side) and CERN-SPS (right side) beam tests.

In the February 2015 setup a MRPC (Tsinghua University) with pad readout was positioned in the same row between Buc2013 and BucRef. The three counters in a row plus the diamond detector (beam monitor) allow for a hit correlation between different counters based on a hit tracking. The obtained efficiency for Buc2013 results to 99% and the corresponding mean cluster size to 3.6 strips (HV: 5.6 kV, 200 mV FEE threshold). During the October-2014-beam-time identical values for HV and FEE threshold had been applied resulting to an equal efficiency but to a slightly lower mean cluster size of 3.3 strips.

For the Buc2013 prototype the system time resolution as a function of cluster size shows the same behavior as for previous beam tests. The best obtained time resolution of 75 ps had been achieved for clusters of 4 strips. The

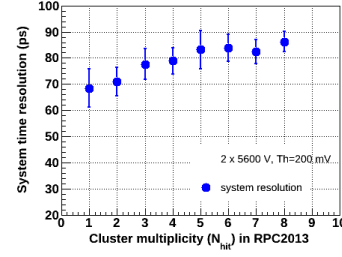


Figure 6: System time resolution as a function of hit multiplicity in Buc2013 (± 5.5 kV HV, 200 mV threshold) for CERN SPS beam test.

system time resolution as a function of the hit multiplicity for CERN SPS beam test is presented in Fig. 6. The best

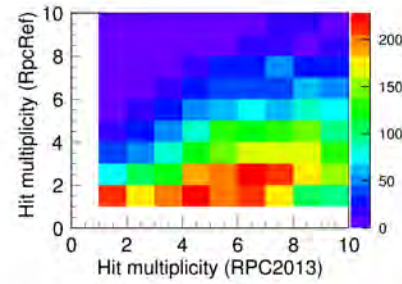


Figure 7: Hit multiplicity correlation in Buc2013 and BucRef (± 5.6 kV HV, 200 mV threshold) for CERN SPS beam test.

time resolution of 69 ps for events with single hit events in Buc2013 confirms the value obtained in the GSI October 2014 beam test.

A preliminary estimation of the counting rate using a plastic scintillator positioned horizontally downstream of the high rate experimental setup gives a value of ~ 4 kHz/cm² for the run used in the present analysis. Because in both experiments the two counters are not exposed to the same flux of reaction products (see Fig. 7), in the mentioned geometry of the experiment, they are not exposed to identical conditions. Therefore, individual contribution of them to the obtained performance is not necessarily the same. These two beam times were followed by a third one at CERN SPS in November 2015 with a Pb beam of 30-A GeV incident on a Pb target, which exposed the counters to a much more harsh environment in terms of hit multiplicity and counting rate. The data analysis is in progress.

References

- [1] V. Aprodu et al., CBM Progress Report 2013 (2014), p.79
- [2] M. Petriș et al., CBM Progress Report 2014 (2015), p.89
- [3] M. Petriș et al., CBM Progress Report 2011 (2012), p.5
- [4] M. Petrovici et al., JINST 7 (2012) P11003
- [5] CBM-TOF Collaboration, CBM-TOF TDR, October 2014
- [6] TRB3 Homepage: <http://trb.gsi.de/>
- [7] I. Deppner et al., CBM Progress Report 2014 (2015), p.86

MGMSRPC prototype with transmission line impedance tuned through the width of the readout strip *

*V. Aprodu*¹, *D. Bartoș*¹, *M. Petriș*¹, *M. Petrovici*¹, *L. Prodan*¹, *A. Radu*¹, *L. Rădulescu*¹, and
*V. Simion*¹

¹NIPNE, Bucharest, Romania

In the free streaming readout considered for the CBM experiment, a very good impedance matching of the counters with the front-end electronics is required in order to minimize the reflections on the transmission lines. It is well known for strip RPCs that it is rather difficult to fulfill this since the width of the transmission line and electrodes - gaps architecture are imposed by both physics and cost requirements. The design of a new MGMSRPC prototype aims to match the input impedance of the front-end electronics in an innovative way, adjusting the strip impedance through the value of the readout strip width, different from the one of the high voltage (HV) electrodes. The inner

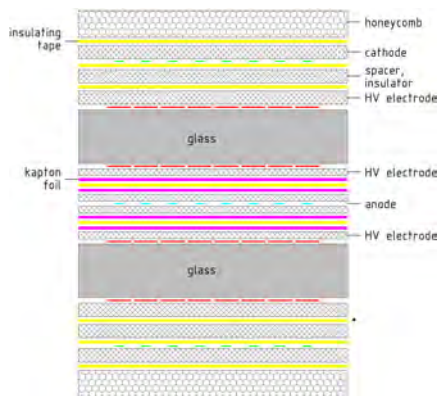


Figure 1: Inner architecture of the detector.

architecture of the counter is presented in Fig. 1. It is a 2×5 gas gaps symmetric structure relative to the central readout electrode (the anode), with a differential readout. The size of the gas gap is given by the $140 \mu\text{m}$ diameter of the nylon fishing line used as spacer. The resistive electrodes made from low resistivity glass [1] define an active area of $300 \text{ mm} \times 96 \text{ mm}$.

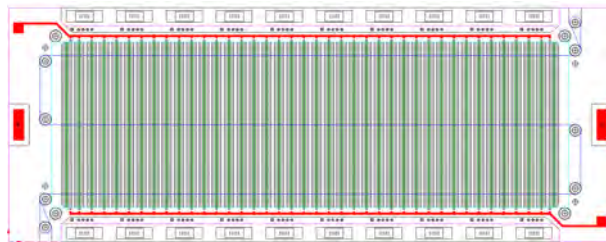


Figure 2: Front view of the detector.

Both HV and readout electrodes have a strip structure with the same strip pitch, but with different strip widths

*Romanian NASR/contract RO-FAIR F02 and NASR/NUCLEU
Project PN09370103

(see Fig. 2). Taking into consideration the compromise between required granularity in the most inner zone of the CBM-TOF wall [1] and the cost of the electronic channels, it was chosen a strip pitch of 7.2 mm, for which an average cluster size of 1.5 strips was reported in [1] for the same inner geometry (2 x 5 gas gaps). The 5.6 mm strip width (W in Fig. 3) of the HV electrodes defines the counter granularity while the 1.3 mm strip width (w in Fig. 3) of the readout electrodes defines the transmission line impedance, of 100 Ω in this particular case. The transmission line impedance of a single detector readout channel was estimated using APLAC simulations. The simulated signals on the anode (input - magenta, output - green) and cathode (input - blue, output - red) electrodes for one half of the structure, read-out on 200 Ω load resistor, are shown in Fig. 3. The parallel transmission lines of the two halves of the detector give an equivalent output impedance of 100 Ω . The output signals reproduce very well the input ones, without any significant distortions of the shape. The prototype

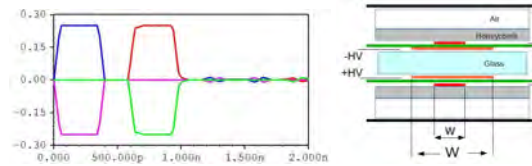


Figure 3: Left side: input/output signals. Right side: half of the detector geometry used in the APLAC simulations.

with the specified strip characteristics was constructed, and its functionality was tested in the Detector Laboratory with a gas mixture of 90% $C_2H_2F_4$ +10% SF_6 . A sample of the obtained signals using ^{60}Co source is shown in Fig. 4. It was recorded using a differential probe connected directly at one end of the detector transmission line.

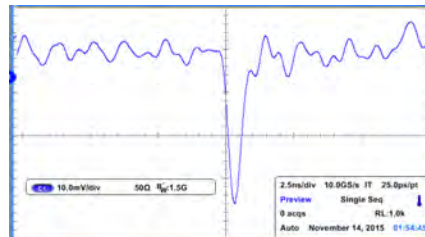


Figure 4: Signal recorded with a differential probe.

The detector was tested in the in-beam campaign of the CBM-TOF collaboration (November 2015) at the SPS-CERN accelerator and data analysis is in progress.

References

- [1] CBM-TOF Collaboration, CBM-TOF TDR, October 2014

Single - sided MGMSRPC prototype with 100 Ω transmission line impedance *

V. Aprodu¹, D. Bartoș¹, M. Petriș¹, M. Petrovici¹, L. Prodan¹, A. Radu¹, L. Rădulescu¹, and V. Simion¹

¹NIPNE, Bucharest, Romania

In this report we present a new Multi Gap Multi Strip RPC (MGMSRPC) prototype with 100 Ω transmission line impedance. It aims to match the input impedance of the front-end electronics with a reduced number of the readout channels, consequently the cost of the electronic channels.

Constructive details of the prototype can be followed in Fig. 1. It is designed as a single-sided architecture of 8 gas gaps, each gap between two resistive electrodes defined by the 140 μm diameter of the nylon fishing line. The resistive electrodes are made from low resistivity glass [1] of 300 mm x 96 mm size, the same as the one used in the construction of a former prototype for which very good performance in high counting rate tests was reported [2, 1]. The pitch of both high voltage and readout electrodes is

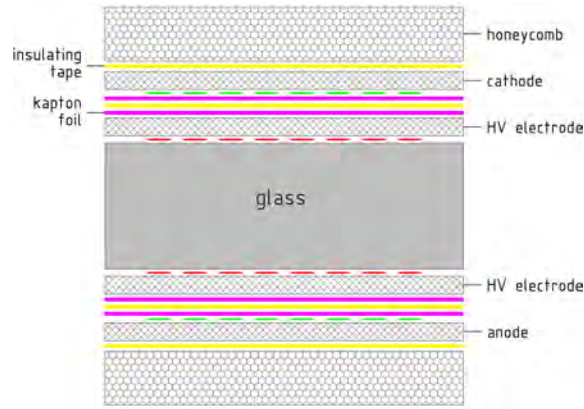


Figure 1: Inner architecture of the detector.

of 10.1 mm with a strip width of 8.6 mm and 1.5 mm gap between two consecutive strips. The strip geometry was defined based on the results of APLAC simulations shown in Fig. 2.

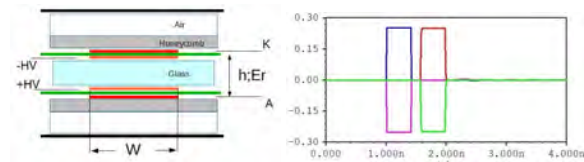


Figure 2: Left side: half of the detector geometry used in the APLAC simulations. Right side: input/output signals.

In the left side of Fig. 2 is shown the schematic structure used to estimate the equivalent relative permittivity constant needed in the performed simulations. The right side plot

shows the input/output simulated signals on the anode (magenta/green) and on the cathode (blue/red). The time difference between the input and output signals corresponds to 96 mm strip length. As can be seen, the output signals reproduce very well the input ones, without any distortion or attenuation, confirming a good matching with 100 Ω load differential impedance of the front-end electronics.



Figure 3: A photo of the assembled prototypes mounted on the Al back panel.

The assembled detector (upper part of Fig. 3) was mounted together with the prototype described in [3] (lower part of Fig. 3) on the back panel of the gas tight box. The

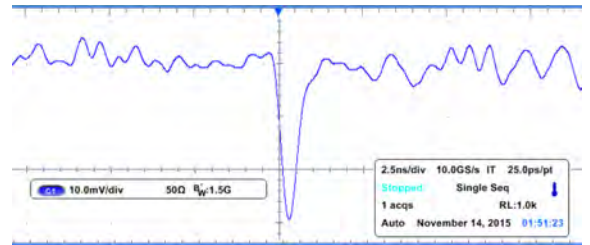


Figure 4: Signal recorded with a differential probe.

counter was tested in the Detector Laboratory using ^{60}Co source and cosmic rays. Figure 4 shows a signal recorded at one end of a transmission line with a differential probe.

The detector was tested in the in-beam campaign of the CBM-TOF collaboration (November 2015) at the SPS-CERN accelerator and data analysis is in progress.

References

- [1] CBM-TOF Collaboration, CBM-TOF TDR, October 2014
- [2] M. Petrovici et al., JINST 7 (2012) P11003
- [3] V. Aprodu et al., this Progress Report

* Romanian NASR/contract RO-FAIR F02 and NASR/NUCLEU Project PN09370103

Progress in Ceramic RPCs for the Beam Fragmentation T0 Counter

R. Sultanov², A. Laso Garcia¹, A. Akindinov², J. Hutsch¹, B. Kämpfer¹, M. Kaspar¹, R. Kotte¹, L. Naumann¹, V. Plotnikov², D. Mal'kevich², M. Sobiella¹, D. Stach¹, K. Voloshin², and J. Wüstenfeld¹

¹Helmholtz-Zentrum Dresden-Rossendorf, Dresden, Germany; ²Institute for Theoretical and Experimental Physics, Moscow, Russia

Every TOF measurement needs the reference time called T0, or start time. One of the proposed solutions for start time determination in the CBM experiment is the Beam Fragmentation T0 Counter (BFTC) [1]. It should cover the region from about 20 to 60 cm from the beam pipe (overlapping with the PSD acceptance). Besides T0 measurement, it will provide particle identification and reaction plane determination in heavy-ion collisions. As was shown with SHIELD simulations [2], the BFTC region is expected to be exposed to harsh conditions with the particle flux as high as $2 \times 10^5 \text{ Hz/cm}^2$. Therefore, ceramic RPCs will be the preferable solution due to their excellent rate capabilities [3].

Production and structure of the ceramic RPCs were already described in the previous CBM progress reports [4, 5]. During the last year, the final design of the outer electrodes was implemented. Cu/Cr layer is coated by evaporation using an improved mask on grooved Al_2O_3 ceramic electrodes sized $2 \times 2 \text{ cm}^2$. For best timing performance, the signal is read-out from the middle of the electrode, see Fig. 1.

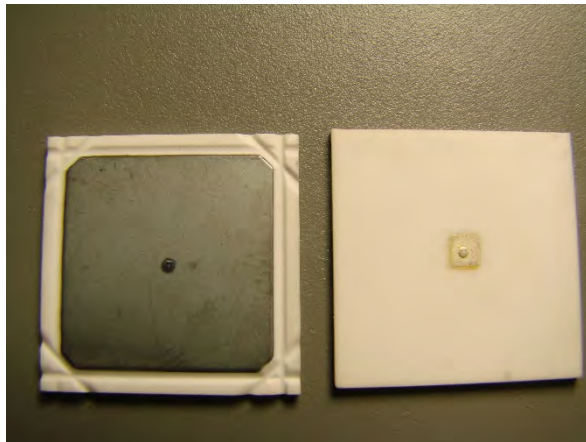


Figure 1: New outer electrodes with the active size of $2 \times 2 \text{ cm}^2$ made of Al_2O_3 ceramics

Two beam tests at HZDR ELBE with 30 MeV electrons were performed in May and November 2015. The main purpose of the first run was to repeat tests with the $5 \times 5 \text{ cm}^2$ ceramic chambers with all the electrodes grooved and ceramics used being the same as in production bunch II (since problems with production bunch III ceramics were found and reported last year [5]). Two chambers, CRPC09 and CRPC10, with a bulk resistivity of 3.5×10^9 and

$2.3 \times 10^{10} \Omega \times \text{cm}$ respectively, 6 gaps $\times 250 \mu\text{m}$ gaps, were tested. Results of the tests are presented in Fig. 2 and compared to those from the previous test [4]. No “strange pulses”, which were observed while using bunch III ceramics, were found with any of the new chambers. As may be seen, the chambers with only outer electrodes grooved (ITEP13) cannot work at the efficiency plateau, while chambers with all the electrodes grooved can work under much higher field values and hence easily reach the plateau. The low resistant CRPC09 can operate steadily within a wide plateau.

The main goal of the November tests was to estimate the range of optimal resistivity of the floating electrodes. For this purpose, four final size chambers ($2 \times 2 \text{ cm}^2$ active size, same structure and gap size) with varying resistivity of the floating electrodes, were produced. Namely, mCRPC0 had floating electrodes with the bulk resistivity of $2 \times 10^{10} \Omega \times \text{cm}$, mCRPC1 – $3 \times 10^9 \Omega \times \text{cm}$, mCRPC2 – $5 \times 10^8 \Omega \times \text{cm}$, mCRPC3 – $7 \times 10^9 \Omega \times \text{cm}$. Test results for the final size chambers are shown in Fig. 3. The chamber mCRPC2 ($5 \times 10^8 \Omega \times \text{cm}$) proved to be unstable already at 87–88 kV/cm where many streamers were observed and the time resolution rose over 140 ps. The rest of the chambers showed stable and efficient work. The chamber mCRPC3 could not be tested within the whole electric field range due to the lack of beam time. RPCs manifested the efficiency of 95–97% under particle fluxes of a few kHz/cm^2 . It has been observed that for higher fluxes, the bulk resistivity of $10^{10} \Omega \times \text{cm}$ is too high, resulting in the drop of efficiency to 74% under 160 kHz/cm^2 . Due to technical problems, the chambers 1 and 3 were measured only up to 70 kHz/cm^2 . The drop of efficiency was related to the resistivity of the chambers in the expected way. The bulk resistivity of the floating electrodes of the order of $10^9 \Omega \times \text{cm}$ has been proven to be the most appropriate for BFTC purposes. For precise determination of the optimal resistivity, a module constructed of 8 chambers with bulk resistivity varying from 1.4×10^9 to $9.4 \times 10^9 \Omega \times \text{cm}$ is planned to be build and tested in 2016.

References

- [1] S. M. Kiselev, CBM Progress Report 2013.
- [2] R. I. Sultanov, CBM Progress Report 2013.
- [3] A. Laso Garcia, PhD thesis. Technische Universität Dresden, 2015.
- [4] A. Laso Garcia et al., CBM Progress Report 2013.
- [5] A. Laso Garcia et al., CBM Progress Report 2013.

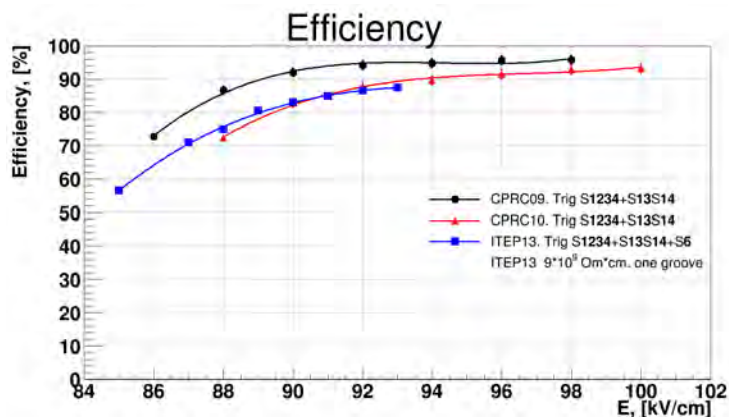


Figure 2: Working curve for chambers sized $5 \times 5 \text{ cm}^2$. ITEP13 has only outer electrodes grooved. CRPC09 and CRPC10 have all the electrodes grooved.

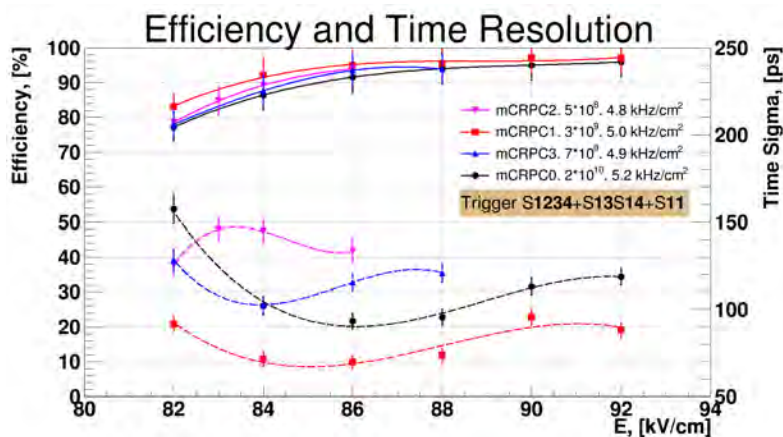


Figure 3: Efficiency and time resolution (after time-walk correction) for $2 \times 2 \text{ cm}^2$ chambers as a function of applied electric field.

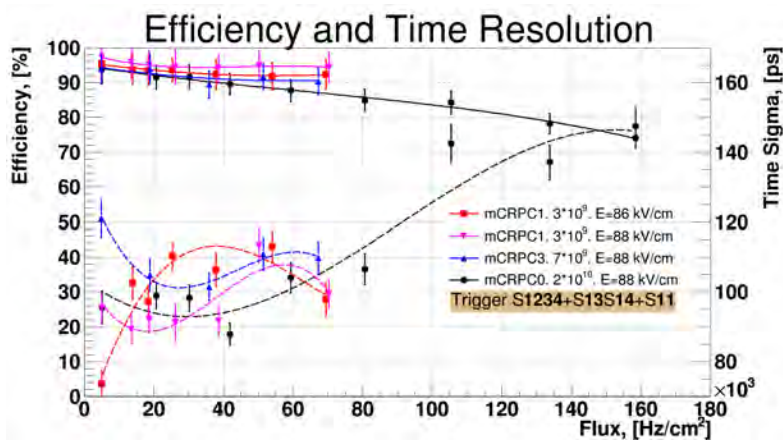
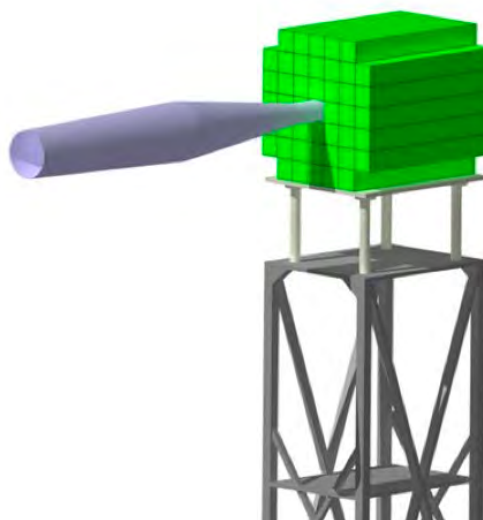
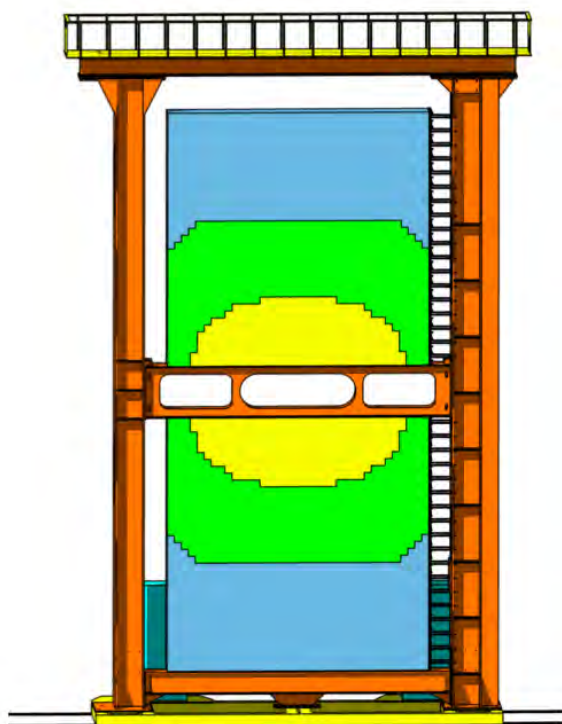


Figure 4: Efficiency and time resolution for $2 \times 2 \text{ cm}^2$ chambers as a function of particle flux.

Calorimeters



Performance studies of the PSD readout board prototype.*

S.G. Reznikov¹, V.P. Ladygin¹, A.Yu. Isupov¹, A.N. Khrenov¹, S.M. Piyadin¹, V. Kushpil², A. Kugler², and V. Mikhaylov^{2,3}

¹LHEP-JINR, Dubna, Russian Federation; ²NPI of ASCR, Řež, Czech Republic; ³CTU, Prague, Czech Republic

The PSD is a basic detector to determine the collision centrality and the orientation of an event plane at CBM [1]. It is a full compensating modular lead-scintillator calorimeter with readout of scintillation light by APDs. The radiation hardness of APDs from different manufactures has been investigated previously at NPI in Řež [2].

A 10 channels scintillation detector prototype has been developed at LHEP JINR for further studies of the PSD readout. The used 10 channels electronic board prototype is based on the design performed for NA61 PSD [3]. The board is able to set the operational voltage for 10 Ketek PM3350 SiPMs individually. Each readout channel contains two linear amplifiers with the amplification factors of 30 and 120. Each Ketek PM3350 is coupled with the scintillator with 20×20 mm² in cross section and 24 mm in length.

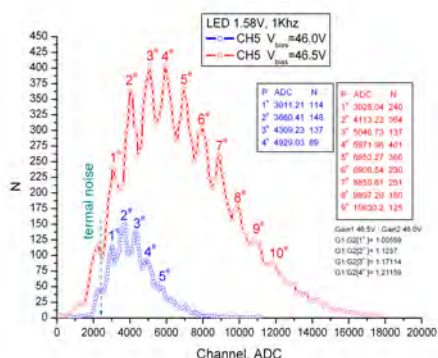


Figure 1: The results of the detector test with LED for different operational voltage for Ketek SiPM are shown by blue and red symbols.

The detector prototype has been investigated with LED and cosmic muons at LHEP JINR. The digitization has been performed using VME based DAQ. The results for one detector obtained with LED are shown in Fig.1 by blue and read histograms for different operational voltage for Ketek PM3350. The separation of the few p.e. peaks is clearly seen, especially for higher value of the operational voltage. The signal from cosmic muons was detected at the level of ~ 3 -4 p.e. .

A prototype was irradiated using quasi-monoenergetic secondary neutron beam from cyclotron facility U120M

* Work supported by GSI(SIS)/GSI(ESR)/GSI(UNILAC)/GSI(PHELIX) /HI Mainz/HI Jena/HIC4FAIR/HGShire/EU, EURONS contract No. 506065/GSI cooperation with university Mainz/Helmholtz-Nachwuchsgruppe

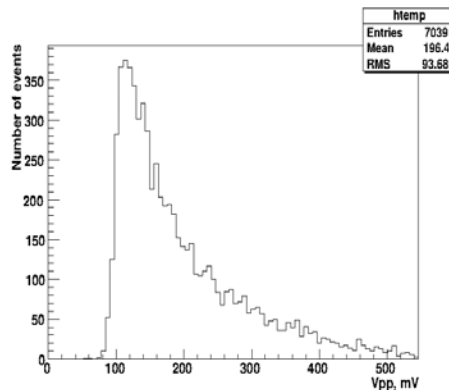


Figure 2: The amplitude of the scintillation detector irradiated by the neutron fluence of $\sim 7.5 \cdot 10^7$ n/cm².

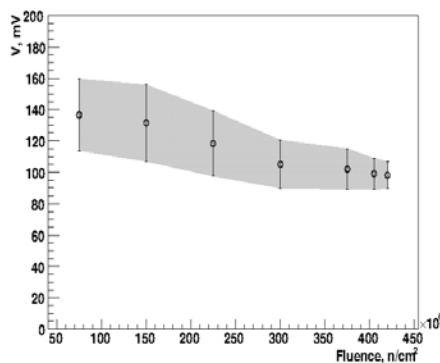


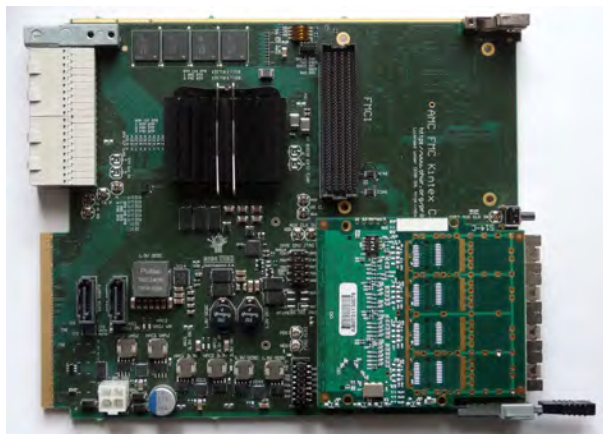
Figure 3: The dependence of the signal amplitude from the scintillation detector as a function of the neutron fluence.

at NPI in Řež. The signal from one of the scintillation detector in the beginning of the irradiation (after $7.5 \cdot 10^7$ n/cm² of the 1 MeV neutron fluence) is shown in Fig.2. The decrease of the SiPM signal with the irradiation dose is demonstrated in Fig.3. The signal decreases by a factor of ~ 1.4 , while the intrinsic noise increases approximately twice after irradiation with the 1 MeV neutron fluence of $4.2 \cdot 10^8$ n/cm². The electronics demonstrated the stable operation during the irradiation.

References

- [1] Technical Design Report for the CBM. Projectile Spectator Detector// <http://www.fair-center.eu/for-users/experiments/cbm/cbm-documents.html>
- [2] V.Kushpil et al., Phys.Part.Nucl.Lett. 13 (2016) 120.
- [3] M.Golubeva et al., Nucl.Instrum.Meth. A610 (2009) 366.

DAQ and Online Event Selection



The AFCK Board as the Data Processing Board prototype for CBM experiment*

W. Zabolotny^{†1}, G. Kasprowicz¹, A. Byszuk¹, M. Guminski¹, K. Pozniak¹, and R. Romaniuk¹

¹Institute of Electronic Systems, Warsaw University of Technology, Warszawa, Poland

The Data Processing Boards (DPB) are an important part of the CBM readout and detector control systems, providing concentration (possibly combined with local preprocessing) of readout data before they are sent to the First Level Event Selector (FLES). Additionally, DPBs should provide fast and slow control for the Front End Electronics (FEE), distribute the reference clock, and time-critical information, like synchronization and flow control messages from the Timing and Fast Control system (TFC). In 2014, the AFCK boards were proposed as the prototyping platform for DPB [1]. In 2015, the second revision of the AFCK boards was manufactured and tested. Thanks to improvements in the PCB design and use of another PCB substrate (ISOLA FR408HR), the 10 Gbps transmission speed was achieved on both FMC connectors, improving the connectivity features of the board. The tests were performed using the FADE-10G protocol [2].

The AFCK boards were used to test firmware blocks implementing the future DPB functionality, by different CBM groups [3, 4].

In particular, different options of Ethernet connectivity were successfully tested (via the AMC backplane, via the SFP transceiver placed in the SFP cage on the FMC board and via SATA type connector). The IPbus compatible controller has been tested in various scenarios, including difficult cases where gigabit transceivers belonging to the same block (“quad”) were used for different functionalities using different transmission speed. The packaged version of the IPbus board controller was prepared by Junfeng Yang from GSI.

The Ethernet interface is characterized by relatively high round-trip latency, which may impair efficiency of control algorithm. Therefore preliminary studies on adaptation of control procedures to such conditions were undertaken [5].

The AFCK communication interfaces require appropriate configuration of the board flexible clocking system. To allow testing of different communication variants without reprogramming of the MMC processor, a special JTAG-controlled firmware was created that allows to configure the AFCK clock crossbar and programmable clock oscillators located on the board itself or on the additional FMC board (e.g., the FM-S14 board [6]).

In certain possible uses of the DPB board (e.g. in certain implementations of the TFC slave or in the GBTx emulator mode used in the development), it is necessary to recover the high-quality clock from the communication links.

The preliminary results show that it is possible [7]. however, further research aimed at optimization of the locking speed is necessary. The desired solution should be based on firmware based PLL with phase detector inside the FPGA and the external digitally controlled programmable clock generator.

The work on usage of the GBT-FPGA cores in the AFCK board was also continued. The visit of Swagata Mandal from VECC was used to cooperate at the development of the GBTx emulator [8]. Additionally, studies on implementation of multiple GBT-FPGA cores in AFCK were performed. The first result is the core, which may be used for testing of the VLDB board. Further research is still required on packaging the GBT-FPGA cores in a way allowing to share the same GTX quad between the GBT-FPGA and 1 Gbps or 10 Gbps Ethernet.

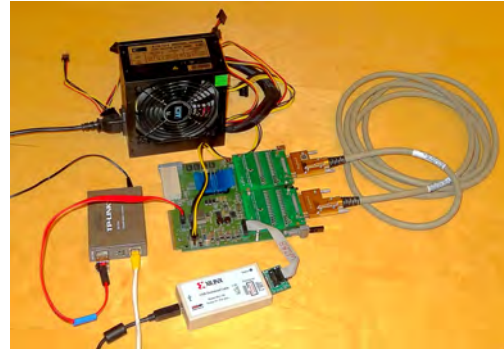


Figure 1: The AFCK board used in a stand-alone mode with an ATX power supply. The Ethernet connectivity is provided by a self-made SATA-SFP cable and a media converter. Two FMC VHDCI cards provide the LVDS link between the STX-XYTER controller and the STS-XYTER model implemented separately in the same FPGA. The external JTAG programmer is used to configure the FPGA and clocking system.

An important topic in 2015 was the development of the STS-XYTER protocol tester. The STS-XYTER controller and model were successfully ported to the AFCK platform. The dedicated FMC cards were designed and manufactured, that allow connecting the STS-XYTER controller with the STS-XYTER model via a VHDCI cable providing the true LVDS link. This allows to perform protocol tests using a single AFCK board (as shown in Figure 1), or two AFCK boards, ensuring that the clocks in the STS-XYTER controller and in the STS-XYTER model are truly

* Work partially supported by GSI

[†] wzab@ise.pw.edu.pl

independent.

New versions of the STS-XYTER model provided by the AGH team were successfully tested. Further progress in the development of the STS-XYTER communication protocol was achieved in the cooperation with the GSI and AGH teams [9].

The current implementation of the STS-XYTER controller uses the black-box emulator of the GBT e-link. Therefore, the current and future work is aimed on allowing the controller to operate via the true e-link, which introduces additional clock-domain crossing issues.

As the complexity of firmwares implemented in the AFCK board increases, it becomes obvious that it is necessary to split them into manageable components. One of possible solutions is the use of the standard IP packager available in the Xilinx Vivado environment. However this approach has also some disadvantages. For example it is not possible to use complex data types in the I/O ports of the modules, which is a standard solution used e.g. in the IPbus modules. Additionally, this approach limits the possibilities of inter-block logic optimization.

Therefore, another Tcl script based approach was proposed. The structure of the design is described with a hierarchy of “extended project files” which may contain HDL sources, associated constraint files and nested “extended project files”. This solution minimizes amount of information which must be stored to preserve the structure of the design, and therefore is better suited for version control systems. The disadvantage of this approach is an incompatibility with Xilinx “Out of Context” compilation mode, that significantly increases the speed of design recompilation.

The optimal method to handle continuously evolving complex firmware projects requires further research.

References

- [1] W.M. Zabolotny and G. Kasproicz, “Data processing boards design for CBM experiment”, November 2014, Proc. SPIE, vol. 9290, pp. 929023-929023-11; doi:10.1117/12.2073377
- [2] W. M. Zabolotny, “Low latency protocol for transmission of measurement data from FPGA to Linux computer via 10 Gbps Ethernet link”, July 2015, Journal of Instrumentation, vol. 10, pp. T07005
- [3] P.A. Loizeau and D. Emscherman and J. Lehnert and W.F.J. Müller and J. Yang, “The prototype readout chain for CBM using the AFCK board and its software components”, September 2015, Proc. SPIE, vol. 9662, pp. 96622X-96622X-11; doi:10.1117/12.2205820
- [4] W.M. Zabolotny and G. Kasproicz and A.P. Byszek and D. Emschermann and M. Gumiński and B. Juszczak and J. Lehnert and W.F.J. Müller and K. Poźniak and R. Romaniuk, “Versatile prototyping platform for Data Processing Boards for CBM experiment”, February 2016, Journal of Instrumentation, vol. 11, pp. C02031
- [5] W. Zabolotny, “Improvement of FPGA control via high speed but high latency interfaces”, September 2015, Proc. SPIE, vol. 9662, pp. 96623G-96623G-8; doi:10.1117/12.2205441
- [6] “FM-S14 Quad SFP/SFP+ transceiver FMC”, <http://www.fastertechnology.com/products/fmc/fm-s14.html>
- [7] M. Gumiński and W. Zabolotny and G. Kasproicz and K. Poźniak and R. Romaniuk, “Time and clock synchronization with AFCK for CBM”, September 2015, Proc. SPIE, vol. 9662, pp. 96622V-96622V-6; doi:10.1117/12.2205798
- [8] S. Mandal and W. Zabolotny and S. Sau and A. Chkrabarti and J. Saini and S. Chattopadhyay and S.K. Pal, “Internal monitoring of GBTx emulator using IPbus for CBM experiment”, September 2015, Proc. SPIE, vol. 9662, pp. 96622Q-96622Q-11; doi:10.1117/12.2205595
- [9] K. Kasinski, “STS-HCTSP: Silicon Tracking System Hit & Control Transfer Synchronous Protocol using GBT’s e-link for the CBM experiment at FAIR”, Poster presentation at iWoRiD-2015 - 17th International Workshop on Radiation Imaging Detectors, 28 June - 2 July 2015, DESY, Hamburg, Germany, <https://www-alt.gsi.de/documents/DOC-2015-Oct-10.html>

Status Update of the Feature Extraction Framework for Automatic FPGA Firmware Generation *

C. de J. García Chávez¹, C. E. Muñoz Castillo¹, and U. Keschull¹

¹Infrastructure and Computer Systems for Data Processing (IRI), Frankfurt University, Frankfurt/Main, Germany

The Feature Extraction Framework

A framework for FPGA firmware generation has already been developed as presented in [1]. The framework implements well-known stream processing algorithms for feature extraction like peak-finding, signal integration, center of gravity, time-over threshold and cluster finder, just to mention a few of them. A Domain Specific Language (DSL) file, specifically developed for the framework, is the primary input to the framework. In such file, high-level directives are used to describe:

- The target FPGA development board.
- The Front-End Electronics.
- Stream-message format.
- The feature extraction algorithms.
- The communication modules.

Development of the Framework as a Web Application

In order to make the interaction with the framework user-friendly and give the user more capabilities to exploit the implemented processing features, the framework was re-structured as a web application. The graphical user interface has been based on the concept of dataflow computing, where a “Stream Network” is made by interconnection of blocks, as Figure 1 shows. Such blocks implement the high-level algorithms available in the framework. One of the main features of the framework as a web service is to leverage the processing effort of the third-party tools required by the framework like Xilinx ISE for example, from the user-side to the server-side.

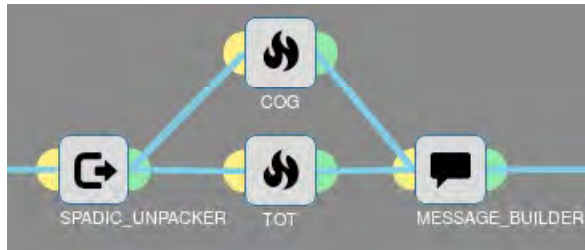


Figure 1: A Stream Network Example

In order to use the web application, a user authentication must be made prior accessing the infrastructure. Therefore a database is used to store user information and the projects

created by the user. A project would include the “Stream Network” description, the generated HDL sources and the third-party synthesis project. The files are stored on the server-side and accessible to the user by means of a network shared folder. Once a user has been authorized and a project has been created, the compilation process is carried out by the framework back-end application without the need of user interaction.

Framework Scalability and Security

The framework implements a virtualization technology based on Docker [2] in order to make the service scalable. This feature would be necessary to handle simultaneous user sessions connected to the web service. The framework’s server creates a virtual container where an instance of the feature extraction framework is running. User’s projects are retrieved from the data base and loaded into the virtual container. For every new user connection, a new virtual instance of the framework is created. Finally, a garbage collector destroys the virtual containers once the user has logged out. Security is an important topic in web services, since potential software weaknesses could grant undesired control access of malicious users to the host infrastructure. By using virtual containers, a security layer is created by sand-boxing both the server and every created instance of the framework.

Current Status and Results

The feature extraction framework was tested in November 2015 during a beam-test at the CERN SPS hall within the TRD data-acquisition readout. A SysCore3 FPGA board was used as a readout controller for two Spadic 1.0 front-end chips. The feature extraction framework was used to generate the pre-processing algorithms implemented in the readout controller. Preliminary results have shown that performance and FPGA resource consumption between the hand-written HDL code versus the framework generated code are similar. However, a significant reduction in design time has been achieved by using the framework.

References

- [1] C. de J. García Chávez and U. Keschull, “A Feature Extraction Framework for Automatic FPGA Firmware Generation”, CBM Progress Report 2014.
- [2] “Docker”, <http://www.docker.com>

* Work supported by BMBF No. 05P12RFFCM.

Control of XYTER emulator from DPB through GBTX emulator for MUCH detector*

Swagata Mandal^{†1}, Wojciech M. Zabołotny², Suman Sau³, Jogender Saini¹, Amlan Chakrabarti³,
and Subhasis Chattopadhyay¹

¹VECC,Kolkata,India; ²Warsaw University of technology,Poland; ³University of Calcutta,Kolkata,India

Introduction

For efficient data aggregation from the Muon Chamber Front End Electronics (MUCH-FEE's), GBTx [1] emulator (In final experiment GBTx emulator is replaced by GBTx ASIC) is planned to be used in between FEE and Data processing board (DPB) [2] in MUCH Data Acquisition (DAQ) system. In the front end, GBTx receives data from FEE through an electrical link (E-link) and in the backend it sends data to DPB through 4.8 Gbps optical link. This article focuses on controlling of E-Link protocol from DPB through optical link.

E-link Protocol Basics

Each E-link basically consists of three signal lines. They are differential clock line (used to provide clock to FEE device), Differential Downlink data output (used to send data from GBTx to FEE) and Differential Uplink data input (used by GBTx to receive data from FEE). A simple synchronous communication protocol was developed [3] using some special characters like K28.5, K28.1, Start of Synchronization (SOS) and End of Synchronization (EOS) for establishing communication between GBTx and FEE through the differential E-Link. A simple flow chart in Figure 1 describes the basic E-Link protocol. In the down link direction, data is transferred using GBT frame with data a rate of 160 Mbps. In the uplink direction, transmission is done via wide frame mode with a data rate of 320 Mbps.

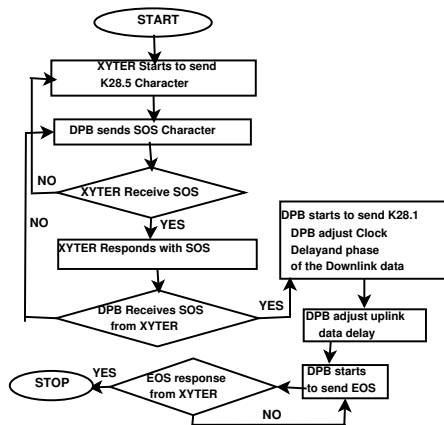


Figure 1: Flowchart for E-Link Protocol

Implementation of E-Link protocol using IPbus

E-Link protocol will be completely controlled from DPB. So for controlling the E-link protocol, different registers in the DPB and GBTx have to be accessed continuously. Internal registers within the GBTx and DPB are monitored online using IPbus protocol over 1 Gbps Ethernet link.

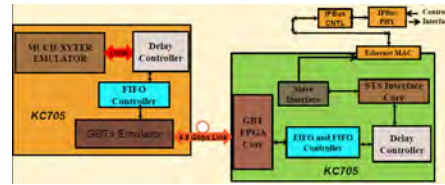


Figure 2: Integration of GBTx with XYTER and DPB

Controlling of XYTER emulator using IPbus through a GBT link is shown in Figure 2. Here, two KC705 evaluation boards have been used and in one board XYTER emulator, delay controller, FIFO and GBTx emulator have been implemented. On the other KC705 board GBT FPGA core, FIFO, delay controller and IPbus over 1 Gbps Ethernet have been implemented. We have used a Python script to continuously monitor internal registers on the two boards.

XYTER emulator sends data at a data rate of 320 Mbps and while the GBT frame rate is 40 Mhz. For clock domain crossing an asynchronous FIFO is used whose write frequency is 320 Mhz and read frequency is 40 Mhz. As the 320 Mhz clock in XYTER and GBTx are different in phase, a delay controller is used to match the phase of these two clock domains. At the output of the FIFO, data width is 40 bit (5x 8 bit) which is sent through the GBT frame. In the downlink direction GBT sends data at 40 Mhz and XYTER receives data at 160 Mbps. The write frequency of FIFO is 40 Mhz and the read frequency is of 160 Mhz in downlink.

References

- [1] P.Moreira, J.Christiansen and K.Wyllie, "The GBTx Link Interface Asic," v1.7 Draft, Oct.2011.
- [2] Wojciech Zabołotny et al., "Data processing boards design for CBM experiment ", September 2014, Proc. SPIE, vol. 9290, pp. 929023; doi:10.1117/12.2073377.
- [3] K. Kasinski, W. Zabolotny, R. Szczygiel, "STSXYTER – DPB Protocol v.1.5," Oct.2014.

* Supported by BI-IFCC,DST and DAE, Govt. of India

[†] swagata.mandal@vecc.gov.in

Timing Synchronizer System Developments for pre-production Beam Test Setups *

L. Meder and J. Becker

KIT-ITIV, Karlsruhe Institute of Technology, Karlsruhe, Germany

For the planned beam tests in 2016, a new timing synchronizer (TS) system is being developed which is required in order to synchronize the data acquisition at the frontend electronics of the composite setup.

Besides the high-speed links that are used to transfer the data recorded by the frontend electronics to a post-processing system, it is mandatory to provide adequate means in order to control the readout system. For the overall system control a slow-control system like the very popular IPBUS system developed at CERN can be used, which relies on gigabit Ethernet connections as physical medium. However, in the CBM beam test readout system it is important that at least the frontend electronics that samples the analog data from the detector elements, shares a common clock which has a known phase relation among the frontend ASICs. For that reason, a timing control system is needed which allows to distribute a clock from a central master to all of the slave nodes that connect to the frontend electronics and provide the data path of the readout chain.



Figure 1: tDPB Master-Slave setup with two AFCK boards

In case of the pre-series test beam setup of the CBM Silicon Tracking System, the detector elements together with the readout ASICs need to be operated with DC-coupled connections. Due to the detector system's physical characteristics, all of the parts of the data acquisition up to the FPGA-based processing nodes need to be operated at a ground potential which is offset by a few hundred volts for the p- and n-side of the detector respectively. As a consequence, all of the control and data links to these processing nodes require a galvanic isolation in order to prevent damage.

Taking into account all of these requirements, a versatile timing synchronizer system is being developed which

allows to provide a common clock and a pulse-per-second (PPS) signal to the FPGA-based slave processing nodes. The firmware running on the FPGA of the timing synchronizer data processing boards (tDPB) itself offers different features like the operation with internally or externally generated clock or PPS, automatic clock switch-over, second and cycle counters and clock fine phase shifting. All of the properties and features of the FPGA core can be controlled through IPBUS. The development of the tDPB system did incorporate the design of an FPGA Mezzanine Card (FMC) which offers galvanically isolated constant latency LVDS links for the transmission over twisted-pair cables and can be mounted on Advanced Mezzanine Cards (AMC) to be used in MicroTCA crates. Using these cards, different system topologies may be composed like a cascaded tDPB system structure with a Grand-Master, Sub-Masters and the Slave processing nodes (see Figure 2). For future setups the tDPB AFCK may be mounted inside a MicroTCA crate, where the Grand-Master clock and PPS is supplied through the backplane of the crate (see Figure 3).

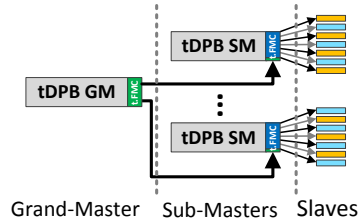


Figure 2: A cascaded tDPB System

A tDPB Master-Slave test system was evaluated, where two AFCK boards with mounted tDPB FMC cards were interconnected by 10 meters of CAT7 twisted-pair cable (see Figure 1). Together with a laboratory PC which was connected through the IPBUS Slow-Control links, the functionality of the concept was verified. Here, the tDPB Slave was able to reuse the clock from the tDPB link as system clock and align the local PPS and cycle/second counters to the received PPS signal.

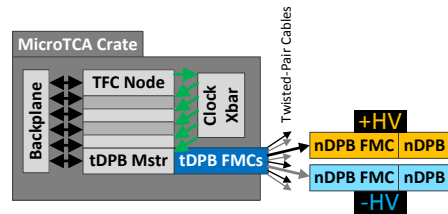


Figure 3: Extending a crate by a tDPB system

* Work supported by BMBF

Development of a channel layer for control and communication via GBT-SCA*

A. Oancea¹ and U. Kebschull¹

¹Infrastructure and Computer Systems for Data Processing (IRI), Goethe-University, Frankfurt, Germany

Introduction

The FPGA-based read-out board (ROB) of the CBM ToF experiment is planned to have a bidirectional connection via GBTx and control through the GBT-SCA. The ToF ROB will be located in a radiation area, and therefore the FPGA configuration needs to be managed, reconfigured and at times reset, when the FPGA is unresponsive. A proof of concept using the Xilinx Soft Error Mitigation IP core, the FPGA's JTAG interface, and GPIOs to implement such resilience in radiation environments has been demonstrated for an AC701 development board and a management application running on a PC [1]. In a next step the management and scrubbing concept needs to be integrated into the GBTx chain by developing a slow control firmware module for the FPGA downstream interfacing the GBTx chip.

The GBT-SCA is controlled via an "e-link", which is essentially a bi-directional bitstream transparently transported by the GBTx to the downstream FPGA. The communication from and to the GBT-SCA is encapsulated in the HDLC link layer protocol [2]. The different functional units inside the GBT-SCA are controlled via the SCA communication protocol, which makes up the channel layer (Figure 1).

A concise component wrapping the already available link layer communication needs to be developed, since from the user application point of view the remote devices and interfaces of the SCA are handled as independent destinations (channels), each channel coming with a defined set of actions and replies [3]. The scope is to develop a channel layer core which is as generic as the channel layer protocol to make it easily usable across various back ends.

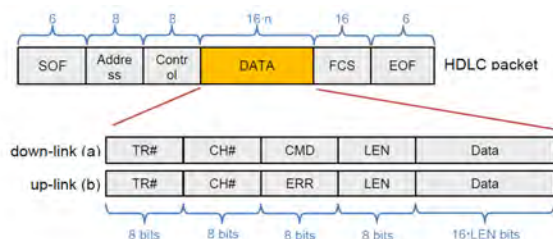


Figure 1: Depiction of the channel layer (bottom) encapsulated in the HDLC-based link layer (top). Figure taken from [3].

* Work supported by HGS-HIRE

Implementation

The conceptual ongoing firmware implementation is depicted in Figure 2. The GBT-SCA provides several interfaces, such as I²C, interrupt-capable GPIOs and JTAG. Through the channel layer wrapper, the GBT-SCA becomes accessible as a user interface, with up to 22 independent channel interfaces. To this interface, a back-end specific core can be developed and attached, e.g. an IPbus component in the case of CBM. Once the GBT-SCA is accessible via IPbus, it is then possible to manage the FPGA configuration of all ToF ROB's from a central management application that is connected e.g. from the control room down to the channel interface of individual FPGAs.

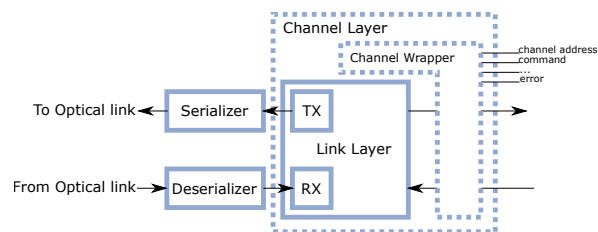


Figure 2: Conceptual channel layer implementation. The existing link layer will stay accessible, but another channel interface is added (dotted boxes).

Next Steps

The implementation will be tested using a GBTx FMC mezzanine card (Utrecht University) connected to an AC701 development board. A small scale system consisting of a front-end FPGA, back-end FPGA running the GBTx link layer core with channel wrapper, and a PC connected to this board running a management application is planned for in-beam testing at the end of 2016.

References

- [1] A. Oancea, C. Stüllein, J. Gebelein, S. Manz and U. Kebschull, "Implementation and test of a flash-free configuration upset mitigation strategy for the CBM ToF ROB FPGA", CBM Progress Report 2014, p. 103
- [2] ISO/IEC 13239:2002, Information technology — Telecommunications and information exchange between systems — High-level data link control (HDLC) procedures
- [3] S. Bonacini, A. Caratelli, R. De Oliveira, K. Kloukinas, A. Marchioro, P. Moreira, C. Paillard, "The Slow Control Adapter ASIC for the GBT System"

A low cost fault tolerant Commercial Of the Shelf MCU adapted with RTEMS/EPICS for controls and instrumentation

*J.A. Lucio Martínez¹, J. Gebelein¹, and U. Kebschull^{*1}*

¹Infrastructure and Computer Systems for Data Processing (IRI), Frankfurt University, Frankfurt/Main, Germany

Following a non negligible effect of soft errors in controls hardware, a micro-controller for safety and real-time applications (TMS-570) was configured with the Open Source RTEMS, whose libraries support real time functionality for some EPICS features. A working version of the Ethernet RTEMS driver for the TMS-570 had to be written from scratch for this purpose. The fault tolerant capabilities of this MCU were tested while running RTEMS/EPICS parasitically to a detector beam-test at CERN.

Background

By considering an ARM Cortex 5RF CPU based MCU for controls, effort is being aimed at low cost, redundancy and fault tolerance with no performance compromising. In environments with ionizing radiation the risk of soft errors should not be neglected, specially if a control system is being designed.

CPU/MPU capabilities

The manufacturer Texas Instruments specifies in [1] that the MCU runs the Dual-Core Lockstep CPUs With ECC-Protected Caches. Substantially, this is by ARM in [2] referred as dual-redundant core. It consists of two cores running the same set of instructions and the outputs being compared by error detection logic. This MCU furthermore possesses interfaces such as UART interfaces (LIN and SCI), Flexray, I^2C , CAN bus, 10 & 100 Mb/s Ethernet, Multi-buffered Serial Peripheral Interface (MibSPI). In addition, ECC on Flash and RAM interfaces, Built in Self Test and Error Signaling Module complement the error tolerance features.

Sensor data collecting with EPICS

Using the test platform (board) the manufacturer commercializes for this MCU, called TMDX570LS31HDK, EPICS was tested by accessing temperature and light sensor included in the board, the record representing the light sensor data was gathered through Channel Access by pyEpics and plotted as new values came through monitoring process, (see fig. 1).

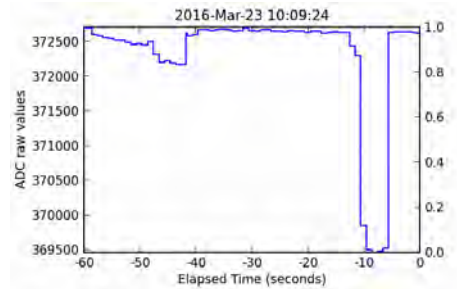


Figure 1: Reading data through EPICS Channel Access from fault tolerant TMS570 MCU

Testing Fault Tolerant Features of TMS570

In order to test the ECC error detection/correction on internal SRAM, a fault was injected by disabling error correction detection feature, changing a bit in the RAM protected space, and then enabling the error correction/detection feature again. The injected error was detected successfully.

Performance in the beam

The board was tested parasitically to a detector beam-test at the CERN SPS and exposed to secondary particles produced by a 30 GeV Pb beam interacting with a thick target. It was placed in front of a particle detector, the flux was approximately $1100 \frac{\text{particles}}{\text{cm}^2}$. No SEU was detected in the internal SRAM memory, there were no errors found in the lockstep register, the MCU unit seemed to work properly. This result motivates tests with higher beam intensities.

References

- [1] Texas Instruments, "TMS570LC4357 Hercules Microcontroller Based on the ARM Cortex-R Core", February 2014, <http://www.ti.com>
- [2] ARM, "Cortex -R5 Technical Reference Manual", Revision: r1p2, 2011, p.2-6, <http://infocenter.arm.com>
- [3] Philip Stanley, Janet Anderson, Marty Kraimer, "EPICS Record Reference Manual", May 1998, <http://aps.anl.gov/epics>

^{*} kebschull@rz.uni-frankfurt.de

CBM FLES input interface developments*

D. Hutter¹, J. de Cuveland¹, and V. Lindenstruth¹

¹FIAS Frankfurt Institute for Advanced Studies, Goethe-Universität Frankfurt am Main, Germany

The First-level Event Selector (FLES) is the central event selection system in the CBM experiment. Its task is to select data for storage based on online analyses including a complete event reconstruction. Before event analysis, the FLES performs timeslice building, which combines the data from all given input links to self-contained, overlapping processing intervals, and distributes them to compute nodes. Partitioning the input data streams into microslice containers allows to perform this task very efficiently.

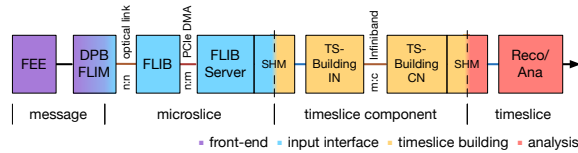


Figure 1: FLES data flow

A schematic overview of the data flow and data types is presented in Fig. 1. The FLES input interface, highlighted in blue, defines the connection between the front-end processing logic in the Data Processing Board (DPB) and the FLES timeslice building framework. The FLES Interface Board (FLIB), a custom FPGA board, receives microslices via optical links, prepares them for subsequent timeslice building, and transfers the data via DMA to the host memory [1]. An accompanying HDL module, the FLES Interface Module (FLIM), implements the front-end logic interface and FLES link protocol in the DPB. In contrast to earlier prototypes, which included additional emulated DPB functionality, the structure now matches the foreseen final setup.

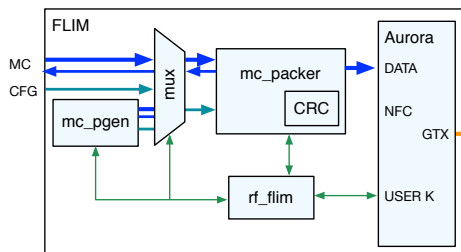


Figure 2: Schematic view of the FLES Interface Module

An overview of the FLIM building blocks can be found in Fig. 2. The front-end logic streams microslice data content and meta data, e. g. microslice time, via an AXI-Stream interface into the FLIM. A protocol engine implements the

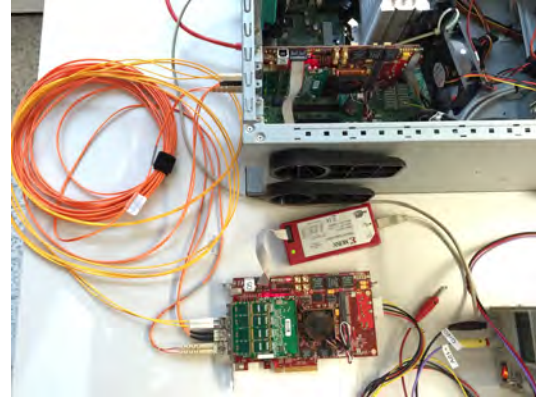


Figure 3: Input interface test setup

upper layer of the FLES link protocol. It builds packages from the incoming data and adds an end-to-end CRC. The communication between FLIM and FLIB is realized via a bidirectional optical link. The link-layer is implemented using the Aurora protocol. The link operates at a line rate of 10,3125 GHz and uses 64B/66B encoding. This results in a net bandwidth of 10 Gbit/s. In addition to the data channel a bidirectional controls channel is implemented. This allows FLIM configuration and control over the FLES link independent of the DPB slow control infrastructure. For in-situ testing, the FLIM features an internal pattern generator which can be used to emulate the front-end input.

Prototypes of all input interface components have been implemented and integrated into the FLES framework. To verify the components in hardware a DPB example design based on a HTG-K7 board has been developed. Fig. 3 shows the lab test setup with a FLIB installed in a PC and a stand alone HTG-K7 running the DPB example design. Utilizing the FLIM pattern generator in conjunction with a full pattern checker in the Flesnet software, the whole chain including timeslice building was tested successfully. In long-term stability tests with 3 links in parallel, a bit error rate of $< 10^{-16}$ for each link was achieved.

References

- [1] D. Hutter, J. de Cuveland, and V. Lindenstruth, “CBM FLES input interface developments”, CBM Progress Report 2014 (2015) 101

* Work supported by BMBF (05P12RFFCP) and HIC for FAIR

The CBM first-level event selector, timeslice building and availability studies *

H. Hartmann¹, J. de Cuveland¹, and V. Lindenstruth¹

¹FIAS Frankfurt Institute for Advanced Studies, Goethe-Universität Frankfurt am Main, Germany

In the CBM experiment the First-level Event Selector (FLES), a high performance computing cluster, is functioning as the central event selection system. Data from the detector links will flow via a custom FPGA-based input interface to the scalable supercomputer largely constructed from standard components including a fast event-building network. Data will first be combined from all detector links into time intervals, i.e., timeslices. These timeslices pose a global format on which the FLES carries out complete event reconstruction and online analyses. Data rates at this point are expected to exceed 1 TByte/s.

High-level timeslice building Previously it was investigated if MPI could be used for a high-level implementation of timeslice building, which requires a high performance due to the high incoming data rate. It was shown that under special conditions a customized MPI benchmark (cMPI-BM) is able to achieve a performance of 6 GB/s on the L-CSC utilizing 24 nodes in a simultaneous all-to-all communication pattern as shown in Fig. 1. This is the highest data rate possible on the underlying InfiniBand network as the comparison to the native InfiniBand Verbs ping-pong benchmark (green line) shows.

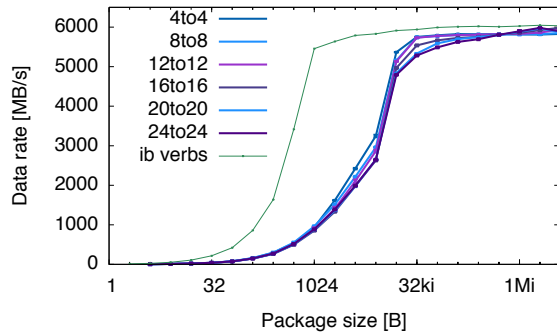


Figure 1: Custom MPI benchmark on the L-CSC with 24 nodes

However, this performance could only be achieved under certain conditions. First, the data flow in the cMPI-BM follows the linear-exchange-shift communication pattern (LSE). Second, the routing needed to be adopted to match the LSE used in the cMPI-BM by rewriting the InfiniBand subnet routing tables. Third, a warmup phase is required before each run of the cMPI-BM, where a few packages of each size are exchanged between every node to allow for MPI to internally set up its buffers [1]. The first and

the third condition can not be fully matched on a complete timeslice building implementation based on MPI and therefore performance drawbacks are to be expected. Additionally it needs to be considered that currently MPI provides no fault tolerance. When in MPI one process crashes all other processes within the same communicator will detect this condition and abort as well. In a standard MPI program this means all process will exit since upon initialization they share the same communicator MPI_COMM_WORLD.

Availability Availability is a measure of a system providing service. Essentially availability is made up out of two aspects: reliability and the ability to recover from faults. Both properties can be expressed mathematically. Reliability is quantified as *mean time between failures* MTBF and recovery from faults as *mean time to repair* MTTR. Hence, availability is defined as:

$$\alpha = \frac{MTBF}{MTBF + MTTR} \quad (1)$$

For the FLES a good objective is 99.9% availability because in this case the impact on the overall CBM efficiency would be only marginal. In order to approach this availability all failure sources need to be evaluated regarding their MTBF and MTTR. One possible scenario is the crash of one node within the cluster. Extrapolating real-world data from the ALICE-HLT we can estimate a MTBF for a crucial node failure of about two weeks. However, during commissioning we expect a significantly higher failure rate. Therefore, to match 99.9% availability the system should be able to recover from faults within seconds. This requirement will not hold if timeslice building was implemented via MPI. The crash of one process causes the crash of the whole distributed program and restarting the timeslice building framework will take one or two minutes.

Due to these restrictions on timeslice building build on top of MPI the original approach of a low-level native InfiniBand implementation is preferred. However, it needs to be equipped with a control system providing high availability. Several existing failure detection methods in combination with key/value stores are under investigation for developing a FLES control system. The available process managers are analyzed regarding the requirements the FLES poses, which are especially scalability and performance.

References

- [1] G. Shipman, T. Woodall, R. Graham, and A. Maccabe. InfiniBand Scalability in Open MPI. In International Parallel and Distributed Processing Symposium (IPDPS), 2006.

* Work supported by BMBF (05P12RFFCP) and HIC for FAIR

Computing



Determination of the cluster position in the CBM-STS

*H. Malygina^{*1,2,3} and V. Friese²*

¹Goethe University, Frankfurt, Germany; ²GSI, Darmstadt, Germany; ³KINR, Kyiv, Ukraine

In the double-sided silicon strip sensors of the CBM-STS, a charged particle activates a number of adjacent strips (“cluster”). From the charge measurements q_i of the strips in the cluster, the particle position has to be reconstructed. An algorithm for such position reconstruction should be unbiased and provide minimal position residuals, i.e., it should minimise the measurement error. Moreover, it should be computationally efficient.

A commonly used method is the centre-of-gravity (COG), which defines the cluster centre as $x_{\text{rec}} = \sum_i x_i q_i / Q$, where x_i is the centre coordinate of strip i and $Q = \sum_i q_i$ the total charge in the cluster. This prescription, however, does in general not provide a bias-free measurement nor does it result in the smallest residuals.

In order to develop a better-suited algorithm, we note that to first order, the detector response in the silicon sensors is a uniform charge distribution, corresponding to the projection of the particle trajectory on the readout (strip) edge. This charge distribution, which is then integrated on the readout strips, can be characterised by two independent variables, namely the entry and exit coordinates of the track in the sensor, x_{in} and x_{out} . Since the thickness of the sensors is small, the trajectory within the sensor can be approximated as a straight line, and we can define the true coordinate $x_{\text{true}} = 0.5(x_{\text{out}} - x_{\text{in}})$. The proper algorithm can now be derived from the requirement that the average residual $\langle x_{\text{rec}} - x_{\text{true}} \rangle$ vanishes:

$$\int dx_{\text{true}} P(x_{\text{true}}) (x_{\text{rec}} - x_{\text{true}}) \stackrel{!}{=} 0.$$

Here, $P(x_{\text{true}})$ is the probability density for x_{true} , which can be derived from that of x_{in} and x_{out} . We assume both variables, for a given cluster size, to be uniformly distributed, which was verified by simulations.

The resulting measurement prescriptions are:

- For single-strip clusters, the centre of the strip is taken: $x_{\text{rec}} := x_i$. The corresponding error is $\sigma_x = p/\sqrt{24}$, with p being the strip pitch.
- For two-strip clusters with strips i and $i+1$:

$$x_{\text{rec}} := \frac{1}{2} (x_i + x_{i+1}) + \frac{p}{3} \frac{q_{i+1} - q_i}{\max(q_i, q_{i+1})}.$$

The corresponding error is

$$\sigma_x = \frac{p}{\sqrt{72}} \frac{q_{i+1} - q_i}{\max(q_i, q_{i+1})}.$$

^{*} Work supported by HIC-for-FAIR, H-QM and HGS-HIRe.

- For clusters with $n > 2$ strips, extending from strip i to j :

$$x_{\text{rec}} := \frac{1}{2} (x_i + x_j) + \frac{p}{2} \frac{q_j - q_i}{q}; \quad q := \frac{1}{n-2} \sum_{k=i+1}^{j-1} q_k.$$

This prescription exactly reproduces the true coordinate, i.e., the corresponding error vanishes.

Several effects lead to deviation from a uniform charge distribution on the readout edge, such as fluctuations in the charge creation along the trajectory, noise, threshold, diffusion and charge discretization. The currently implemented STS digitizer software allows to add those one-by-one [1]. These effects increase the position resolution as demonstrated in Fig. 1, such that the residual distribution alone does not favour the new algorithm over the COG. However, as shown in [2], the new algorithm has the advantage that the hit position errors can be estimated a-priori, which is important for the correct determination of the track parameters.

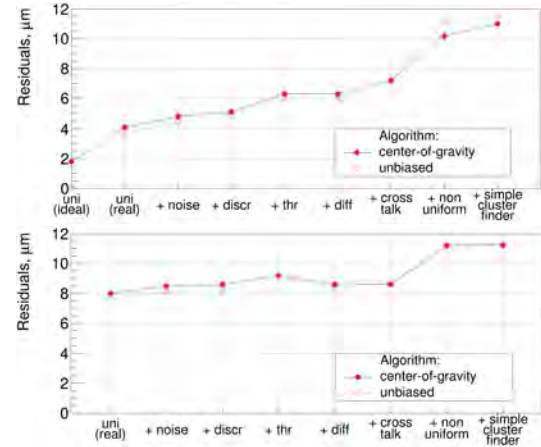


Figure 1: Width of the residual distribution from simulation for 3-strip clusters (top) and all clusters with cluster size distribution as expected for Au+Au events at 10A GeV (bottom) when taking into account different processes (see text). For the difference of “uni (ideal)” and “uni (real)”, see [2].

References

- [1] H. Malygina, V. Friese and J. M. Heuser, CBM Progress Report 2013, Darmstadt 2014, p. 96
- [2] H. Malygina and V. Friese, *Estimation of the hit position error in the CBM-STS*, this report

Estimation of the hit position error in the CBM-STS

H. Malygina^{*1,2,3}, V. Friese², and M. Zyzak^{1,2,4}

¹Goethe University, Frankfurt, Germany; ²GSI, Darmstadt, Germany; ³KINR, Kyiv, Ukraine;

⁴FIAS, Frankfurt, Germany

Relevant physical processes which occur in the detector should be taken into account for its numerical modelling. In the current implementation of the STS digitization model [1], such processes can be included separately. This allows investigating their individual influence on the reconstructed hit positions and their errors. A reliable estimate of the hit position error is important to obtain a proper track χ^2 , which is used to discard ghost track candidates. This affects the signal-to-background ratio of the reconstructed physical signals and the corresponding efficiencies.

In this report we present a procedure of hit error estimation which is obtained from first principles and is independent of measured spatial resolution or simulated residuals. For verification of the procedure, we use the pull distribution (pull = residual/error) of the hit position. Its width must be ≈ 1 , and its shape must reproduce the shape of the residuals distribution.

There are several contributions to the total hit position error:

$$\sigma^2 = \sigma_{\text{alg}}^2 + \sum_i \left(\frac{\partial x_{\text{rec}}}{\partial q_i} \right)^2 \sum_{\text{sources}} \sigma_j^2. \quad (1)$$

Here, σ_{alg} is the error of the cluster position finding algorithm (CPFA) and x_{rec} the reconstructed hit position. The index $i = 1 \dots n$ denotes the strip number in the cluster with n being the cluster size. Among the already included other error sources σ_j are the detector noise (the equivalent noise charge), the charge discretization, and the non-uniformity of energy loss.

The derivatives $\partial x_{\text{rec}} / \partial q_i$ in (1) depend on the chosen CPFA. We here use the unbiased algorithm described in [2]. This yields e.g. for a 2-strip cluster

$$\left| \frac{\partial x_{\text{rec}}}{\partial q_i} \right| = \frac{p}{3} \frac{q_1 q_2}{\max(q_1, q_2)^2} \frac{1}{q_i}.$$

To single out σ_{alg} , we consider the simplest model of an ideal detector response: the charge distribution is proportional to a geometrical projection of an incident particle trajectory onto the read-out plane. The CPFA of [2] yields the following errors σ_{alg} for different cluster sizes:

$$\sigma_1 = \frac{p}{\sqrt{24}}, \quad \sigma_2 = \frac{p}{\sqrt{72}} \left(\frac{q_2 - q_1}{\max(q_1, q_2)} \right), \quad \sigma_{n>2} = 0.$$

The estimate of the signal discretization error is given by

$$\sigma_{\text{discr}} = \frac{\text{dynamic range}}{\sqrt{12} \text{ number of ADC}}.$$

^{*} Work supported by HIC-for-FAIR, H-QM and HGS-HIRe.

The contribution from the non-uniformity of energy loss is more difficult to take into account because the actual energy deposit along the track is not known. The following approximations allow a straightforward solution:

- the registered charge corresponds to the most probable value (MPV) of energy loss;
- the incident particle is ultrarelativistic ($\beta\gamma \gtrsim 100$).

The second assumption is very strong but it uniquely relates the MPV and the distribution width [3]

$$MPV = \xi[\text{eV}] \times (\ln(1.057 \times 10^6 \xi[\text{eV}]) + 0.2).$$

Solving this with respect to ξ gives the estimate for the FWHM [4]

$$\sigma_{\text{non}} = w/2 = 4.018\xi/2.$$

Figure 1 shows the verification of the error estimation procedure with simulated Au+Au events in the STS. The pull width exceeds unity. This can be a consequence of an artificial increase in the residuals caused by the discretization of the trajectory in Geant, such that the coordinates of the entry and exit points of the track do not perfectly coincide with the actual sensor surfaces.

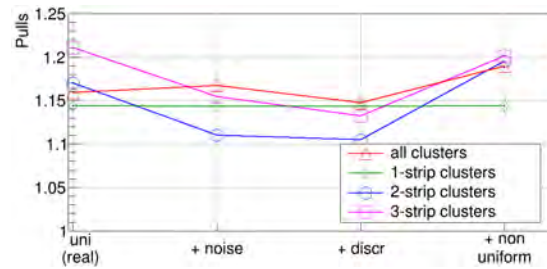


Figure 1: Widths of pull distributions when taking into account different physical effects. The label "uni (real)" corresponds to the perfect detector model affected by the trajectory discretization in Geant.

References

- [1] H. Malygina, V. Friese and J.M. Heuser, CBM Progress Report 2013, Darmstadt 2014, p. 96
- [2] H. Malygina and V. Friese, *Determination of the cluster position in the CBM-STs*, this report
- [3] K. A Olive *et al.* (Particle Data Group), Chin. Phys. C **38** (2014) 090001
- [4] S. Meroli, D. Passeri and L. Servoli, JINST **6** (2011) P06013

Time-based cluster finder for the CBM-STS detector

G. Kozlov^{1,2,3,4} and I. Kisel^{1,2,4}

¹Goethe-Universität, Frankfurt, Germany; ²GSI, Darmstadt, Germany; ³JINR, Dubna, Russia; ⁴FIAS, Frankfurt, Germany

A feature of the CBM experiment is that the collected data will not be divided into events by a hardware trigger system. Instead, the data acquisition will deliver a free stream of data, where the event boundaries are not defined. At the maximal interaction rate of 10 MHz targeted by CBM, some events may overlap in time, and they cannot be disentangled before reconstruction. This scenario requires special algorithms for cluster, hit and track finding. Cluster and hit finder have to take into account not only spatial coordinates of digis (raw data messages), but also the time of their activation. In the following, we consider in detail a time-based clustering algorithm for the CBM-STS detector [1].

Cluster finding is the first step of STS hit reconstruction. A cluster is a group of adjacent active strips in a sensor with a similar time stamp. In an event-based scenario, fired strips are combined into a cluster only by their location and measured charge. In reality, however, the input object for the cluster finder is a time-slice, comprising the raw data of many events distributed in time. As a consequence, it will contain several digis for a given strip (channel), which necessitates changes in the clustering algorithm and in the data structures.

A time-based clustering algorithm was developed and implemented in CbmRoot. The logical scheme of this algorithm is shown in Fig. 1. First, data from the time-slice are sorted sensor-wise. For each sensor, they are stored in a multimap, the key being the strip number. At the beginning, the algorithm takes the first element (digi) from the multimap, creates a new cluster, and associates the first digi with this cluster. Then it takes the next digi and checks for compliance with the following conditions:

- **Correct time and channel.** If the channel number is the same as the previous digi, or if the time difference between this and the previous digi is greater than 20 ns (which means that the digis cannot originate from the same particle), the program goes to the next digi from the multimap.
- **Next channel.** If the channel number of this digi exceeds the channel number of previous digi in cluster by more than one, this and all next digis cannot be used for this cluster. The cluster is written to the output and the algorithm starts a new cluster with the new first element of the multimap.

If the digi satisfies all conditions, it is added to the cluster, and the algorithm takes the next digi from the multimap. It should be noted that every digi can be used only in one cluster.



Figure 1: Simple scheme of the time-based clustering algorithm

Tests and comparison between event- and time-based clustering algorithms were carried out using 1000 minimum bias Au+Au events at 25.4 GeV. Events were packed into time-slices with duration of 10000 ns at interaction rates of 10 and 100 MHz. At 10 MHz, the maximal interaction rate for Au+Au collisions in CBM, some events do overlap, but most are well separable. Using the extremely high interaction rate of 100 MHz we can test our algorithm in an increasingly difficult context with high data density and non-separable events.

The STS hit finder usually creates a large number of fake combinatorial hits, formed by the intersection of clusters from two different particles. For the event-based cluster and hit finding, the percentage of correct hits is only 54.7%. The hit finding efficiency is 98.3%. The results using time-based clusterization at 10 MHz are close to these numbers: the efficiency is 97.4%, with 52.8% true hits. The cluster size distribution and accuracy of hits are the same in these two cases. The calculation speed of the time-based algorithm is comparable to the event-based version for the same number of fired digis. After increase of the interaction rate up to 100 MHz we can see a drop in efficiency (91.8%) and growth of the ghost number (correct hits: 36.5%). However, we still can find most of hits even at such high an interaction rate.

References

- [1] J. Heuser et al., *Technical Design report for the CBM Silicon Tracking System*, GSI Report 2013-4 (2013)

Improvements to the CBM TOF simulation in CBMROOT*

P.-A. Loizeau¹, N. Herrmann², and the CBM ToF working group

¹GSI, Darmstadt, Germany; ²Physikalisches Institut, Universität Heidelberg, Germany

Charged hadrons will be identified in CBM through the Time-Of-Flight method (TOF), using measurements from a wall built out of Resistive Plate Chambers (RPC). This report presents the improvements done to the simulation of this TOF wall in the CBMROOT framework.

First, new QA data containers and analysis classes were added in CBMROOT, to measure the quality of the TOF simulation and to quantify the performance changes when new TOF wall geometries or software are used. The new data containers are arrays of CbmMatch and CbmLink objects, which provide for each TofHit (reconstructed signal on detector) the indices of the corresponding TofDigis (simulated electronic signals) and TofPoints (Monte Carlo points on detector active area). Each index is associated to a weight indicating its contribution to the TofHit properties (position and time). This allows to build comparisons of the expected (derived from the TofPoints) and reconstructed properties of the TofHit. Examples of such comparisons are the residuals (quality of measurement) and pulls (quality of errors). The new CbmTofHitFinderQa class provides these comparisons and all distributions needed to calculate the efficiency of the simulation steps as function of position, momentum or phase space.

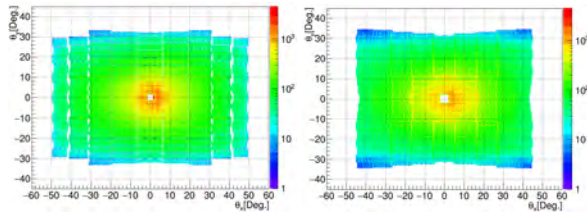


Figure 1: TofHits distribution in angular coordinates for old (v13-5b, top) and new (v16a_1e) geometries (both at $Z = 6$ m) with 100k Au+Au URQMD events at 10 AGeV.

These QA improvements were used to validate new geometries for the CBM TOF wall in CBMROOT: the generation v16a. This new geometry generation provides the following improvements: (i) a realistic description of the inner wall (low angles around the beam pipe), (ii) improved modules positions (better coverage for all wall positions), (iii) an extended outer wall. Five versions of the 16a geometry were produced, 16a_1h (4.5 m from target), 16a_1e (6 m), 16a_1m (6.5 m), 16a_3e (8.5 m) and 16a_3m (10 m), for use in the CBM SIS 100 hadron, electron and muon setups and the SIS 300 electron and muon setups, respectively. A comparison of the simulated hit distributions with the old and new geometries at 6 m from target (SIS100 electron

setup) can be found in Fig. 1. Using the CbmTofHitFinderQa task, the distributions of the residuals and pulls in X, Y, Z and T for both geometry generations were compared and no difference (or slight improvements) were observed. The efficiency of the TOF wall (from MC tracks to hits) gained a few percent with the new geometries thanks to the improved angular coverage. Therefore the generation 16a is the default TOF geometry starting from the NOV15 release of CBMROOT.

TOF QA was also used to check that the more realistic event-based digitizer and clusterizer chain for TOF [1] provides reasonable results. For this, a comparison was made between the residuals, pulls and efficiency obtained with this simulation chain and those obtained with the idealistic TOF simulation task (direct TofHits production from MC points, default in NOV15 release). Figure 2 presents for example the comparison for the residuals on the X coordinate. The effect of the more realistic “cluster” description of the new chain can be seen in the wider distribution, as the direct production is limited at the width of a single channel. For the hit time, the new method is closer to the MC “truth” thanks to the averaging effect of multiple channel clusters, as expected from real data. For all

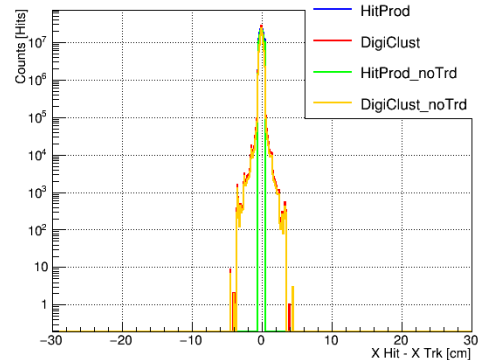


Figure 2: Comparison of the residuals in X between TofHit and TofPoint for the old simulation chain (“HitProd”) and the new (“DigiClust”) one, with and without TRD.

available comparisons, results are more realistic and either equivalent or better with the Digitizer+Clusterizer simulation chain. Therefore it is the TOF default simulation chain starting from CBMROOT release FEB16.

References

- [1] P.-A. Loizeau *et al.*, CBM Progress Report 2013, Darmstadt 2014, p. 100

* Work supported by BMBF (05P12VHFC7)

Further development of the “vector finding” method for track reconstruction in the CBM-MUCH

A. Zinchenko*, V. Myalkovskiy, D. Peshekhonov, and V. Peshekhonov

LHEP JINR, Dubna, Russia

In Ref. [1] we proposed a track reconstruction method for the CBM-MUCH based on a vector finding approach and presented first very preliminary results on its performance. In this report the results of a more detailed study of the method are presented.

The vector finding method is based on building vectors for each MUCH station separately and matching them to each other and to STS tracks through the absorbers. Presumably, such an approach should better handle a heterogeneous tracking environment (GEM and straw tube detectors) and offer higher flexibility with respect to algorithm tuning as compared with a track following method (implemented, for instance, in the *littrack* package of *CbmRoot*). Moreover, this algorithm is naturally parallelizable and extendable to the triggering application.

The results below are obtained for different SIS100 MUCH configurations using the vector finding and *littrack* packages. The configurations studied are *allGEM*, *straw4* (Fig. 1, where two last stations consist of four double layers of straw tubes) and *straw3* (reduced straw sets with three double layers). These detector geometries were studied each with 5k UrQMD central gold-gold events at 8A GeV and the same amount of events containing one additional ω -meson forced to decay into two muons from the Pluto generator. As figure of merit we chose the number of background pairs from the first event set for a given signal pair efficiency (2% or 3%) from the second one. The required efficiency level is achieved by varying the χ^2 cut on the reconstructed tracks.

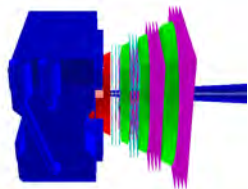


Figure 1: SIS100 CBM muon system configuration with the two last detector stations consisting of straw tubes

Once the vectors in all stations are found, they should be merged [2] and matched to STS tracks. Several approaches were tried (e.g., going upstream from the last station or the other way around). So far, the most winning strategy found is a track continuation from STS. It allows to take into account the track momentum information which is important not only for a more precise treatment of the multiple scattering but also for better following the track evolution,

i.e. deciding whether to keep or drop tracks with low momentum and do not propagate them through absorbers preventing possible false combinations with downstream vectors.

For the *straw3* configuration, there can be the situation when only three tubes (one per each doublet) in a station are activated by a track. In this case there are not enough measurements to constrain a vector. To overcome this difficulty it was chosen to run a combined vector finder for two stations (neglecting the intermediate absorber influence) in order to produce approximate parameter estimates which are later refined using the standard Kalman Fitter formalism.

The results obtained are presented in Table 1. The best result is achieved by the vector finder approach for the *straw4* configuration; it also outperforms the *littrack* method for the *straw3* option. For the *allGEM* geometry it concedes to *littrack* presumably due to the fact that in the last MUCH stations the size of the GEM readout elements becomes quite large making vector selection in one station rather inefficient. It can be expected that by shifting the selection more to the two-station combination level it will be possible to regain the performance.

Table 1: Number of background pairs for different SIS100 MUCH configurations for two values of signal efficiency and two track reconstruction methods

Configuration	Efficiency,%	Contamination	
		LIT	Vector finder
All GEM	3	340	381
	2	137	169
3 straw doublets	3	416	367
	2	167	136
4 straw doublets	3	251	245
	2	108	89

It should be noted that the results presented here are still preliminary and additional work is required to better tune the vector finder-based tracking procedure in terms of performance quality and processing speed. Also, the performance figures should include more direct ones like signal-to-background ratios for dimuon invariant mass distributions.

References

- [1] A. Zinchenko *et al.*, CBM Progress Report 2014, Darmstadt (2015), p. 116
- [2] P. Billoir *et al.*, Nucl. Instrum. Meth. **A 241** (1985) 115

* Alexander.Zinchenko@jinr.ru

Visualization of track reconstruction in the MUCH detector

T. O. Ablyazimov¹ and V. V. Ivanov^{1,2}

¹JINR, Dubna, Russia; ²National Research Nuclear University “MEPhI”, Moscow, Russia

A library of algorithms suitable for standalone track reconstruction in MUCH called Lx is being developed by the authors starting from 2013 [1]. The main goal of this library is to allow online triggering of $J/\psi \rightarrow \mu^+\mu^-$ events in the CBM experiment. The way of its application to this task is described in [2, 3, 4].

The efficiency of track reconstruction algorithms is usually evaluated in terms of combinatorial values such as the percentage of correctly reconstructed tracks, the amount of reconstructed ghost tracks etc. But it is often helpful to give the researcher a direct way of qualitative evaluation of the phenomenon under consideration. An important tool in this context is to visualize it. Fortunately, visualization is quite straightforward in case of a track finder.

A drawing subsystem has been implemented in the Lx package to allow visualization of tracks and hits during reconstruction on demand. It is able to visualize reconstructed tracks as well as Monte Carlo (MC) ones. In order to make the pictures more apperceptive, some details of the experimental plant are also drawn. The drawing is carried out by means of the ROOT 2D graphic API.

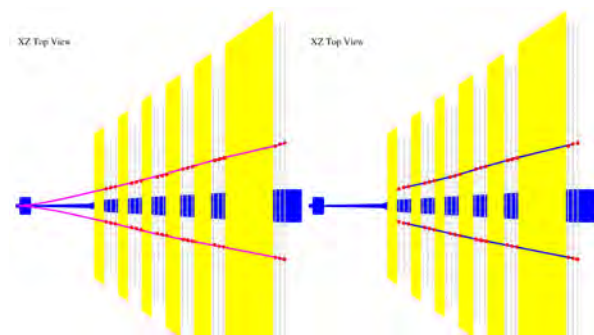


Figure 1: MC (left) and reconstructed (right) tracks in XZ projection

The drawing procedures are implemented as methods of the LxDraw class. The LxDraw methods can be called in any place of the Lx library where the needed entities (MC or reconstructed tracks) are present. They cannot be called outside of the context of the Lx track reconstruction. The LxDraw class uses TGeoManager to parse the MUCH geometry and optionally draw some of its elements like the absorbers, detecting layers and the pipe. LxDraw does not provide general techniques for drawing hierarchically composed ROOT geometries, but it performs visibility checks for those graphical elements which have the ROOT

types handled by the library. Hits are drawn as coloured spots with the TPolyMarker class. Reconstructed and MC tracks are implemented as polylines (TPolyLine). Reconstructed tracks are drawn as segments connecting their hits on the middle layers of the adjacent MUCH stations. MC tracks are drawn in a more precise manner. For their drawing all their MC points are used, and the track coordinates are interpolated in between with step of 0.5 cm using the CbmKF::Propagate() method. The LxDraw class represents an event by drawing its elements in projections to the three planes XY, XZ, YZ. The drawn projections can be saved in files of different formats (PDF, EPS, PNG etc).

Figures 1 and 2 show the XY and XZ projections of a MC and the corresponding reconstructed event drawn and saved by LxDraw. A $J/\psi \rightarrow \mu^+\mu^-$ decay event generated by PLUTO was used in these simulation and reconstruction.

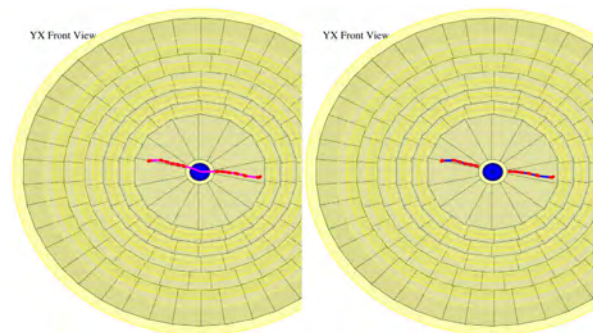


Figure 2: MC (left) and reconstructed (right) tracks in XY projection

References

- [1] T. O. Ablyazimov and V. V. Ivanov, CBM Progress Report 2014, Darmstadt 2015, p. 117
- [2] T. O. Ablyazimov and V. V. Ivanov, CBM Progress Report 2014, Darmstadt 2015, p. 119
- [3] T. O. Ablyazimov and V. V. Ivanov, Phys. Part. Nucl. Letters **12** (2015) 559
- [4] T. O. Ablyazimov and V. V. Ivanov, EPJ Web Conf. **108** (2016) 02001

Development of databases for the CBM experiment

E. P. Akishina¹, E. I. Alexandrov¹, I. N. Alexandrov¹, I. A. Filozova¹, V. Friese², and V. V. Ivanov^{1,3}

¹LIT JINR, Dubna; ²GSI, Darmstadt, Germany; ³National Research Nuclear University "MEPhI", Moscow, Russia

Component Database

The Component Database (Component DB) serves to store and manage the properties of detector hardware and electronics components [1]. The development of a prototype for the Component DB was continued; the database structures for several detector systems (magnet, STS, MVD) were confirmed with the responsible persons. Currently, the Component DB includes eleven tables, six of which are the catalogs [2]. The tables were modified according to the needs of the various detector systems. The system of catalogs was refined. A catalog is a list of unique positions rarely changing (or not changing at all) which makes working with the database more convenient. The following catalogs are currently approved: the catalog of production companies, the catalog of component categories, the catalog of component batches, the catalog of statuses, the catalog of the units of quality measurements, and the catalog of quality criteria.

As an example of refining the system of the catalogs, the catalog "Componentscategories" was added for the convenience of stocktaking of a variety of same-type components (e.g., cables or sensors). The procedure of entering and editing is the same for all the catalogs. A click on the appropriate link initiates the display of the form with the catalog content (see Fig. 1). A friendly and compact user interface allows to easily switch from view mode to enter mode, to edit mode and back. A Users Guide for using of the Component DB is available [3].

ctid_	value	description
1	sensor	Si microstrip sensor
9	FEB	front-end board
10	cable	Kapton microcable
11	11	Module

Figure 1: System GUI: the form with the content of the catalog of component categories

Geometry Database

A new objective is the implementation of a Geometry Database (Geometry DB), which is now adopted for development. The CBM geometry describes the CBM detector setup on the detail level required for transport simulation (GEANT). It represents the "ideal" geometry in the sense of the construction blueprint. Deviations from this ideal geometry, as e.g. obtained by optical surveillance after installation or by alignment procedures, will be described as

additional datasets, which will be handled by a different database (parameter / conditions DB).

The geometry of the CBM detector systems ("modules") is described in ROOT format, with one separate file for each system. Each module geometry is versioned, reflecting changes in the detector design as well as different detector versions for different contexts (e.g., SIS100, SIS 300, beam test setups, mCBM). An entire CBM geometry is then defined by a set of such geometry files with given versions.

Currently, the geometry files are stored and distributed through the CBM software repository. Setups as combinations of geometry files are defined on the ROOT macro level. This situation is rather complicated and error-prone and thus not ideal. Moreover, handling by the software repository does not match the requirement that a given geometry version must not change in time. The distribution of the module geometries as well as entire setups through a database thus appears a desirable solution.

As a first step towards the realisation of the Geometry DB, the User Requirements Document (URD) was established [4]. This document defines the basic entities of the Geometry DB which are specific for the CBM experiment: *Geometry Module*, *Setup*, *Setup Module*, and *Setup Subset*. The Geometry DB will store the CBM geometry and setup modules as well as setups as combination of setup modules. It shall provide appropriate interfaces to view, retrieve and update setup modules and setups.

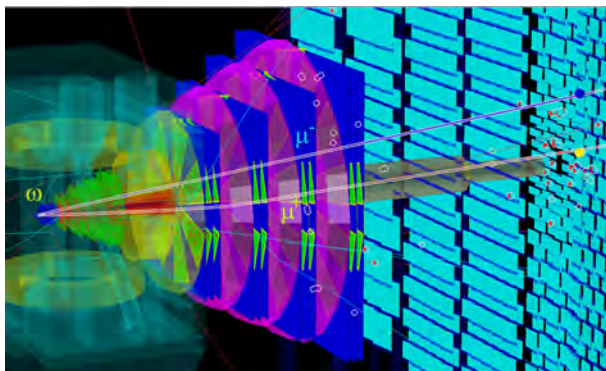
The URD also characterizes three categories of users of the Geometry DB: *CBM user*, *Developer*, and *Lead Developer*. The basic use cases for those categories are *Load Geometry*, *Download Geometry*, *WEB View*, *Add Geometry*, *Add Setup Module*, and *Add Setup*, the detailed description of which is in progress.

This functional model shall be the basis for the design and implementation of the Geometry DB for the experiment CBM.

References

- [1] E. P. Akishina *et al.*, CBM Progress Report 2014, Darmstadt 2015, p. 112
- [2] E. P. Akishina *et al.*, *Component database development for the CBM experiment*, Communication of the Joint Institute for Nuclear Research, E10-2015-106, Dubna 2015
- [3] E. P. Akishina *et al.*, *Users Guide for CBM Component Database*, <http://lt-jds.jinr.ru/record/67404?ln=en>
- [4] E. P. Akishina *et al.*, *User Requirements Document of the Geometry DB for the CBM experiment*, <http://lt-jds.jinr.ru/record/69336?ln=en>

Physics Performance



J/ψ detection via di-muon channel in 15 A GeV Ni+Ni collisions with the CBM detector at FAIR

P. P. Bhaduri* and A. Toia

GSI, 64291 Darmstadt

The goal of the Compressed Baryonic Matter (CBM) experiment [1], at FAIR is the investigation of the strongly interacting matter at high net baryon densities produced in relativistic heavy-ion collisions. In the first phase of FAIR, the SIS-100 accelerator ring will be operational, which will provide beams up to an energy of 30 GeV for protons, 12 A GeV for heavy ions (eg:Pb, Au, In, ...) and 15 A GeV for light ions (eg:C, Ca, Ni, ...). The proposed key observables include the measurement of J/ψ mesons. In this article we report our latest results based on realistic simulation, on performance of J/ψ detection via di-muon channel in 15 A GeV central Ni+Ni collisions. Depending on the collision energy, different MUCH configurations are proposed in [2]. For our present investigations, we have employed the SIS-100-C set up of the muon system. It comprises of 5 hadron absorbers and 5 tracking stations. The first absorber made of carbon (graphite), has a thickness of 60 cm. The other four are made of iron of variable thickness (20 + 20 + 30 + 100 cm), total thickness (iron) being 170 cm. Each tracking station consists of three layers of high resolution Argon + CO₂ based gaseous chambers. In our study, the event generators PLUTO and UrQMD-3.3 have been used for generating signals and background particles respectively. PLUTO generates the J/ψ mesons following a thermal fireball model with thermal m_T ($T=170$ MeV) and Gaussian rapidity ($\sigma_y = 0.16$) distributions. For central Au+Au collisions, HSD model predicts the J/ψ multiplicity in 15 A GeV as $m_{J/\psi} = 2.44 \times 10^{-6}$. The corresponding value for Ni+Ni system is obtained by scaling the value down by factor of 5, the ratio of average number of binary collisions for Ni+Ni and Au+Au systems, and comes out to be 5×10^{-7} . We simulated 1M central Ni+Ni collisions at 15 A GeV. The particles from the event generators have been transported through the CBM detector set up using GEANT 3 and reconstructed using standard reconstruction procedure of CBMROOT package. For the analysis, a set of track quality cuts is applied to the global tracks to identify the muon candidates. In the present analysis tracks are selected having i) more than 6 STS hits ii) more than 14 muon hits iii) track STS $\chi^2 \leq 1.5$ iv) track much $\chi^2 \leq 1.5$ and v) vertex $\chi^2 \leq 2$. The invariant mass spectra for the J/ψ mesons along with the combinatorial background is shown in the top panel of Fig. 1. The signal extracted from the embedded events is normalized according to the J/ψ multiplicity calculated above. The combinatorial background is calculated with the mixed event technique applied to 10^6 events generated by UrQMD. The J/ψ mass peak is clearly visible over the background. The bottom panel shows the acceptance of the reconstructed

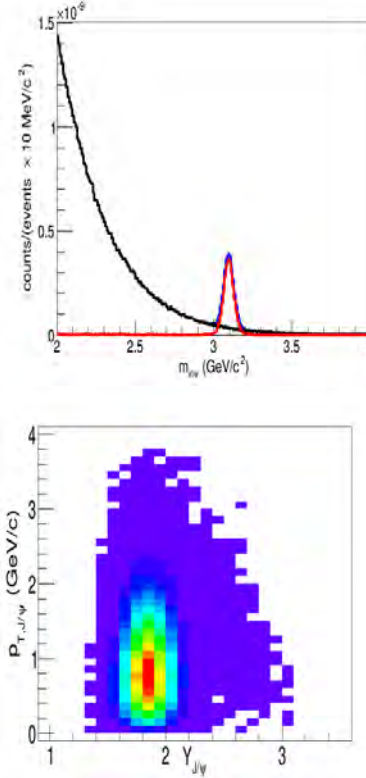


Figure 1: (Top) J/ψ invariant mass spectra in di-muon channel reconstructed in 15 A GeV central Au+Au collisions. The properly normalized spectra for signal (red line) and combinatorial background (black line) are shown separately. Total spectrum (blue line) is the sum of signal and background. (Bottom) Acceptance distribution of the reconstructed J/ψ mesons in the (y, p_T) plane. Mid-rapidity is at $y \simeq 1.73$.

signals. The pair reconstruction efficiency (including the geometrical acceptance of the detector) and S/B ratio are respectively found to be 9.8 % and 3.6. The J/ψ mass resolution is found to be $\sigma_M = 57$ MeV. For minimum bias collisions, J/ψ multiplicity will be factor of 4 lower compared to central collisions. With the maximum foreseen event rate of 10 MHz, the J/ψ yield in di-muon channel, comes out to be 7.35×10^{-3} per second.

References

- [1] P. Senger, Nucl. Phys. A **862-863**, 139 (2011).
- [2] MUCH Technical Design Report.

* p.bhaduri@gsi.de

Simulation of di-muon continuum from correlated open charm decay at FAIR

Partha Pratim Bhaduri^{*1} and Alberica Toia¹

¹GSI, 64291 Darmstadt, Germany

In relativistic heavy-ion collision, various processes of different physical origins contribute to the di-muon invariant mass spectrum measured experimentally. To isolate different sources from the total spectrum and to estimate their respective experimental acceptances, each process needs to be studied independently using input Monte Carlo (MC) simulation method within given experimental conditions. In the continuum region of the invariant mass the relevant contributions arise from the Drell-Yan process, dominating at large di-muon masses and semi-muonic simultaneously decays from two open charm hadrons ($D\bar{D}$ pairs or $\Lambda_C\bar{D}$ pairs). Simulation efforts for development of a MC code to generate muon pairs from Drell-Yan (DY) process, in the FAIR energy regime, was described earlier [1]. In addition to DY di-muons, another component of the physical continuum comes from the electro-weak decays of open charm mesons, which are believed to induce a substantial background to the potentially overwhelming thermal radiation in the intermediate mass region. They also contribute to the J/ψ mass region as well. In this report we describe our first results on the modelling and reconstruction of the di-muon continuum originating from open charm decays, at FAIR energy domain.

In Table 1 we list the possible elementary reactions to produce open charm hadrons, along with the kinematic production thresholds. At FAIR energies, open charm hadrons are produced close to their kinematic production threshold. Thus in addition to D mesons the open charm baryons are also important, owing to smaller production threshold. Note that Σ_c immediately undergoes strong decay to Λ_c via: $\Sigma_c \rightarrow \Lambda_c + \pi^0$. Charm quark distributions are unknown at FAIR energies due to unavailability of data. A standard practice would be to simulate the di-muon distributions from open charm decays with PYTHIA event generator, for generation of the open charm hadrons and their decay into muonic channel. However PYTHIA is based on pQCD calculations and direct use of PYTHIA in the FAIR energy domain is debated. In the present report we developed a toy MC using the momentum and rapidity distributions from HSD [2], and a uniform azimuthal distribution, to create a open charm hadron pair. Two independent production channels are considered namely the $D\bar{D}$ and $\Lambda_C\bar{D}$, relative occurrence of which are decided according to the respective multiplicities of D and Λ_C hadrons. The multiplicities of different open charm mesons, in 25 A GeV central $Au + Au$ collisions, from HSD model are shown in Table 2. Owing to much smaller yield, we ne-

Table 1: Different processes yielding open charm hadrons, relevant at FAIR energy domain. These charmed hadrons further contribute to di-muon mass spectrum via semi-muonic decay channels. N stands for both proton (p) or neutron (n).

Reaction	$\sqrt{s_{th}}$ (GeV)
$N + N \rightarrow N + N + D^+ + D^-$	5.62
$N + N \rightarrow N + N + D^0 + \bar{D}^0$	5.62
$N + N \rightarrow N + N + D_S^+ + D_S^-$	5.82
$N + N \rightarrow N + \Lambda_C^+ + D^0(D^-)$	5.2
$N + N \rightarrow N + \Sigma_C^+ + D^0(D^-)$	5.3

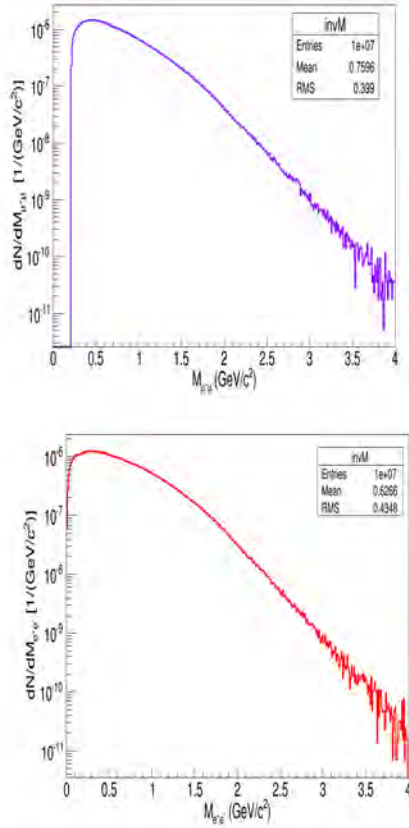
Table 2: Multiplicities of different charmed mesons, in 25 A GeV central $Au + Au$ collisions from HSD [2].

Particle	Multiplicity
D^0	3.74×10^{-5}
\bar{D}^0	1.15×10^{-4}
D^+	4.17×10^{-5}
D^-	8.91×10^{-5}
Λ_c	12.5×10^{-5}

glect the contribution from strange-charm mesons. During random production, open charms hadron pairs are thus produced via $\Lambda_C\bar{D}$ channel with 69% probability and via $D\bar{D}$ channel with 31% probability.

The produced pairs are then independently decayed via semi-muonic channel, weighted by their respective branching ratios, with isotropic decay angular distributions. For D mesons both 3 body (eg: $D^+ \rightarrow \bar{K}^0 \mu^+ \nu_\mu$) and 4 body (eg: $D^+ \rightarrow K^- \mu^+ \pi^+ \nu_\mu$) decay schemes are implemented with 55% and 45% respective probabilities. The resulting di-muon spectrum form a continuum where the yield depends on the product of the branching ratios of two decaying open charm hadrons and the pair multiplicity. The same code can be used to generate the di-electron continuum from open charm decays. Fig. 1 shows the di-muon (top panel) and di-electron (bottom panel) normalized invariant mass spectra from charm decays, generated using our toy MC, for 25 AGeV $Au+Au$ collisions. The di-muon distribution has a mean around 760 MeV, whereas the di-electron distribution peaks around 626 MeV. The single muons from this input di-muon continuum, have also been tracked in GEANT along with all other particles from UrQMD, and reconstructed with the CBMROOT analysis package. The SIS-300 muon detector set up, optimized for J/ψ detection has been used for this purpose. The standard muon analysis

^{*}p.bhaduri@gsi.de



- [2] W. Cassing, E. Bratkovskaya, and A. Sibirtsev, Nucl. Phys. A **691**, 753 (2001); arXiv:nucl-th/0010071 [nucl-th].

Figure 1: Invariant mass distribution of the di-muons (top panel) and di-electrons (bottom panel), originating from correlated decay of open charm hadrons in 25 A GeV Au+Au collisions.

framework has been employed, to select muon tracks from charm decays. The reconstructed invariant mass spectra, is calculated from 100,000 simulated events. The contribution of charm to the di-muon spectra is found to be a few orders of magnitude smaller than that of combinatorial background and even than the Drell-Yan process. For all realistic di-muon analysis at CBM energies, the contribution from open charm decays thus can be safely neglected. At SIS-100 open charm contribution will be absent, as the relevant beam kinetic energies are below the production threshold.

Acknowledgement

We would like to thank Subhasis Chattopadhyay and Tetyana Galatyuk for many stimulating discussions. PPB is supported by the research grant of Prof. A. Toia.

References

- [1] P. P. Bhaduri and S. Chattopadhyay, CBM Progress Report 2014, Darmstadt 2015, p. 131

Online reconstruction of Multi-strange hyperons at SIS 100

*Hamda Cherif^{*1}, Iouri Vassiliev², and Alberica Toia^{1,2}*

¹Goethe University Frankfurt Am Main, Germany; ²GSI, 64291 Darmstadt, Germany

The Compressed Baryonic Matter (CBM) experiment at the future Facility for Antiproton and Ion Research (FAIR) in Darmstadt is designed for precision measurements of observables which are sensitive to high density effects and phase transitions, using the high intensity heavy ion beams provided by the SIS 100/300 accelerators at FAIR. One among the possible signatures of the phase transition from nuclear matter to deconfined phase and formation of the Quark Gluon Plasma (QGP) is the enhanced production of multi-strange particles. As those observables are very rare probes, interaction rates up to 10 MHz are needed to guarantee high-statistics measurements, and the experimental task to identify hadrons, leptons and secondary vertex in collisions with up to about 1000 charged particles requires complex global triggers selections. In this report we investigate the performance of multi-strange hyperons measurement in CBM experiment at SIS 100 the first phase of FAIR project.

Multi-strange hyperons are reconstructed via their weak decay into charged hadrons ($\Lambda \rightarrow p\pi$, $\Xi \rightarrow \Lambda\pi$, $\Omega \rightarrow \Lambda K$). The momentum and the topology of the tracks is measured by the Silicon Tracking System (STS) detector which is installed in a large acceptance dipole magnet. Identification of the decay products is performed by a time-of-flight measurement with TOF detector located at a distance of 6 to 10 m behind the target. We studied the hyperons reconstruction in Au-Au collisions at different energies achievable with SIS 100. We used the UrQMD event generator, coupled to a Geant3-based description of the CBM detector. Tracks were reconstructed with a Cellular Automaton and a Kلمان filter algorithms using the KF Particle Finder package [1]. An example of reconstructed invariant mass spectra of Ξ^- , Ξ^+ , $\bar{\Lambda}$ and Ω^- is shown in Fig. 1 for Au-Au central collisions at 10 AGeV. The red

Table 1: Reconstruction efficiency of $\bar{\Lambda}$, Ξ^- , Ξ^+ , Ω^- and Ω^+ in Au-Au central collisions at 10 AGeV:

	Λ	Ξ^-	Ξ^+	Ω^-	Ω^+
Efficiency(%)	20.6	8.5	6.3	5.1	2.3

line indicates the fit by the sum of a polynomial and Gaussian function. Efficiency of the reconstruction is shown in Table 1.

The measurement of multi-strange hyperons requires a high interaction rates up to 10 MHz. With the high multiplicity of charged particles produced in heavy ions collisions, this leads to huge data rates of up to 1 TB/s. In this environment, the CBM experiment requires a Rejection Factor (RF) of 400 or more. The online event selection is performed by the First Level Event Selector (FLES), a scalable high performance computer with a high-bandwidth interconnect network, whose flexibility allows the implementation of a large variety of trigger signatures.

The rejection factor for a multi-strange hyperons software-trigger at SIS 100 energies has been studied and is shown in Fig. 2 and reported Table 2. It is calculated by dividing the total number of events by the number of selected events containing at least one of the multi-strange hyperons in Table 1. As shown in Fig. 2, the rejection increases with the decreasing energy since multi-strange hyperons become increasingly rare at low energy, thus we achieve the RF's CBM requirement. Fig. 3 shows the rejection factor in Au-Au minimum bias collisions at 8 and 10 AGeV, calculated separately for events containing Ξ^- , Ξ^+ , $\bar{\Lambda}$ and Ω^- . From the comparison to the rejection obtained when selecting events containing at least one of those hyperons, we conclude that selection is mostly dominated by the Ξ^- .

References

- [1] I. Kisel, I. Kulakov and M. Zyzak, IEEE Transactions on Nuclear Science, vol. 60, No. 5, October 2013, p. 3703.

*h.cherif@gsi.de

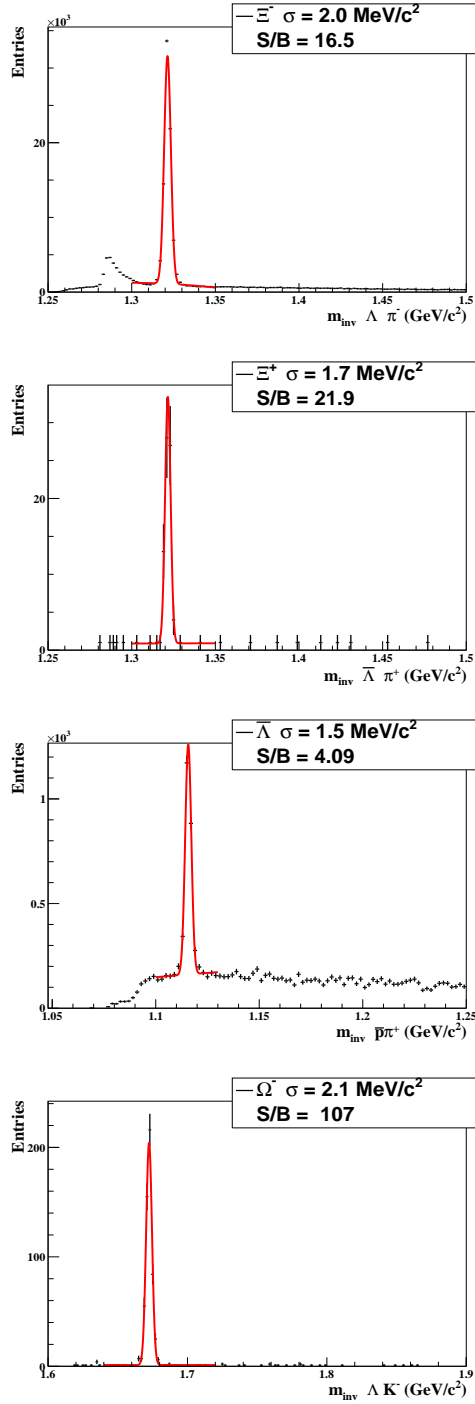


Figure 1: Invariant mass distribution of Ξ^- , Ξ^+ , $\bar{\Lambda}$ and Ω^- reconstructed from their charged weak decays products in Au-Au central collisions at 10 AGeV.

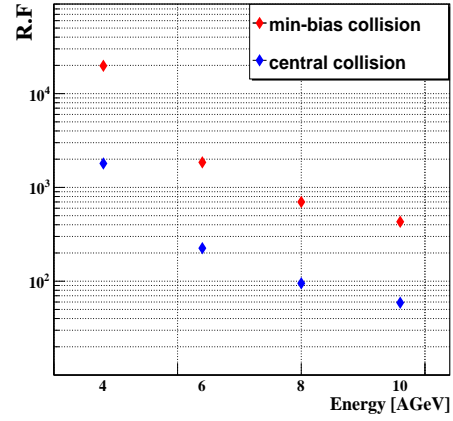


Figure 2: The rejection factor calculated for central and minimum bias collisions at different energies.

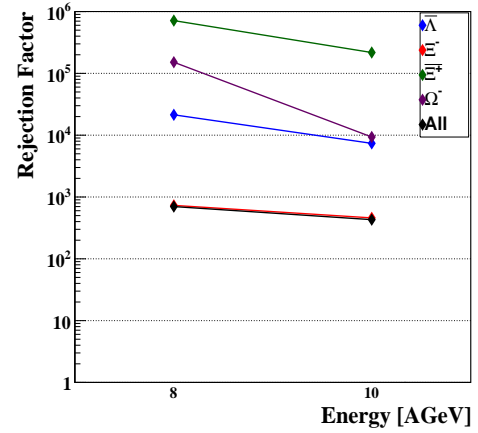


Figure 3: The rejection factor calculated for individual hyperons and compared to the one calculated for all hyperons in minimum bias Au-Au collisions at 8 and 10 AGeV.

Table 2: The rejection factor calculated at SIS 100 energies for central and minimum bias collisions:

	4AGeV	6AGeV	8AGeV	10AGeV
Minimum bias	19800	1850	700	430
Central	1800	225	95	59

Σ^+ and Σ^- reconstruction by the missing mass method*

I. Kisel^{1,2,3}, P. Kisel^{†1,2,4}, P. Senger¹, I. Vassiliev¹, and M. Zyzak^{1,2,3}

¹GSI, Darmstadt, Germany; ²Goethe-Universität Frankfurt, Frankfurt am Main, Germany; ³Frankfurt Institute for Advanced Studies, Frankfurt am Main, Germany; ⁴Joint Institute for Nuclear Research, Dubna, Russian Federation

One of possible signals of QGP formation is enhanced strangeness production. Being abundant particles (several particles per collision are produced at the CBM energies), Σ^+ and Σ^- carry out large fraction of produced strange quarks. Reconstruction of Σ -particles together with other strange particles completes the picture of strangeness production and allows to compare yields of Σ and Σ^* . Reconstruction of Σ -particle will open a possibility to investigate H-dybarion objects, if such exist, by the decay channel $\Sigma^- p$, which is expected to be the dominant one.

All strange mesons and hyperons, except Σ -particles, can be either registered directly by the tracking system and identified by the PID detectors or have decay modes with all charged particles and, as a result, can be reconstructed through their daughters. Σ^+ and Σ^- have all decay modes with at least one neutral daughter, which can not be registered by the CBM detector at all (decay modes with n or ν) or can be registered with an efficiency on the 10^{-7} level (decay modes with π^0). The main channels of Σ^+ , Σ^- and their antiparticles together with the corresponding branching ratios (BR) are:

$\Sigma^+ \rightarrow p\pi^0$	$\bar{\Sigma}^+ \rightarrow \bar{p}\pi^0$	BR 51.57%
$\Sigma^+ \rightarrow n\pi^+$	$\bar{\Sigma}^+ \rightarrow \bar{n}\pi^-$	BR 48.31%
$\Sigma^- \rightarrow n\pi^-$	$\bar{\Sigma}^- \rightarrow \bar{n}\pi^+$	BR 99.8%

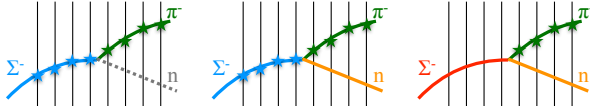


Figure 1: The missing mass method for reconstruction of $\Sigma^- \rightarrow n\pi^-$.

Having a lifetime sufficient to be registered by the tracking system ($c\tau_{\Sigma^+} = 2.4$ cm and $c\tau_{\Sigma^-} = 4.4$ cm), these particles can not be identified by the PID detectors. The missing mass method can be applied for their identification, as illustrated in Fig. 1:

1. tracks of the mother (Σ^-) and the charged daughter (π^-) particles are reconstructed in the tracking system;
2. the neutral daughter particle (n) is reconstructed from these tracks;

* Work supported by BMBF, HICforFAIR and HGS-HIRE for FAIR.

[†] P.Kisel@gsi.de

3. a mass constraint is set on the reconstructed neutral daughter, that modifies also its momentum;
4. the mother particle is constructed out of the charged and reconstructed neutral daughter particles and the mass spectrum is obtained, by which the particle can be identified.

True Σ particles form a peak, while the background will form a continuous structure (Fig. 2).

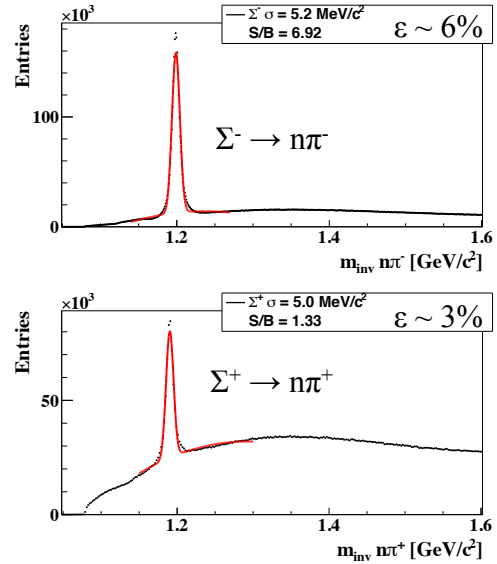


Figure 2: Reconstructed $\Sigma^- \rightarrow n\pi^-$ and $\Sigma^+ \rightarrow n\pi^+$.

The method can be applied for reconstruction of other strange particles, such as:

$$\begin{aligned}
 \Xi^- &\rightarrow \Lambda\pi^- \quad \text{with} \quad \Lambda \rightarrow n\pi^0; \\
 \bar{\Xi}^+ &\rightarrow \bar{\Lambda}\pi^+ \quad \text{with} \quad \bar{\Lambda} \rightarrow \bar{n}\pi^0; \\
 \Omega^- &\rightarrow \Lambda K^- \quad \text{with} \quad \Lambda \rightarrow n\pi^0; \\
 \bar{\Omega}^+ &\rightarrow \bar{\Lambda} K^+ \quad \text{with} \quad \bar{\Lambda} \rightarrow \bar{n}\pi^0; \\
 \Omega^- &\rightarrow \Xi^0\pi^-; \\
 \bar{\Omega}^+ &\rightarrow \bar{\Xi}^0\pi^+.
 \end{aligned}$$

Their investigation will allow to increase the efficiency of the corresponding particles and to investigate systematic errors comparing yields of different decay channels.

Another possible application of the method is suppression of the $\mu^+\mu^-$ background by identifying muons produced in π^\pm and K^\pm decays.

Reconstruction of $\omega(782)$, $\eta'(958)$, Σ^+ and Σ^0 with ECAL in p+C at SIS-100

S.M. Kiselev¹

¹ITEP, Moscow, Russia

The feasibility of the reconstruction of the decays $\omega(782) \rightarrow \pi^+\pi^-\pi^0$, $\eta'(958) \rightarrow \pi^+\pi^-\eta$, $\Sigma^+ \rightarrow p\pi^0$ and $\Sigma^0 \rightarrow \Lambda\gamma$ was studied on a sample of 10^7 p+C (b=0 fm) events from UrQMD at the SIS-100 energy 30 GeV. The set-up consists of STS, RICH, TOF(at 6 m) and the ECAL wall of the size $X \times Y = 4.08 \times 4.80$ m² with the beam gap $|Y| < 0.48$ m distanced from a target at 7.5 m. Reconstructed photons with $p > 0.5$ GeV/c and $\chi^2_{cluster} < 1000$ have been taken for the analysis.

1. $\omega(782) \rightarrow \pi^+\pi^-\pi^0$ (BR=89%). To analyze a signal, we assume that primary π^+ , π^- and π^0 tracks with $0.770 < M_{\pi^+\pi^-\pi^0} < 0.796$ GeV are from "primary" ω . For π^0 candidates the $\gamma\gamma$ pairs with $0.118 < M_{\gamma\gamma} < 0.142$ GeV/c were selected. No particle identification was applied for the selection of π^+ and π^- candidates, but a cut on the impact parameter in the target plane ($< 4\sigma$) was used to suppress secondary charged tracks. Figure 1 (left) shows the invariant mass spectra of signal and background $\pi^+\pi^-\pi^0$ triples.

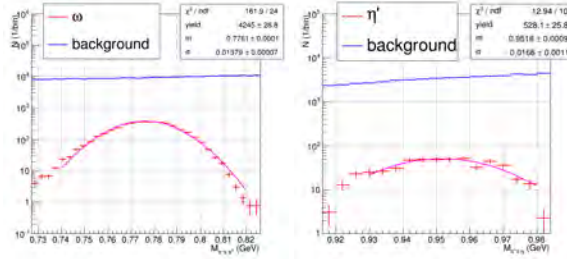


Figure 1: Invariant mass spectra of signal and background $\pi^+\pi^-\pi^0$ (left) and $\pi^+\pi^-\eta$ (right) triples for head-on p+C at 30 GeV

2. $\eta'(958) \rightarrow \pi^+\pi^-\eta$ (BR=43%). We assume that triples of primaries in the range $0.960 < M_{\pi^+\pi^-\eta} < 0.964$ GeV are from "primary" $\eta'(958)$. For η candidates the pairs with $0.530 < M_{\gamma\gamma} < 0.560$ GeV/c were selected. The selection of π^+ and π^- candidates is the same as for the previous decay. Figure 1 (right) shows the invariant mass distributions for selected $\pi^+\pi^-\eta$ triples.

3. $\Sigma^+ \rightarrow p\pi^0$ (BR=52%). For π^0 candidates the pairs with $0.124 < M_{\gamma\gamma} < 0.144$ GeV/c were selected. No PID was used to select the proton candidates. The positive tracks with the impact parameter in the target plane (in σ) > 5 have been used to reject the positive primaries. Figure 2 (left) shows the invariant mass distributions of signal and background $p\pi^0$ pairs of selected candidates.

4. $\Sigma^0 \rightarrow \Lambda\gamma$ (BR=100%). Λ has to be reconstructed through its decay into $p\pi^-$ (BR=64%). For the selection of Λ candidates, no PID is used, but we apply single-track

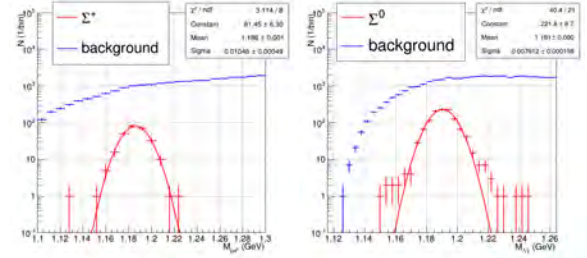


Figure 2: Invariant mass spectra of signal and background $p\pi^0$ (left) and $\Lambda\gamma$ (right) pairs for head-on p+C events at 30 GeV

cuts on the impact parameter in the target plane ($> 4\sigma$) as well as pair cuts on the vertex quality ($\chi^2 < 2$, distance of closest approach < 2 cm). In addition, topological cuts on the pair were applied (impact parameter of pair momentum < 0.15 cm; decay vertex z position 3 -25 cm). Pairs of oppositely charged tracks fulfilling these criteria and having an invariant mass of $m_\Lambda \pm 25$ MeV were taken as a Λ candidate. Figure 2 (right) shows the invariant mass distributions of signal and background $\Lambda\gamma$ pairs.

Table 1 summarizes characteristics of the analysis: signal yield, acceptance, reconstruction, cut and total efficiencies, signal-to-background ratios $S/B_{\pm 2\sigma}$ and significances.

Table 1: Characteristics of the analysis

	yield /event	acc. eff.	rec. eff.	cut eff.	tot. eff.	S/B /sign.
ω	0.03	0.029	0.62	0.84	0.0154	0.02 / 10
η'	0.01	0.012	0.96	0.50	0.0057	0.01 / 2
Σ^+	0.02	0.014	0.46	0.26	0.0017	0.05 / 3
Σ^0	0.03	0.031	0.52	0.21	0.0033	0.09 / 10

For ω and Σ^0 we present the p_t dependence of the S/B ratio, Table 2.

Table 2: (S/B) / significance for ω and Σ^0

p_t (GeV/c)	0.4 - 0.8	0.8 - 1.2	1.2 - 1.6	1.6 - 2.0
ω	0.02 / 6	0.04 / 7	0.06 / 6	0.08 / 4
Σ^0	0.08 / 6	0.13 / 6	0.18 / 4	0.26 / 2

Centrality determination in heavy-ion collisions with the CBM experiment

V. Klochkov and I. Selyuzhenkov

GSI, Darmstadt, Germany

The size and evolution of the medium created in heavy-ion collisions depends on collision geometry, defined by the impact parameter vector, number of participants and binary collisions. The geometric quantities however cannot be measured directly. Experimentally, collisions can be characterized by the measured particles multiplicities around midrapidity or the energy measured in the forward rapidity region, which is sensitive to the spectator fragments. Collisions are grouped into centrality classes with the most central class defined by events with the highest multiplicity (smallest forward energy), corresponding to small values of the impact parameter. In the CBM experiment, the multiplicity of produced particles is measured with the silicon tracking system (STS) [1] with an acceptance in polar angle $2.5^\circ < \Theta < 25^\circ$. We used the total number of reconstructed tracks with at least 3 hits in the 8 STS stations. The projectile spectator detector (PSD) [2], which covers the range in x (y) of $0.21^\circ < \Theta < 5.7^\circ$ (4.3°) at a distance of 8 m from the target, is sensitive mostly to spectator fragments (outer modules are also sensitive to produced particles). The PSD modules were grouped into PSD1, PSD2 and PSD3 as shown in the Fig. 1.

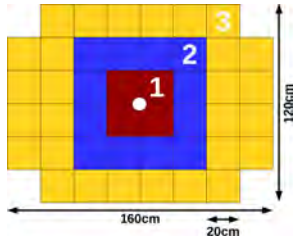


Figure 1: Layout of the PSD modules transverse to the beam. Colors show the groups used in the analysis: PSD1 (red), PSD2 (blue) and PSD3 (yellow).

To study the performance of the centrality determination, 10K Au+Au collisions with beam energy of 10 AGeV simulated with DCM-QGSM (see Ref. [18–28] in [2]) and UrQMD [3] event generators were used. The CBM setup (simulated with CBMRooT version Jul15) includes the beam pipe, the standard STS and magnet configuration, and the PSD geometry with 44 modules elongated in x direction with a 6 cm hole in the center. Event-by-event centrality is determined with the following procedure:

1. STS multiplicity (M_{STS}) and energy deposited in PSD subgroup (E_{PSD}) scaled by their maximum value (M_{STS}^{max} and E_{PSD}^{max}).
2. Parameterise the 2D correlation between multiplicity and/or PSD subgroup energies (see Fig. 2 right panel):
 - (a) initial fit of the profile (red circles) of the correlation using a polynomial function (red line);
 - (b) recalculate the profile (black triangles) according to the fit slope and refit (red line).
3. Slice the 2D correlation perpendicular to the fit (Fig. 2 left panel) or 1D distribution (not shown) in percentiles of total number of events.

- (b) recalculate the profile (black triangles) according to the fit slope and refit (red line).
3. Slice the 2D correlation perpendicular to the fit (Fig. 2 left panel) or 1D distribution (not shown) in percentiles of total number of events.

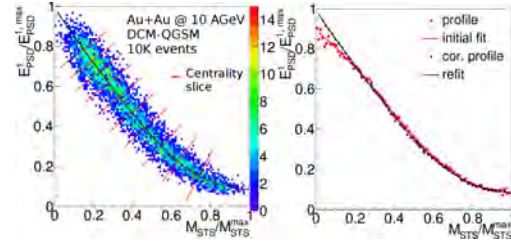


Figure 2: Illustration of the centrality determination procedure (left) with equal percentiles. The correlation between the energy deposited in the PSD1 and the STS multiplicity overlaid with the result of the fit procedure (right).

For each centrality class, the mean value of the impact parameter and its corresponding standard deviation was found using simulated information. In the Fig. 3 centrality dependence of the impact parameter resolution for different centrality estimators and two different generators is shown.

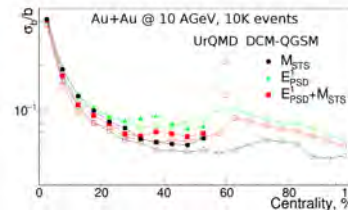


Figure 3: The impact parameter resolution with different centrality estimators calculated with UrQMD and DCM-QGSM models. Centrality class 0-5% corresponds to most central events, while 95-100% to the most peripheral.

In summary, we observe that the impact parameter resolution obtained with the PSD is comparable to that of the STS. Using correlations between STS and PSD slightly improves the resolution in central (0-30%) collisions. In the future the procedure for centrality determination will be extended to estimate the total cross-section and determine the absolute scale of the centrality using a Glauber model.

References

- [1] J. Heuser et al. [CBM Collaboration], TDR for the CBM STS, <http://repository.gsi.de/record/54798>.
- [2] F. Guber et al. [CBM Collaboration], TDR for the CBM PSD, <https://repository.gsi.de/record/109059>.
- [3] M. Bleicher et al., J.Phys. G25, 1859 (1999).

Background rejection in the dielectron analysis with the CBM Micro-Vertex Detector*

E. Krebs¹, T. Galatyuk^{2,3}, and J. Stroth^{1,3}

¹Goethe-Universität, Frankfurt, Germany; ²Technische Universität Darmstadt, Germany; ³GSI Darmstadt, Germany

The leptonic decay channels of the light vector mesons ρ , ω and ϕ are excellent probes of the strongly interacting matter under extreme conditions. This study aims at exploring the use of the CBM Micro-Vertex Tracker (MVD) to reduce the background from π^0 -Dalitz decays and γ -conversions.

To do so, electron pairs from meson decays have been simulated from a thermal source for central Au+Au reactions at SIS-100 energies such that the meson spectra are consistent with p_T and rapidity distributions measured by NA49 [1]. The decays of various sources simulated with the Pluto [2] event generator are embedded into the hadronic environment generated with UrQMD. In-medium modifications of the ρ spectral functions calculated by Rapp and Wambach [4] and dileptons from QGP radiation have been included in the Pluto cocktail [5]. The magnetic field was set to 100% strength. Particle identification is only based on the acceptance of Monte-Carlo tracks in the RICH and TRD detectors. No δ -electrons have been added.

The strategy of background rejection comprises several steps. In order to identify leptons from photon conversions that were produced outside of the target region, each reconstructed track is extrapolated to the primary decay vertex and removed from the analysis depending on its deviation to the vertex. One characteristic for conversion pairs is their small opening angle. A wedge-cut is applied taking into account the opening angle of an identified electron to its closest neighbor without particle identification and the product of the momenta of the two tracks [3].

The MVD of the CBM experiment can further contribute to reduce this background by including points from the MVD into the track reconstruction. An improved rejection of pairs originating from the target region could be observed. Previous studies have shown that the MVD stations are also a source for γ -conversions which can not be effectively rejected by the vertex extrapolation cut, especially in the first two stations closest to the target. Extrapolating tracks to the first MVD station and requiring that they are in its acceptance improved the suppression off-vertex tracks from γ -conversions.

Adding the MVD into the analysis results in a higher signal-to-background ratio. However, the cut efficiency is around 12% lower. As the significance is higher there is still a gain with the MVD (see Tab. 1). The signal-to-background as a function of invariant mass of the full cocktail after all analysis steps is presented in Fig. 1.

Mass Range [$\frac{\text{GeV}}{c^2}$]	Cut Efficiency	S/B	S/ $\sqrt{S+B}$
Without MVD			
0 – 0.15	$(25 \pm 1)10^{-2}$	4.7 ± 0.1	238 ± 1
0.15 – 0.5	0.75 ± 0.01	0.19 ± 0.01	57.2 ± 0.4
0.5 – 1.2	0.81 ± 0.01	0.26 ± 0.01	46.6 ± 0.4
$\omega \rightarrow e^+e^-$	0.81 ± 0.02	0.73 ± 0.01	42.8 ± 0.5
$\phi \rightarrow e^+e^-$	0.83 ± 0.07	0.20 ± 0.01	6.3 ± 0.4
With MVD			
0 – 0.15	$(21 \pm 1)10^{-2}$	5.8 ± 0.1	234 ± 1
0.15 – 0.5	0.67 ± 0.01	0.28 ± 0.01	64.4 ± 0.4
0.5 – 1.2	0.69 ± 0.01	0.46 ± 0.01	53.4 ± 0.5
$\omega \rightarrow e^+e^-$	0.68 ± 0.01	1.3 ± 0.1	45.4 ± 0.6
$\phi \rightarrow e^+e^-$	0.71 ± 0.06	0.38 ± 0.03	7.5 ± 0.5

Table 1: Signal-to-background ratios and significance (with statistical errors) for dilepton decays in different mass regions. A cut efficiency of 1 corresponds to the amount of dielectrons after PID.

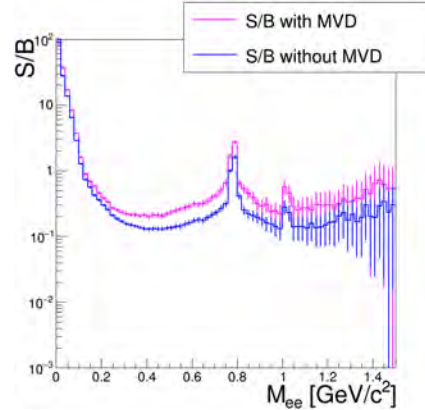


Figure 1: Signal-to-background ratio over invariant mass spectrum after all cuts are applied for central AuAu collisions at 8A GeV, with statistical error bars.

References

- [1] C. Alt et al. (NA49 Collab.), Phys. Rev. C 78, 044907 (2008)
- [2] I. Froehlich et al., arXiv:0708.2382
- [3] T. Galatyuk, PhD Thesis, Goethe-Universität, Frankfurt am Main, (2009)
- [4] R. Rapp and J. Wambach, Adv. Nucl. Phys. 25(2000) 1
- [5] F. Seck et al., Towards a realistic even generator for in-medium and QGP dileptons, CBM Progress Report 2014

*This work has been supported by BMBF (05P12RFFC7), HIC for FAIR, HGS-HIRE, H-QM, and GSI.

Deuteron coalescence for central $Au + Au$ collisions at 4 A·GeV

V.P. Ladygin^{*1}, M.I. Baznat^{1,2}, K.K. Gudima^{1,2}, and N.B. Ladygina¹

¹LHEP-JINR, Dubna, Russian Federation; ²IAP, ASM, Kishinev, Moldova

The measurements of the yields of light nuclei, which are formed by the coalescence of individual nucleons is an alternative to HBT interferometry method to extract the information on the source at freeze-out. The coalescence factor B_2 at SIS100 energies [1] can be expressed through the invariant cross sections of the deuteron and proton production as following $B_2 = 0.84 \cdot E_d \frac{d^3 N_d}{dp_d^3} / \left(E_p \frac{d^3 N_p}{dp_p^3} \right)^2$, where $E_d \frac{d^3 N_d}{dp_d^3}$ and $E_p \frac{d^3 N_p}{dp_p^3}$ are the invariant cross sections of the deuteron and proton production, respectively.

The simulation has been performed for 10K of the $Au + Au$ central events at 4 A·GeV using Dubna Cascade Model [2] for the hadron version of the CBM detector at SIS100. The secondary particles have been selected using m^2 - p/Z correlation, where momentum and time-of-flight were reconstructed from STS and TOF information, respectively. The purity of the selection for the both protons and deuterons was found $\sim 97\%$ [3].

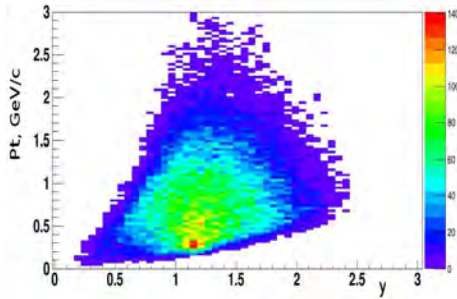


Figure 1: $y - p_T$ distribution for deuterons from $Au + Au$ central collisions at 4 A·GeV [2].

The transverse momentum- rapidity, $y - p_T$, distribution for deuterons from the $Au + Au$ central collisions at 4 A·GeV [2] is presented in Figure 1. The dominant reaction mechanism is a coalescence. The deuterons and protons with the rapidity of $1.0 \leq y \leq 1.5$ were selected for further analysis of the coalescence factor B_2 . The yield of the reconstructed deuterons and protons in this rapidity range are ~ 2.7 and ~ 25.2 per event, respectively.

The $1/m_t \cdot d^2 N / dm_t dy$ distribution for deuterons from the $Au + Au$ central collisions at 4 A·GeV [2] is presented in Figure 2. The events are selected within the rapidity region of $1.0 \leq y \leq 1.5$. The line is the results of the exponential fit at $m_t - m_0 \geq 0.4$ GeV/ c^2 . The similar distribution has been obtained for protons. The inverse slopes of

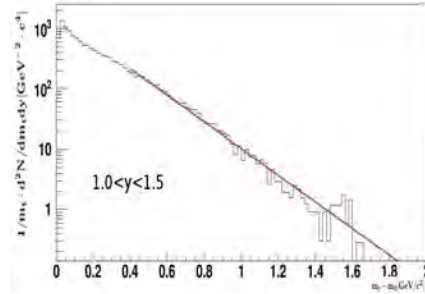


Figure 2: Transverse mass distribution for deuteron produced in the $Au + Au$ central collisions at 4 A·GeV [2].

the transverse mass distributions are $T_p = 166 \pm 1$ MeV and $T_d = 197 \pm 4$ MeV for protons and deuterons, respectively. The value of coalescence factor, calculated at $p_t = 0$, $B_2(m_t = m_0) = (3.1 \pm 0.2) \cdot 10^{-3}$ GeV² is larger by one order of magnitude than that measured in central $Pb + Pb$ collisions at SPS [4]. The B_2 factor increases exponentially as a function of the transverse mass difference $m_t - m_0$ with the inverse slope $T \approx 1.56$ GeV.

In a simplified coalescence model [5] a relation between the source radius R_G and the B_2 factor is defined as $R_G^3 = 3/4 \cdot \sqrt{\pi}^3 \cdot m_d / (m_p^2 \cdot B_2)$. Therefore R_G , calculated using the B_2 value, also depends on m_t , decreasing for increasing m_t , and is 2.80 ± 0.07 fm at $m_t - m_d = 0$. The source size value found from the deuteron coalescence is a twice smaller than that obtained by the two-pion HBT correlation techniques [6].

The systematic studies of the energy and centrality dependencies of the light nuclear fragments production with CBM setup at SIS100 could allow to obtain additional information on the source size evolution.

References

- [1] T.A. Armstrong et al., Phys.Rev. C61 (2000) 064908.
- [2] V.D. Toneev, N.S. Amelin, K.K. Gudima, S.Y. Sivoklov, Nucl.Phys. A519 (1990) 463C.
- [3] V.P. Ladygin et al., CBM Progress Report 2014, Darmstadt 2015, p.112.
- [4] S.V. Afanasiev et al., Phys.Lett. B486 (2000) 22.
- [5] W. Llope et al., Phys.Rev.C52 (1995) 2004.
- [6] S.Y. Panitkin et al., Phys.Rev.Lett. 87 (2001) 112304.

*vladygin@jinr.ru

Results on the reconstruction of π^0 with the conversion method*

S. Reinecke¹, K.-H. Kampert¹, C. Pauly¹, C. Höhne², and T. Mahmoud²

¹Bergische Universität, Wuppertal, Germany; ²Justus-Liebig-Universität, Gießen, Germany

The studies presented in last years Progress Report have been further extended towards an analysis only based on reconstructed data. Also a deeper investigation with the combined method (i.e. particle identification with the matched MC-true data of a global track and combination with the reconstructed momenta) has been done. The results shown here are based on $5 \cdot 10^6$ simulated UrQMD events for the SIS100 electron setup with a beam energy of 10 AGeV and central Au+Au collisions. The latest geometry version from September 2015 is used, the magnetic field was scaled to 70 % of nominal value.

With the combined method it is possible to estimate the maximum possible number of reconstructed π^0 based on the identified electrons in the RICH and their matching MC-true tracks. Different properties of those π^0 can then be studied in detail. One important parameter, especially for the efficiency of this method, is the phase-space coverage of the reconstructed particles, shown in Fig. 1 (right).

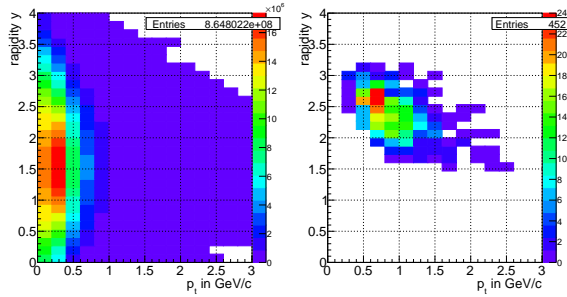


Figure 1: Phase-space coverage of simulated (left) and reconstructed (right) π^0 calculated with the combined method, i.e. identification with the matched MC-true data, but based on all reconstructed tracks in the RICH, and combination with refitted momenta.

A clear cut for a rapidity $y < 1.5$ can be identified, resembling the maximum detector acceptance of 25° , and a cut for very small transversal momenta p_t of the π^0 . The limitation towards small p_t is caused by the magnetic field and can be extended by only requiring three of the four leptons from a π^0 to be detected in the RICH detector, with the fourth lepton only leaving a signal in the STS. In addition a slight improvement towards lower rapidity regions can be achieved and a high gain in statistics of the π^0 peak (factor 3 – 4). Simulations with an even lower magnetic field of only 30 % proof this limitation due to the magnetic field.

Based on reconstructed data only few cuts are applied, including a cut on the $\chi^2_{\text{prim.}}$ of the momentum fit ($\chi^2 \leq 31 - 70 \cdot p_t$ for $p_t < 0.4$ GeV/c, $\chi^2 \leq 3$ for $p_t \geq 0.4$ GeV/c), and on the opening angle ($\theta \leq 1.8^\circ - 0.6^\circ \cdot p_t$) and invariant mass ($m_{\text{inv}} \leq 0.03$ GeV/c²) of the e^+e^- pairs. With these cuts applied to the data the invariant mass spectrum in Fig. 2 (red histogram) can be derived for the requirement of 4 identified electrons in the RICH and integrated over the whole p_t and rapidity range. The background was estimated with the Event Mixing Technique (EMT; blue histogram) and was subtracted from the spectrum (black histogram).

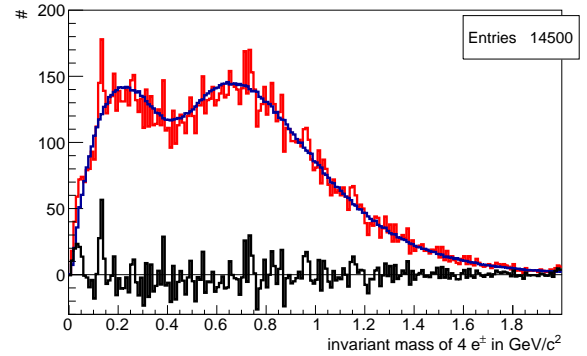


Figure 2: Invariant mass spectrum for the reconstruction of π^0 with the conversion method (red) and the estimated background from EMT (blue). The black histogram shows the background-subtracted spectrum.

A clear π^0 peak can be identified although the statistical errors per bin are significant. Fitting the π^0 peak with a Gaussian and considering the complete range of the spectrum yields a width of 6 – 7 MeV/c². Counting the number of π^0 within this peak results in about 80 reconstructed π^0 with a signal-to-background ratio of around 15 % within the 3σ region of the peak.

There is a second peak at low invariant masses, which is not visible in the EMT background and must therefore stem from correlated photons within one single event. A detailed analysis of this contribution is still ongoing.

In summary these studies show, that the reconstruction of π^0 (and for higher statistics probably also η) with the conversion method works and gives very good results, although the reconstruction efficiency is very low. The low amount of available statistics leads to high (but manageable) variances within the spectrum. Therefore statistics of at least a factor of 10 more are highly required.

* Work supported by BMBF Verbundforschung, grant 05P15PXPCA.

Reconstruction of D^0 with KF Particle Finder*

I. Kisel^{1,2,3}, I. Vassiliev¹, and M. Zyzak^{†1,2,3}

¹GSI, Darmstadt, Germany; ²Goethe-Universitaet Frankfurt, Frankfurt am Main, Germany; ³Frankfurt Institute for Advanced Studies, Frankfurt am Main, Germany

Investigation of the charm production is one of the main tasks for the CBM experiment. According to the current theoretical models charm is expected to be an extremely sensitive probe of the properties of the dense matter created in heavy ions collisions. Moreover, charm production mechanisms at the CBM energies are not studied yet. At these energies charm quarks are expected to be produced in primary hard scattering processes, thus, providing a possibility to study the early phases of the collision. Depending on the interaction with the medium, they hadronize into D mesons, charmed baryons, or charmonium.

Open charm is considered as one of the possible triggers for the CBM experiment. Therefore reconstruction of the open charm was added to the KF Particle Finder package, which will be run at the CBM online computing farm as a part of the FLES package.

Because of the low multiplicity, studies of open charm background can not be performed on the event-by-event level. Therefore the mixed event technique for the background simulation was added to the KF Particle Finder: tracks produced in different UrQMD collisions are mixed and combined with each other, that gives the random combinations growing quadratically with the number of events. Such technique allows to estimate the background for the several orders higher statistics than a usual event-by-event analysis.

With these new tools, feasibility of D^0 and \bar{D}^0 reconstruction was studied in central NiNi events at 15 AGeV. For these studies, a configuration of the CBM detector including realistic geometries of the MVD (version 14b), the STS (version 13d) and the TOF (version 13b) detectors was used. Tracks were reconstructed by the Cellular Automaton based track finder in STS and MVD, their identification was performed using TOF information. In order to reproduce a realistic response of the MVD detector, the simulation also includes delta electrons produced by the Ni ions passing through the target and pileup events corresponding to the interaction rate of 100 kHz.

Particle	$\varepsilon_{method}, \%$	$\varepsilon_{4\pi}, \%$	S/B	$\sigma, \text{MeV}/c^2$
D^0	7.6	1.7	0.4	10.6
\bar{D}^0	7.6	1.7	0.7	11.1

Table 1: Efficiency of D^0 and \bar{D}^0 reconstruction, widths of the signal peaks, and S/B for 10^{11} simulated central NiNi events at 15 AGeV using TOF PID.

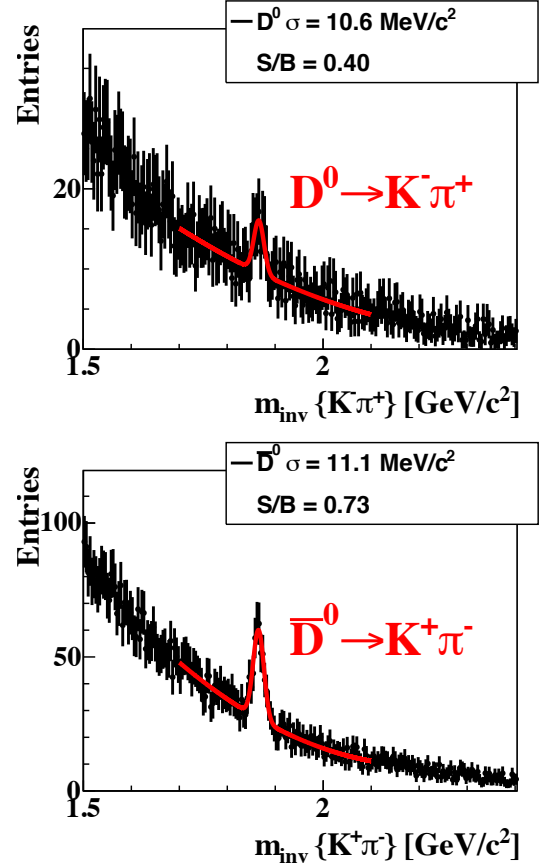


Figure 1: Mass spectra of D^0 and \bar{D}^0 mesons obtained by the KF Particle Finder package together with their signal to background (S/B) ratios for 10^{11} simulated central NiNi events at 15 AGeV using TOF PID. The mixed event technique is used for the background estimation.

The mass spectra of D^0 and \bar{D}^0 obtained by the KF Particle Finder for 10^{11} central NiNi events at 15 AGeV using TOF PID are shown in Fig. 1. Corresponding efficiencies, signal to background (S/B) ratios, and widths of the peaks are given in Table 1. A small lifetime ($c\tau$ of hundreds μm) together with a low multiplicities of open charm particles require tight cuts in order to achieve high S/B ratio, that leads to a smaller reconstruction efficiency.

Summarizing, tools for open charm analysis are added to the KF Particle Finder package.

* Work supported by HICforFAIR, FIAS and HGS-HiRe for FAIR.

[†] m.zyzak@gsi.de

Hypernuclei reconstruction at the CBM experiment*

I. Kisel^{1,2,3}, I. Vassiliev¹, and M. Zyzak^{1,2,3}

¹GSI, Darmstadt, Germany; ²Goethe-Universitaet Frankfurt, Frankfurt am Main, Germany; ³Frankfurt Institute for Advanced Studies, Frankfurt am Main, Germany

In the CBM experiment at FAIR ultra-high net-baryon densities and moderate temperatures will be reached in heavy-ion collisions. Model calculations predict structures in the QCD phase diagram at large baryon chemical potentials, like the critical endpoint followed by a first order phase transition. Moreover, new phases are predicted, such as quarkyonic matter.

Theoretical models predict that single and double hypernuclei are produced via coalescence in heavy-ion collisions with the maximum yield in the region of SIS100 energies. Discovery and investigation of new hypernuclei and of hypermatter will shed light on the hyperon-nucleon and hyperon-hyperon interactions, which are essential ingredients for the nuclear equation-of-state at high densities and moderate temperatures. Beam energies available at SIS100 appear to be especially well suited for generating signals of the phase transition. To study the performance of multi-strange hyperon and hypernuclei reconstruction, several sets of $5 \cdot 10^6$ central Au+Au UrQMD events (Fig. 1) at the FAIR energy range have been simulated.

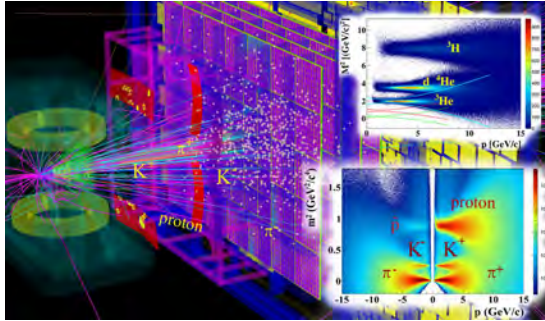


Figure 1: A simulated CBM event of a Au + Au collision at 15 AGeV. The TOF detector identifies hadrons i. e. pions, kaons, protons and fragments.

The combination of MVD and STS segmented strip detectors, cables and support frames was used for event simulation and reconstruction. The TOF detector identifies hadrons i.e. pions, kaons, protons, and fragments, i. e. d , t , ${}^3\text{He}$ and ${}^4\text{He}$ in the angular range covered by the STS detector.

The current KF Particle package includes searching for the bound state $\{\Lambda n\}_b$, ${}^3_\Lambda\text{H}$, ${}^4_\Lambda\text{H}$, ${}^4_\Lambda\text{He}$, ${}^5_\Lambda\text{He}$ and corresponding anti-particles. Searching for double hypernuclei ${}^4_{\Lambda\Lambda}\text{H}$ and ${}^6_{\Lambda\Lambda}\text{He}$ is under development. Hypernuclei will be reconstructed in the CBM experiment by

* Work supported by HICforFAIR, FIAS and HGS-HiRe for FAIR.

their detached from the primary vertex decays into charged hadrons and fragments, like d , t , ${}^3\text{He}$ and ${}^4\text{He}$. A reconstructed ${}^4_\Lambda\text{He} \rightarrow \pi^- p {}^3\text{He}$ decay is shown in Fig. 2.

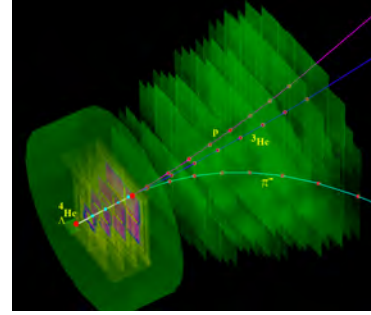


Figure 2: A reconstructed ${}^4_\Lambda\text{He} \rightarrow \pi^- p {}^3\text{He}$ decay topology.

${}^4_\Lambda\text{He}$ hypernuclei are created at the primary vertex and decay to $\pi^- p {}^3\text{He}$ several centimeters downstream of the target. Presence of the ${}^3\text{He}$ fragment in a 3-prong vertex is a unique signature of such decay. The reconstructed invariant-mass spectrum of $\pi^- p {}^3\text{He}$ is shown in Fig. 3.

Small amount of background events in the high-mass region is due to misidentified high-momentum hadrons in the sample of ${}^3\text{He}$ selected particles.

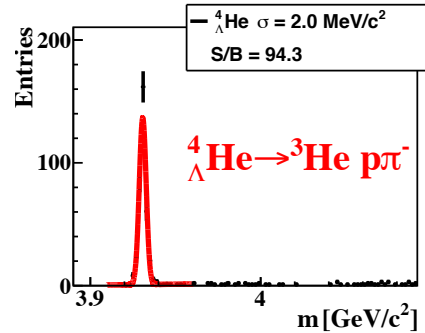


Figure 3: The reconstructed invariant-mass spectrum of $\pi^- p {}^3\text{He}$ in $5 \cdot 10^6$ central Au+Au collisions at 10 AGeV. The red line indicates the signal plus background fit by a polynomial plus Gaussian function.

Assuming the ${}^4_\Lambda\text{He}$ production multiplicity for minimum bias Au+Au events at 10 AGeV about $5 \cdot 10^{-4}$, the branching ratio of 20% to $\pi^- p {}^3\text{He}$ decay, taking into account the 14.7% ${}^4_\Lambda\text{He}$ detection efficiency, one would expect the ${}^4_\Lambda\text{He}$ collection rate of up to $5.4 \cdot 10^5$ per hour.

Feasibility studies for the measurement of J/ψ mesons in central Au+Au collisions at 25 AGeV beam energy

A. Weber, S. Lebedev, and C. Höhne

Justus-Liebig Universität, Giessen, Germany

Feasibility studies of the measurement of J/ψ production in central Au+Au collisions at 25 AGeV beam energy using the newest CBM geometry and detector response have been performed. More details can be found in Ref. [1]. We investigated the leptonic decay mode $J/\psi \rightarrow e^+ + e^-$. The event background was created with UrQMD v3.3. The J/ψ mesons were simulated with PLUTO and the corresponding multiplicity was taken from HSD calculations. GEANT was used in Version 3. In CbmRoot the following geometries were used: STS *v_13d* ; RICH *v_14a.3e* ; TOF *v_13b* ; TRD: *v_14a.3e*. The MVD was not used. For hit reconstruction in the TRD the so called "hit smearing" was used. Track reconstruction was done with L1 and Lit-track.

Each electron candidate was required to have at least 4 hits in the STS, 7 hits in the RICH, 6 hits in the TRD and minimum 1 hit in the TOF detector. The final analysis used the STS, RICH and TRD detectors. For PID (RICH and TRD) the technique of artificial neural networks was used. For track selection $\chi^2_{prim} < 3$ was required, for electron ID RichANN > 0.7 and TrdANN > 0.8 and for background suppression $P_t > 1$ GeV/c.

First, a simulation with a 250 μm target was done. Fig.1 shows the invariant mass spectrum of this simulation. Only a small peak on top of the background is seen. The background was created by using the superevent technique which combines a negative charged particle with all positive charged particles from all simulated events. After applying all cuts the efficiency reached 5.3 % with a signal to background ratio of 0.168. Although the Pion suppression factor reached 74819.

An analysis of the background showed that most of the background stemmed from γ -conversion inside the target. Therefore, the target thickness was reduced to 25 μm for the second simulation. This change should decrease the dominant background from γ -conversion by approximately a factor 10. The corresponding invariant mass spectrum is shown in Fig. 2 showing a clear peak of the J/ψ above the background. Under these conditions, we obtain an efficiency of 6% with a 1.673 S/B ratio and a Pion suppression factor of 82499 .

In summary it was shown, that also with the most realistic detector setup of CBM the J/ψ meson can be successfully measured in the di-electron channel. However, the study again underlines that a thin, i.e. finally segmented target has to be used in order to suppress significantly background from γ -conversions in the target.

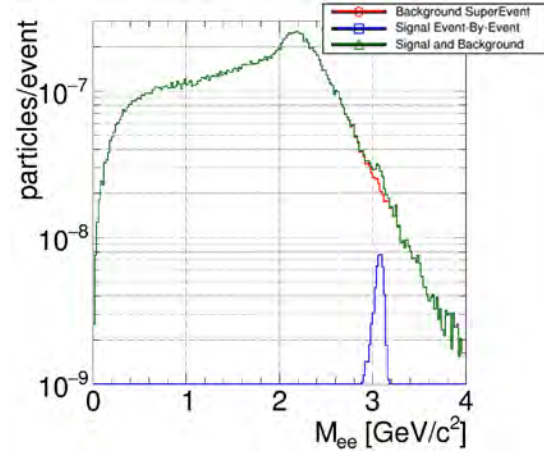


Figure 1: J/ψ meson in central Au+Au collisions at 25 AGeV beam energy, 250 μm target. The spectrum corresponds to 9.614.039.330 events in the superevent technique.

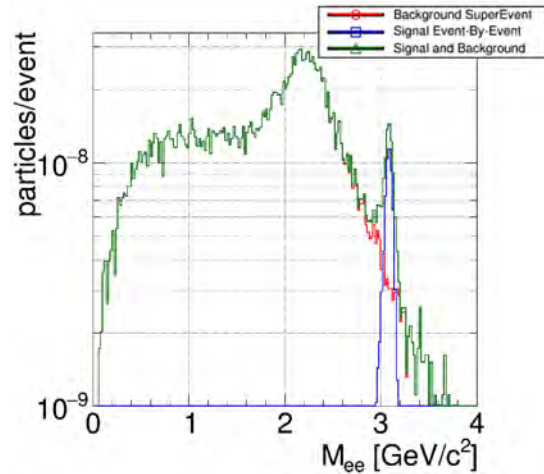


Figure 2: J/ψ meson in central Au+Au collisions at 25 AGeV beam energy, 25 μm target. The spectrum corresponds to 9.700.394.300 events in the superevent technique.

References

- [1] A. Weber, "Feasibility studies for the measurement of J/ψ mesons in central Au+Au collisions at 25 AGeV beam energy at the CBM experiment at FAIR", September 2015, Giessen, <https://www-alt.gsi.de/documents/DOC-2015-Nov-5.html>

Reconstruction of dimuons with KF Particle Finder*

I. Kisel^{1,2,3}, D. Radevych⁴, I. Vassiliev¹, and M. Zyzak^{† 1,2,3}

¹GSI, Darmstadt, Germany; ²Goethe-Universitaet Frankfurt, Frankfurt am Main, Germany; ³Frankfurt Institute for Advanced Studies, Frankfurt am Main, Germany; ⁴Taras Shevchenko National University of Kyiv, Kyiv, Ukraine

One of the most promising observables for the CBM experiment are J/ψ and low mass vector mesons (LMVM), which are extremely important for investigation of the dense baryonic matter. The probability of the charmonium creation strongly depends on the properties of the baryonic medium formed in the collision, that makes it well suited for the QCD phase diagram exploration. LMVM are perfectly suited for investigation of early stages of the collision because of their extremely low lifetime.

J/ψ and LMVM can be reconstructed through the dimuon channel. Muons do not interact strongly, therefore they pass through the baryonic matter that is formed during the collision without interaction and carry out exactly the information about the parent particle and its properties.

Reconstruction of dimuons using MuCh PID was added to the KF Particle Finder package. The low multiplicities (J/ψ) and branching ratio of the dimuon channel (LMVM) require tight cuts on the PID stage. Tracks which are used for reconstruction of dimuon should fulfill additional criteria of being primary, the STS track should be matched with a MuCh track, both STS and MuCh tracks should pass cuts on χ^2 value and on the minimum number of hits. In case of J/ψ the cut on the number of hits in MuCh track is tighter since muons produced in its decay are high energetic. Also, as it follows from the decay topology, muons from J/ψ decay should have $p_t > 1.5$ GeV each.

Particle	$\varepsilon_{method}, \%$	$\varepsilon_{4\pi}, \%$	S/B	$\sigma, \text{MeV}/c^2$
$J/\psi \rightarrow \mu^+\mu^-$	15.1	6.9	0.79	29.3
$\rho \rightarrow \mu^+\mu^-$	45.4	1.2	0.007	149.0
$\omega \rightarrow \mu^+\mu^-$	42.1	1.1	0.147	8.5
$\phi \rightarrow \mu^+\mu^-$	48.5	2.1	0.045	4.2

Table 1: J/ψ and LMVM reconstructed by the dimuon channel: efficiency, width of the signal peak, and S/B.

Due to the low multiplicities of the muons and tight cuts, analysis of the background can not be performed on the event-by-event level. For simulation of the background the mixed event technique implemented in the KF Particle Finder is used: tracks produced in different UrQMD collisions are mixed and combined with each other, that gives the number of arbitrary combinations growing quadratically with the number of events. Such technique allows to estimate the background for the several orders higher statistics than a usual event-by-event analysis.

* Work supported by HICforFAIR, FIAS and HGS-HiRe for FAIR.

[†] m.zyzak@gsi.de

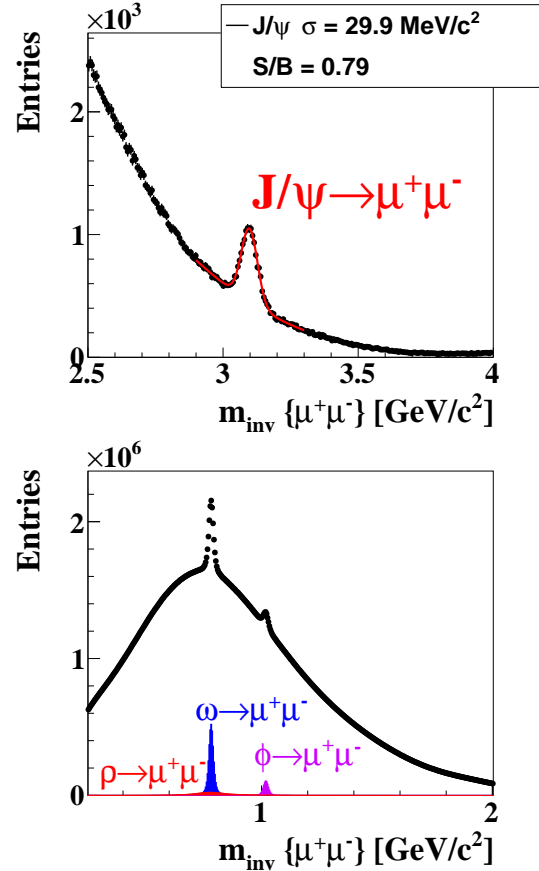


Figure 1: Mass spectra of J/ψ and LMVM together with their signal to background (S/B) ratios in dimuon channel for 10^{11} simulated central AuAu events at 25 AGeV using MuCh PID and mixed event technique.

The mass spectra of J/ψ and LMVM decaying by the dimuon channel obtained by the KF Particle Finder for 10^{11} central AuAu events at 25 AGeV using MuCh PID is shown in Fig. 1. Corresponding efficiencies, signal to background (S/B) ratios, and widths of the peaks are given in Table 1.

Summarizing, tools for dimuon analysis with MuCh PID are added to the KF Particle Finder package.

CBM Physics

$$\frac{\chi_q}{T^2} = \sum_{i \in baryons} 9F(T, m_i) \cosh \frac{3\mu_q}{T}$$

$$\begin{aligned} \frac{\chi_I}{T^2} &= \sum_{i \in mesons} (2I_i^{(3)})^2 F(T, m_i) + \sum_{i \in bary} \\ &= \frac{8}{3} G^{(3)} + (F^{(2)} + 5F^{(4)}) \cosh \frac{3\mu_q}{T} \end{aligned}$$

Mass and Quark number dependence of elliptic flow with the AMPT model at FAIR Energies

S. Bashir, S. Ahmad, and M. Farooq Mir

University of Kashmir, Srinagar India

Elliptic flow is the second Fourier coefficient of anisotropy of the momentum space particle distribution in the x-y plane defined as:

$$v_2 = \langle \cos 2(\phi - \psi) \rangle \quad (1)$$

where ϕ is the azimuthal angle of an outgoing particle ψ is the orientation of the reaction plane and the angular brackets denote averaging over many particles and many events. In this preliminary investigation we report some aspects of the elliptic flow in Au + Au collision at E_{lab} of 25 A GeV FAIR energies by the event plane method i.e by taking ψ into account in the mid-pseudorapidity of $|\eta| \leq 0.35$ by the AMPT model with both the versions default and the string melting version as shown in fig 1.

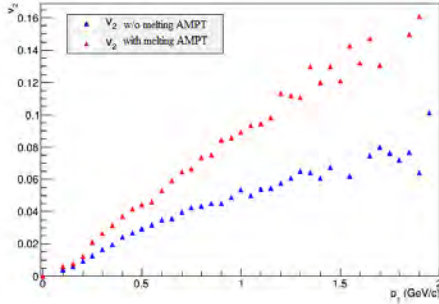


Figure 1: variations of v_2 for all particles with p_T by the default i.e hadronic and the string melting i.e partonic versions of the AMPT model

In both the models we have observed that there is a linear rise of v_2 with p_T and then levels off. At higher p_T the contribution from particles that are not correlated to the reaction plane grows which results in a deviation from thermodynamic behaviour. Also we observe that the elliptic flow is greater in string melting than the default model as in the default model the constituents are mainly hadrons for which ingredients (strings and di quarks) do not interact with others during their formation time where as in partonic model the partons interact with each other and with the increase in partonic cross section v_2 increases. Also we have studied the elliptic flow of identified hadrons with the same parameters by the default and the string melting version of the AMPT model as shown in fig 2. Again we observe a linear rise and greater v_2 in string melting than the default as the partonic flow dominates and both the models have shown mass ordering effect that is lighter mesons have greater elliptic flow than heavier baryons which remains almost same through out the p_T range in default and

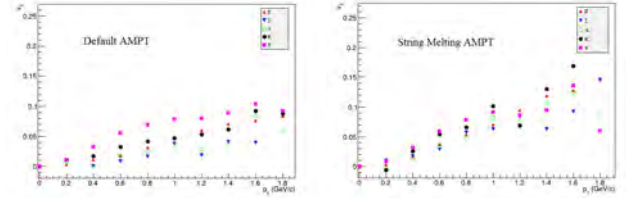
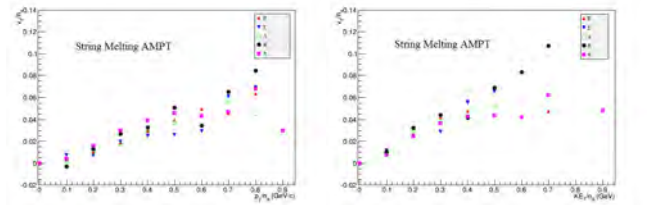


Figure 2: variations of v_2 for identified hadrons with p_T by the default i.e hadronic and the string melting i.e partonic versions of the AMPT model

it breaks for higher p_T $p_T \geq 1 \text{ GeV}$ in the string flow resulting in a baryon meson crossing. This mass ordering has been predicted by hydrodynamic model calculations [1] $v_{2,baryon} < v_{2,meson}$.

Then we have studied the scaling effect of elliptic flow first by the transverse momentum p_T then with the transverse kinetic energy $KE_T = m_T - m$ as it takes into account the relativistic effects which are especially important for lightest particle and also the pressure gradient that derives elliptic flow is directly linked to the collective energy of the emitted particles as shown in fig 3. Here a re-



(a) Variations of v_2/n_q with p_T/n_q (b) Variations of v_2/n_q with KE_T/n_q

Figure 3: Constituent Quark number scaling of elliptic flow v_2 with the p_T and KE_T by the string melting version of AMPT model

markable scaling is observed with KE_T/n_q than with the p_T/n_q results that models in the investigated p_T regime do not show behaviour that would be expected if quark coalescence were dominant and indicates that the early stage when v_2 has been built up is partonic in nature and effective constituent quark degrees of freedom play an important role in the hadronization process.

References

- [1] P.Huovinen et al., Phys. Lett. B 503 58 (2001).

CBM Publications 2015

- R. P. Adak *et al.*:
Thermal di-muon from QGP source at FAIR energy
Proc. DAE Symposium on Nuclear Physics **60** (2015) 798
<http://sympnp.org/proceedings/60/E47.pdf>
- J. Adamczewski-Musch *et al.*:
Influence of wavelength-shifting films on multianode PMTs with UV-extended windows
Nucl. Instrum. Methods A **783** (2015) 43
[doi:10.1016/j.nima.2015.02.014](https://doi.org/10.1016/j.nima.2015.02.014)
- S. Ahmad *et al.*:
Design and performance simulation of a segmented-absorber based muon detection system for high energy heavy ion collisions
Nucl. Instrum. Methods A **775** (2015) 139
[doi:10.1016/j.nima.2014.12.018](https://doi.org/10.1016/j.nima.2014.12.018)
- V. Akishina and I. Kisel:
Time-based Cellular Automaton track finder for the CBM experiment
J. Phys. Conf. Ser. **599** (2015) 012024
[doi:10.1088/1742-6596/599/1/012024](https://doi.org/10.1088/1742-6596/599/1/012024)
- P. P. Bhaduri:
Charmonium suppression in a baryon rich quark-gluon plasma
J. Phys. Conf. Ser. **599** (2015) 012018
[doi:10.1088/1742-6596/599/1/012018](https://doi.org/10.1088/1742-6596/599/1/012018)
- S. Biswas *et al.*:
Measurement of the spark probability of a GEM detector for the CBM muon chamber (MuCh)
Nucl. Instrum. Methods A **800** (2015) 93
[doi:10.1016/j.nima.2015.08.022](https://doi.org/10.1016/j.nima.2015.08.022)
- S. Biswas *et al.*:
Discharge probability measurement of the GEM detector for the CBM Muon Chamber
Proc. DAE Symposium on Nuclear Physics **60** (2015) 910
<http://sympnp.org/proceedings/60/G4.pdf>
- M. Deveau *et al.*:
Development of CMOS Monolithic Active Pixel Sensors for the ALICE ITS Outer Barrel and for the CBM-MVD
PoS(Vertex 2015)045 (2015)
http://pos.sissa.it/archive/conferences/254/045/VERTEX2015_045.pdf
- V. Friese:
Heavy-ion physics at high baryon densities
EPJ Web Conf. **95** (2015) 03010
[doi:10.1051/epjconf/20159503010](https://doi.org/10.1051/epjconf/20159503010)

- J. Gebelein *et al.*:
Smart Module Redundancy – Approaching Cost Efficient Radiation Tolerance
in: Transforming Reconfigurable Systems - A Festschrift Celebrating the 60th Birthday of Professor Peter Cheung, World Scientific Publishing 2015, pp. 83–99
[doi:10.1142/9781783266975_0005](https://doi.org/10.1142/9781783266975_0005)

- M. Guminski *et al.*:
Time and clock synchronization with AFCK for CBM
Proc. SPIE **9662** (2015) 96622V
[doi:10.1117/12.2205798](https://doi.org/10.1117/12.2205798)

- J. Heuser for the CBM Collaboration:
Status of the CBM experiment
EPJ Web Conf. **95** (2015) 01006
[doi:10.1051/epjconf/20159501006](https://doi.org/10.1051/epjconf/20159501006)

- J. Heuser:
The Silicon Tracking System of the CBM Experiment at FAIR
JPS Conf. Proc. **8** (2015) 022007
[doi:10.7566/JPSCP.8.022007](https://doi.org/10.7566/JPSCP.8.022007)

- C. Höhne for the CBM Collaboration:
Investigating compressed baryonic matter - the CBM experiment at FAIR
PoS(CPOD2014)028 (2015)
http://pos.sissa.it/archive/conferences/217/028/CPOD2014_028.pdf

- K. Kasinski, R. Kleczek and C. J. Schmidt:
Optimization of the microcable and detector parameters towards low noise in the STS readout system
Proc. SPIE **9662** (2015) 96622T
[doi:10.1117/12.2205699](https://doi.org/10.1117/12.2205699)

- K. Kasinski *et al.*:
Noise optimization of the time and energy measuring ASIC for silicon tracking system
Proc. MIXDES-2015, p. 490
[doi:10.1109/MIXDES.2015.7208569](https://doi.org/10.1109/MIXDES.2015.7208569)

- I. Kisel:
Scientific and high-performance computing at FAIR
EPJ Web Conf. **95** (2015) 01007
[doi:10.1051/epjconf/20159501007](https://doi.org/10.1051/epjconf/20159501007)

- P. Kurilkin *et al.*:
Compressed baryonic matter at FAIR: JINR participation
Int. J. Mod. Phys. Conf. Ser. **39** (2015) 1560098
[doi:10.1142/S2010194515600988](https://doi.org/10.1142/S2010194515600988)

- P. Larionov for the CBM Collaboration:
Overview of the Silicon Tracking System for the CBM experiment
J. Phys. Conf. Ser. **599** (2015) 012025
[doi:10.1088/1742-6596/599/1/012025](https://doi.org/10.1088/1742-6596/599/1/012025)

- J. Lehnert, W. F. J. Müller and C. J. Schmidt:
The GBT-based readout concept for the silicon tracking system of the CBM experiment
Proc. SPIE **9662** (2015) 96622S
[doi:10.1117/12.2205623](https://doi.org/10.1117/12.2205623)
- P. Loizeau *et al.*:
The prototype readout chain for CBM using the AFCK board and its software components
Proc. SPIE **9662** (2015) 96622X
[doi:10.1117/12.2205820](https://doi.org/10.1117/12.2205820)
- S. Mandal *et al.*:
Internal monitoring of GBTx emulator using IPbus for CBM experiment
Proc. SPIE **9662** (2015) 96622Q
[doi:10.1117/12.2205595](https://doi.org/10.1117/12.2205595)
- A.-D. Oancea *et al.*:
A resilient, flash-free soft error mitigation concept for the CBM-ToF read-out chain via GBT-SCA
Proc. FPL 2015 (2015)
[doi:10.1109/FPL.2015.7293999](https://doi.org/10.1109/FPL.2015.7293999)
- P. Otfinowski *et al.*:
Offset correction system for 128-channel self-triggering readout chip with in-channel 5-bit energy measurement functionality
Nucl. Instrum. Methods A **780** (2015) 114
[doi:10.1016/j.nima.2015.01.048](https://doi.org/10.1016/j.nima.2015.01.048)
- P. Senger:
The Compressed Baryonic Matter Experiment at FAIR
JPS Conf. Proc. **8** (2015) 022001
[doi:10.7566/JPSCP.8.022001](https://doi.org/10.7566/JPSCP.8.022001)
- M. Singla for the CBM Collaboration:
Radiation tolerance studies of neutron irradiated double sided silicon microstrip detectors
Nucl. Instrum. Methods A (2015), in press
[doi:10.1016/j.nima.2015.09.003](https://doi.org/10.1016/j.nima.2015.09.003)
- W. Zabołotny:
Improvement of FPGA control via high speed but high latency interfaces
Proc. SPIE **9662** (2015) 96623G
[doi:10.1117/12.2205441](https://doi.org/10.1117/12.2205441)

CBM presentations 2015

<http://cbm-wiki.gsi.de/cgi-bin/view/Public/PublicPresentations2015>

Doctoral, diploma, master and bachelor theses 2015

<http://cbm-wiki.gsi.de/cgi-bin/view/Public/Thesis2015>

Workshops and Meetings 2015

Workshops on module assembly for the Silicon Tracking System

16 –20 March 2015 and 23-27 November 2015, GSI, Darmstadt, Germany
2 –4 September 2015, LTU Ltd., Kharkiv, Ukraine

Progress with the development and production of module components as well as module assembly for the Silicon Tracking System were discussed during three workshops held in Germany and Ukraine. The teams established further optimized production parameters and equipment for read-out cables at LTU and achieved a complete work flow of the module assembly involving custom-made tools. The workshop in November also moved to KIT, Karlsruhe, to discuss STS module production in its Institute for Data Processing and Electronics.



Work meeting at GSI and KIT (left top/bottom) and LTU (right top/bottom).

<https://indico.gsi.de/conferenceDisplay.py?confId=3542>
<https://indico.gsi.de/conferenceDisplay.py?confId=4060>
<https://indico.gsi.de/conferenceDisplay.py?confId=4311>

25st CBM Collaboration Meeting

20 – 24 April 2015, GSI, Darmstadt, Germany

<https://indico.gsi.de/conferenceDisplay.py?confId=2960>**26st CBM Collaboration Meeting**

14 – 18 September 2015, Prague, Czech Republic

<https://indico.gsi.de/conferenceDisplay.py?confId=3009>

CBM STS-XYTER 2.0 submission review

21 – 23 October 2015, AGH Cracow, Poland

In October 2015, the CBM Silicon Tracking System Project carried out a comprehensive internal submission review of the STS-XYTER ASIC v2.0, the front-end chip for the read-out of the Silicon Tracking System. The event took place at the AGH University of Science and Technology, Cracow, home of the micro electronics design team. After tests of the previous prototype, the chip design was revised in order to improve the noise requirements, the testability and to accommodate a back-end compatible with the CERN GBT chip-set. The agenda covered the general status of developments and went through detailed aspects of the analogue front-end for application in the STS and MUCH detector systems as well as the new digital back-end with its protocol logic. Options for the chip submission were discussed, targeting the beginning of 2016. A post-submission planning made for a thorough testing of the chip and its application in final prototype detectors.



<https://indico.gsi.de/conferenceDisplay.py?confId=4230>

The CBM Collaboration

- **Aligarh, India, Department of Physics, Aligarh Muslim University**
N. Ahmad, M.D. Azmi, M. Irfan, H. Jahan, M.M. Khan
- **Beijing, China, Department of Engineering Physics, Tsinghua University**
Jianping Cheng, Zhi Deng, Dong Han, Xinjie Huang, Yuanjing Li, Pengfei Lyu, Yi Wang, Xianglei Zhu
- **Berlin, Germany, Konrad-Zuse-Zentrum für Informationstechnik Berlin (ZIB)**
A. Reinefeld, F. Schintke
- **Bhubaneswar, India, Institute of Physics**
N.R. Panda, P.K. Sahu, S.K. Sahu
- **Bucharest, Romania, Horia Hulubei National Institute of Physics and Nuclear Engineering (IFIN-HH)**
C. Andrei, D. Bartoș, I. Berceanu, A. Bercuci, G. Caragheorgheopol, V. Cătănescu, F. Constantin, A. Herghelegiu, M. Petriș, A. Petrovici, M. Petrovici, A. Pop, L. Radulescu, C. Schiaua, M.-G. Târziă
- **Bucharest, Romania, Atomic and Nuclear Physics Department, University of Bucharest**
D. Argintaru, V. Baban, C. Beșliu, M. Călin, T. Eșanu, A. Jipa, I. Lazanu, C. Ristea, O. Ristea, N.G. Tutas
- **Budapest, Hungary, Eötvös Loránd University (ELTE)**
M. Csanád
- **Budapest, Hungary, Institute for Particle and Nuclear Physics, Wigner Research Centre for Physics, Hungarian Academy of Sciences**
T. Kiss, T. Tölyhi, D. Varga, Gy. Wolf
- **Chandigarh, India, Department of Physics, Panjab University**
M.M. Aggarwal, A.K. Bhati, M. Kaur, L. Kumar
- **Darmstadt, Germany, Facility for Antiproton and Ion Research in Europe GmbH (FAIR)**
J. Eschke¹, W.F.J. Müller¹, M. Teklishyn²
- **Darmstadt, Germany, GSI Helmholtzzentrum für Schwerionenforschung GmbH (GSI)**
A. Abuhoza¹², M. Al-Turany, A. Andronic, R. Averbeck, E. Badura, T. Balog, D. Bertini, O. Bertini, P.P. Bhaduri³, V. Blinov, M.I. Ciobanu¹³, H. Deppe, D. Emschermann, H. Flemming, U. Frankenfeld, V. Friese, J. Frühauf, J. Hehner, J.M. Heuser, R. Holzmann, M. Ivanov, R. Karabowicz, M. Kiš, V. Kleipa, V. Klochkov⁴, K. Koch, P. Koczoń, W. Koenig, D. Kresan, A. Lebedev⁵, J. Lehnert, Y. Leifels, S. Löchner, P.-A. Loizeau, A. Lymanets², A.M. Marin Garcia, J. Markert, S. Masciocchi, D. Miskowiec, T. Morhardt, W. Niebur, J. Pietraszko, A. Rodriguez Rodriguez, C.J. Schmidt, K. Schweda, S. Seddiki, I. Selyuzhenkov, A. Senger, P. Senger⁴, C. Simons, M. Singla, D. Soyk, C. Sturm, A. Toia⁴, M. Träger, F. Uhlig, I. Vassiliev, O. Vasylyev, R. Visinka, C. Wendisch, N. Winckler, Junfeng Yang⁶, P. Zumbach, M. Zyzak
- **Darmstadt, Germany, Institut für Kernphysik, Technische Universität Darmstadt**
T. Galatyuk¹, A. Rost, F. Seck
- **Dresden, Germany, Institut für Strahlenphysik, Helmholtz-Zentrum Dresden-Rossendorf (HZDR)**
Xingming Fan, B. Kämpfer¹⁴, R. Kotte, A. Laso García¹⁴, L. Naumann, J. Wüstenfeld
- **Dubna, Russia, Laboratory of Information Technologies, Joint Institute for Nuclear Research (JINR-LIT)**
T. Ablyazimov, P. Akishin, E. Akishina, T. Akishina, E. Alexandrov, I. Alexandrov, D. Belyakov, O. Derenovskaya, I. Filozova, Valery Ivanov, Victor Ivanov, A.V. Kryanev⁷, G. Ososkov, A. Raportirenko, P. Zrelov

- **Dubna, Russia, Veksler and Baldin Laboratory of High Energy Physics, Joint Institute for Nuclear Research (JINR-VBLHEP)**
Yu. Anisimov, S. Avdeev, M. Baznat, G. Berezin, A. Bychkov, V. Chepurinov, D. Dementiev, S. Dubnichka, Z. Dubnichkova, V.V. Elsha, O. Fateev, V. Golovatyuk, K. Gudima, Yu. Gusakov, A. Ierusalimov, V. Karnaukhov, G. Kekelidze, A. Khvorostukhin, V. Kirakosyan, V. Kramarenko, A. Kurilkin, P. Kurilkin, S. Kuznetsov, V. Ladygin, A. Malakhov, V. Mialkovski, Yu. Murin, S. Parzhitskiy, D. Peshekhonov, V. Peshekhonov, S. Razin, A. Shabunov, A.D. Sheremetiev, N. Shumeiko, I. Tsakov, Aleksey Voronin, B. Yuldashev, N.I. Zamiatin, Yu. Zanevsky, A. Zinchenko, V. Zryuev
- **Frankfurt, Germany, Frankfurt Institute for Advanced Studies, Goethe-Universität Frankfurt (FIAS)**
V. Akishina^{5,1}, J. de Cuveland, S. Gorbunov, H. Hartmann, D. Hutter, I. Kisel, G. Kozlov⁵, V. Kucher, V. Lindenstruth¹, M. Pugach^{1,2}, V. Vovchenko
- **Frankfurt, Germany, Institut für Kernphysik, Goethe-Universität Frankfurt**
S. Amar-Youcef, H. Appelshäuser, C. Blume, J. Book, H. Cherif¹, M. Deveau, D. Doering, I. Fröhlich, P. Ghosh¹, S. Gläsel, P. Kisel^{1,5}, P. Klaus, M. Koziel, E. Krebs, G. Kretschmar, P. Larionov¹, Qiyan Li⁸, B. Linnik, H. Malygina^{1,2}, J. Michel, I. Momot^{1,2}, C. Müntz, M. Penschuck, M. Petri, F. Roether, J. Scholten, P. Sitzmann, S. Strohauer, J. Stroth¹, M. Tanha, T. Tischler, M. Wiebusch
- **Frankfurt, Germany, Institute for Computer Science, Goethe-Universität Frankfurt**
T. Breitner, LuYao Chen, H. Engel, C. García Chávez, J. Gebelein, A. Gómez Ramírez, T. Janson, U. Kerschull, C. Lara, J. Lehrbach, J.A. Lucio Martínez, S. Manzh, A. Oancea
- **Gatchina, Russia, National Research Center "Kurchatov Institute" B.P.Konstantinov, Petersburg Nuclear Physics Institute (PNPI)**
V. Baublis, V. Dobryn, V. Golovtsov, D. Ivanischev, Vladimir Ivanov⁷, A. Khanzadeev⁷, L. Kochenda⁷, B. Komkov, V. Kozlov, P. Kravtsov⁷, E. Kryshen, L. Kudin, N. Miftakhov, V. Nikulin, E. Rostchin⁷, Yu. Ryabov, V. Samsonov^{7,9}, O. Tarassenkova, S. Volkov, M. Vznuzdaev, M. Zhalov
- **Gießen, Germany, Justus-Liebig-Universität Gießen**
J. Bendarouach, C.A. Deveau, M. Dürr, C. Höhne, S. Lebedev⁵, E. Lebedeva, T. Mahmoud
- **Guwahati, India, Department of Physics, Gauhati University**
B. Bhattacharjee, B. Debnath, K. Dey
- **Hefei, China, Department of Modern Physics, University of Science & Technology of China (USTC)**
Ping Cao, Dongdong Hu, Di Jiang, Xin Li, Ming Shao, Guofeng Song, Yongjie Sun, Zebo Tang, Rongxing Yang, Yifei Zhang, Lei Zhao, Jiajun Zheng
- **Heidelberg, Germany, Physikalisches Institut, Universität Heidelberg**
A. Akram, E. Bao, I. Deppner, D. Gottschalk, N. Herrmann, C. Simon
- **Indore, India, Indian Institute of Technology Indore**
R. Sahoo, S. Tripathy
- **Jaipur, India, Physics Department, University of Rajasthan**
R. Raniwala, S. Raniwala
- **Jammu, India, Department of Physics, University of Jammu**
A. Bhasin, A. Gupta, S. Mahajan, B.V.K.S. Potukuchi, S.S. Sambyal
- **Karlsruhe, Germany, Karlsruhe Institute of Technology (KIT)**
S. Bähr, M. Balzer, J. Becker, T. Blank, S.P.D. Figuli, L. Meder, O. Sander, M. Weber
- **Katowice, Poland, Institute of Physics, University of Silesia**
A. Bubak, E. Kaptur, S. Kowalski

- **Kharagpur, India, Indian Institute of Technology Kharagpur**
T.K. Bhattacharyya, S. Sarangi, A.K. Singh, I. Som
- **Kolkata, India, Department of Physics, Bose Institute**
R.P. Adak, S. Biswas, Supriya Das, S.K. Ghosh, S. Raha, R. Ray, S. Samanta
- **Kolkata, India, Department of Physics and Department of Electronic Science, University of Calcutta**
S. Bandyopadhyay, A. Bhattacharyya, A. Chakrabarti, Sanatan Chattopadhyay, G. Gangopadhyay, S. Sau
- **Kolkata, India, Variable Energy Cyclotron Centre (VECC)**
Subhasis Chattopadhyay¹⁰, A.K. Dubey, V. Jain, A. Kumar, S. Mandal, C. Nandi, E. Nandy, T. Nayak, V.S. Negi, S. Pal, J. Saini, V. Singhal
- **Kraków, Poland, AGH University of Science and Technology (AGH)**
M. Baszczyk, A. Drozd, J. Gajda, P. Gryboś, K. Kasiński, R. Kłeczek, P. Kmon, W. Kucewicz, P. Maj, L. Mik, P. Otfinowski, J. Rauza, R. Szczygieł, M. Żoładź
- **Kraków, Poland, Marian Smoluchowski Institute of Physics, Jagiellonian University**
M. Adamczyk, T. Barczyk, J. Brzychczyk, L. Dutka, Z. Majka, R. Najman, R. Płaneta, Z. Sosin, P. Staszczel, A. Wieloch
- **Kyiv, Ukraine, High Energy Physics Department, Kiev Institute for Nuclear Research (KINR)**
A. Chaus, A. Kovalchuk, V. Kyva, V. Militsija, V. Pugatch
- **Kyiv, Ukraine, Department of Nuclear Physics, Taras Shevchenko National University of Kyiv**
O. Bezshyyko, L. Golinka-Bezshyyko, I. Kadenko, Yu. Onishchuk, V. Plujko, A. Volochniuk
- **Mannheim, Germany, Institut für Technische Informatik, Universität Heidelberg**
P. Fischer, M. Krieger, S. Schatral
- **Moscow, Russia, Institute for Nuclear Research (INR)**
O. Andreeva, D. Finogeev, M. Golubeva, F. Guber, A. Ivashkin, A. Kurepin, N. Kurepin, A. Maevskaya, S. Morozov, O. Petukhov, A. Reshetin, A. Shabanov, N. Topil'skaya, E. Usenko
- **Moscow, Russia, Institute for Theoretical and Experimental Physics (ITEP)**
A. Akindinov, I. Alekseev, S. Belogurov, A. Chernogorov, D. Golubkov, F. Khasanov, S. Kiselev, I. Korolko, D. Malkevich, K. Mikhailov, A. Nedosekin, E. Ovcharenko⁵, V. Plotnikov, M. Prokudin, I. Rostovtseva, A. Semennikov, R. Sultanov, D. Svirida, Yu. Zaitsev
- **Moscow, Russia, National Research Nuclear University MEPhI**
E. Atkin, Yu. Bocharov, V. Butuzov, P. Ivanov, E. Malankin, O. Malyatina, D. Normanov, A. Petrovskiy, V. Shumikhin, A. Simakov, M. Strikhanov
- **Moscow, Russia, National Research Centre "Kurchatov Institute"**
D. Blau, A. Kazantsev, V. Manko, I. Sibiryak, I. Yushmanov
- **Moscow, Russia, Skobeltsyn Institute of Nuclear Physics, Lomonosov Moscow State University (SINP-MSU)**
N. Baranova, D. Karmanov, M. Korolev, M. Merkin, Alexander Voronin
- **Münster, Germany, Institut für Kernphysik, Westfälische Wilhelms-Universität Münster**
R. Berendes, C. Bergmann, N. Heine, P. Kähler, Ch. Klein-Bösing, M. Kohn, J.P. Wessels
- **Prague, Czech Republic, Czech Technical University (CTU)**
V. Petráček, L. Škoda

- **Protvino, Russia, Institute for High Energy Physics (IHEP)**
S. Golovnya, S. Gorokhov, A. Kiryakov, I. Lobanov, E. Lobanova, Yu. Tsyupa, A. Vorobiev
- **Pusan, Korea, Pusan National University (PNU)**
Kunsu Oh, Jihye Song, Sanguk Won, In-Kwon Yoo
- **Řež, Czech Republic, Nuclear Physics Institute of the Czech Academy of Sciences**
A. Kugler, V. Kushpil, V. Mikhaylov, A. Prakash, O. Svoboda, P. Tlustý
- **Split, Croatia, University of Split**
M. Anđelić, I. Carević, M. Dželalija
- **Srinagar, India, Department of Physics, University of Kashmir**
F. Ahmad, S. Ahmad, S. Bashir, S.A. Lone, M.F. Mir, W. Raja
- **St. Petersburg, Russia, Ioffe Institute, Russian Academy of Sciences**
V. Eremin, E. Verbitskaya
- **St. Petersburg, Russia, V.G. Khlopin Radium Institute (KRI)**
O. Batenkov, V. Jakovlev, V. Kalinin, A. Veshikov
- **St. Petersburg, Russia, St. Petersburg Polytechnic University (SPbPU)**
A. Berdnikov, Y. Berdnikov
- **Strasbourg, France, Institut Pluridisciplinaire Hubert Curien (IPHC), IN2P3-CNRS and Université de Strasbourg**
G. Claus, A. Dorokhov, M. Goffe, A. Himmi, K. Jaaskelainen, F. Rami, I. Valin, M. Winter
- **Tübingen, Germany, Physikalisches Institut, Eberhard Karls Universität Tübingen**
Susovan Das, E. Friske, B. Heß, E. Lavrik, I. Panasenکو², H.R. Schmidt
- **Varanasi, India, Department of Physics, Banaras Hindu University**
B.K. Singh, C.P. Singh
- **Warsaw, Poland, Institute of Electronic Systems, Warsaw University of Technology**
A. Byszuk, M. Gumiński, G. Kasproicz, J. Pluta, K. Poźniak¹¹, R. Romaniuk, D. Wielanek, W. Zabołotny¹¹
- **Warsaw, Poland, Institute of Experimental Physics, University of Warsaw**
M. Kuc, T. Matulewicz, K. Piasecki, J. Rozynek, B. Sikora, K. Siwek-Wilczyńska, I. Skwira-Chalot, J. Tarsiuk, K. Wiśniewski
- **Wuhan, China, College of Physical Science and Technology, Central China Normal University (CCNU)**
Wendi Deng, Sheng Dong, Guangming Huang, Feng Liu, Xiaofeng Luo, Shusu Shi, Dong Wang, Changzhou Xiang, Nu Xu, Zhongbao Yin, Daicui Zhou
- **Wuppertal, Germany, Fakultät für Mathematik und Naturwissenschaften, Bergische Universität Wuppertal**
K.-H. Becker, J. Förtsch, K.-H. Kampert, I. Kres, C. Pauly, D. Pfeifer, J. Pouryamout, S. Querschfeld, J. Rautenberg, S. Reinecke
- **Yichang, China, College of Science, China Three Gorges University (CTGU)**
Shengqin Feng, Xi-Wei Wang, Ke-Jun Wu, Sheng Zheng, Jing Zhou

Additional affiliations:

- ¹ GSI Helmholtzzentrum für Schwerionenforschung GmbH (GSI), Darmstadt, Germany
- ² High Energy Physics Department, Kiev Institute for Nuclear Research (KINR), Kyiv, Ukraine
- ³ Variable Energy Cyclotron Centre (VECC), Kolkata, India
- ⁴ Institut für Kernphysik, Goethe-Universität Frankfurt, Frankfurt, Germany
- ⁵ Laboratory of Information Technologies, Joint Institute for Nuclear Research (JINR-LIT), Dubna, Russia
- ⁶ Department of Modern Physics, University of Science & Technology of China (USTC), Hefei, China
- ⁷ National Research Nuclear University MEPhI, Moscow, Russia
- ⁸ College of Physical Science and Technology, Central China Normal University (CCNU), Wuhan, China
- ⁹ St. Petersburg Polytechnic University (SPbPU), St. Petersburg, Russia
- ¹⁰ Department of Physics, Bose Institute, Kolkata, India
- ¹¹ Institute of Experimental Physics, University of Warsaw, Warsaw, Poland
- ¹² also: King Abdulaziz City for Science and Technology (KACST), Riyadh, Saudi Arabia
- ¹³ also: Institute of Space Science, Bucharest, Romania
- ¹⁴ also: Technische Universität Dresden, Dresden, Germany

Contacts

Chairman of the Collaboration Board

Yuri Zaitsev
zaitsev@itep.ru

Spokesman

Peter Senger
p.senger@gsi.de

Deputy Spokesman

Norbert Herrmann
n.herrmann@physi.uni-heidelberg.de

Deputy Spokesman

Subhasis Chattopadhyay
sub@veccal.ernet.in

Technical Coordinator

Walter Müller
w.f.j.mueller@gsi.de

Physics Coordinator

Volker Frieze
v.frieze@gsi.de

Ressource Coordinator

Jürgen Eschke
j.eschke@gsi.de

Management Board

S. Chattopadhyay, N. Herrmann, M Petrovici, F. Rami, J. Stroth, Y. Zaitsev

<http://www.fair-center.eu/for-users/experiments/cbm.html>

